UNIVERSITY OF ADELAIDE LIBRARY
4.1.95

Simultaneous Coating and Erosion of an Object Immersed in a Fluidized Bed

by

Gordon Douglas Ingram

Department of Chemical Engineering,

The University of Adelaide

A thesis submitted for the degree of

Master of Engineering Science

May 1994

Amended in response to examiners' comments, October 1994

Awarded 1995

DECLARATION

I declare that this thesis contains no material which has been accepted for the award of any other degree or diploma in any university or other tertiary institution and that, to the best of my knowledge and belief, contains no material previously published or written by another person, except where due reference is made in the text of the thesis.

I give consent to this copy of my thesis, when deposited in the University Library, being available for loan and photocopying.

Gordon Douglas Ingram

26 May 1994.

ABSTRACT

The aim of this study is to determine the behaviour of a surface subjected to competing deposition and erosion processes in a fluidized bed. Experiments were performed on an electrically-heated, vertical U-tube in a bubbling fluidized bed of glass ballotini. To support the principal coating-erosion experiments, melting temperature, fluidization and heat transfer studies were conducted. High-temperature sintering caused particle deposition which was opposed by the natural erosive action of the fluidized bed. The experimental results were analysed by a one-dimensional mathematical model which combines fluidized bed powder coating theory with knowledge of the erosion of tubes in a fluidized bed. While simple analytical steady state solutions exist, dynamic solution of the model requires numerical techniques.

Two regimes of behaviour are encountered: (i) ***low power*** in which the surface remains below the sintering temperature, and (ii) ***high power*** where the formation of an insulating deposit raises the immersed surface temperature. The low/high power transition is sudden; near the boundary, small changes in the bed's operating conditions can substantially alter the state of the system.

The sintering temperature - the temperature of an immersed surface at which particles start to adhere permanently to the surface - is a key system parameter. It was found to vary with the superficial gas velocity and the temperature of the fluidized bed; a preliminary correlation was developed.

Deposits that form on an immersed surface may be porous; this porosity strongly affects the properties of the coating, and hence the predictions of the mathematical model.

Although a constant porosity was used throughout the present calculations, in reality a deposit's porosity will decrease with time and temperature through interparticle sintering. A method for including these sintering effects in the model was outlined.

This study furthers the understanding of the fouling of firetube heat transfer surfaces immersed in fluidized beds. Particularly significant is the relationship that was discovered between the fluidizing gas velocity, the bed temperature and the surface temperature that leads to deposition. The above findings were related to an important, emerging technology - the pulse-enhanced, indirectly-heated fluidized bed gasifier developed by Manufacturing and Technology Conversion International.

ACKNOWLEDGEMENTS

First of all, I must thank Professor Pradeep Agarwal, my supervisor, for his concern, boundless enthusiasm and wise guidance throughout this project. I thank the other academic staff of the Department for their help, particularly Professor John Agnew and Dr Brian O'Neill who supervised me during Professor Agarwal's absence.

The Chemical Engineering Department's workshop staff - Bruce Ide, Ted Jones, Peter Kay and Brian Mulcahy - have my thanks for the effort they put into the experimental apparatus. I am especially indebted to Ted for his speed and skill in performing the majority of this work, for sharing his knowledge of the business world with me, and for his friendship. I am grateful to Andrew Wright for his guidance in laboratory procedures.

Mary Barrow, Jeanette Holman and Elaine Minerds, the Department's administrative staff, I thank for their willing assistance in the preparation of this manuscript and throughout my time at the University of Adelaide. My thanks go particularly to Mary who typed part of this document.

Ta-Sanh Tran has my thanks for his help with computer problems. I am also grateful to Vicki Greenwood and Corina Stamatoiu for their guidance and help in photographic matters.

For their friendship and advice, I thank my fellow postgraduate students in the Department of Chemical Engineering. Mark Biggs, Ashley Hull, Kok Seng Lim and Temi Linjewile contributed most of all to my growth as a chemical engineering researcher. They have my great respect and thanks.

The Australian Government provided me with a Commonwealth Postgraduate Research Award (Priority) for which I am grateful.

Finally, I thank my family for their support throughout this terribly long and trying project.

TABLE OF CONTENTS

LIST OF TABLES

LIST OF FIGURES

UNIVERSITY OF ADELAIDE LIBRARY

Chapter 1:

INTRODUCTION

Fluidization is the operation by which solid particles are transformed into a fluidlike state through suspension in a gas or liquid (Kunii and Levenspiel, 1991, p1). It is the bubbling, gas-solid system that is the focus of this study. Gas fluidized beds have many useful properties including: excellent temperature uniformity, rapid solids mixing, high rates of gas-particle heat and mass transfer, and ease of control. Accordingly, they find wide application in industry - from large-scale continuous units in petroleum refineries through to tiny batch systems used to prepare pharmaceuticals. Catalytic, non-catalytic and biochemical reactors, adsorbers, heat exchangers, and granulators are among the roles that fluidized beds play.

It is significant that, in many of these processes, the particles may become cohesive. Of course, some attractive forces are always present (for example, Van der Waals and electrostatic forces), but cohesion can also result from the formation of solid or liquid *bridges* between particles. The addition of a liquid binder, drying and crystallisation, high-temperature sintering, and chemical reaction can all cause bridging. In some applications, particle cohesion is desirable - it is a convenient way to remove ash from fluidized bed combustors and gasifiers; a granulator operates solely through the stickiness of the particles. At other times, cohesion is undesirable and results in the formation of agglomerates that sink through the bed and eventually block the distributor. Rapid defluidization of the bed may also occur and this is almost certainly catastrophic. Defluidization and agglomeration may be avoided by a number of measures: increasing

the gas velocity or the particle size, using vibrofluidization, and introducing additives to the bed, among others. *The state of a fluidized bed is determined by the balance between the interparticle binding and breaking forces.*

The preceding statements are concerned with particle-particle cohesion. However, stickiness may be encountered in another fluidized bed situation - the interaction of particles with a surface immersed in the bed. Immersed surfaces occur as: in-bed heat transfer tubes, objects undergoing powder coating or heat treatment, baffles and packings designed to modify the bed hydrodynamics, the containing walls and distributor of the bed. As in the particle-particle case, there are a number of processes that may lead to the adhesion of particles onto an immersed surface. These include: electrostatic attraction (both natural and artificially-induced), capture by a liquid binder coated on the surface, solidification, and sintering. Now, are there processes, analogous to interparticle breaking mechanisms, that tend to remove particles from an immersed surface? High-velocity impact by particles carried in the wake of passing bubbles may be one such process.

The objective of this project is to determine the behaviour of an immersed surface that is subject to both particle deposition and removal.

For simplicity and concreteness, a particular model system was adopted from the outset. It involved only one physical mechanism for each of particle deposition and removal, a single type of bed material, and a reasonably simple geometry. More exactly, the immersed surface was a U-tube heater fixed centrally in a cylindrical fluidized bed and operated under constant heat flux conditions. The bed itself comprised glass beads fluidized by heated air. In this configuration, high-temperature sintering causes the particles to adhere to the immersed surface. Erosion induced by the impact of particles carried by passing bubbles counteracts the deposition. This model system does not have any direct industrial significance - it was used as the basis for a fundamental study.

However, it is related to a new and very promising energy and environmental technology which is described below.

Near the end of this project, the author became aware of a system developed by Manufacturing and Technology Conversion International (MTCI) of Columbia, Maryland, U.S.A. and licensed to ThermoChem Inc. (Santa Fe Springs, California, U.S.A.). Their pulse-enhanced, indirectly-heated fluidized bed gasifier is unique because the energy needed for gasification is supplied by in-bed heat transfer tubes through which pass the exhaust gases of a pulse combustor (ThermoChem, 1993). In conventional gasifiers, the bed is fluidized by an air-steam mixture - the combustion and hydrogasification reactions of the carbonaceous material provide the energy needed for the endothermic steam and carbon dioxide gasification reactions. Gururajan et al. (1992) have shown that carbon conversion in these circumstances may be dominated by combustion and devolatilisation. Gasification, the desired process, can be quite limited. In contrast, MTCI's gasifier is fluidized by steam only, so no combustion of the feed material takes place and the product gas is not diluted by nitrogen or oxygen. A portion of the gasifier product, a hydrogen-rich medium-BTU gas, is burnt to drive the pulse combustor (and hence the gasifier itself); the rest is available for export to other parts of the plant as a chemical feedstock or fuel.

The development of this technology was motivated by the environmental and economic advantages of converting waste into clean energy. MTCI claims that their system will successfully treat a wide range of agricultural, industrial and municipal wastes, which are otherwise disposed of by landfill. As the cost of landfilling increases and as the prices of fossil fuels rise, converting waste into energy becomes more attractive. In addition, since the gasifier produces a clean-burning gas, less money has to be spent on flue gas processing to meet increasingly-stringent atmospheric emission regulations. MTCI and ThermoChem Inc. are pursuing other applications of the pulse-enhanced, indirectly-heated fluidized bed gasifier. A chemical and energy recovery process has been

developed for the spent liquors of the paper industry - which eliminates the significant safety problems of previous technologies. Importantly, ThermoChem Inc. has been awarded funding from the U.S. Department of Energy's Clean Coal IV program to construct a 430 t/day coal gasification demonstration plant.

Do the immersed heat transfer tubes of MTCI's gasifier experience simultaneous particle deposition and removal? How may this affect the gasifier's performance?

As in the model system used in this thesis, high-temperature sintering may cause the bed particles to deposit onto the gasifier's tubes. Other coating mechanisms may also be active - for example, adhesion by chemical reaction promoted by the high surface temperature of the tubes, or through the action of a sticky substance such as molten ash. Erosion caused by the bed material will oppose deposition, as it does in the model system. If a deposit does form on the gasifier's immersed tubes, then the efficiency of heat transfer will decline, with a number of consequences. Overheating of the tubes, decreased metal wastage and changes to the tubes' corrosion resistance are all possibilities.

Clearly, the operation of an industrial gasifier is much more complex than that of the bench-scale model system studied in this project. However, if a surface deposition problem does arise in a commercial unit, the trouble-shooter will benefit from a knowledge of the underlying principles gained from the study of a simpler system. The author believes that this project will lead to a better understanding of the fouling behaviour of a surface immersed in a fluidized bed.

In *Chapter 2*, two fields related to the problem under consideration are reviewed with an emphasis to mathematical modelling - fluidized bed powder coating and the erosion of immersed heat transfer tubes. Several instances of combined coating and erosion processes in fluidized beds are cited. *Chapter 3* describes the apparatus and procedures

used in the experimental part of this study. Results from a series of supporting experiments are discussed in that chapter also. A theoretical model is developed and explored in *Chapter 4*, which includes a detailed parametric study of the non-dimensionalised model. *Chapter 5* compares the coating-erosion experiments with the model developed in the previous chapter. The relevance of this study to the pulse-enhanced, indirectly-heated fluidized bed gasifier is discussed further. Finally, the conclusions of the project and recommendations for future work are presented in *Chapter 6*.

Chapter 2:

LITERATURE REVIEW

In this chapter, two fields relevant to the problem at hand are briefly reviewed - fluidized bed powder coating and the erosion of tubes in fluidized beds. A few cases of combined coating and erosion are mentioned.

2.1 INTRODUCTION

When an object, heated above the particle sintering temperature, is immersed in a bubbling fluidized bed of fusible material, a coating of particles will form on its surface. The thickness of this coating is determined by a balance between two competing processes:

- a **thermal process** which causes particles near the object to become partially molten and adhere to its surface, hence increasing the thickness of the coated layer;
- a **hydrodynamic process** wherein other particles in the bed act to shear off those forming the outer layer of coating, thus causing the thickness to decrease.

Since the 1950s, the practice of fluidized bed powder coating has taken advantage of the first mechanism. A great variety of metallic objects are coated with a thin layer of plastic

by this method. More recently, much attention has been devoted to the study of fluidized bed combustors for the efficient and environmentally-acceptable utilisation of coal and low-grade fuels. The erosion (or wastage) of immersed heat transfer tubes, which is a hydrodynamic phenomenon, has emerged as an issue of some importance. In the following, fluidized bed powder coating and the erosion of immersed heat transfer tubes are reviewed with an emphasis on mathematical modelling. Finally, reported instances of combined coating and erosion are discussed briefly.

2.2 FLUIDIZED BED POWDER COATING

In its simplest form, fluidized bed powder coating involves heating the object that is to be coated above the softening temperature of the polymer that will form the coating. The hot object is then immersed in an incipiently fluidized bed of the plastic powder for a given time. When the object is removed, an even coating of fused plastic powder is observed over its entire surface. Afterwards, it may be necessary to reheat the object in a conventional oven for extended times to produce a smooth, non-porous coating.

There are several variations on the basic process. Instead of preheating the object, it may be heated while inside the bed by a high-frequency induction coil. Plastic insulation is often applied to electrical wire in a continuous powder coating process - the wire is continuously fed into and removed from the fluidized bed. While it is within the bed, the wire is heated by induction. Two other approaches do not require heating of the object to be coated. One involves the application of an electrostatic charge to the bed particles and grounding of the object, so that the particles are attracted to the object. In the other approach, the object is coated with a sticky substance before immersion in the fluidized bed. To make the plastic coating permanent, it is necessary with both methods to bake the object in a conventional oven afterwards. An early, but comprehensive, discussion of the practical aspects of fluidized bed powder coating is given in Landrock (1965). More recent information on powder coating in general appears in Richart (1985). This review,

however, is confined to the coating of a stationary object in a fluidized bed due to thermal effects alone. Both preheating and in-bed heating are considered.

From a mechanistic point of view, the coating process initially involves the transfer of heat from the object directly to the fluidized bed. The particles in contact with the object heat up, melt and adhere to its surface. In a similar way, the particles which touch the first layer of adhered particles will heat up and stick to those already there. Thus, after the initial layer has formed, heat is transferred from the immersed body into the continuously-growing layer of coating and thence, to the fluidized bed. In essence, the process involves the transfer of heat to an interface that moves because of a change of phase. Such processes comprise an important class, and are known generically as Stefan Problems.

Melting and solidification are the most important instances of Stefan problems and much of the available theory is stated in such terms. Because the position of the moving boundary is not specified beforehand, Stefan problems are, in general, non-linear. Separate solutions cannot be superposed. Many early analytical solutions appear in Carslaw and Jaeger (1959) and Bankoff (1964). All of these are one-dimensional and most use rectangular coordinates, although there are a few based on the radial direction in a cylindrical coordinate system. The majority of the solutions assume constant thermal and physical properties and have restrictive boundary conditions. A more recent comprehensive discussion of Stefan problems and their solution is given in Crank (1984). Meirmanov (1992) explores the fundamental aspects of existence, uniqueness and the basic structure of the solutions.

Unsurprisingly, realistic Stefan problems are often solved by numerical methods. Sometimes, analytical solutions are used to start off a numerical scheme. Both finite element and finite difference methods are employed to solve Stefan problems (Bankoff,

1964; Crank, 1984). A detailed discussion of numerical techniques appears in Crank (1984).

In both analytical and numerical work, Landau's transformation (Landau, 1950) or a variant thereof is commonly used to anchor the moving boundary and thus simplify the problem. An aspect of the implementation of Landau's transformation in this project is discussed in Appendices A and B.

Despite its widespread use in industry and the extensive modelling of related Stefan problems, relatively few mathematical descriptions of fluidized bed powder coating have been presented. Indeed, only two groups seem to have published models - Gutfinger and associates; and Elmas.

The variables that influence the coating process are numerous. Many are listed in Table 2.1 (Landrock, 1965; Gutfinger and Chen, 1969; Elmas, 1973). Because of the large number of variables that effect the process and the inherent complexity of Stefan problems, many assumptions are made to develop and solve a model. The assumptions which are common to the works of Gutfinger and associates, and Elmas are discussed next.

2.2.1 Common Assumptions

It is assumed that the physical and thermal properties of the immersed body remain constant. For example, the body is not allowed to contract on cooling. Its shape must be sufficiently simple that the coating can be described in a one-dimensional manner. The object is assumed to be reasonably small and orientated so that it experiences the same type of fluidized environment over its entire surface. Another important assumption is that the temperature in the object is uniform at all times. Both groups argue that since the objects to be coated are always metallic, this assumption will be

Table 2.1: Factors affecting fluidized bed powder coating (Landrock, 1965; Gutfinger and Chen, 1969; Elmas, 1973).

Properties of the immersed body:

- density
- specific heat capacity
- thermal conductivity
- volume
- surface area
- surface finish
- nature of surface material
- shape

Properties of the plastic powder:

- density
- specific heat capacity
- latent heat of fusion (if significant)
- thermal conductivity
- softening temperature
- viscosity of the molten polymer
- nature of the polymer
- particle size
- particle size distribution
- particle shape

Properties of the fluidizing gas:

- density
- thermal conductivity
- viscosity
- moisture content

Operational parameters:

- initial temperature of the immersed body
- rate of in-bed heating of the immersed body
- temperature of the fluidized bed
- immersion (or residence) time of the body in the fluidized bed
- superficial gas velocity
- location and orientation of the immersed body while in the bed
- size of the fluidized bed
- feed and recycle rates of the powder

valid. Certainly, it is likely to be true for objects made of high thermal conductivity metals such as copper. However, for iron and steels, which have substantially lower thermal conductivities, this assumption may be questionable. When coating does not occur, a simple "lumped heat capacity" analysis may be used to predict the temperature of an isothermal object exposed to a convective environment. The object may be considered to be isothermal when its Biot number is low - commonly (Holman, 1989):

$$Bi_b = \frac{h\,(V_b / A_b)}{k_b} < 0.1 \qquad (2.1)$$

However, when coating does occur, another condition for isothermality - based on the resistance to heat transfer through the coated layer - is needed. Without such a criterion, the reasonableness of the assumption of a uniform object temperature cannot be judged directly. If it cannot be assumed that the object is isothermal, the unsteady state conduction equation must be employed inside the object, thereby increasing the complexity of the problem.

The properties of the plastic powder - density, specific heat and thermal conductivity - are assumed to be constant during coating. Elmas (1970) advocates the use of polymer properties averaged over the temperature range of interest. Thus, for any property, p, over the temperature range T_1 to T_2:

$$\bar{p} = \frac{\int_{T_1}^{T_2} p(T)\,dT}{\int_{T_1}^{T_2} dT} \qquad (2.2)$$

is an appropriate average. Note that the corresponding effective properties of the coating layer depend strongly on the porosity of the coating. Elmas, in his dip-coating experiments with polystyrene, reports that the porosity of the coating was 0.4, about the same as that of a homogeneously fluidized bed (Elmas, 1973, p39,43). It is well known

that at elevated temperatures, particulate solids sinter together to reduce their combined surface area (Askeland, 1990). Eventually, all the voids will disappear, leaving a continuous solid. Now, another assumption is evident - the porosity of the coated layer known and constant. For the short immersion times used in fluidized bed powder coating, the use of effective coating properties based on a porosity of about 0.4 may be most appropriate. In addition, it is assumed that the partially molten plastic does not flow down the sides of the object. This is reasonable since, molten polymers have a high viscosity and the times involved are short. For polymers that possess a definite latent heat of fusion, the particles will become sticky at their melting temperature. Plastics without a latent heat of fusion will melt over a temperature range. It is assumed that this behaviour may be represented by a single effective melting temperature. Elmas (1973, p28-29) describes how this temperature may be measured:

> *"the object to be coated is heated to various temperatures and dipped into the fluidised bed. The minimum object temperature at which the particles begin to stick to its surface can be taken as the sticking temperature [the effective melting temperature] of the polymer.".*

Still, the specific heat is assumed to be constant.

The particle diameter is assumed to be small compared to the size of the immersed body. This is so the coating process may be viewed as the continuous growth of a film, rather than as a sequence of discrete events in which individual particles adhere to the object. Elmas notes that the plastic particles used in industry have diameters in the range 20-200 $x10^{-6}$m, while the objects to be coated have characteristic dimensions around 1000 $x10^{-6}$m. In practice, the continuous nature of the coating process is a reasonable assumption. In any cases where it may be inappropriate, the adhesion of single particles must be considered - perhaps in a manner similar to those of Tsao et al. (1982) and Rehmat et al. (1988), among others. No specific assumptions are made about the shape

of the particles or their size distribution. The only requirement is that the powder may be fluidized.

On the operational side, when there is no in-bed heating, the object to be coated is preheated above the melting temperature. The analyses apply only while the coated layer is actively growing. It is assumed that all parts of the object's surface spend exactly the same time immersed in the bed. This assumption is clearly better for small objects than for large ones. Implicitly, the superficial velocity of the fluidizing gas is assumed to remain constant.

All the models on review here assume that the surface temperature of the coated layer is constant at the melting (or effective melting) temperature of the polymer. However, Gutfinger and Chen (1970) state that this is:

> *"a very questionable assumption in the developed theory. The temperature on the surface of the coating must remain higher than the softening point of the polymer if the coating is to continue to build up."*

Unfortunately, they propose no better assumption.

Finally, the existence and uniqueness of the temperature profile in the coated layer and the thickness of the coating is assumed. Gutfinger and Chen (1969) make this claim on the strength of the classical analysis of Stefan problems.

2.2.2 Elmas

Elmas (1970, 1973) performed an extensive theoretical and experimental study of fluidized bed powder coating. It included:

- a study of the hydrodynamics of fluidization;
- a description of particle motion in the bed;
- an investigation of the thermal properties of the fluidized bed and the immersed body-to-bed heat transfer coefficient;
- coating studies - on stationary objects and the continuous coating of wire;
- a brief discussion of the practical aspects of fluidized bed powder coating, including post-heating of the object.

The particle motion studies were performed on a 0.0555 m diameter fluidized bed filled with 900-1100 $x10^{-6}$ m polyethylene particles of density 960 kgm^{-3}. An X-ray technique was used to observe the movement of a few tracer particles which had the same size and density as the bulk material. The polyethylene particles may have had an irregular shape - it is unclear if the tracer did also. Elmas noted that the polyethylene particles were prone to static; consequently, they were coated with a very thin layer of graphite powder.

The bed fluidized homogeneously between $u_{mf} \approx 0.30$ ms^{-1} and $u_{mb} \approx 1.4\ u_{mf}$; and aggregatively at higher velocities. Under homogeneous fluidization, no particle movement was observed. Above the minimum bubbling point, it was found that particles vibrated in response to passing bubbles. However, their mean position was essentially fixed - at least for the short times of interest in powder coating.

Elmas carried out experiments to measure the heat transfer coefficient between a thin vertical plate and the fluidized bed. Polystyrene particles with a wide size range were used (modal diameter of mass distribution = 460 $x10^{-6}$ m, $u_{mf} = 5.8x10^{-2}$ ms^{-1}, $u_{mb} = 1.5\ u_{mf}$). These experiments were performed at two superficial gas velocities: $u_o = u_{mf}$ and $u_o = 1.2\ u_{mf}$.

The heat transfer coefficient was calculated from a lumped capacity analysis of the temperature history of the preheated plate as it cooled in the bed. It was found that the heat transfer coefficient apparently varied with (residence time of object in bed)$^{-1/2}$. The preheating temperature had comparatively little effect. These observations, combined with the lack of particle motion in the homogeneous regime, suggested that the heat transfer could be viewed as steady state conduction through an emulsion layer that is not often swept from the surface (Elmas 1973, p74-76). This approach, which Elmas terms "penetration theory", is likely to work well for fluidized beds used in the powder coating industry. Economic considerations dictate that industrial powder coating facilities operate at, or slightly above, the minimum fluidization velocity. However, the approach is not valid for vigorously bubbling beds, in which emulsion packets are swiftly replaced.

It must be noted that in these heat transfer experiments, the object was heated above the melting temperature of the bed particles. Indeed, Elmas clearly states that particles sintered onto the plate. It is thought that the heat transfer coefficients calculated by Elmas represent two thermal processes - convective heat transfer to the bed, but also energy consumption by coating formation. This is because both processes occurred when the heat transfer coefficient was being measured. Use of these apparent values of the heat transfer coefficient seems valid for the calculation of the temperature history of a body being coated. However, to predict the coating thickness, it is necessary to discriminate between the amount of energy that is convected to the bed and that which is consumed in the formation of coating. It is thought that the use of these apparent heat transfer coefficients will not accurately represent the fraction of energy that produces coating. Heat transfer coefficients for temperatures greater than the softening point of the bed particles should be extrapolated from lower temperature data.

In the coating studies themselves, Elmas performed experiments and compared the data with a selection of mathematical models. Most experiments were performed on vertical flat plates 0.06 m high x 0.04 m wide x 0.005 m thick, although thinner plates and a

0.02 m diameter sphere were also employed. The fluidized bed could be heated via the fluidizing air. Two types of polymer particles were used:

- **polystyrene** - which melts over a range of temperatures and has no distinct enthalpy of fusion;
- **polyethylene** - which has a definite melting point and latent heat of fusion.

Both preheating and in-bed heating experiments were undertaken. The coating thickness was not measured directly. It was inferred from the mass of the deposited particles by assuming a given porosity for the coating, probably 0.4.

Firstly, Elmas presents a number of approximate models for the coating thickness based on penetration theory. All are one-dimensional and use Cartesian coordinates. A linear temperature profile is assumed throughout the coating layer and in the adjacent part of the fluidized bed. The temperature of the object is either assumed to be constant or is calculated from a lumped heat capacity analysis and the imposed temperature profile. Separate solutions are given for:

- a polymer with a melting range and no significant latent heat of fusion, so that:

$$\begin{pmatrix} \text{energy per unit volume} \\ \text{required to form coating} \end{pmatrix} = \rho c_p (T_m - T_\infty)$$

and

$$\Delta H \approx 0;$$

- a polymer with a very high latent heat of fusion, so that:

$$\begin{pmatrix} \text{energy per unit volume} \\ \text{required to form coating} \end{pmatrix} = \rho \Delta H$$

and

$$c_p (T_m - T_\infty) << \Delta H.$$

When both effects are important, Elmas uses a weighted average of the corresponding separate solutions which he claims is valid for short times. Preheating and constant heat flux cases were considered. Within their reported ranges of validity, these approximate solutions agree reasonably well with the experimental data.

Next, Elmas (1970; 1973, p56-64) presents a general system of equations to describe the coating of a preheated flat plate. A few key features will be discussed. The principal differential equation is the one-dimensional unsteady conduction equation which applies in the region $x = 0$ to $x = \delta(t)$. The energy balance on the coating-bed interface includes the effect of both sensible and latent heat:

$$-k \left.\frac{\partial T}{\partial x}\right|_{x=\delta(t)} = h\,(T_m - T_\infty) + \left\{ \rho c_p (T_m - T_\infty) + \rho \Delta H \right\} \frac{d\delta(t)}{dt} \qquad (2.3)$$

However, the temperature of the object is left as an unspecified function of time.

After performing some transformations and integrations and substituting boundary conditions, an equation implicitly relating the coating thickness, object temperature and time is obtained. This equation involves an integral of the temperature profile in the coated layer. The exact temperature profile is unknown, but it is possible to find upper and lower bounds on its integral. Elmas calculates these bounds then assumes that the value of the integral is their average. In effect, the temperature in the coated layer is assumed to be uniform. Elmas remarks that the temperature history of the object may be obtained by a lumped capacity / penetration theory analysis. However, he further simplifies the problem by assuming that the object temperature is fixed. Finally, he obtains an algebraic expression which implicitly relates the coating thickness with time. An alternative relation is presented in which the temperature profile in the coating was assumed to be linear; other aspects are identical. Elmas concludes that the coating process involves six parameters, so that:

$$\frac{h\delta}{k} = fn\left(\frac{\alpha_e t h^2}{k^2}, \frac{\Delta H}{c_p T_m}, \frac{T_b - T_m}{T_m - T_\infty}, \frac{\rho c_p}{\rho_b c_{pb}}, \frac{\rho_b c_{pb} V_b}{A_b}\right)^{\dagger} \qquad (2.4)$$

Through the use of an intermediate result of this theory, before the introduction of any simplifications, Elmas states that the heat transfer coefficient between the fluidized bed and the object may be calculated. This method relies on the measurement of the steady state (final) coating thickness. The value so obtained is constant for given operating conditions - that is, time independent. It is claimed that this heat transfer coefficient can be used in any of the coating equations in place of the one predicted by penetration theory. This statement is difficult to reconcile since the heat transfer coefficients determined by penetration theory and the apparent experimental results are clearly dependent on time.

The general system of equations developed for a preheated object was adapted to in-bed heating. This involved replacing the unspecified object temperature by an energy balance over the object:

$$\rho_b c_{pb} V_b \frac{dT_b}{dt} = Q_{b\,ext} - \left(-k A_b \left.\frac{\partial T}{\partial x}\right|_{x=0}\right) \qquad (2.5)$$

where $Q_{b\,ext}$ is the power supplied to the object. It is unclear why Elmas did not use this energy balance (with $Q_{b\,ext} = 0$) in the previous solution for a preheated object. Use of similar techniques for constant $Q_{b\,ext}$ and the assumption that the object temperature is T_m yields an explicit expression for the coating thickness.

Two additional solutions based on general equations were presented for the coating of cylindrical and spherical objects under restricted conditions.

† Note that the last term is dimensional and has typical units: $Jm^{-2}K^{-1}$.

No direct comparisons between any of these general solutions and the experimental data were presented. For the case of coating with a preheated object at least, it is claimed that the theory agrees with the data to an accuracy of better than 10%.

Elmas considered a wide range of coating situations. His approximate solutions are simple and are likely to be sufficiently accurate for use in practical powder coating problems. The general equations he provides lead to a greater understanding of the phenomena involved. Unfortunately, Elmas does not present full solutions to the general equations. Instead, he makes simplifying assumptions - most often that the object temperature is constant; the coating temperature profile is linear or uniform; and the residence time is short. By doing this, the solutions to the general equations lose much of their potential improvement in accuracy. In all his solutions, Elmas relies heavily on the penetration theory of heat transfer with infrequent replacement of the emulsion layer next to the surface. Consequently, these solutions do not apply to bubbling fluidized beds. (However, note that economics dictate that commercial powder coating units operate at minimum fluidization.) Elmas remarks that a one-dimensional flat plate coating analysis can apply to an object of a different shape, provided that its curvature is not high and the coating is relatively thin. Finally, it is noted that true convective heat transfer coefficients should be estimated by the extrapolation of low-temperature data. When the object is above the softening point of the bed particles, both convection and energy consumption due to coating occur.

2.2.3 Gutfinger et al.

Gutfinger and associates considered only the powder coating of a vertical flat plate by preheating (Gutfinger and Chen, 1969, 1970; Abuaf and Gutfinger, 1973). As well as those in common with Elmas (Section 2.2.1), a few additional assumptions are made. The heat transfer coefficient between the object and the bed is assumed to be constant during coating. Further, the bed is supposed to have a steady uniform temperature.

These assumptions are in contrast to those of Elmas. Slow-replacement penetration theory leads to a time-varying heat transfer coefficient and an unsteady, non-uniform temperature profile in the bed. The assumptions made by Gutfinger and co-workers are probably more realistic for bubbling fluidized beds. Gutfinger and Chen (1969) also assume that the object temperature is constant. The model developed in that paper will not be discussed further because the subsequent formulations have greater generality.

The model equations developed in Gutfinger and Chen (1970) and Abuaf and Gutfinger (1973) are similar to the general equations given by Elmas. The energy balance on the coating-bed boundary is the same as the one used by Elmas, equation (2.3). However, for convenience the latent heat of fusion is neglected in their solutions of the model equations. An energy balance over the body from time 0 to t is used to couple the temperature history of the body to the formation of coating. It includes distinct terms for convective heat transfer to the bed and for energy consumption due to coating formation. This is in contrast with the method of Elmas, where no distinction was made.

Abuaf and Gutfinger (1973) solve the coating equations for a variable object temperature. The approach again is similar to that of Elmas - dimensionless variables are formed, then an integral technique is used. They obtain a set of three integral and differential equations implicitly relating the object temperature, coating thickness and time. After remarking that these equations are difficult to solve analytically, an approximation is proposed to simplify the problem. They assume that the temperature profile in the coating may be represented by a second degree polynomial. The coefficients of the polynomial are determined from the boundary conditions of the model. They argue that this approximation is reasonable since only the integral of the temperature profile is needed and this is relatively insensitive to small errors in the shape of the profile. In this way, the problem is reduced to the solution of two equations - one purely algebraic; the other involving an integral. These equations were solved numerically to give the object temperature and the coating thickness as functions of time.

Inspection of the two simultaneous equations mentioned above suggests that the coating thickness is determined by three parameters:

$$\frac{\delta}{\delta_s} = \text{fn}\left(\frac{T_m - T_\infty}{T_{bo} - T_\infty} \, , \, \frac{\rho c_p}{\rho_b c_{pb}} \cdot \frac{\delta_s}{L_b} \, , \, \frac{kt}{\rho c_p \, \delta_s^{\,2}}\right) \tag{2.6}$$

where:

$$\delta_s = \frac{k}{h} \cdot \frac{T_{bo} - T_m}{T_m - T_\infty} \tag{2.7}$$

It may be noted that δ_s is the steady state coating thickness that would be obtained if the object were to remain at its original temperature, T_{bo}.

The results of the powder coating model for the case of a constant-temperature object will be discussed now (Gutfinger and Chen, 1969, 1970). The temperature of a preheated object will be reasonably constant when $\rho_b c_{pb}$ is high, the surface area to volume ratio is low or the residence time is short. Alternatively, heat may be supplied to the object (by induction for example) to maintain a steady temperature. In other cases, this assumption will provide an upper bound for the coating thickness. Since the density, specific heat capacity and thermal conductivity of the coating are difficult to change, the main operating variables are: the residence time, temperature driving force and the heat transfer coefficient.

At first, the coating builds up quickly, but as time passes, the rate of coating decreases and eventually a steady state thickness is reached. An increase in the dimensionless temperature driving force, $(T_{bo} - T_m)/(T_m - T_\infty)$, causes thicker coatings to form, but the final thickness is obtained after a longer time. The heat transfer coefficient has the opposite effect - high values of h lead to rapidly-formed, but thin, coatings. Both the heat transfer coefficient and the temperature driving force strongly affect the coating process. A simple expression relates the steady state coating thickness, δ_s, to the process variables - equation (2.7) given earlier. For high values of h, the final coating thickness is

almost independent of the heat transfer coefficient. As the heat transfer coefficient is decreased, equation (2.7) indicates that the final coating thickness will increase significantly. Indeed, Gutfinger and Chen (1969, 1970) consider the limiting case of $h = 0$ - that is, when no convection occurs. They find that the coating will grow indefinitely and that its instantaneous thickness is proportional to $\sqrt{t}$.

Experimental data of other workers were compared with the model predictions. Generally, the theory overpredicted the experimental coating thickness by around 10%, although the maximum deviation was 30%. None of the experimental workers published values for the heat transfer coefficient. Where possible, h was calculated from the steady state coating thickness and equation (2.7). Otherwise, it was estimated from heat transfer studies conducted under similar conditions. Because of the sensitivity of the powder coating process to the heat transfer coefficient, greater agreement between theory and experiment might be obtained if h were better known. Further, since the model always overpredicted the coating thickness, relaxation of the assumption of a constant object temperature would likely be profitable.

This deficiency was remedied in Abuaf and Gutfinger (1973). The behaviour of the variable object temperature model is similar to the constant-temperature one. However, since the temperature of the object falls, the thickness of the coated layer is always less than that in the constant-T_b case under identical circumstances. The parameter that determines the difference in behaviour is ZY:

$$ZY = \frac{\rho c_p}{\rho_b c_{pb}} \cdot \frac{k}{hL_b} \cdot \frac{T_{bo} - T_m}{T_m - T_\infty} \tag{2.8}$$

For low values of ZY, the object remains close to its original temperature. If $ZY \leq 0.1$, the final coating thickness may be within 20% of the constant-temperature solution. However, when ZY is high, the error introduced by the assumption of a constant body

temperature is significant. The steady state coating thickness may be overestimated by a factor of five if the constant-T_b model is used when ZY = 10. In addition, when ZY is high, the response of the system is quick - the object cools down rapidly and coating is finished in a short time.

Although similar, it is thought that the model equations developed by Gutfinger and co-workers are more physically realistic than those presented by Elmas. The implicit assumption of penetration theory and ambiguities in the energy balance over the immersed object seem to limit Elmas' work. Gutfinger and associates consider only a flat plate geometry with preheating of the object. However, it is a small matter to modify the equations for cylindrical and spherical coordinates and to include in-bed heating. In common with Elmas, material properties are supposed to remain constant and a shape for the temperature profile in the coating is assumed. These simplifications may be avoided if numerical methods are considered.

2.2.4 Ahmed

A numerical solution of the powder coating problem for a preheated flat plate was presented in Ahmed (1989). An experimental study involving a range of geometries - flat plate, cylinder and sphere - was also undertaken. The heat transfer coefficient between the object and the bed was determined by experiment at temperatures lower than the melting point of the polymer used. This is the recommended technique. Temperature-dependent material properties were not implemented in the numerical work. It appears that energy consumption due to the formation of new coating was neglected at the coating-bed interface. The temperature of the object was calculated from an energy balance similar to that of Abuaf and Gutfinger (1973). A fully explicit finite difference formulation and Euler's method (Kreyszig, 1983) were used to solve the one-dimensional Cartesian conduction equation. It was not necessary to impose any particular temperature profile on the coated layer to obtain a solution. A correction factor for the

coating thickness was reported - it varied with: the steady-state coating thickness, surface to volume ratio of the object, bed particle size and time. It is unclear if the correction factor was needed to bring the numerical solution into agreement with experiment, or if it was intended to broaden the range of applicability of the simulation. Ahmed claims that the predicted and experimental values of the coating thickness agreed within 10%.

The powder coating models and solutions that have been considered in this brief review are summarised in Table 2.2.

2.3 The Erosion of Tubes Immersed in Fluidized Beds

It should be noted from the beginning that this study is concerned with the coating and erosion of the layer of particles that forms on a heated object immersed in a fluidized bed. Erosion of the object itself is not considered. So, while we review the wastage of metal tubes, we wish, in fact, to apply the results to a coating of particles on such objects.

Fluidized bed combustion has the potential to utilise a wide variety of coals and low-quality fuels in an efficient and environmentally-acceptable manner. However, the application of both atmospheric and pressurised fluidized bed combustors has been retarded by excessive wastage of the immersed heat transfer tubes. It was been suggested that the rate of erosion must be decreased by over an order of magnitude before commercial combustors become viable (Bouillard and Lyczkowski, 1991). While corrosion and vibrational fatigue also contribute, it is thought that erosion by impinging particles is the main cause of tube failure (Zhu et al., 1990; Nieh et al., 1991). Lack of effective remedies for in-bed tube erosion from industry and the poor state of knowledge generally has prompted the intense research activity seen currently.

Table 2.2: Summary of solutions presented for fluidized bed powder coating models.

Author	Geometry	Body Temperature	Coating Temperature Profile	External Heat Input	Coating Energy Mechanism[1]	Comments
Gutfinger & Chen (1969,1970)	1-D Cartesian	constant	parabolic	no	c_p	additional solution: h = 0
Elmas (1970)[2]	1-D Cartesian	constant	uniform[3]	no	c_p & ΔH	additional solution: h = 0
Abuaf & Gutfinger (1973)	1-D Cartesian	variable[4]	parabolic	no	c_p	
Elmas (1973)[2]	1-D Cartesian	constant	linear	no	c_p	
		variable	linear	no	c_p	(A)
		variable	linear	yes - constant	c_p	(B)
		variable	linear	no	ΔH	(C)
		variable	linear	yes - constant	ΔH	(D)
		-	-	no	c_p & ΔH	average of (A) & (C)
		-	-	yes - constant	c_p & ΔH	average of (B) & (D)
		constant	uniform[3]	no	c_p & ΔH	
		constant	linear	no	c_p & ΔH	
		constant	?	yes - constant	c_p & ΔH	
	radial - cylindrical	constant	?	yes - constant	c_p & ΔH	
	radial - spherical	constant	?	no	ΔH	
Ahmed (1989)	1-D Cartesian	variable[5]	no assumption	no	?	numerical solution

Notes:

1. Formulation for energy consumed in creation of new coating: c_p indicates specific heat term; ΔH indicates latent heat term.
2. Penetration theory of heat transfer with infrequent emulsion replacement used.
3. Temperature used is average of upper and lower bounds.
4. Time-integrated energy balance includes convection and storage in coating.
5. Energy balance includes convection and storage in coating.

Following Finnie (1960), an understanding of the erosion of surfaces immersed in fluidized beds may be divided conceptually into two parts:

- knowledge of the relationship between the erosion rate and the hydrodynamic conditions existing immediately adjacent to the eroding surface;

- an appreciation of the effects of operating parameters on the hydrodynamics of a fluidized bed when immersed objects are present.

Studies to elucidate the first part need have no connection with fluidized beds nor any other particular application. Most often, they seek to relate the erosion rate to the number, speed and direction of the impinging particles. Material properties, such as hardness, and the natures of the particles and the immersed surface are also involved. Research into the second part provides the link between the detailed erosion work and variables such as the gas velocity and geometry of the fluidized bed. A number of hydrodynamic models for fluidized beds - some of great complexity - have been presented.

2.3.1 Modelling Erosion with Known Hydrodynamics

When a particle strikes a target, the damage it causes depends on the force it exerts on the surface. According to Neilson and Gilchrist (1968), the normal and parallel components of the force lead to different mechanisms of erosion. The normal component leads to "deformation wear" in which surface cracks are initiated, grow and finally intersect, causing material loss. Both ductile (after extensive work hardening) and brittle materials are affected. In ductile materials, the component of the impact force parallel the surface causes "cutting wear" or "micromachining" as described by Finnie (1960). There, particles gouge out surface material in a fashion similar to the operation of a machining tool. Bellman and Levy (1981) suggested an alternative description for

the erosion of ductile materials based on detailed scanning electron microscope observations. They proposed *"a combined forging-extrusion mechanism which produces highly distressed platelets of target material that are knocked off the surface by succeeding particle impacts"*. This view was supported by Zhu et al. (1991). Whatever the detailed mechanism, this phenomenon is known generally as *impact erosion*.

Laboratory tests suggest that impact erosion is the dominant mechanical process that causes tube wastage in fluidized beds. However, some abrasion (or three-body abrasion), in which particles scrape over the surface rather than strike it, may also occur (Zhu et al., 1990; Liu and Levy, 1991).

In this brief review, ductile materials only will be considered hereafter. It is thought that when materials are hot enough to sinter onto an object, they are unlikely to retain any low-temperature, brittle character.

While there have been a number of studies of impact erosion (see references in Bellman and Levy, 1981, and Zhu et al., 1991, for example), they have involved high particle velocities - around 100-300 ms^{-1}. Those works were motivated by processes such as: the erosion of aircraft, rockets and turbine blades; sand blasting; and erosive drilling. Zhu et al. (1991) noted that such speeds are two orders of magnitude higher than those experienced in conventional fluidized beds. Thus, they argued, direct application of the results of those studies is inappropriate for the erosion of tubes in bubbling fluidized beds. Nevertheless, high velocity studies are still useful for the case in hand since they indicate which parameters control erosion. The more important factors are (Hutchings, 1987; Zhu et al., 1991):

- angle of particle impact
- particle velocity
- time subjected to erosion (some materials exhibit an incubation period)
- particle hardness
- particle shape
- particle size
- material properties of the eroding surface

It is the objective of erosion modelling to relate these factors to the rate of target material loss.

Based on the "classical" approach of deformation wear and cutting wear, three mechanistic models were developed for the erosion of ductile materials - those of Finnie (1960), Bitter (1963a,b) and Neilson and Gilchrist (1968). They can reproduce, to differing degrees of success, the variation of erosion rate with the mass flowrate and velocity of a stream of impinging particles. For quantitative predictions, each required the fitting of a few empirical parameters that depended on the eroding system. This group of models will not be discussed further. Instead, we will concentrate upon more recent efforts which have been motivated by the problems experienced in fluidized bed combustors.

Due to the scarcity of relevant published data, Zhu et al. (1991) developed a particle dropping apparatus to investigate low velocity erosion. In their experimental program, seven parameters were varied and care was taken to ensure that they ranged over conditions of interest in fluidized bed combustion. However, all experiments were performed at room temperature. Multi-variable regression yielded an expression for the erosion rate, R_{eZE}:

$$R_{eZE} = k_{ZE} M d_p^{1.5} v_p^{2.3} (1.04 - \psi)(0.448 \cos^2 \theta + 1) \qquad (2.9)$$

where M is the mass flux of particles, θ is the impact angle and d_p, v_p and ψ are, respectively, the particle diameter, velocity and approximate sphericity. The coefficient k_{ZE} was found to depend on material properties, particularly the Youngs modulus of the eroding surface. In equation (2.9), it is vital to use the units reported by the authors. Zhu and co-workers claim that M in equation (2.9) may be replaced by $N_p\rho_p$, where N_p is the number of particles striking the surface, so that:

$$\mathcal{R}_{eZE'} = k_{ZE'} N_p \rho_p d_p^{1.5} v_p^{2.3} (1.04 - \psi)(0.448 \cos^2 \theta + 1) \qquad (2.10)$$

is an alternative empirical relation for the erosion rate. The author believes that the form of equation (2.10) is misleading, since embedded in the parameter $k_{ZE'}$ are important dependencies on the target area, erosion time and particle diameter.

To rationalise their experimental results, Zhu and associates formulated a simple model. Briefly, the postulates are:

- erosion occurs by surface fatigue;
- material loss is proportional to the volume of target material that experiences substantial **elastic deformation** through particle impact;
- the erosion rate is proportional to ℓ_d^3, where ℓ_d is the maximum deformed depth;
- all impinging particles transfer the same fraction of their kinetic energy to the surface, irrespective of their size, density and velocity.

By considering the kinetic energy per particle and the work needed to elastically deform a volume ℓ_d^3 of target material, they obtained:

$$\mathcal{R}_{eZT} = k_{ZT} N_p \rho_p d_p^2 v_p^2 / Y_m \qquad (2.11)$$

where k_{ZT} is expected to vary with the hardness, shape and impact angle of the particles. Moreover, k_{ZT} includes the effects of the target area and the duration of exposure. In equation (2.11), the effect of the Youngs modulus of the target, Y_m, is seen explicitly. Comparison of equations (2.10) and (2.11) shows that the simple model reproduces reasonably well the experimental trends. In both theory and experiment, the erosion rate decreases with increasing Youngs modulus of the target material.

Another approach to the prediction of erosion rates was presented by Bouillard et al. (1989) and Bouillard and Lyczkowski (1991). Their Monolayer Energy Dissipation (MED) model requires more complex hydrodynamic information than the works cited previously. Instead of the velocity and flux of the impinging particles, the *total kinetic energy dissipation rate per unit volume of the gas-solid mixture immediately adjacent to the eroding surface* is needed. According to the MED model, the kinetic energy of the gas-solid mixture which extends about one particle diameter out from the eroding surface (- a monolayer) may be dissipated by three competing mechanisms:

- heating of the gas, particles and surface of the object;
- attrition of the particles;
- erosion of the object.

Thus, only a portion of the kinetic energy dissipated in the monolayer will contribute to erosion. An energy balance links the rate of kinetic energy dissipation to the erosion rate, $\mathcal{R}_{eBT}$:

$$k_{BT} E_v A_b d_p = P_t \mathcal{R}_{eBT} A_b \qquad (2.12)$$

where E_v is the kinetic energy dissipation rate per unit volume that leads to erosion; A_b and P_t are, respectively, the area and the "material pressure" of the eroding surface.

Estimation of E_v will be discussed in Section 2.3.2. A few points should be made regarding equation (2.12):

- $A_b.d_p$ is the volume of the monolayer in which the energy is dissipated;
- k_{BT} is an empirical factor (less than unity) which recognises that not all of the energy dissipated leads to plastic deformation and subsequent material loss, but some causes elastic deformation of the surface. Bouillard et al. (1989) suggest that $k_{BT} \approx 0.1$ based on rough experimental observation. In Bouillard and Lyczkowski (1991), k_{BT} was related to the coefficient of restitution;
- P_t is related to the hardness of the eroding surface, H_t. Bouillard et al. (1989) use $P_t = H_t$, but also quote other authors who state $P_t \approx 2.0\ H_t$.

Rearrangement of equation (2.12) yields:

$$\mathcal{R}_{eBT} = k_{BT} E_v d_p / P_t \qquad (2.13)$$

where it is noted that E_v is a complex function of the hydrodynamic conditions near the surface of an object.

Direct confirmation of equation (2.13) is not possible. E_v is inherently a calculated quantity, reliant on additional assumptions. When these calculations are performed, however, the authors claim good agreement with published experimental values for erosion rates experienced by tubes in a fluidized bed. In later papers, this research team seems to have shifted their focus away from the MED erosion model (refer below).

2.3.2 Hydrodynamic Modelling of Fluidized Beds with Immersed Objects

In the previous section, it was stated that the rate of erosion depends on the force that an impinging particle exerts on the surface. This impact force depends on the other forces acting upon the particle which are in turn related to the local hydrodynamics (Hutchings, 1987). At this point, it is profitable to report key observations on the erosion of tubes in bubbling fluidized beds. Wear is:

> *"due to a large number of impacts by particles travelling at relatively low velocities (1-5 m/s) carried in the wakes or pushed up at the noses of rising and coalescing voids"* (Zhu et al., 1991)

and that:

> *"bubbles striking the tube as they are in the process of coalescing (referred to as double bubbles) ... [result] in particularly high velocity wake impacts. ... [Information] is needed on the relative frequencies of impact of different types of bubbles and on their respective sizes and velocities"* (Levy et al., 1992).

Clearly, tube erosion and bubble motion are strongly connected. A few relevant experimental studies are discussed next.

Bubble motion around single horizontal tubes and the forces consequently experienced by the tubes have been investigated by a number of workers (for example: Nguyen and Grace, 1978; Hosny and Grace, 1984 and studies cited thereby; Levy et al., 1992). Single bubble experiments revealed how the force acting on a tube varied with the passage of a bubble. When a pair of bubbles (double bubbles) coalesce at tube level, the velocity of the wake particles striking the tube is around three times that for single bubbles (Levy et al., 1992). In freely bubbling beds, tubes experience forces with both

periodic and random components. It was found that double bubbles occur about 10% of the time.

There are several studies of the wear rates of isolated horizontal tubes in fluidized beds - among the more recent are: Zhu et al. (1990), Liu and Levy (1991), and Nieh et al. (1991). All indicate that circumferential wear profiles are not uniform. Some authors report that maximum wear rates occur on the bottom of the tubes, while others find the greatest erosion 30-50° displaced from the bottom. The *average* wear rate over a tube may be only one third of the maximum. The top half of a tube suffers comparatively little wear. Tubes within horizontal bundles may erode more quickly or more slowly than those in isolation (Zhu et al., 1991) and circumferential wear patterns may also change (Zhu et al., 1990). For details of the influence of experimental parameters such as particle size and superficial gas velocity on erosion, the above references should be consulted.

Yates et al. (1984) investigated the effect of vertical rods on bubble motion. The size and rise velocity of bubbles were increased by the presence of a single vertical rod (volume change: +50%; velocity change: +40% under conditions used). When the rod was artificially roughened by coating it with a layer of bed particles, the effect was even more pronounced - volume change: +70%; velocity change: +160%. Results showing the influence of the separation distance of two vertical rods on bubble size, velocity and stability were also reported. The effect of three rods was briefly discussed.

There seem to be few studies on the erosion of inclined and vertical tubes. Nieh et al. (1991) present results suggesting that the average erosion rate decreases linearly with the angle of inclination from the horizontal. They found that a vertical tube suffered only 47% of the erosion experienced by a horizontal one under similar conditions. Zhu et al. (1990) found that a tube inclined at 15° eroded at essentially the same rate and had a similar erosion profile as a horizontal tube.

Finally, an experimental technique used by Meijer (1983) for the investigation of scale formation in a liquid fluidized bed heat exchanger is mentioned. A scaled-up fluidized bed system was constructed which had geometric and hydrodynamic similarity with the one of interest. The frequency and momentum change of particles hitting a section of the wall were measured by a piezo-electric transducer. In this way, hydrodynamic data were gathered for use in subsequent erosion modelling.

There several options for modelling the hydrodynamics - that is, the gas and solid motion - of a bubbling fluidized bed with immersed tubes. Various authors have used:

- bubble growth models that ignore the presence of tubes;
- bubble tracking models that take tubes into account;
- models of solids circulation;
- fundamental "two-fluid" hydrodynamic models.

These approaches differ substantially in their flexibility and computational requirements.

The simplest approach is to ignore the presence of the tubes. Thus, readily-available relationships for bubble size and rise velocity developed for freely bubbling beds may be used (see, for example, Clift and Grace, 1985). The solids velocity is then related in a simple way to the bubble motion. Small to moderate computational facilities are needed, depending on the model chosen. However, the approach is not flexible - indeed, it may only be acceptable for a single tube. Nevertheless, it is a valuable starting point.

Using this method, Yates (1987) concluded that the erosion rate is proportional to the bubble diameter raised to the fourth power. Zhu et al. (1991) used standard bubbling bed concepts to relate their particle dropping experiments (which yielded equation (2.10)) to a previous experimental investigation of fluidized bed tube wear. They argued that the number of particles impinging on a tube is proportional to the void frequency, f_b,

and that the particle impact velocity varies as (void rise velocity)^n. Further, the average angle of particle impingement (which influences the erosion rate) is approximately the same for all fluidizing conditions. Regression of their single tube wear data yielded the expression:

$$\mathcal{R}_{eZR} = k_{ZR} f_b \rho_p d_p^{1.2} u_b^{2.1} (1.04 - \psi) \qquad (2.14)$$

for the average erosion rate. It should be a reliable indicator of erosion rates, despite the apparent ambiguities in the particle-dropping expressions, equations (2.10) and (2.11). Indeed, equation (2.14) successfully correlated their own data and agreed reasonably well with another data set available in the literature.

The second approach to hydrodynamic modelling is based on Clift and Grace's "discrete-bubble Lagrangian" formulation which has lead to the recent paper by Rafailidis et al. (1992). Here, the motion of each bubble is calculated from formation to eruption, with allowance for coalescence. The influence of other bubbles, bed walls and tube bundles of arbitrary geometry is taken into account. Hence, it is an approach of considerable versatility. The model may be run on an augmented desktop personal computer or a workstation in a reasonable time. In common with the simpler approach mentioned above, the solid velocity needs to be linked with the motion of the bubbles. So far, no erosion studies using the latest version of this model seem to have been published. Bayat et al. (1990) used an earlier version to predict the relative effects of single and double bubble collisions on the erosion of the first row of a horizontal tube bank.

Solids circulation models are another option for describing the bed hydrodynamics. Bouillard and Lyczkowski (1991) combined their MED model for erosion with an extended version of the approximate solids circulation model presented in Gidaspow and Ettehadieh (1983). Circulation of the bed is driven by the average porosity difference in the "jet" and "downcomer" regions. The solids velocity is combined with the coefficient

of restitution and particle drag coefficient to estimate the kinetic energy dissipation rate per unit volume - as required by the MED model. It is thought that at least one of the model parameters has doubtful significance, particularly in the context of complex tube geometries. Further, the observed dependence of erosion on bubble impact does not seem to be considered. However, Bouillard and Lyczkowski (1991) demonstrate good agreement between this model and some published data. For comparison, they also present results obtained by combining the solids circulation model with the erosion theories of Finnie (1960) and Neilson and Gilchrist (1968). The computational load is low - it is comparable with the first approach.

The final possibility discussed here involves a fundamental hydrodynamic description. Conservation equations for mass, energy and momentum are solved for two interpenetrating "fluids" - the solid and gas phases. This is potentially the most complete and flexible approach; it even allows computation of the object's erosion profile. However, the computational resources required are vast; many hours of supercomputer time are needed to simulate a few seconds of real time. Further, there is debate over the very formulation of the equations (Rafailidis et al., 1992; Clift, 1993).

Bouillard et al. (1989) used a two-dimensional, two-fluid hydrodynamic model with their MED theory to simulate the erosion of a rectangular object and separately, of three square tubes (to mimic part of a tube bank). Due to uncertainties in the correct boundary conditions and the lack of appropriate experiments, three different approximations were presented for the volumetric kinetic energy dissipation rate leading to erosion. The authors claimed that their model can predict average erosion rates. The simulated wear profiles, however, do not agree with experiment - far too much erosion is predicted on the top of the tube.

In subsequent work (Ding and Lyczkowski, 1992; Ding et al. 1992), the hydrodynamic model was extended to three dimensions and a kinetic theory granular flow model was

added (to eliminate some empiricism used in the earlier formulation). The erosion theory of Finnie (1960) was used in place of the MED model. Predictions of the three-dimensional model agree well with experimental average erosion rate and circumferential wear profile data.

2.4 COMBINED COATING AND EROSION

It is interesting to note a few studies in which both "coating" and "erosion" processes take place.

Szekely and Jassal (1978) performed experiments and carried out modelling on the solidification of a binary dendritic system (NH_4Cl - H_2O). In this combined Stefan / fluid mechanics problem, the solidification front advances by dendrite formation. It was observed that convection currents in the melt could shear off newly-formed dendrites. Thus, both "coating" (solidification) and erosion occurred together. Modelling of the erosion was not attempted, but was left for future effort (Szekely, 1983).

In an interesting study, Meijer (1983) was concerned with scale formation on the walls of a liquid fluidized bed heat exchanger. Separate experiments were performed to develop predictive equations for the erosion rate and the growth rate of the scale. Hydrodynamic data, obtained from an instrumented scaled-up fluidized bed, were combined with particle impact tests to derive the erosion rate expression. The rate of growth was related to the concentration of the scale-forming species. If conditions inside the heat exchanger are maintained so that the erosion rate exceeds the growth rate, no scale will form - the desired result.

In their study of the erosion of aluminium plates by aluminium oxide particles, Neilson and Gilchrist (1968) found that the plate sometimes experienced a gain in mass before suffering a sustained loss. The oxide particles were initially embedded in the plate. This

behaviour depended upon the particle velocity, impingement angle and sphericity; no deposition was observed for spherical particles. It should be noted that their study was conducted at particle velocities significantly higher than those associated with bubbling fluidized beds.

A somewhat similar phenomenon was reported by Liu and Levy (1991). In a fluidized bed wear testing rig, they investigated the erosion of a horizontal aluminium rod by various proportions of calcium-based bed material and substantially harder SiO_2 particles. High rates of wear were experienced with a pure SiO_2 bed. As the fraction of calcium-based bed particles was increased, some angular positions on the rod experienced a net gain of material, thus preventing further metal wastage. When only calcium-based particles were used, deposition occurred over the entire surface of the rod. In these erosion studies, the "coating" process was not thermally driven.

Finally, we turn to the fouling of heat transfer tubes in fluidized bed combustors (FBCs). Schofield et al. (1990) measured oxygen concentrations on the surface of uncooled horizontal tubes in a FBC which burnt coal in the presence of limestone. Deposits of calcium-based material formed on the tubes. Two key observations were made:

- the most severe metal wastage occurred along the bottom of the tubes, yet this was where the thickest deposits formed;
- the oxygen sensor signals and post-experiment inspection of the tubes indicated that erosion proceeded steadily throughout the experiments.

Consequently, they concluded that erosion and deposition occurred simultaneously, and that the rates of both processes were high at locations of frequent particle impact. Further, they believed that very fine particles [$O(10^{-6}$ m)] sintered together to form the deposit which was eroded by larger particles [$O(10^{-3}$ m)].

Mann et al. (1987) conducted 1000-hour tests with seven coal / limestone mixtures in a pilot-scale atmospheric bubbling fluidized bed combustor. Their work included a detailed study of the immersed heat transfer surfaces (both horizontal tubes and waterwalls), which were subject to the combined effects of erosion, corrosion and deposition. In many cases, there was evidence that the formation and erosion of deposits occurred simultaneously. Some deposits on the tubes had a rough texture, and others had particles embedded in the surface - both possible results of high velocity particle impact. The variation of the thickness and nature of the deposit with its angular position on the tubes was also reported. Further, the authors noted that deposition can significantly reduce the rate of heat transfer between the fluidized bed and an immersed surface. In one of the tests, after 700 hours of operation with Beulah lignite (North Dakota, USA), a deposit of about 20 mm thickness had formed on the heat transfer tubes (32 mm outside diameter)! The overall heat transfer coefficient between the bed and the tube had been reduced to approximately 60% of its original value.

Thimsen et al. (1991) investigated fouling in two coal-fired bubbling FBCs used in the power industry (capacities: 80 and 130 MW electrical). The combustors burned subbituminous and lignitic coals with inert or sulphur-retaining bed material. Four kinds of deposit formed on the heat transfer tubes. One type, which appeared on the in-bed superheater tubes, was both tough and highly insulating. In one of the combustors, the deposit grew at a rate of 0.75 mm per 1000 hours of operation - it had to be removed manually in routine shutdowns every 4-5 months. Over this time, the temperature rise across the superheater tube bundle decreased by 25-30 °C. The other FBC experiences a deposition rate of 35 mm / 1000 hours, yet, it has operated for five years without cleaning. Erosion, presumably, balances the growth of the deposit, which has attained a steady thickness of 2-3 mm. The deposit's thermal conductivity was determined as 0.94 ± 0.42 $Wm^{-1}K^{-1}$.

The pulse-enhanced, indirectly-heated fluidized bed gasifier developed by MTCI (ThermoChem, 1993) may operate with similar materials, close to the conditions used in FBCs, although combustion reactions themselves do not take place. As indicated in Chapter 1, there may be physical and chemical mechanisms present that lead to deposition on the gasifier's immersed heat transfer tubes. Some erosion is certain to occur. Whether or not deposits form on the tubes of MTCI's gasifier, the extent to which the deposits erode and any reduction in heat transfer has not been reported in the literature.

2.5 SUMMARY

Many processes can lead to the simultaneous build up and removal of a deposit on a surface immersed in a fluidized bed. In the system of interest here, the deposit accumulates through high-temperature sintering, while it is reduced by particle impact erosion. To the author's knowledge, a unified analysis of this phenomenon has not been presented in the literature, although the separate processes have been studied in the guise of fluidized bed powder coating and the erosion of tubes immersed in a fluidized bed.

Fluidized Bed Powder Coating:

Fluidized bed powder coating falls within the class of Stefan problems. Despite the long industrial use of fluidized beds for powder coating and the enormous literature on related Stefan problems, comparatively few mathematical models of the process have been reported. Of these, the formulation of Abuaf and Gutfinger (1973), seems the clearest and most realistic, yet even this is not free from ambiguity. Although somewhat restricted in its as-published form, this model may be extended with relative ease to other situations. If numerical methods are adopted, temperature-independent material properties and other simplifications desired for analytical solutions may be relaxed. Szekely (1983) highlights the trade-off between mathematical rigour, physical reality and engineering utility that is often encountered in Stefan problems.

The Erosion of Tubes Immersed in Fluidized Beds:

Prediction of the erosion rate of tubes in a fluidized bed requires an understanding of both its hydrodynamics and the niceties of erosion. While some theory exists, descriptions of erosion are largely empirical. In all cases, for the quantitative prediction of erosion rates, experiments should be performed on the system of interest. Hydrodynamic models range from the standard relations used in the absence of tubes to fundamental approaches that are the subject of current research. The test of such models is their ability to reproduce experimental observations such as: circumferential wear profiles; the presence of double bubbles; the behaviour of multiple tubes; bubble size and velocity effects with vertical and inclined tubes; and the importance of tube roughness. In a review of the hydrodynamic modelling of fluidized beds, Clift (1993) argues that approach of Rafailidis et al. (1992) should be used in the development of engineering design tools as it yields sufficient information with appropriate computing resources.

Combined Coating and Erosion:

Heat transfer surfaces in fluidized bed combustors experience simultaneous deposition and erosion. Tenacious, insulating deposits can severely reduce heat transfer. Deposit-related tube corrosion effects must also be considered. In general, our knowledge of the separate processes of erosion and deposition in fluidized beds, let alone their combined action, is not complete. Both physical and chemical mechanisms may be involved. Further, the behaviour experienced in industrial systems may be difficult to reproduce in small-scale apparatus.

In this study, the coating of an immersed surface by particles through physical means only and their simultaneous erosion is investigated. A mathematical description is developed which combines powder coating theory with erosion modelling through a simple mass balance.

Chapter 3:

EXPERIMENTAL STUDY

In this chapter, an experimental investigation into the coating-erosion phenomenon is reported. The apparatus and procedures used are described in detail. Results from three preliminary studies - determination of the particle melting temperature, the minimum fluidization velocity and the heat transfer coefficient - are discussed.

3.1 INTRODUCTION

The simultaneous thermal coating and erosion of an object immersed in a fluidized bed was studied in a laboratory scale apparatus. The major operating variables included the temperature of the fluidized bed, the superficial gas velocity, the power supplied to the immersed body and the duration of the heating.

As indicated in Chapter 2, the heat transfer coefficient is a particularly important parameter in the powder coating process. Rather than relying on correlations available in the literature, it was decided to measure the heat transfer coefficient directly. Similarly, the minimum fluidization velocity and the effective melting temperature of the bed particles were determined by experiment. These three supporting studies appear complete in this chapter. The procedure used in the coating-erosion experiments is also described here. However, the results and discussion of those experiments - in the light of the theory developed in the next chapter - are presented in Chapter 5.

3.2 APPARATUS

The experimental apparatus consisted of:

- an in-bed heater;
- a high-temperature fluidized bed;

and associated instrumentation and control equipment.

3.2.1 In-Bed Heater

The purpose of the in-bed heater is to provide a surface which may be immersed within the fluidized bed and which can maintain a temperature high enough to cause adhesion of the bed particles. It must also be easy to position the hot surface in the fluidized bed and withdraw it rapidly at the end of an experiment.

The heating tube used in these experiments was fabricated to supplied specifications by Helios Heating Pty Ltd, Beverley, South Australia. A positioning clamp with a handle was constructed so that the heating tube could be easily centred in the fluidized bed at any desired height. The heater system, with important dimensions included, is depicted in Figure 3.1. Note that the heating element is a U-tube design - it was the only shape of heater that could be built which could withstand the operating temperatures required and still be easily removed from the bed. Only the bottom 100 mm (approximately) of the heater contains heating coils; the rest is unheated. This was around the shortest length that could be built without a high risk of having unevenly spaced heating coils. Even so, the heater does suffer from a hot spot and the lengths of the heated legs are slightly unequal. These points will be discussed further in Section 3.5.3.

The heating element consists of a protective tube, 0.7 mm thick, made of Incoloy 800. Inside the tube, in the heated section, lies a coil of resistance wire (which is connected with "cold leads" to the electrical terminals at the tops of the legs). The rest of the tube

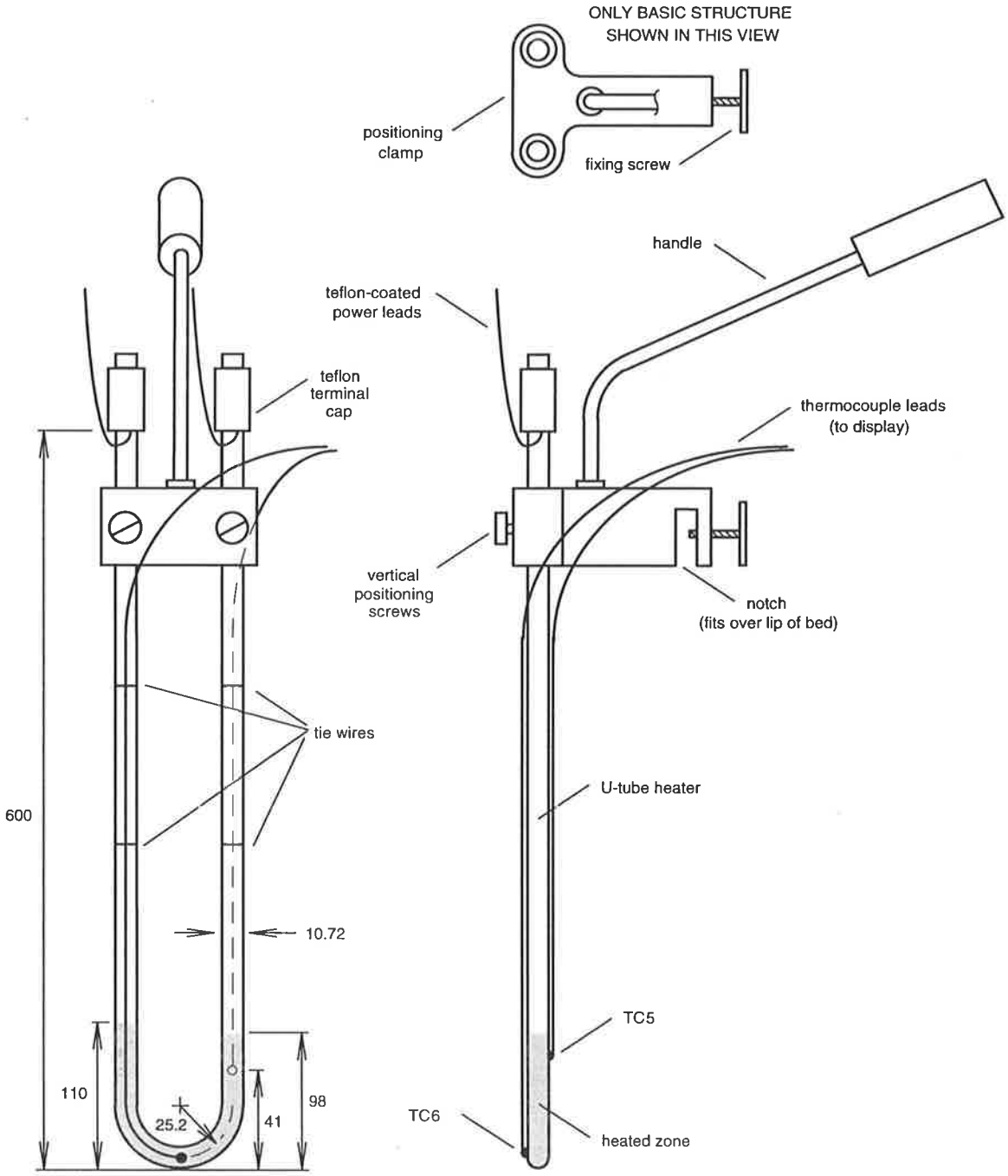

ALL DIMENSIONS ARE IN MILLIMETRES

NOT TO SCALE

Figure 3.1: Schematic diagram of the U-tube heater.

is packed with magnesium oxide powder for electrical insulation and mechanical support of the heating coil. Power is supplied to the heater through teflon coated silver wires which can operate at around 350°C. Teflon caps insulate the heater's electrical terminals.

Two Chromel-Alumel (type K) thermocouples 1 mm in diameter and 1.5 m in length were fixed onto the heater to provide surface temperature information. One thermocouple is placed on the right leg, over the heater's hotspot (TC5); the other is attached at the bend of the tube (TC6). These temperatures could be displayed on a digital readout. Initial attempts at fixing the thermocouples to the surface were not wholly successful. At first, a high temperature silver solder was used to connect the tips of the thermocouples to the heater. Several tacks were also placed along the legs of the heater to anchor the thermocouple wires in place. After operating the heater a few times, the solder failed and the thermocouples came away from the heater. This was detected while the heater was immersed in the bed from the sudden apparent drop in the heater's surface temperature. Subsequently, a manganese bronze solder was tried, but eventually, this failed too. The final method involved cutting a groove approximately 20 mm long, 1 mm wide and 0.8 mm deep along the length of the heater tube where the thermocouple tip was to lie. Pure copper was used to braze the tip of the thermocouple into the groove. Excess metal was carefully removed so that the thermocouple was attached with a small, low-profile nodule of copper. The rest of the thermocouple wire was anchored to the heater leg by two thin wire ties. With this method, it is thought that reasonable temperature measurements could be made of the hot surface without much affecting the heater's performance.

The heater was rated as producing 750 W when the potential imposed across its terminals was 250 V, 50 Hz, AC. A Variac was used to control manually the amount of power supplied to the heater from the mains. Initially, the supplied power was measured using a switching box and multimeter arrangement. This was difficult to use and may

have introduced errors. In later experiments, the instantaneous power supplied to the heater was measured with a PA-2 Siemens (Australia) AC power analyser.

3.2.2 High-Temperature Fluidized Bed

The fluidized bed used for these experiments (Figure 3.2) is a modification of an existing apparatus.

Compressed air is supplied to the system from a laboratory compressor equipped with a refrigerated dryer. After an isolation valve, the air pressure is measured with a 0-1000 kPa (gauge) Bourdon tube gauge. From a second isolation valve, the air passes through a pressure regulator, two further valves, then into two volumetric flowmeters connected in series. The first is a Type 35XA rotameter with a duralumin float (Fischer Controls Ltd, Croydon, England); the second an MT5 integrating flowmeter (Toyo Gas Meter Co., Japan). After the two flowmeters, the air pressure is measured by a selection of three Bourdon tube type gauges which range over the intervals: 0-10, 0-160 and 0-400 kPa (gauge). The air temperature is also measured here by a type K thermocouple and a digital readout.

Next, the air passes through a silica gel packed bed dryer onto an air heater (Leister Hot Air Tool type 5000-804, Kagiswil, Switzerland). The power input to the air heater, which is continuously adjustable, is controlled manually. It is claimed that an air temperature of 700 °C can be achieved at full power and high flowrates. After the heater, the air flows through a drilled plate distributor into the plenum (300 mm long) and then onto the fluidized bed section itself. If desired, the plenum can be partly filled with sand to provide a thermal reservoir. In these experiments, the plenum was empty.

The fluidized bed section itself was constructed from a length of 316 stainless steel pipe, 508 mm long, 102.7 mm internal diameter and 5.6 mm wall thickness. The top of the

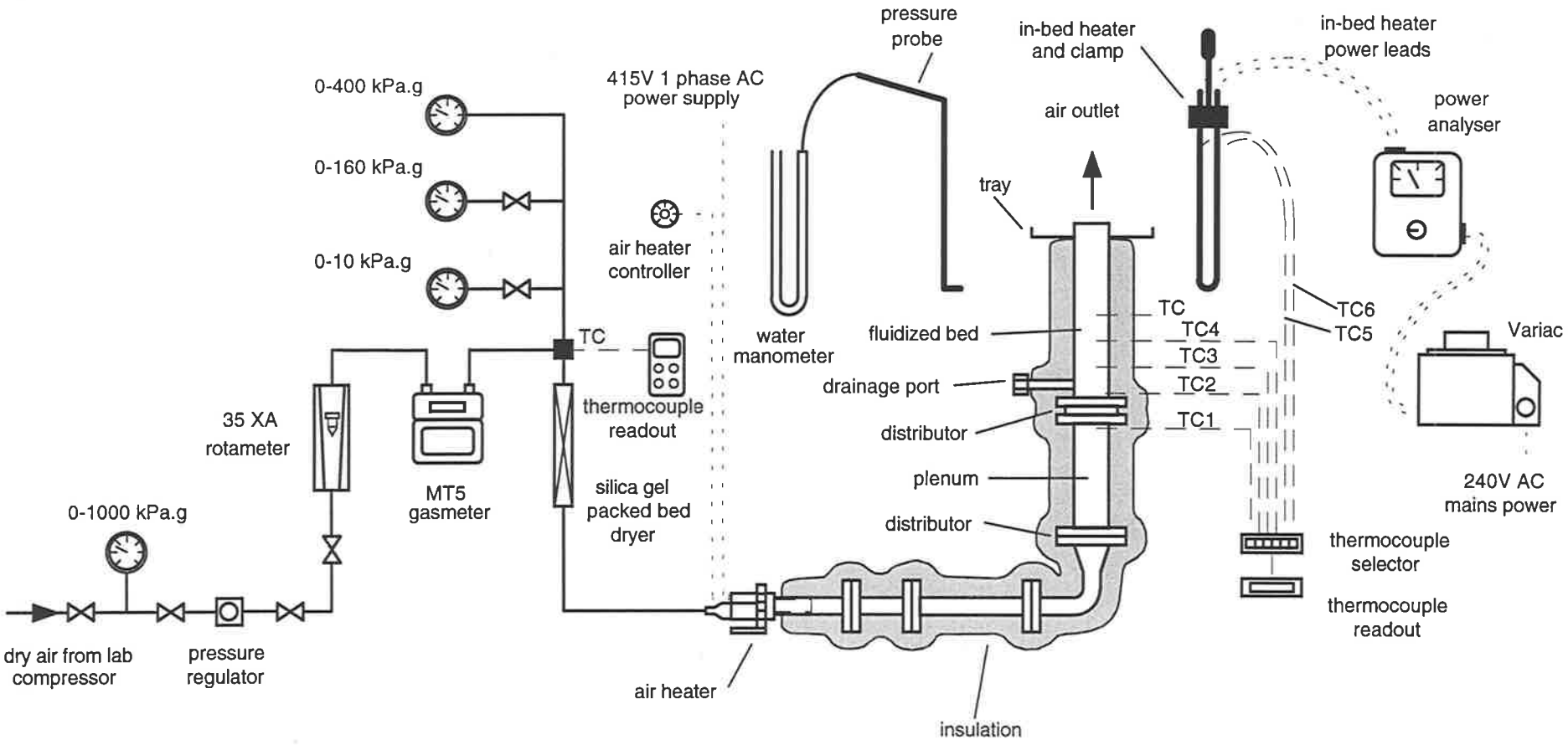

Figure 3.2: Schematic diagram of the high-temperature fluidized bed with associated instrumentation and control equipment.

bed is open to the atmosphere. A tray (380 x 380 mm) with a plug has been fitted around the top of the bed to collect any particles that escape the interior. A port is located approximately 15 mm above the bottom of the main bed section to allow removal of the bed contents. Attached to the bottom of the main bed section is a flange which connects to another on the top of the plenum section. A distributor plate is held in place between the two flanges. It is 1.7 mm thick and has 121 holes of 0.4 mm diameter on a 9 mm square pitch. A tight seal between the flanges and the distributor was ensured by the liberal application of a high-temperature cement, Autostic (Carlton Brown and Partners Ltd, Elford, England). To reduce heat loss, Fibrefax insulation was used to cover all the piping from the exit of the air heater to the top of the fluidized bed. Around the fluidized bed section, the insulation was about 75 mm thick.

Five type K thermocouples are available to measure the temperatures of the fluidized bed. One is located approximately 10 mm below the bed's distributor, while the other four are inside the bed itself. These are 1 mm in diameter, protrude 15 mm into the bed and are positioned 18, 90, 171 and 250 mm above the distributor. A digital readout was used to display four of the temperatures. As shown in Figure 3.2, the thermocouple below the distributor was TC1 and, inside the bed, from bottom to top, the first three thermocouples were labelled TC2-TC4.

A thin, L-shaped tube could be temporarily positioned in the bed to measure its pressure drop. The pressure difference was read off a water-filled U-tube manometer. Atmospheric pressure was measured by a barograph (JISB7307, Ota Keiki Seisakusho Co. Ltd, Tokyo, Japan).

With this apparatus, several experiments may be performed to study the behaviour of a heated surface immersed in a fluidized bed. Gas flowrate, bed temperature and power input to the heater are among the quantities that may be varied. However, some

characteristics of this system are difficult to analyse and control. The problems and limitations of the apparatus are discussed in Section 3.5 and Chapter 5.

3.3 BED MATERIAL

The particles used in the experiments were carefully sieved ballotini impact spheres (Potters Industries, Laverton, Victoria). Table 3.1 lists the physical properties of the particles. Only one particle size was employed throughout the experimental study. This is a clear deficiency and should be remedied in future work.

Table 3.1: Physical properties of the particles used in the experimental study.

Property	
Material	soda-lime glass
Density	2470 kgm^{-3}
Size range[1]	589-701 $x10^{-6}$ m
Mean size	645 $x10^{-6}$ m
Shape	rounded, nearly spherical

Note:

1. As indicated by the sieve openings.

3.4 PROCEDURES

To understand the coating-erosion phenomenon, it is necessary to characterise the thermal and fluidization properties of the bed. Consequently, four types of experiments were performed:

- estimation of the effective melting temperature of the bed particles;
- determination of the minimum fluidization velocity at several temperatures;
- measurement of the heat transfer coefficient between the U-tube heater and the fluidized bed under various conditions;
- the coating-erosion experiments themselves.

3.4.1 Melting Temperature

A known mass of the sieved ballotini, around 2.2 kg, was loaded into the bed; the static bed depth was about 190 mm. The U-tube heater was centred in the bed and held firmly by the positioning clamp so that the bottom of the heater was fixed 51 mm above the distributor. Fluidizing air was admitted to the system and the air preheater control was adjusted. Throughout the experiment, the fluidized bed was maintained at a given temperature on the point of minimum fluidization (as determined visually).

Power was supplied to the in-bed heater; care was taken to avoid any temperature overshoot in the heating-up process. After a while, the heater became stabilised at the required temperature. For 15 minutes afterwards, the temperature of the in-bed heater - as indicated by TC5 - was maintained as close as possible to the target value. Frequent small changes to the air flowrate and the in-bed heater power were needed. Regular temperature readings from TC1-TC6 were recorded. At the end of the time, the in-bed heater was very carefully removed from the bed and inspected. It was noted whether any particles had sintered onto the heater near the tip of TC5.

The above procedure was repeated for a series of in-bed heater temperatures. Between each experiment, the heater was scraped clean of any adhering particles. The lowest temperature at which particles would sinter onto the heater was taken as the effective melting temperature of the bed particles.

3.4.2 Minimum Fluidization Velocity

In this study and the previous one, the same bed material was used. However, this experiment did not require the U-tube heater. The L-shaped differential pressure tube was positioned inside the bed with its end about 10 mm above the centre of the distributor. The air flow through the system was started and set to a high value. The air heater was turned on and adjusted to give the required bed temperature. When the bed had stabilised at the desired temperature, the following measurements were recorded:

- rotameter scale reading and pressure in the rotameter;
- differential pressure tube manometer readings;
- temperature readings: TC1-TC4.

The air flowrate was decreased slightly and the same measurements were taken. This procedure was repeated until the air flowrate was quite low. The point at which the bed apparently ceased bubbling was noted. In addition, before and after the experiment, the atmospheric pressure and the rotameter air temperature were recorded. All the experimental measurements had to be taken quickly, since the bed temperature tended to fall as the flowrate decreased.

From the data so gathered, the superficial gas velocities and bed pressure drops were calculated. The bed temperature was taken to be the average of TC2, TC3 and TC4. A straight line was regressed through the low-velocity portion of the data. The average pressure drop over the bed for the high-velocity data was calculated. The superficial velocity corresponding to the intersection of the lines describing the high and low velocity data was taken as the minimum fluidization velocity.

3.4.3 Heat Transfer Coefficient

These experiments started with the material left in the bed from the minimum fluidization velocity experiments. The U-tube heater was placed in the bed as described in Section 3.4.1. Next, the air flow was commenced and the air heater control was adjusted.

Two types of experiments were performed: those in which the superficial velocity (measured at the bed conditions) was held approximately constant and the bed temperature was varied; and those in which the bed temperature remained roughly constant while the superficial velocity changed. For the first type of experiment, the gas flowrate was appropriately decreased as the bed heated up. In the second type of experiment, the air heater setting was adjusted to keep the bed temperature as constant as possible, while the air flowrate was increased. The procedure for measuring the heat transfer coefficient was the same for both. Power was supplied to the in-bed heater. When the heater / bed system was reasonably steady, usually 3-10 minutes was required, the following measurements were taken:

- rotameter: scale reading, pressure and temperature;
- temperature readings: TC1-TC6;
- power supplied to the in-bed heater - either directly from the power analyser, or, in earlier experiments, from the current and voltage measured by the multimeter.

Atmospheric pressure was also recorded. Care was taken to maintain as large a temperature difference as possible between the heater and the bed. At no time did the heater exceed the effective melting temperature of the glass ballotini. For each run ("constant velocity" or "constant bed temperature") twenty or so readings were taken.

The bed temperature, T_∞, was calculated as the average of TC2-TC4, as before. Similarly, the mean of TC5 and TC6 was assumed to be the heater temperature, T_b. When the multimeter was used, the power supplied to the heater, $Q_{b\,ext}$, was taken to be the product of the voltage and the current, since the heater is almost a pure resistance. The heat transfer coefficient, h, was calculated from:

$$h = \frac{Q_{bext}}{A_b\,(T_b - T_\infty)} \tag{3.1}$$

It was not possible to measure the heat transfer area, A_b, precisely, since there was some conduction of heat up the legs of the heater. The heated zone was identified as the region which glowed when the heater was operated at reasonably high power in still air. Simple geometry was used to infer A_b.

3.4.4 Coating-Erosion Experiments

This set of experiments used the same particles as the previous heat transfer study. The position of the in-bed heater was not changed. After starting the air flow to the apparatus, the air heater was set appropriately.

When the bed had stabilised at the desired conditions of temperature and superficial velocity, an initial set of readings was recorded. The in-bed heater was turned on and quickly brought up to the required power level. Experimental readings were taken as often as possible or as seemed necessary. The set of measurements recorded was identical to that of the heat transfer study but with the addition of the time elapsed since the in-bed heater had been switched on. Each set of readings was taken together as quickly as possible. As the experiments proceeded, small adjustments were made to maintain a constant level of power supplied to the in-bed heater and a steady flowrate

through the rotameter. Power to the in-bed heater was cut either after a given time, or when a desired heater or bed temperature had been achieved.

Immediately after cutting the power, the in-bed heater was carefully removed from the fluidized bed and positioned in a container to cool. The heater was slowly cooled to room temperature with the aid of air from the laboratory supply. Any particles that detached from the heater during cooling were collected in the bottom of the container.

Atmospheric pressure was recorded. The experiments lasted from two minutes to just over one hour. The temperature of the fluidized bed was not allowed to exceed the melting point of the glass ballotini. Once again, the bed temperature, heater temperature and the amount of power supplied to the heater were calculated as indicated in the heat transfer experiments.

While the heater was cooling down, a record was made of the approximate spatial distribution of the coating that had formed on the heater. When cool, any coating which remained on the heater was removed. The mass of all the particles that adhered to the heater (including those that detached during cooling) was carefully determined with a Mettler AE 166 analytical balance. The maximum thickness of the coating was also measured. Coating fragments were observed with an optical microscope.

3.5 RESULTS AND DISCUSSION

In this section, the supporting experiments - measurement of the melting temperature, the minimum fluidization velocity and the heat transfer coefficient - are considered. Discussion of the coating-erosion experiments, including their comparison with the theory developed in the next chapter, is deferred until Chapter 5.

3.5.1 Melting Temperature

It was consistently found that particles sintered onto the in-bed heater at 625 °C, but did not at 620 °C. Consequently, 625 °C was assumed to be the effective melting temperature of the particles. In these experiments, TC5 could be controlled to within 1 or 2 °C. The temperature of the fluidized bed was around 390 °C which was merely convenient for the operation of the apparatus. However, there were axial temperature gradients in the bed and the average temperature fell slowly throughout. To varying degrees, these problems were encountered in all of the experimental studies presented in this thesis; they will be discussed in later sections.

The method used here for the determination of the effective melting temperature of the glass ballotini is a slight variation on a technique employed by the powder coating industry for polymers (see Elmas quoted in Section 2.2.1). It was necessary to perform these experiments because a value of "the melting temperature" of soda-lime glass could not be found in the literature. Of course, this trouble arises because purely amorphous glasses do not have a latent heat of fusion. However, when glasses are cooled slowly from the molten state, some crystallisation may take place - that is, the glass devitrifies to an extent. Energy is needed to form the crystals and this causes a bend in the specific heat capacity - temperature curve, which is not present for the fully amorphous glass. These matters are explored by Sharp and Ginther (1951). Nevertheless, it is interesting to compare some of the temperatures that characterise the behaviour of soda-lime glass - see Table 3.2.

Table 3.2: Comparison of various temperatures that characterise the behaviour of soda-lime glass.

Name of property	Temperature (°C)	Method of measurement	Comments	Reference
strain point	473	ASTM C 336-71 (1981)[1] or ASTM C 598-72 (1978)[1]	• marks the transition between brittle and viscoelastic behaviour • internal stresses are relieved to an acceptable level in 4 hours • used to set annealing schedules and estimate stress relief	de Jong (1989)[2]
annealing point	514		• internal stresses are relieved to an acceptable level in 15 minutes • used to set annealing schedules and estimate stress relief	
softening point	696	ASTM C 338-73	• below this temperature, glass behaves as a rigid solid in forming operations • also used as a guide to indicate changes in composition	
working point	1005	based on viscosity measurements	• corresponds to a viscosity of exactly 10^3 Pa.s • glass is sufficiently fluid to be formed and shaped by most methods	
minimum sintering temperature[3]	530 - 570	CHR[4] dilatometry	• the temperature varies with particle size and applied interparticle force • d_p: various, from 60 to 390 µm • F_p: various, from $5x10^{-4}$ to $7.5x10^{-3}$ N	Mazzone (1986)
	580	CHR[4] dilatometry	• d_p: 510 µm	Compo (1989)
	620, 635	defluidization	• d_p: 275, 720 µm	
	(650)	CHR[4] dilatometry	• d_p: 1100, 1300 µm	Siegell (1976) [5]
	(690)	defluidization	• some effect of bed height to diameter ratio in delfuidization experiments	
effective melting temperature[3]	625	Section 3.4.1	• slight variation on technique used in powder coating industry for polymers • d_p: 645 µm	this work

Notes:

1. New or revised standard available.
2. Values are for soda-lime glass, code 0080.
3. These definitions apply only for glass in particulate form.
4. Constant Heating Rate.
5. Silicate glass. These values are not directly comparable with the others.

The effective melting temperature of the particles found in this study lies between the annealing and softening points of the bulk glass. Therefore, at T_m the particles are viscoelastic (as opposed to brittle), and behave more like a rigid solid than a liquid. Further, the value of T_m found in this study is very similar to the minimum sintering temperature, T_{ms}, deduced from the defluidization experiments of Compo (1989). The minimum sintering temperature originates from the study of defluidization and high-temperature particle cohesion in fluidized beds. It is the temperature of a fluidized bed above which the gas velocity needed to maintain fluidization must be increased to overcome the tendency of the particles to stick together at high temperatures. Properly, T_{ms} is obtained from a series of defluidization experiments in which the effective minimum fluidization velocity of the particles is determined over a wide range of temperatures. Constant heating rate dilatometry has been useful for estimating T_{ms}. It is certainly much more convenient than the defluidization approach, but is not wholly reliable. Both methods, their significance and interpretation are discussed by Siegell (1976), Mazzone (1986) and Compo (1989).

One of the conclusions of these studies was that the surfaces of particles at and above T_{ms} are liquid-like. This is because the particles can form weak bonds with each other in a very short time. It was also found for a variety of substances with a definite melting point, T_{mpt}, that the relative minimum sintering temperature T_{ms}/T_{mpt} ranged from 0.4 to 0.98 (both temperatures are measured in Kelvin). If the effective melting temperature as determined in Section 3.4.1 is the same as the minimum sintering temperature, then particles may adhere to an immersed object which is below the melting point proper. This is in contrast to Elmas' statement that $T_m = T_{mpt}$. It would be interesting to measure T_m as described in Section 3.4.1 for a wide range of materials and to compare the results with published values of T_{ms} and T_{mpt}.

3.5.2 Minimum Fluidization Velocity

Some typical pressure drop and superficial velocity data used to determine the minimum fluidization velocity are presented in Figure 3.3. The complete set of results is given in Table 3.3.

Table 3.3: Experimentally determined minimum fluidization velocities of 589-701x10^{-6} m glass ballotini at various temperatures.

Bed Temperature Range (°C)	**Atmospheric Pressure (kPa)**	**Minimum Fluidization Velocity (ms^{-1} at T_∞, p)**
18	102.2	0.326
248-268	103.0	0.254
328-348	103.1	0.233
433-448	102.9	0.225
520-528	100.9	0.203
518-538	102.7	0.214
538-552	101.2	0.210

These experiments were reasonably straightforward. The only complication was the presence of temperature gradients along the height of the fluidized bed at low gas velocities. When the gas flowrate is high, the particles in the fluidized bed are well mixed and the temperature is quite uniform, often within a few degrees. However, near u_{mf}, the motion of the solids is sluggish and, of course, below u_{mf}, it ceases altogether. By itself, this would not cause a temperature gradient in the fluidized bed. Unfortunately, in this experimental system, the temperature of the air entering the bed depends on the flowrate through the air heater; low flowrates cause low temperatures. Combined with

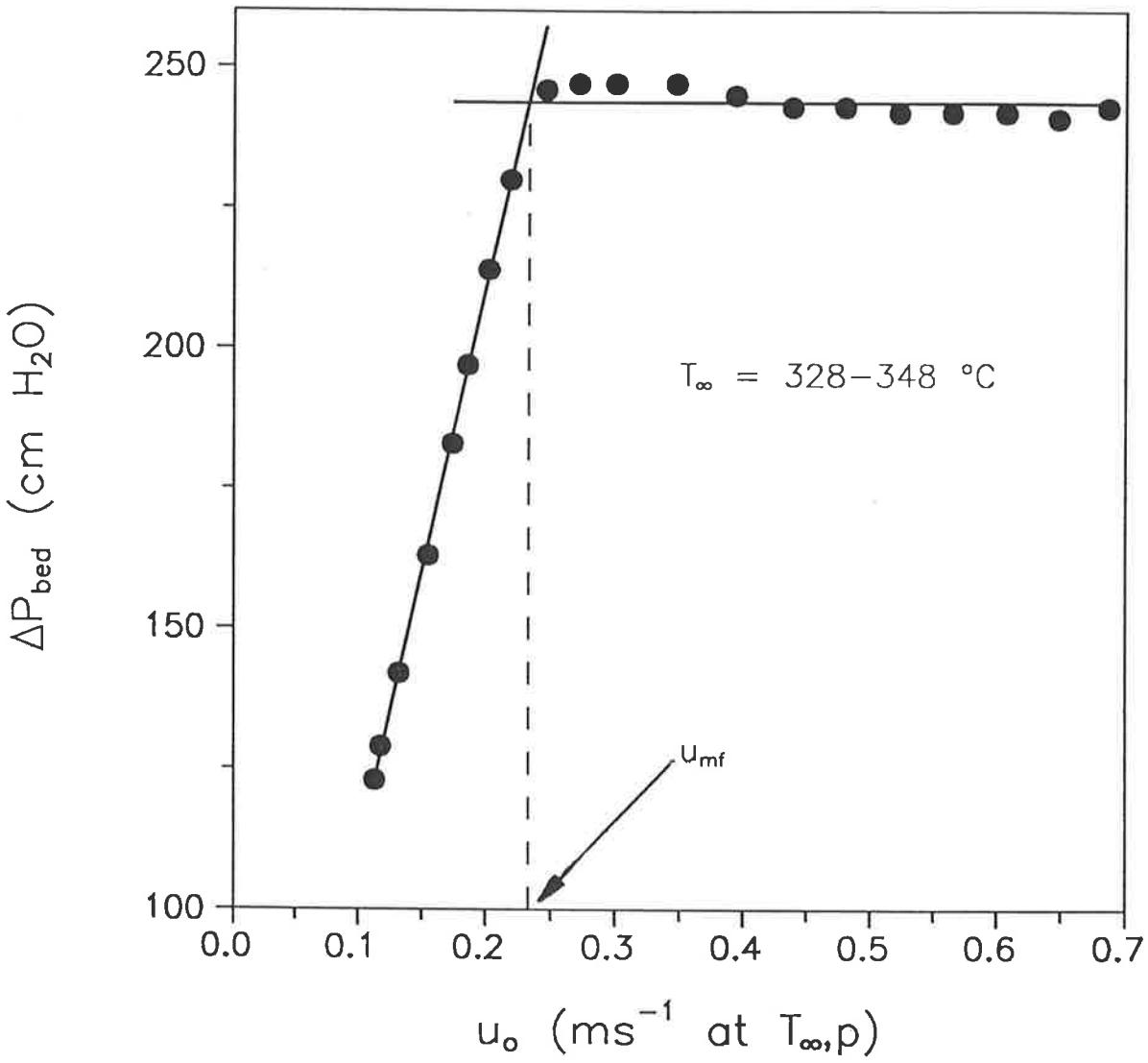

Figure 3.3: Typical data used to calculate the minimum fluidization velocity of 589-701 x10^{-6} m glass ballotini at a particular temperature.

the absence of solids mixing, this effect produced temperature differences in the bed of generally about 20 °C at the lowest gas flowrates used (50 °C in the worst case). As mentioned earlier, the experiments were performed quickly in an attempt to keep the fluidized bed temperature as uniform and constant as possible. Despite this problem, the velocities, calculated as described in Section 3.4.2, are fairly self-consistent and agree well with the points of bubble disappearance noted visually.

In order to compare the coating-erosion model of the next chapter with experiments, it is necessary to be able to predict the minimum fluidization velocity under different conditions. Throughout all the experiments, atmospheric pressure varied little - the main influence was bed temperature. Regression of the data contained in Table 3.3 yields an expression for the minimum fluidization velocity, u_{mf} (ms^{-1} at T_∞, p):

$$u_{mf} = 0.334 - 4.22\text{x}10^{-4}T_\infty + 4.67\text{x}10^{-7}T_\infty^2 - 2.11\text{x}10^{-10}T_\infty^3 \qquad (3.2)$$

where the bed temperature, T_∞, is measured in degrees Celsius.

In Figure 3.4 and Table 3.4, the experimental values of the minimum fluidization velocity are compared with equation (3.2) and the correlations published by:

Wen and Yu (1966):

$$Re_{mf} = \sqrt{(33.7)^2 + 0.0408\,Ga} - 33.7; \qquad (3.3)$$

Saxena and Vogel (1977):

$$Re_{mf} = \sqrt{(25.28)^2 + 0.0571\,Ga} - 25.28; \qquad (3.4)$$

and **Agarwal and O'Neill (1988):**

$$C_D.Re_{mf} = \sqrt{(6.84)^2 + 0.027\,Ga.C_D} - 6.84. \qquad (3.5)$$

Re_{mf} is the Reynolds number at incipient fluidization from which the minimum fluidization velocity may be simply calculated, Ga is the Galileo number, and C_D is the isolated-sphere drag coefficient. Note that equation (3.5) requires iterative solution because the drag coefficient varies with the Reynolds number.

Table 3.4: Comparison of the accuracy of several expressions for the minimum fluidization velocity of 589-701 $x10^{-6}$ m glass ballotini.

Author	RMS Error (ms^{-1})	Mean Percentage Error
Wen and Yu (1966)	0.042	18
Saxena and Vogel (1977)	0.106	45
Agarwal and O'Neill (1988)	0.041	15
This work, equation (3.2)	0.004	2

Note: The RMS and Mean Percentage Errors are defined in Appendix F.

The literature correlations either over- or under- predict the experimental results, although they all show the trend of decreasing u_{mf} with increasing bed temperature. The expressions of Wen and Yu (1966) and Agarwal and O'Neill (1988) represent the data within 20%, which is considered to be good for predictions of this type. Equation (3.2) represents the data very well, although, of course, it is not a general expression.

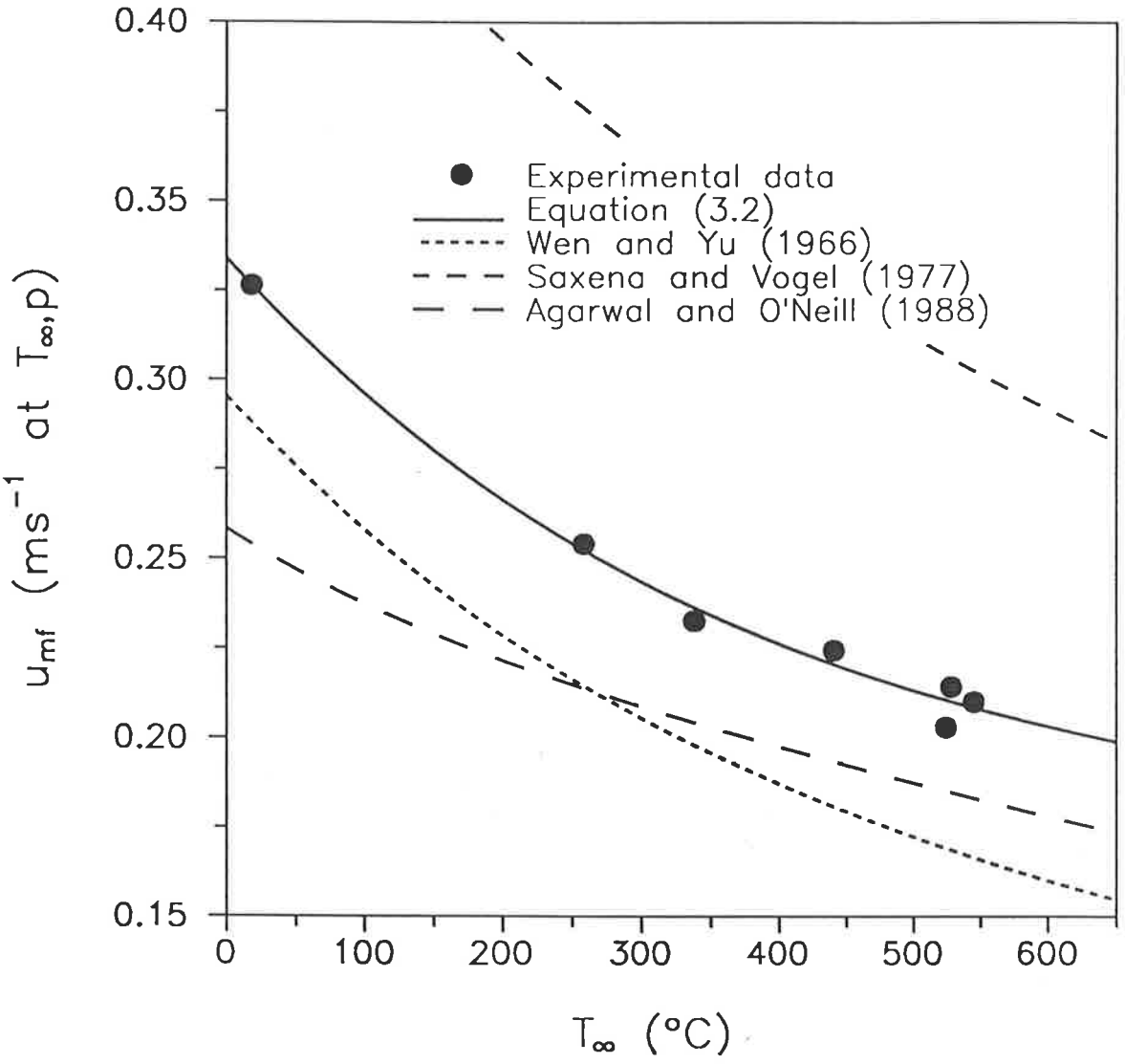

Figure 3.4: Variation of the minimum fluidization velocity of 589-701 x10^{-6} m glass ballotini with temperature, including comparison with equation (3.2) and several published correlations.

3.5.3 Heat Transfer Coefficient

Five heat transfer experiments were performed under "constant velocity" conditions; the results appear in Figure 3.5. Data obtained in the three "constant bed temperature" experiments are presented in Figure 3.6. Figure 3.7 shows the range of experimental conditions - bed temperature and superficial gas velocity - that were covered in the heat transfer study. Note that none of the experimental runs were truly constant-u_o or constant-T_∞; there was always some deviation. Although this does not invalidate the data, it does make its interpretation more difficult. In total, 180 data points were collected.

Before discussing the author's results, relevant experimental observations made by previous workers will be outlined (Gelperin and Einstein, 1971; Saxena et al., 1978; Saxena, 1989).

Bed temperature: The heat transfer coefficient increases in an approximately linear fashion with the temperature of the fluidized bed, provided that T_∞ is not too high. For high bed temperatures (given as above 1000-1200 °C), the rate of increase is superlinear.

Superficial gas velocity: At low and moderate temperatures, the heat transfer coefficient exhibits a rising-then-falling variation with increasing superficial gas velocity. A whole range of geometries behave in this way: immersed single horizontal, vertical and slanted tubes; tubes in horizontal and vertical bundles; spheres; and the walls of the bed itself. At high temperatures, the heat transfer coefficient usually does not reach a maximum then decrease, but passes through an inflection point and continues to rise with u_o.

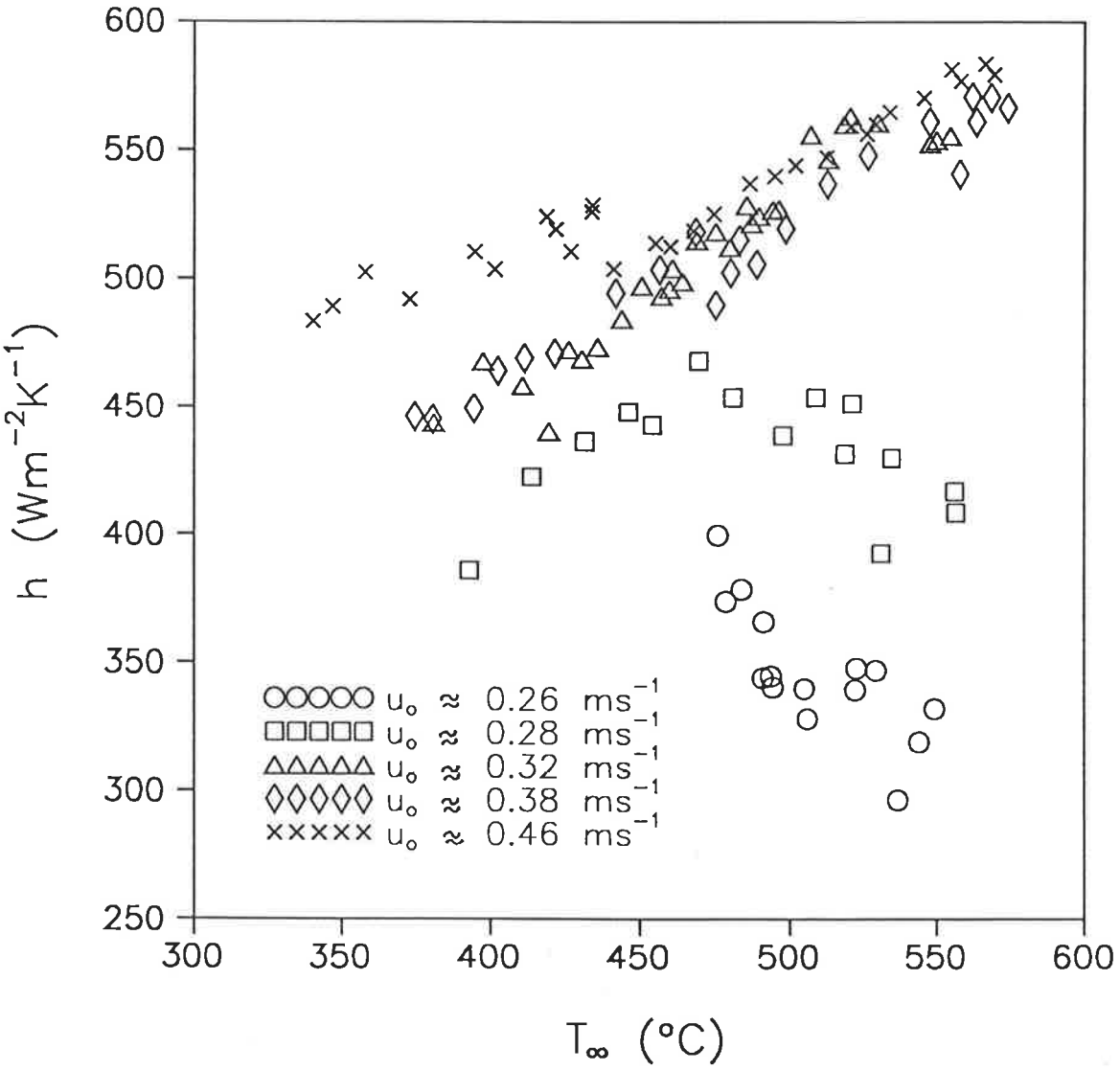

Figure 3.5: Variation of the experimental heat transfer coefficient with the temperature of the fluidized bed under "constant velocity" conditions.

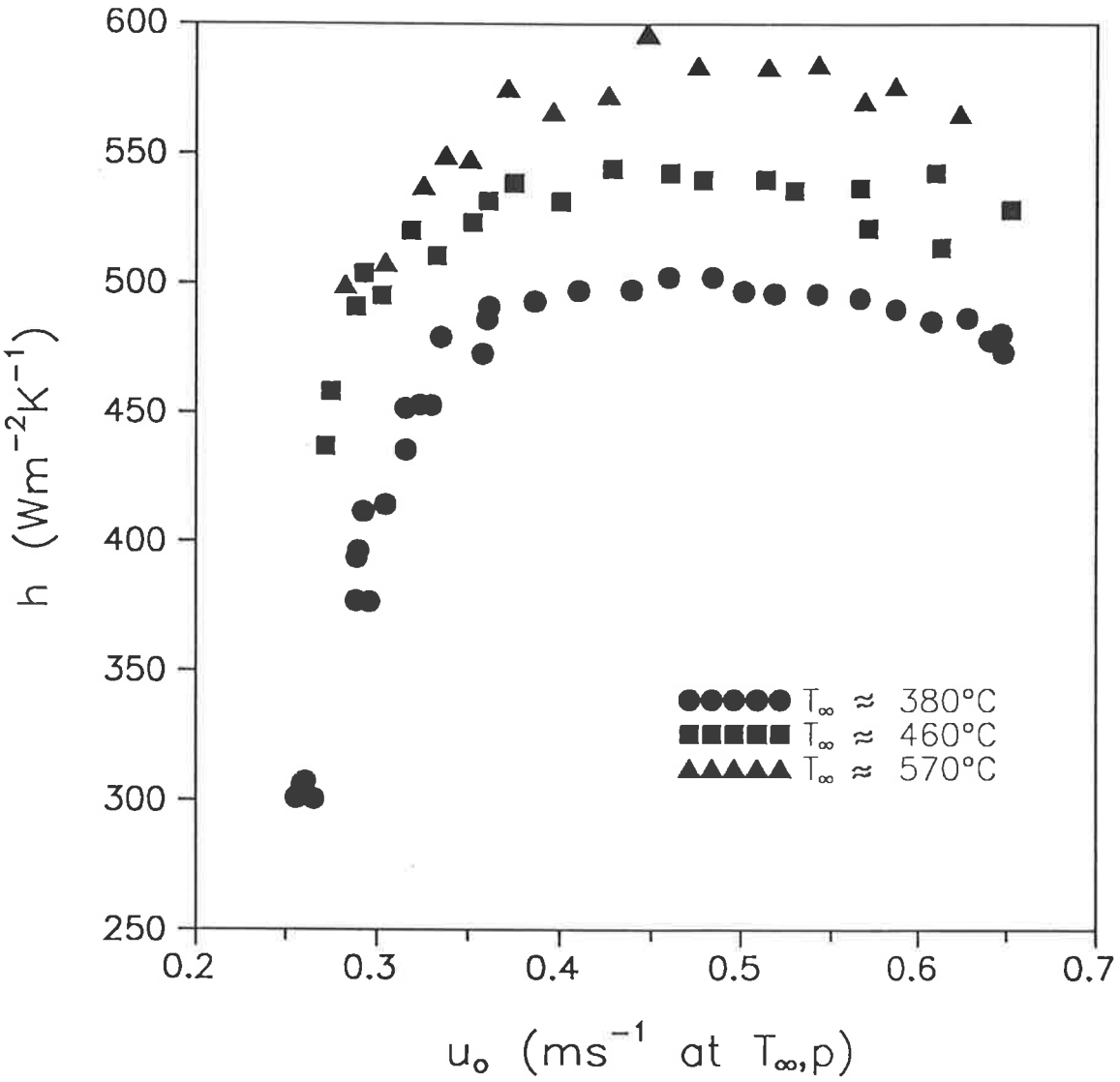

Figure 3.6: Variation of the experimental heat transfer coefficient with the superficial gas velocity under "constant bed temperature" conditions.

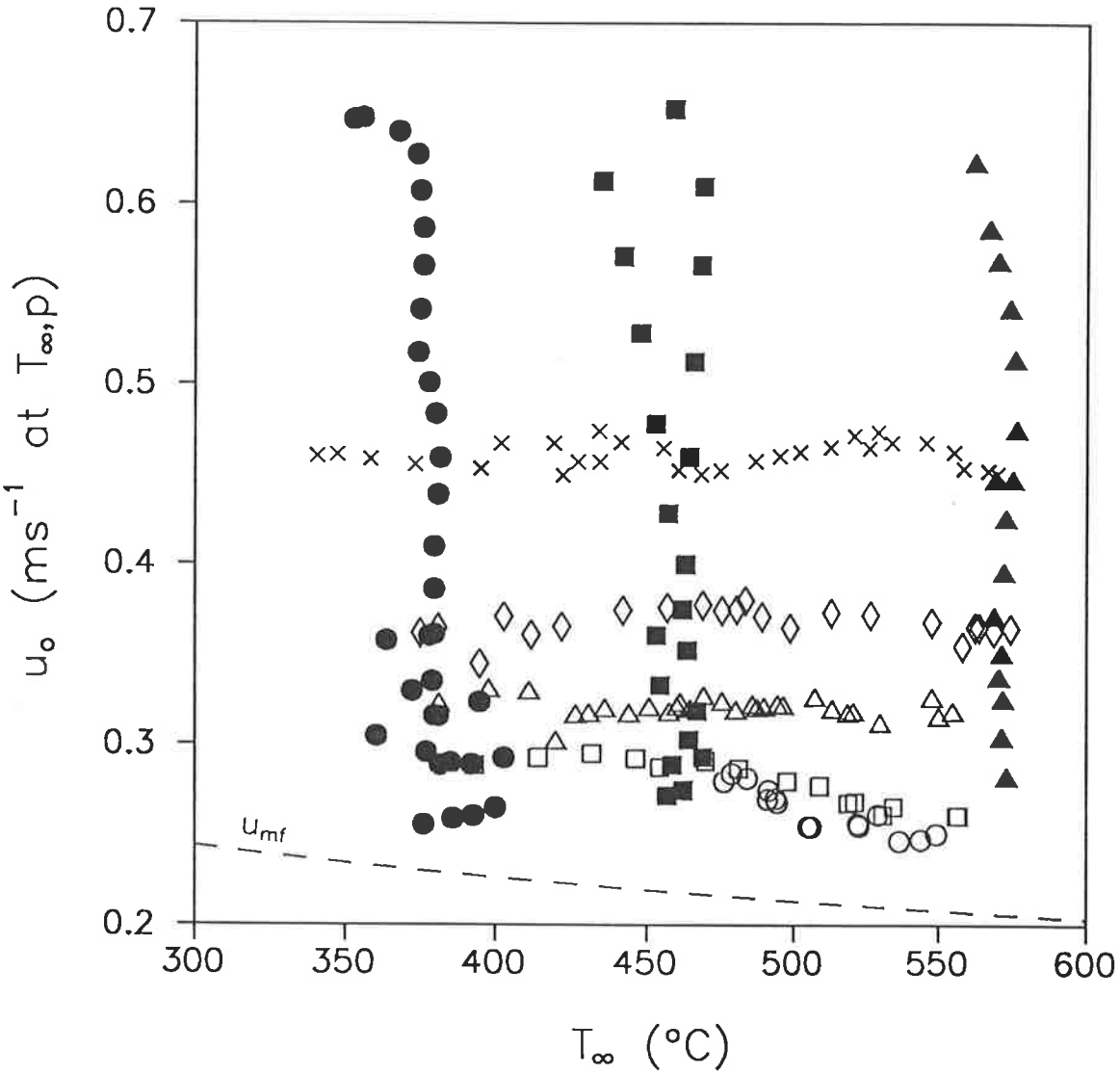

Figure 3.7: Range of conditions of bed temperature and superficial gas velocity covered in the heat transfer study (symbols are as defined in Figures 3.5 and 3.6). Also shown is the minimum fluidization velocity curve, given by equation (3.2).

Tube orientation: Some authors report that heat transfer coefficients for vertical tubes are normally 5-15% higher than for horizontal ones; others find a "slight" increase. In one study, minimum values of h were observed for a tube inclined at 45°.

Tube diameter: The variation of the heat transfer coefficient with the diameter of the immersed tube is difficult to predict, since it is intimately connected with the local solids motion. Consequently, all of the experimental variables and the geometry of the system are involved. For horizontal tubes, some authors state that h is independent of the tube diameter, d_h. Others find that: $h \propto d_h^{-0.18}$ to $d_h^{-0.7}$; $h \propto d_h^{0.2}$; and that h first decreases then increases with d_h. Similarly, for vertical tubes, the heat transfer coefficient has been reported to: increase; decrease; increase then decrease; and remain constant with increasing tube diameter.

Tube roughness and fins: There have been a number of heat transfer studies that deal with modifications to the surface of an immersed body. Methods of altering a smooth surface included: treatment with abrasive particles; machining of grooves and threads; knurling; and the addition of fins (of various types) and spines. Of these, perhaps the most relevant here is knurling - the process machining two sets of intersecting V-grooves so as to tessellate the surface with pyramids. Grewal and Saxena (1979) present results which suggest that h is weakly proportional to P_k/d_p. The pitch of the knurling, P_k, is the distance between identical points on adjacent knurls, as measured along a non-curved part of the surface.

Local heat transfer coefficients: For a horizontal tube, the local (but time-averaged) heat transfer coefficient varies with angular position. At low u_o, the local heat transfer coefficient is small directly below the tube (because of gas pockets that tend to form there) and directly above it (due to a defluidized cap of particles). The greatest h occurs a little above the tube's equator, where the solids motion is most vigorous. As the gas velocity increases, the angular heat transfer profile becomes more uniform. Around the

superficial velocity that gives the maximum mean heat transfer coefficient, the local h is reported to vary, at most, by between 0 and 25% with angular position. For vertical tubes, the local heat transfer coefficient has no angular variation, but can change with vertical position on the tube. The variation with height may be complex.

It can be seen in Figure 3.5 that, for the three highest velocity data sets, the heat transfer coefficient increases in an approximately linear manner with the temperature of the fluidized bed, as expected. The two lower velocity data sets seem to show different behaviour. This is because u_o was not truly constant in those data sets, but decreased somewhat as T_∞ increased (Figure 3.7). It is thought that the effect of decreasing u_o overwhelmed the influence of the bed temperature, causing the apparently contradictory results.

The characteristic rising-falling behaviour of the heat transfer coefficient with superficial gas velocity is well demonstrated in Figure 3.6. However, the declining part of the h-u_o curve should perhaps be a little flatter, since the bed temperature did decrease slightly at high u_o in each of the three data sets - again, refer to Figure 3.7.

At low superficial gas velocities, as in the minimum fluidization velocity study, axial temperature gradients appeared in the fluidized bed. Under all conditions, the top part of the bed was nearly uniform in temperature (as indicated by close agreement between TC3 and TC4). When u_o is low, however, the bottom section of the bed may be substantially cooler. In the worst case, the lower part of the fluidized bed was about 30 °C colder than the top.

As mentioned in Section 3.2.1, the U-tube heater had a hotspot. According to the manufacturer, this was caused by bunching of the resistance wire coils during the bending of the tube. Recall that TC5 was placed at the centre of the hotspot, while TC6 was positioned near the bottom of the heater (Figure 3.1). The average temperature

difference between these points, taken over all the experiments, was 9 °C, although differences as low as 1 °C and as high as 43 °C were recorded. The greatest discrepancies seemed to occur at low superficial gas velocities and low bed temperatures. It should be noted that the hottest part of the heater was never allowed to exceed the melting temperature of the particles.

Figure 3.1 shows the extent of the heated zone. The length of the zone on each of the heater's legs is slightly different, but it is thought that this is unimportant. Of more concern is the possibility of conduction up the legs of the heater. Modifications to the apparatus could have reduced this effect, but they would have made the U-tube more bulky. Conduction is not taken into account in the calculation of the heat transfer coefficient by equation (3.1). The heat loss by conduction in the worst case is estimated as 20 W†, which would lead to an overestimation of h of less than 10%. The conductive heat loss is greatest when the heat transfer coefficient is high and the temperature difference between the U-tube and the fluidized bed is large.

It is well known that the instantaneous heat transfer coefficient varies with the passage of bubbles (Kunii and Levenspiel, 1991, p318-319) and that there are local variations in h over the immersed object's surface. The heat transfer coefficients determined in this work, however, are average ones - averaged both in time and in space, over the surface of the heater. In part, the nature of the heat transfer data influenced the development of the mathematical model described in Chapter 4.

For use in a simulation program, it is convenient to represent the heat transfer data by a simple mathematical expression. This approach should be quicker than the interpolation of a table of values. In addition, the function would be "smoother", thus improving the stability of subsequent calculations.

† Estimated from solution of Case 1 fin problem (Holman, 1989, p43-46).

In a comprehensive review of heat transfer to immersed objects in fluidized beds, Saxena (1989) recommends certain heat transfer coefficient correlations for small bed particles. According to the powder classification scheme of Saxena and Ganzha, small-particle heat transfer is dominated by conduction through the gas lens that exists between a bed particle and the immersed surface (Saxena, 1989). Such systems, denoted as Group I, are characterised by $3.55 \leq Ar \leq 21700$, where Ar is the Archimedes number. In the present heat transfer study, Ar ranged from 1950 to 4120 - clearly it is a Group I system. The correlations recommended by Saxena (1989) were those of:

Wender and Cooper (1958) for vertical tubes:

$$\frac{Nu_p}{(1-\varepsilon)}\alpha_g^{0.43} = 3.5\text{x}10^{-4} C_R \, Re^{0.23}\left(\frac{c_{pp}}{c_{pg}}\right)^{0.8}\left(\frac{\rho_p}{\rho_g}\right)^{0.66}; \tag{3.6}$$

and **Grewal and Saxena (1980)** for horizontal tubes

$$\frac{Nu_h}{(1-\varepsilon)} = 47\left(\frac{d_h u_o \rho_p}{\mu_g}\frac{\mu_g^2}{d_p^3 \rho_p^2 g}\right)^{0.325}\left(\frac{\rho_p c_{pp} d_h^{3/2} g^{1/2}}{k_g}\right)^{0.23} Pr^{0.3}. \tag{3.7}$$

where Nu_p and Nu_h are, respectively, the Nusselt numbers based on the particle diameter and tube diameter, from which the heat transfer coefficients may be simply obtained. C_R is a factor that allows for non-axial tube location. It should be noted that equation (3.6) is dimensionally inconsistent, so, care must be taken with the units (for the given constant, α_g is in m^2s^{-1}). The bulk bed porosity, ε, is given by the correlation of Grewal (Grewal and Saxena, 1980):

$$\varepsilon = \frac{1}{2.1}\left[0.4 + \left\{4\left(\frac{u_o \mu_g}{(\psi d_p)^2(\rho_p - \rho_g)g}\right)^{0.43}\right\}^{1/3}\right] \tag{3.8}$$

Wender and Cooper (1958) used a "brute force" approach - investigation of the effect of each experimental variable separately - and thus made few assumptions about the form that the correlation should take. It is thought that the other authors used a more conventional technique - arrangement of the variables into dimensionless groups. Thus, both correlations are empirical, rather than the results of theoretical modelling. There seem to be no heat transfer correlations for U-tubes, as used in this study, but, it can be argued that a U-tube is just a combination of horizontal and vertical sections. In view of the similarity between the behaviour of horizontal and vertical tubes, it expected that correlations developed for them should also represent U-tube data.

The recommended correlations were compared with the experimental heat transfer coefficient data. On average, both correlations tended to underpredict the data (Wender and Cooper (1958) by $\approx$ 13%; Grewal and Saxena (1980) by $\approx$ 6%). In addition, the data scattered reasonably widely about the predicted values, but were within the expected deviations reported for the correlations. In an effort to improve the agreement, a multiplication factor was sought, which, when applied to the leading coefficient of the correlations, would further minimise the SSE. The SSE, or Sum of the Square Error (Appendix F), was used as the merit function for the fit between a correlation and the data. Modifying the leading coefficient improved the fit in both cases, so that the mean behaviour was well predicted and average deviation was around 10%.

Xavier and Davidson (1985) reviewed the theoretical modelling of fluidized bed heat transfer. They concluded that the heat transfer coefficient between a vertical or horizontal immersed object and a fluidized bed may be represented by:

$$h = h_{pc} + h_{gc}; \tag{3.9a}$$

where:

$$h_{pc} = \frac{1}{(1/h_p)+(1/h_f)}(1-\varepsilon_b); \tag{3.9b}$$

$$h_p = \left(\frac{4\,k_{mf}\,\rho_{mf}\,c_{pmf}\,(u_o - u_{mf})}{\pi \min(L, d_b/2)}\right)^{1/2}; \tag{3.9c}$$

$$h_f = \frac{k_g}{\delta}, \qquad d_p/10 \le \delta \le d_p/4; \tag{3.9d}$$

$$k_{mf} = k_e^{\,o} + 0.1\rho_g c_{pg} d_p u_{mf}; \tag{3.9e}$$

$$h_{gc} = \left(\frac{4\,k_{mf}\,\rho_g\,c_{pg}\,u_{mf}}{\pi L}\right)^{1/2} + \frac{k_{mf}}{d_h} \tag{3.9f}$$

In equations (3.9), ε_b is the bubble fraction of the fluidized bed calculated by two-phase theory; L is the vertical dimension of the immersed surface; d_b is the bubble diameter estimated from Darton et al. (1977); δ is the average thickness of the gas lens between the particles and the surface; and $k_e^{\,o}$ is the effective thermal conductivity of a packed bed with stagnant fluid obtained from the correlation of Gelperin et al. (Gelperin and Einstein, 1971, p487-488).

The mechanistic heat transfer model developed in Xavier and Davidson (1981, 1985) was compared with the author's experimental data. This work underestimated the heat transfer coefficient by about 6% for $\delta = d_p/10$ and by around 50% for $\delta = d_p/4$. Despite the use of a multiplication factor, there was still considerable scatter of the experimental data about the predicted behaviour.

At this point, it was decided to investigate whether a simple function of the operating variables - T_b, T_∞ and u_o - could better represent the experimental heat transfer data. From a pragmatic point of view, it may be said that the correlations and model

mentioned above are only complex functions of the three experimental variables anyway. The criteria for selection of the function were:

- it should yield a small SSE;
- it should not behave unexpectedly when applied not-too-far-outside the range of experimental conditions under which it was determined;
- it should be a smooth (that is, not discontinuous) function and be quick to calculate.

The second condition was included because, some extrapolation of the heat transfer data to higher immersed body temperatures is essential. Heat transfer coefficients, calculated by equation (3.1), must be obtained in the absence of coating formation (see also Section 2.2.2). A consideration of the execution speed of the simulation program leads to the third criterion. The evaluation of the physical and thermal properties of the fluidizing gas - especially viscosity and thermal conductivity - needed in the correlations recommended by Saxena, is quite time consuming. Similarly, the determination of the bubble rise velocity and the effective bed thermal conductivity used in Xavier and Davidson (1981) would slow down the simulation program.

A number of simple functions of T_b, T_∞ and u_0 were tested. Two additional principles guided the search for the best equation. The heat transfer coefficient should first rise, then fall with superficial gas velocity and, it should increase in an approximately linear manner with temperature. Both of these effects were observed in the experimental study and are confirmed in the literature. Some typical candidate equations are listed in Table 3.5. The parameters of the equations were found by minimising the SSE by Powell's method (Press et al., 1989, Section 10.5) from a number of randomly chosen starting points.

Table 3.5: Typical equations tested for representation of the heat transfer data.

$h = \left[k_1(1-e^{-k_2 u_x}) + k_3(1-e^{-k_4 u_x})\right]\left[1+k_5 T\right]$
$h = \left[k_1(1-e^{-k_2 u_x}) + k_3(1-e^{-k_4 u_x})\right]\left[1+k_5 T + k_6 T^2\right]$
$h = k_1(1-e^{-k_2 u_x})\left[1+k_5 T\right] + k_3(1-e^{-k_4 u_x})\left[1+k_6 T\right]$
$h = \left[k_1 u_x^{k_2} + k_3 u_x^{k_4}\right]\left[1+k_5 T\right]$
$h = \left[k_1(1-e^{-k_2 u_x}) + k_3 u_x^{k_4}\right]\left[1+k_5 T\right]$

Notes:

1. k_i are constants found by minimising the SSE.
2. T may be either T_b, T_∞ or T_f (equation 3.12).
3. u_x is the excess gas velocity.

The best equation was found to be:

$$h = k_1(1-e^{-k_2 u_x})\left[1+k_5 T_f\right] + k_3(1-e^{-k_4 u_x})\left[1+k_6 T_f\right] \qquad (3.10)$$

where u_x is the excess gas velocity:

$$u_x = u_o(T_\infty, p) - u_{mf}(T_\infty, p) \qquad (3.11)$$

and T_f is the film temperature:

$$T_f = (T_b + T_\infty)/2 \qquad (3.12)$$

The best-fit values of k_1 - k_6 for equation (3.10) are given in Table 3.6. This combination yielded a SSE substantially smaller than either Saxena's recommended correlations or the model of Xavier and Davidson (1981, 1985). Further, the experimental data are approximately normally distributed about the predicted curve. In Table 3.7, the various expressions trialed for representing the heat transfer coefficient are compared with the experimental data through their RMS (Root Mean Square) and mean percentage errors - see Appendix F. Note that both the bed temperature and the film temperature were used in the determination of the gas properties needed by the published correlations.

Table 3.6: Best-fit parameters for the heat transfer coefficient function, equation (3.10).

Parameter	Value
k_1	634
k_2	18.7
k_3	-332
k_4	14.1
k_5	1.24×10^{-3}
k_6	1.02×10^{-3}

Note that these parameters apply when the following units are used in equation (3.10):

h: $Wm^{-2}K^{-1}$;
T_f: °C;
u_x: ms^{-1} at T_∞, p.

Table 3.7: Comparison of the heat transfer data with several published correlations and equation (3.10).

Author	RMS Error ($Wm^{-2}K^{-1}$)		Mean Percentage Error (%)	
	with gas properties evaluated at the bed temperature	with gas properties evaluated at the film temperature	with gas properties evaluated at the bed temperature	with gas properties evaluated at the film temperature
Wender and Cooper (1958)	81.6	84.8	15.0	15.8
with leading coefficient:	54.9 (0.890)	55.4 (0.884)	9.5	9.6
Grewal and Saxena (1980)	52.8	63.2	8.3	10.3
with leading coefficient:	49.0 (0.961)	50.1 (0.927)	8.3	8.6
Xavier and Davidson (1981)				
$\delta = d_p/4$	263	257	49.6	48.2
with leading coefficient:	101 (2.018)	102 (1.963)	18.5	18.7
$\delta = d_p/10$	96.9	94.0	18.1	17.5
with leading coefficient:	90.6 (1.076)	91.1 (1.050)	16.6	16.7
This work, equation (3.10)	21.3		3.4	

Note: The numbers in parenthesis are the multiplication factors for the leading coefficients, as found by regression.

It was decided to adopt equation (3.10) for the description of the heat transfer coefficient for the following reasons:

- correlation of the heat transfer coefficient is not the central theme of this work, it is merely an intermediate step in the experimental investigation of the coating-erosion phenomenon. No generalisation of these heat transfer results is sought;
- it is much quicker to use than correlations that require physical and thermal property evaluation - an important consideration in the simulation program;
- it should predict realistic values of h outside the range of experimental conditions used in its development (Figure 3.7), except in the direction of lower u_o;
- a theoretically-based model should only be used in preference to equation (3.10) if it can represent the data more accurately through having subtler dependencies on the experimental variables.

Equation 3.10 is purely empirical, but its form is based on the observed variation of h with the major experimental variables. It is not claimed that equation (3.10) or the values of k_1 - k_6 are applicable to any other system.

A comparison between the experimental data and the predictions of equation (3.10) is made in Figure 3.8. Most of the predicted values lie within ±10% of the data, and only one (out of 180) deviates by more than 20%. The average difference is 3.4%.

Before we use equation (3.10) in the analysis of the coating-erosion experiments, a further question needs to be answered. *Will the heat transfer coefficient change when a coating of particles is formed?* A coating may affect the heat transfer coefficient in three ways - by increasing the effective diameter of the immersed body, and by adding roughness to the surface, and by effectively changing the body's shape.

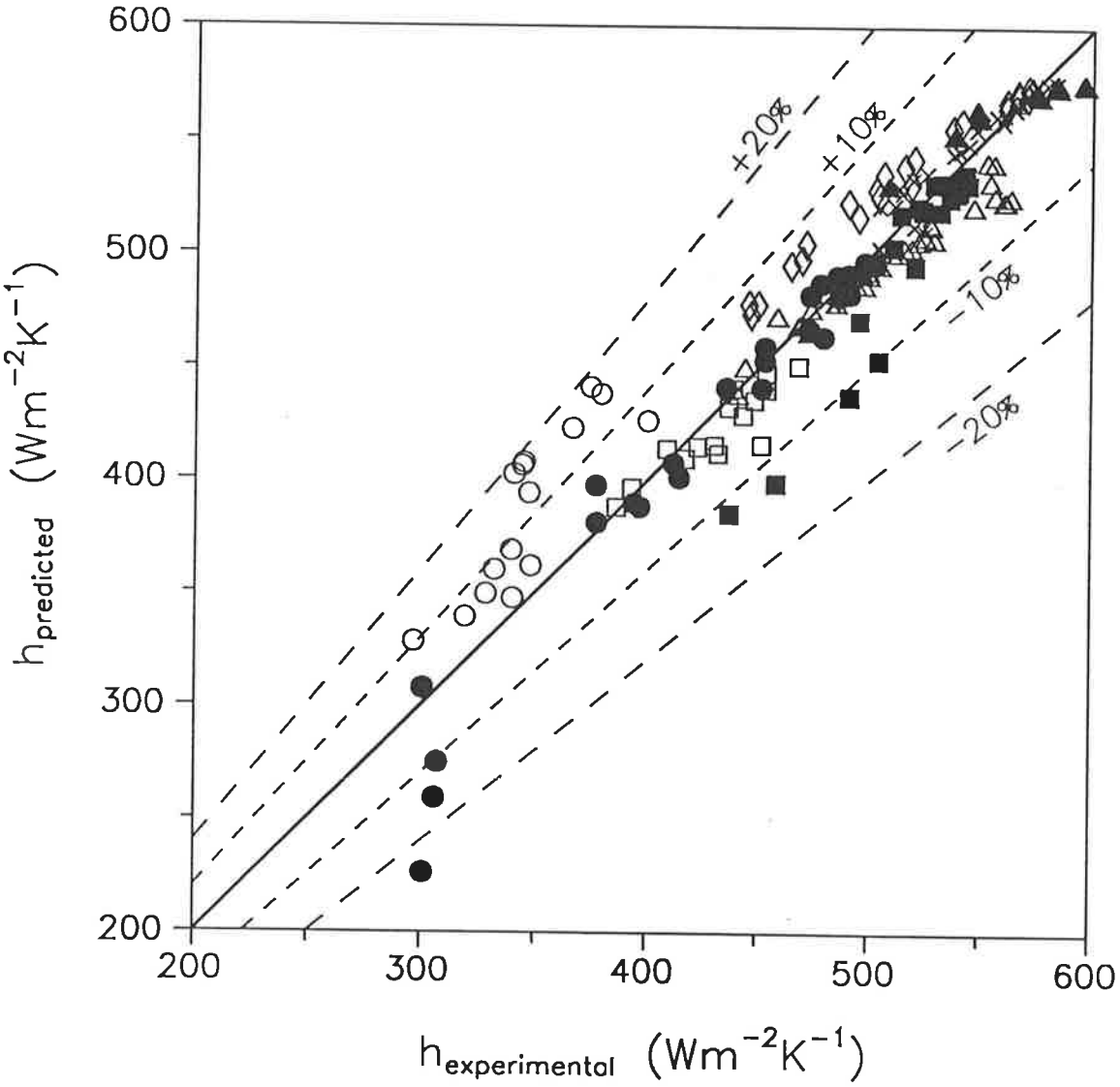

Figure 3.8: Comparison of the experimental values of the heat transfer coefficient with those predicted by equation (3.10) (symbols are as defined in Figures 3.5 and 3.6).

As mentioned before, the influence of the diameter of the immersed body on h is difficult to predict. Maybe the only way to be certain of the effect of d_h is to acquire a series of U-tube heaters of larger diameters and to repeat the heat transfer experiments already described. However, that is left as future work; for the present, it is assumed that the heat transfer coefficient does not change with the thickness of the coating.

If the particles do not melt completely on adhering to the heater, it is inevitable that the surface of the coating will not be smooth. An estimate of the change in the heat transfer coefficient may be made from the work of Grewal and Saxena (1979), if the surface is considered to be knurled. The pitch of the knurling is somewhat open to interpretation in this case, since, the knurls are effectively hemispherical and unevenly spaced.

Two estimates for the pitch will be given - in any case, a range of P_k is to be expected, because particles do not adhere to the surface with a set geometry. The lowest likely value of P_k is simply the smallest distance that the centres of two adjacent particles can be apart, that is, one particle diameter. A reasonable upper bound may be the diagonal centre-to-centre distance of four particles forming a square, which leads to $P_k = \sqrt{2}.d_p$. Hence, P_k/d_p may range from 1 to $\sqrt{2}$, at least to a first approximation. The knurling data in Grewal and Saxena (1979) cover only P_k/d_p = 2.5 - 4, so some extrapolation is required. Further, it is assumed that operating variables affect knurled and smooth tubes in the same way - which seems reasonable from the data presented by the above authors. It is estimated that the heat transfer coefficient is decreased by around 2 - 6% when the surface is roughened because of incompletely melted particles. Of course, an experimental investigation into the effects of this type of roughness would resolve this problem. Once again, it is left for future efforts.

Finally, coating formation may occur such that the effective cross-section of the body changes shape, becoming non-circular. For vertical tubes, h is believed to be unaffected by the cross-sectional shape (provided that it is convex). However, h for horizontal tubes seems to be strongly influenced by tube shape, apparently increasing with aspect ratio for vertically-elongated shapes (Kurochkin, 1966, *J. Eng. Phys.* **10**(6), p447-449; Saxena et al., 1978). Results from Chapter 5 suggest that, in the most extreme case, the cross-section of the tube's horizontal portion could be considered as a prolate ellipse of aspect ratio about 1.28. Use of Kurochkin's correlations with averaging over the U-tube, suggests that $h_{average}$ may have been ***at most, under 20%*** above that predicted by equation (3.10). In most of the experiments, the error would be *much* less than this figure. For the U-tube heater used in these experiments, equation (3.10) should still yield a good estimate of h; however, for purely horizontal tubes, shape effects should be carefully considered.

3.6 SUMMARY

In this chapter, the apparatus, materials and procedures used in an experimental study of the coating-erosion phenomenon have been described. A vertical, U-shaped, electrically-heated tube acted as the immersed body in a laboratory scale, high-temperature fluidized bed. The presence of unwanted temperature gradients in the fluidized bed and a drifting average bed temperature added to the difficulty of the analysis of the experimental data.

Effective Melting Temperature:

Glass ballotini, the bed material, is an amorphous substance which softens over a range of temperatures. Its effective melting temperature, which is needed for later theoretical work, was obtained by a technique similar to that used in the powder coating industry for polymers. Perhaps coincidentally, the effective melting temperature obtained in this study, 625 °C,† is very similar to the minimum sintering temperature reported by Compo (1989) from high-temperature defluidization experiments.

Minimum Fluidization Velocity:

The experimentally determined minimum fluidization velocity varied with the operating conditions of the fluidized bed as expected. A simple, system-specific expression, equation (3.2), was able to correlate the data within 2% - better than several general literature correlations.

Heat Transfer Coefficient:

Three recommended literature relationships were compared with the experimental data for the heat transfer coefficient between the U-tube heater and the fluidized bed. Although they reproduced the experimental trends, there was an unacceptable degree of scatter. The heat transfer data were correlated within 3% by an easily-calculated, non-general function of the bed temperature, the heater temperature and the superficial gas velocity, equation (3.10).

† For d_p= 589-701 μm glass ballotini, and measured as described in Sections 3.4.1 and 3.5.1.

Chapter 4:

THEORETICAL ANALYSIS

In this chapter, the coating-erosion model is developed from the powder coating work of Abuaf and Gutfinger (1973). Analytical steady state solutions are presented, followed by a description of **CEMODEL**, *a dynamic simulation program. The rich transient behaviour of the system is revealed through a parametric study. Finally, we contrast sintering and non-sintering systems.*

4.1 INTRODUCTION

In analysing the experimental results, the usual trade-off between the realism of the mathematical description and the tractability of its solution must be made. Chapter 3 revealed that the U-tube heater suffered from a hotspot, there were temperature gradients in the fluidized bed under some conditions and that the coating of particles was uneven. To model all of these features would be a mammoth task - and likely have little value. The aim of this project is to investigate the principles of combined coating and erosion in a fluidized bed, and not to study the behaviour of this particular U-tube heater in itself.

On this basis, it was decided to perform a reasonably simple analysis of the phenomenon. For example, it was assumed that the object immersed in the fluidized bed was cylindrical

and that the coating was of uniform thickness. In following this approach, however, comparison with the experimental work is made more difficult and good agreement is less likely. Nevertheless, considerable insight may be gained even from a simple model.

The powder coating equations of Abuaf and Gutfinger (1973) provide the starting point for the development of the coating-erosion model. They are reproduced in the next section so that they may be compared with the final model equations.

4.1.1 Abuaf and Gutfinger (1973)

Under the assumptions outlined in Sections 2.2.1 and 2.2.3, Abuaf and Gutfinger (1973) presented the following system of equations for the description of the one-dimensional, flat plate powder coating problem:

$$\rho c_p \frac{\partial T}{\partial t} = k \frac{\partial^2 T}{\partial x^2} \tag{4.1}$$

$$T(0,0) = T_{bo} \tag{4.2}$$

$$T(0,t) = T_b(t) \tag{4.3}$$

$$T(\delta(t),t) = T_m \tag{4.4}$$

$$m_b c_{pb}(T_{bo} - T_b(t)) = hA_b(T_m - T_\infty)t + \rho A_b c_p \int_0^{\delta(t)} (T - T_\infty)dx \tag{4.5}$$

$$-kA_b \left.\frac{\partial T}{\partial x}\right|_{x=\delta(t)} = hA_b(T_m - T_\infty) + \rho A_b c_p (T_m - T_\infty) \frac{d\delta(t)}{dt} \tag{4.6}$$

$$\delta(0) = 0 \tag{4.7}$$

Equation (4.1), applicable for $0 < x < \delta(t)$, describes energy conservation in the coated layer where conduction only occurs. The energy balance over the immersed body from time 0 to t, equation (4.5), shows that the energy lost by the body is both convected to the bed and consumed in the formation of coating. Equation (4.6) is an energy balance at the coating-bed interface. It states that part of the energy conducted to the interface through the coating is lost to the bed while the rest goes to form additional coating. The remaining equations are associated boundary and initial conditions.

4.2 MODEL DEVELOPMENT

The coating-erosion model is based on the following assumptions:

- the behaviour of the immersed body depends on the balance between two competing processes - coating and erosion. Sintering of particles onto a hot immersed body is the coating process. Erosion of the coating is caused by the impact of particles carried by passing bubbles;
- growth and erosion of the coating may be treated as continuous processes;
- the immersed body is cylindrical and the coating layer that forms on the body may be fully described by a single spatial coordinate - the radial coordinate;
- the immersed body has a constant density and a uniform temperature;
- the density of the coating formed on the immersed body is constant;
- there is no coating layer on the body initially;
- when coating is in progress, the surface of the coating in contact with the fluidized bed is at the sintering temperature of the particles (defined later).

The second assumption requires that many particles are involved in both the coating and erosion processes - little attention is paid to the adhesion and detachment history of an individual particle. The third assumption means that the coating will have the same thickness over the curved surface of the cylinder and no coating forms on the ends. Implied by this assumption is the need to use properties that have been suitably averaged over the immersed body if a comparison is to be made between the theory and the experiments.† In this thesis, the **sintering temperature** (T_s) is defined as the *lowest temperature of a surface immersed in a fluidized bed at which particles will adhere to the surface under a given set of operating conditions*. The sintering temperature, which may be different from the (effective) melting temperature of the particles, is discussed further in Section 5.4.4. It may be seen that the above assumptions are less restrictive than those encountered in Chapter 2. The key variables and assumptions are depicted diagrammatically in Figure 4.1.

The equations comprising the coating-erosion model are now presented.

Status Variables:

It is convenient to define two logical symbols which discriminate between alternative states of the system. One relates to the existence of a layer of coating on the immersed body. The symbol $\mathcal{CL}$ applies if a coating layer is present and $\overline{\mathcal{CL}}$ if it is not. The other symbol reflects the system's potential to form coating. That coating may form is indicated by $\mathcal{CJ}$ and the opposite by $\overline{\mathcal{CJ}}$. Coating will commence when the temperature of the immersed body is greater than or equal to the sintering temperature, and it will continue as long as the outer surface of the coating layer remains at T_s. More exactly, the definitions are:

$$\begin{cases} \mathcal{CL}, & r_c > r_b \\ \overline{\mathcal{CL}}, & r_c = r_b \end{cases} \tag{4.8}$$

† Practically, this assumption means that the present, one-dimensional formulation of the model will apply better to short vertical tubes than to similar horizontal ones due to the latter's strong circumferential asymmetry. These matters are discussed further in Section 5.4.2.

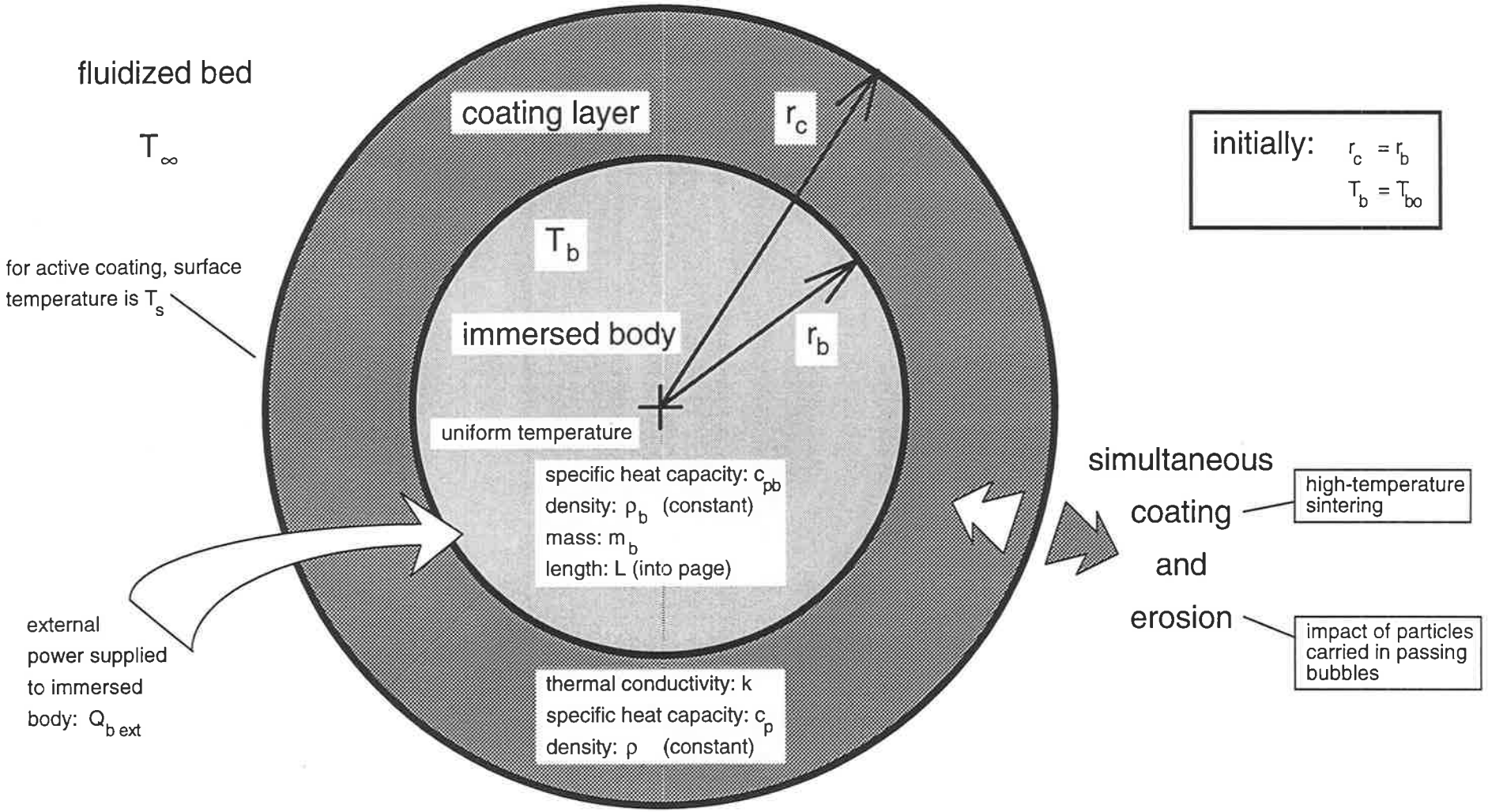

Figure 4.1: Diagram of the coating-erosion system showing key variables and assumptions.

and

$$\begin{cases} \mathcal{CJ}, & T|_{r=r_c} \geq T_s \\ \overline{\mathcal{CJ}}, & T|_{r=r_c} < T_s \end{cases} \tag{4.9}$$

Energy Balance over the Immersed Body:

$$m_b \frac{d(c_{pb}\, T_b)}{dt} = \begin{cases} Q_{b\,ext} - h\,2\pi r_b L (T_b - T_\infty), & \overline{\mathcal{CL}}\ \&\ \overline{\mathcal{CJ}} \quad (4.10a) \\ Q_{b\,ext} - \left(-k\,2\pi r_b L \left.\frac{\partial T}{\partial r}\right|_{r=r_b} \right), & \mathcal{CL}\ \text{or}\ \left(\overline{\mathcal{CL}}\ \&\ \mathcal{CJ}\right) \quad (4.10b) \end{cases}$$

Equation (4.10a) describes the body when there is no coating layer present and it is below the sintering temperature of the particles. The difference between the energy supplied to the body and that lost *by convection to the fluidized bed* is accumulated in the body. When a coating layer is present or when it is about to form, equation (4.10b) becomes applicable instead. In this case, the body looses energy *by conduction through the coating layer*. (For the purposes of modelling, if a coating is just about to form, it is assumed that an infinitesimally thin coating is already present.)

The initial condition of the body must be specified:

$$T_b = T_{bo}, \qquad t = 0 \tag{4.11}$$

In addition, the coating immediately adjacent to the body is assumed to be at the body temperature:

$$T\Big|_{r=r_b} = T_b \tag{4.12}$$

Equation (4.12) implies that there is no thermal contact resistance between the body and the coating.

Energy Balance inside the Coating:

$$\rho\frac{\partial(c_p T)}{\partial t} = \frac{1}{r}\frac{\partial}{\partial r}\left(k\,r\frac{\partial T}{\partial r}\right), \qquad \mathcal{CL}\ \text{or}\left(\overline{\mathcal{CL}}\ \&\ \mathcal{CT}\right), (r_b < r < r_c) \tag{4.13}$$

Energy is transferred through the coating by conduction. Equation (4.13) applies when a coating layer exists or is just about to form. Its solution requires the specification of two boundary conditions and one initial condition.

The first boundary condition for the coated layer is:

$$T\Big|_{r=r_c} = T_s, \qquad (\mathcal{R}_c - \mathcal{R}_e) > 0 \tag{4.14}$$

where $\mathcal{R}_c$ and $\mathcal{R}_e$ are the potential rates of coating and erosion, respectively. $\mathcal{R}_c$ is the rate of increase of the coating thickness that would take place if no erosion were occurring. Similarly, $\mathcal{R}_e$ is the rate at which the coating thickness would decrease in the absence of active coating formation. Equation (4.14) indicates that if the coating process is proceeding, then the outer surface of the coating is at the sintering temperature.

The second boundary condition is:

$$-k\,2\pi r_c L\left.\frac{\partial T}{\partial r}\right|_{r=r_c} = \begin{cases} h\,2\pi r_c L\left(T\Big|_{r=r_c} - T_\infty\right), & \overline{\mathcal{CT}} \quad (4.15a) \\ h\,2\pi r_c L(T_s - T_\infty) + \rho c_p (T_s - T_\infty) 2\pi r_c L(\mathcal{R}_c - \mathcal{R}_e), & \mathcal{CT} \quad (4.15b) \end{cases}$$

Equations (4.15a) and (4.15b) are energy balances on the coating-bed interface. When coating does not take place, heat loss is by convection only, and this determines the surface temperature of the coating - as seen in equation (4.15a). However, while coating continues, some energy is lost to the bed by convection, while the rest is consumed in the

formation of additional coating - shown in equation (4.15b). During coating, the surface temperature remains at T_s.

Mass Balance over the Coating Layer:

$$\frac{dr_c}{dt} = \begin{cases} \mathcal{R}_c - \mathcal{R}_e \ , & \mathcal{CL} \text{ or} \left(\overline{\mathcal{CL}} \ \& \left(\mathcal{R}_c \geq \mathcal{R}_e \right) \right) \quad (4.16a) \\ 0 \ , & \overline{\mathcal{CL}} \ \& \left(\mathcal{R}_c < \mathcal{R}_e \right) \quad (4.16b) \end{cases}$$

The position of the interface, r_c, is determined by a balance between the rates of coating and erosion - equation. (4.16a). However, no erosion of the immersed body itself is allowed - equation. (4.16b). Note that no particular form is imposed on the erosion rate, $\mathcal{R}_e$, by the coating section of the model. The erosion rate may be constant, or it may be calculated from an erosion model. Coupling between the erosion model and the coating model only occurs through equation (4.16) (provided that the coating does not grow so much that it changes the hydrodynamics of the fluidized bed).

Initially, there is no coating present:

$$r_c = r_b \ , \qquad t = 0 \qquad (4.17)$$

Equations (4.8) to (4.17) constitute the coating-erosion model for a one-dimensional, radial geometry.

It may appear that the model presented above does not allow for the coating of materials with a significant latent heat of fusion. Equations (4.13) and (4.15b) contain only specific heat terms. However, since c_p may vary, the latent heat of fusion may be incorporated into the model through an effective specific heat, c_p', defined as:

$$c_p'(T) = \begin{cases} c_p(T), & T \neq T_m \quad (4.18a) \\ c_p(T) + \dfrac{\Delta H}{(T_m - T_\infty)}, & T = T_m \quad (4.18b) \end{cases}$$

All that is needed is to replace c_p in equations (4.13) and (4.15b) with c_p'.

The coating-erosion model is essentially based on the powder coating equations of Abuaf and Gutfinger (1973) which have been reproduced in Section 4.1.1. Many similarities are present in these two sets of equations. Apart from the inclusion of erosion, there are key differences; the coating-erosion model:

- is based on a radial - cylindrical geometry as opposed to the flat plate;
- covers two "regimes" of behaviour - convective heat transfer from the immersed body only, and coating of the body accompanied by convection;
- allows variable system properties (except for density);
- includes provision for energy to be supplied to the immersed body from an external source;
- assumes that the coating-bed interface is at the sintering temperature of the particles, which may be different from the melting temperature;
- uses a different form of the energy conservation equation for the immersed body - a rate-of-transfer balance, equation (4.10), in place of an amount-of-energy balance, equation (4.5).

An amount-of-energy balance was not used because it is restricted to the constant property case and is not suitable for the radial direction.

4.2.1 Non-Dimensionalisation

To aid in the parametric study and to simply the coating-erosion equations, a non-dimensionalisation was performed. It must be stressed that in so doing, the generality of the model is reduced. Now, we insist that the physical and thermal properties of the immersed body, the coating and the fluidized bed be constant. In Section 4.2, arbitrary variation in most of these properties was allowed.

With the understanding that the physical and thermal properties of the system are constant, the following quantities are defined:

- Dimensionless Temperature, T^*:

$$T^* = \frac{T - T_\infty}{T_m - T_\infty} \tag{4.19}$$

- Dimensionless radial position, r^*:

$$r^* = r / r_b \tag{4.20}$$

- Dimensionless time, t^*:

$$t^* = \frac{k\,t}{\rho c_p r_b^2} = \frac{\alpha\,t}{r_b^2} \tag{4.21}$$

  which is otherwise known as the Fourier number.

- Heat capacity parameter, Z:

$$Z = \frac{m_b c_{pb}}{\rho c_p 2\pi r_b^2 L} = \frac{\rho_b c_{pb}}{2\rho c_p} \tag{4.22}$$

Z is half of the reciprocal of the Z parameter of Abuaf and Gutfinger (1973).

- Dimensionless Initial Temperature of the Immersed Body, T_{bo}^*:

$$T_{bo}^* = \frac{T_{bo} - T_\infty}{T_m - T_\infty} \tag{4.23}$$

- Dimensionless external heat input rate, $Q_{b\,ext}^*$:

$$Q_{b\,ext}^* = \frac{Q_{b\,ext}}{2\pi k L (T_m - T_\infty)} \tag{4.24}$$

- Biot number, Bi:

$$Bi = \frac{h r_b}{k} \tag{4.25}$$

- Dimensionless Sintering Temperature, T_s^*:

$$T_s^* = \frac{T_s - T_\infty}{T_m - T_\infty} \tag{4.26}$$

- Dimensionless Potential Erosion Rate, $\mathcal{R}_e^*$:

$$\mathcal{R}_e^* = \frac{\rho c_p r_b \mathcal{R}_e}{k} = \frac{r_b \mathcal{R}_e}{\alpha} \tag{4.27}$$

In addition, the dimensionless coating rate, $\mathcal{R}_c^*$, arises in the non-dimensionalisation:

$$\mathcal{R}_c^* = \frac{\rho c_p r_b \mathcal{R}_c}{k} = \frac{r_b \mathcal{R}_c}{\alpha} \tag{4.28}$$

Under the transformations embodied in equations (4.19) to (4.28), the coating-erosion model equations (4.8) to (4.17) become:

$$\begin{cases} \mathcal{CL}, & r_c^* > 1 \\ \overline{\mathcal{CL}}, & r_c^* = 1 \end{cases} \tag{4.29}$$

$$\begin{cases} \mathcal{CJ}, & T^*\big|_{r^*=r_c^*} \geq T_s^* \\ \overline{\mathcal{CJ}}, & T^*\big|_{r^*=r_c^*} < T_s^* \end{cases} \tag{4.30}$$

$$Z\frac{dT_b^*}{dt^*} = \begin{cases} Q_{b\,ext}^* - Bi.T_b^*, & \overline{\mathcal{CL}}\,\&\,\overline{\mathcal{CJ}} \quad (4.31a) \\ Q_{b\,ext}^* + \left.\frac{\partial T^*}{\partial r^*}\right|_{r^*=1}, & \mathcal{CL}\ \text{or}\left(\overline{\mathcal{CL}}\,\&\,\mathcal{CJ}\right) \quad (4.31b) \end{cases}$$

$$T_b^* = T_{bo}^*, \qquad t^* = 0 \tag{4.32}$$

$$T^*\big|_{r^*=1} = T_b^* \tag{4.33}$$

$$\frac{\partial T^*}{\partial t^*} = \frac{1}{r^*}\frac{\partial}{\partial r^*}\left(r^*\frac{\partial T^*}{\partial r^*}\right), \qquad \mathcal{CL}\ \text{or}\left(\overline{\mathcal{CL}}\,\&\,\mathcal{CJ}\right), \left(1 < r^* < r_c^*\right) \tag{4.34}$$

$$T^*\big|_{r^*=r_c^*} = 1, \qquad (\mathcal{R}_c^* - \mathcal{R}_e^*) > 0 \tag{4.35}$$

$$-\left.\frac{\partial T^*}{\partial r^*}\right|_{r^*=r_c^*} = \begin{cases} Bi.T^*|_{r^*=r_c^*}, & \overline{\mathcal{CJ}} \quad (4.36a) \\ Bi.T_s^* + (\mathcal{R}_c^* - \mathcal{R}_e^*).T_s^*, & \mathcal{CJ} \quad (4.36b) \end{cases}$$

$$\frac{dr_c^*}{dt^*} = \begin{cases} \mathcal{R}_c^* - \mathcal{R}_e^*, & \mathcal{CL}\ \text{or}\left(\overline{\mathcal{CL}}\,\&\left(\mathcal{R}_c \geq \mathcal{R}_e\right)\right) \quad (4.37a) \\ 0, & \overline{\mathcal{CL}}\,\&\left(\mathcal{R}_c < \mathcal{R}_e\right) \quad (4.37b) \end{cases}$$

$$r_c^* = 1, \qquad t^* = 0 \tag{4.38}$$

Note that no "convective" term appears in equation (4.34) for the particular transformation of r*, equation (4.20), used here (Appendix B). In summary, subject to the restrictions of constant material and system properties, the temperature of the immersed body and the coating thickness at any time are determined by seven dimensionless parameters, *viz:*

$$T_b^*, r_c^* = \text{fn}\,(Z, T_{bo}^*, Q_{b\,ext}^*, Bi, T_s^*, \mathcal{R}_e^*, t^*).^{\dagger}$$

4.3 SOLUTION OF THE MODEL

When the system's physical and thermal properties are constant, the coating-erosion model admits some remarkably simple analytical steady state solutions. However, the transient behaviour and steady state solutions for variable properties are more difficult to obtain. Numerical methods are required.

4.3.1 Steady State Solutions of the Non-Dimensional Model

An important result of the coating erosion model, equations (4.29) - (4.38), is the steady-state solution - that is, when the system is unchanging with time. Formally, the following quantities must be constant:

- thickness of the coating;
- temperature of the immersed body;
- temperature profile in the coated layer.

Of course, if a coating is not present at steady state, the third criterion is inapplicable. The above conditions may be expressed as:

† Note that $\mathcal{R}_c^*$ is ***not*** an independent model parameter, and so is not included in this list. Practical considerations dictate which parameters are classified as independent.

$$\frac{dr_c^*}{dt^*} = 0 \tag{4.39}$$

$$\frac{dT_b^*}{dt^*} = 0 \tag{4.40}$$

$$\frac{\partial T^*}{\partial t^*} = 0, \quad (1 < r^* < r_c^*) \tag{4.41}$$

Equation (4.39) covers two possibilities. The first is simply that the potential rate of coating equals the potential rate of erosion. The second is that the potential erosion rate exceeds the potential coating rate, so that, by equation (4.37b), no coating is present.

We will only seek steady state solutions to the model in which erosion actively takes place, that is, when the potential erosion rate is non-zero. If erosion does not occur, then it is simply a powder coating problem and may be solved by the techniques referred to in Section 2.2. Paradoxically, the presence of erosion simplifies the steady state solution, but may complicate the dynamic one.

Since erosion takes place, the initial temperature and "thermal capacity" of the immersed body have no effect on the steady state solution. Even if a layer of coating forms in the beginning due to a high initial body temperature, it will be eroded away until it reaches a thickness that can be sustained by the given rate of heat input. It is convenient to classify the behaviour of the system in terms of the dimensionless power supplied to the body, $Q_{b\,ext}^*$:

- **Case I:** if the heat input rate is low, the temperature of the immersed body will be below the sintering temperature of the particles - no coating layer will be present;
- **Case II:** when the heat input rate is high, the potential coating and erosion rates will come to balance and there will be an enduring layer of coating.

The cases will be considered separately.

Case I - Low Power:

By definition, no coating exists at steady state, so immediately we may write:

$$r_c{}^*{}_{st} = 1$$

where the subscript "st" denotes steady state conditions.

To determine $T_b{}^*{}_{st}$, it is necessary only to consider the dimensionless energy balance over the immersed body when no coating is present, equation (4.31a). Using the steady state condition (4.40), equation (4.31a) yields:

$$T_b{}^*{}_{st} = \frac{Q_{b\,ext}{}^*}{Bi}. \qquad (4.42)$$

Over what region of parameter space is this solution valid? Since no coating is present, the immersed body must be below the sintering temperature of the particles - that is, $T_b{}^*{}_{st} < T_s{}^*$. Consequently, from equation (4.42) Case I applies when:

$$Q_{b\,ext}{}^* < Bi.T_s{}^*.$$

Case II - High Power:

In Case II, it is supposed that the power supplied to the heater is high enough to cause a coating layer to exist in the presence of erosion. The potential coating rate exactly balances the potential erosion rate. For solution, all three of the steady state conditions must be satisfied.

On substitution of (4.39) to (4.41) into the model equations (4.29) to (4.38), we obtain:

$$Q^*_{bext} + \left.\frac{\partial T^*}{\partial r^*}\right|_{r^*=1} = 0 \tag{4.43}$$

$$T^*|_{r^*=1} = T_b{}^* \tag{4.44}$$

$$\frac{1}{r^*}\frac{\partial}{\partial r^*}\left(r^*\frac{\partial T^*}{\partial r^*}\right) = 0 \tag{4.45}$$

$$T^*|_{r^*=r_c{}^*} = T_s{}^* \tag{4.46}$$

$$-\left.\frac{\partial T^*}{\partial r^*}\right|_{r^*=r_c{}^*} = Bi.T_s{}^* + (\mathcal{R}_c{}^* - \mathcal{R}_e{}^*).T_s{}^* \tag{4.47}$$

$$\mathcal{R}_c{}^* - \mathcal{R}_e{}^* = 0, \quad \left(r_c{}^* > 1\right) \text{ or } \left(\left[r_c{}^* = 1\right] \& \left[\mathcal{R}_c{}^* - \mathcal{R}_e{}^* \geq 0\right]\right) \tag{4.48}$$

Substitution of (4.48) into (4.47) yields:

$$-\left.\frac{\partial T^*}{\partial r^*}\right|_{r^*=r_c{}^*} = Bi.T_s{}^* \tag{4.49}$$

Multiplication of (4.45) by r^* and integration with respect to r^* from 1 to $r_c{}^*$ gives:

$$1.\left.\frac{\partial T^*}{\partial r^*}\right|_{r^*=1} = r_c{}^*.\left.\frac{\partial T^*}{\partial r^*}\right|_{r^*=r_c{}^*} \tag{4.50}$$

which is simply a statement that the rate at which energy enters the coating layer from the body must equal the rate at which it leaves through the coating-bed interface. Combining equations (4.43), (4.49) and (4.50) yields the steady state position of the outer coating as:

$$r_c{}^*{}_{st} = \frac{Q_{bext}{}^*}{Bi.T_s{}^*} \tag{4.51}$$

The temperature distribution in the coating and the temperature of the immersed body may be derived as follows. Equation (4.45) is multiplied by r^* and integrated from 1 to r^* to give:

$$r^* \cdot \frac{\partial T^*}{\partial r^*} = 1 \cdot \frac{\partial T^*}{\partial r^*}\bigg|_{r^*=1}$$

Elimination of the derivative at $r^* = 1$ by equation (4.43) followed by division by r^* yields:

$$\frac{\partial T^*}{\partial r^*} = -\frac{Q_{b\,ext}{}^*}{r^*} \tag{4.52}$$

A further integration of equation (4.52) from r^* to $r_c{}^*{}_{st}$ and use of equation (4.46) gives:

$$T_s{}^* - T^* = -Q_{b\,ext}{}^* \ln\left(r_c{}^*{}_{st} / r^*\right)$$

Thus, the steady state temperature profile in the coating, $T^*{}_{st}\,(r^*)$, is:

$$T^*{}_{st} = T_s{}^* + Q_{b\,ext}{}^* \ln\left(r_c{}^*{}_{st} / r^*\right) \tag{4.53}$$

By combining equations (4.53) and (4.44), the steady state temperature of the immersed body may be obtained as:

$$T_b{}^*{}_{st} = T_s{}^* + Q_{b\,ext}{}^* \ln\left(r_c{}^*{}_{st}\right)$$

Finally, we need to check the range of applicability of the solution. In this case, the key assumption is that a coating layer is present at steady state, that is, $r_c{}^*{}_{st} > 1$. Clearly, by equation (4.51), this is true if:

$$Q_{b\,ext}{}^* > Bi.T_s{}^*.$$

The steady state solution of the non-dimensional coating-erosion model may be summarised as:

Case I:

$$\left.\begin{aligned} r_c^{*}{}_{st} &= 1 \\ T_b^{*}{}_{st} &= \frac{Q_{bext}^{*}}{Bi} \end{aligned}\right\} \quad Q_{bext}^{*} \le Bi.T_s^{*} \qquad \begin{aligned} &(4.54a) \\ &(4.54b) \end{aligned}$$

Case II:

$$\left.\begin{aligned} r_c^{*}{}_{st} &= \frac{Q_{bext}^{*}}{Bi.T_s^{*}} \\ T_b^{*}{}_{st} &= T_s^{*} + Q_{bext}^{*}\, ln(r_c^{*}{}_{st}) \\ T^{*}{}_{st} &= T_s^{*} + Q_{bext}^{*}\, ln(r_c^{*}{}_{st} / r^{*}) \end{aligned}\right\} \quad Q_{bext}^{*} \ge Bi.T_s^{*} \qquad \begin{aligned} &(4.55a) \\ &(4.55b) \\ &(4.55c) \end{aligned}$$

It can be seen that the steady state solution depends on only three of the system parameters - $Q_{b\,ext}^{*}$, Bi, and T_s^{*} - not the full seven of the dynamic model. It must be remembered that this solution applies only when the erosion rate is non-zero, or, if $\mathcal{R}_e = 0$, then only for $T_{bo}^{*} < T_s^{*}$. Note that the partial solutions are consistent at the point $Q_{b\,ext}^{*} = Bi.T_s^{*}$.

The solution may be "generalised" by the use of T_i, the **interface temperature**. If no coating layer is present, T_i is the temperature of the immersed body; if a layer is present, T_i is the temperature of the outer surface of the coating. So, from the above at steady state:

$$T_i^{*}{}_{st} = \begin{cases} \dfrac{Q_{bext}^{*}}{Bi}, & Q_{bext}^{*} \le Bi.T_s^{*} \qquad (4.56a) \\ T_s^{*}, & Q_{bext}^{*} \ge Bi.T_s^{*} \qquad (4.56b) \end{cases}$$

and Cases I and II are generalised as:

$$r_c^{*}{}_{st} = \frac{Q_{b\,ext}^{*}}{Bi \, . \, T_i^{*}{}_{st}} \tag{4.57a}$$

$$T_b^{*}{}_{st} = T_i^{*}{}_{st} + Q_{b\,ext}^{*} \, ln\left(r_c^{*}{}_{st}\right) \tag{4.57b}$$

The relationship between the steady state temperature of the immersed body and the power supplied to body is shown in Figure 4.2a for several values of the Biot number and the sintering temperature. Corresponding results for the coating radius are presented in Figure 4.2b. Temperature profiles in the coating layer for several values of $Q_{b\,ext}^{*}$ appear in Figure 4.3.

4.3.2 Dynamic Solutions

While the steady state solutions of Section 4.3.1 are important, they do not reveal much of the complexity of the coating-erosion model, nor do they indicate how long the system will take to reach its final state. As will be shown in Section 4.4.2, the behaviour of the immersed body is not necessarily monotonic. Dynamic solutions are needed.

Abuaf and Gutfinger (1973) remarked that their powder coating model was difficult to solve analytically. The transient coating-erosion model, which is essentially an extension of their work, seems even less amenable to analytical treatment. In addition, restrictions such as constancy of physical and thermal properties, are often needed in analytical work. In the experimental section of this project, it was clear that the system's properties did vary. For these reasons, a numerical approach was adopted from the outset.

The prediction of the rate of coating is the most difficult task in the solution of the coating-erosion model. It is essentially a Stefan problem. Crank (1984) discusses

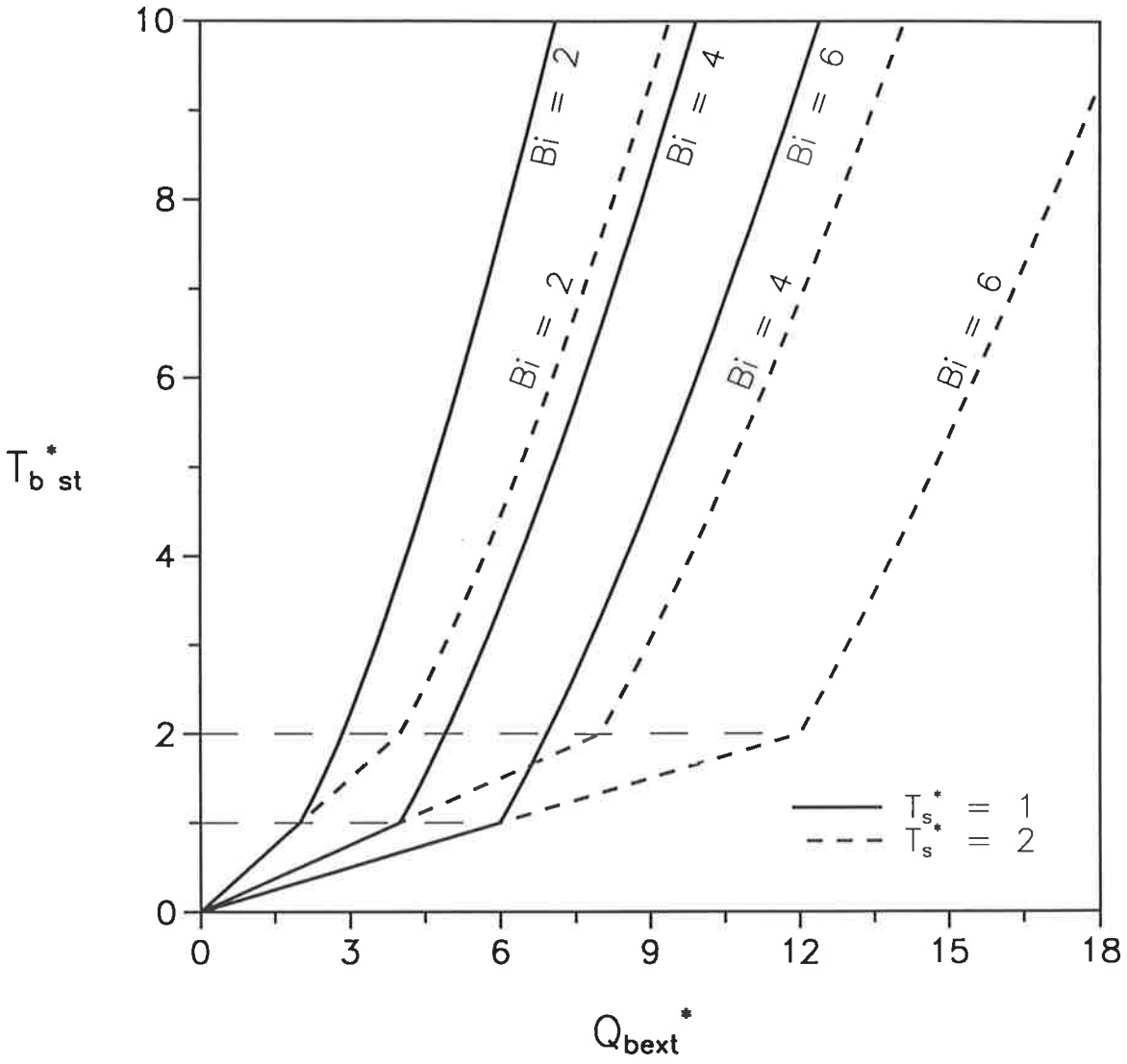

Figure 4.2a: Influence of the power supplied on the steady state temperature of the immersed body for several values of the sintering temperature and Biot number.

UNIVERSITY OF ADELAIDE LIBRARY

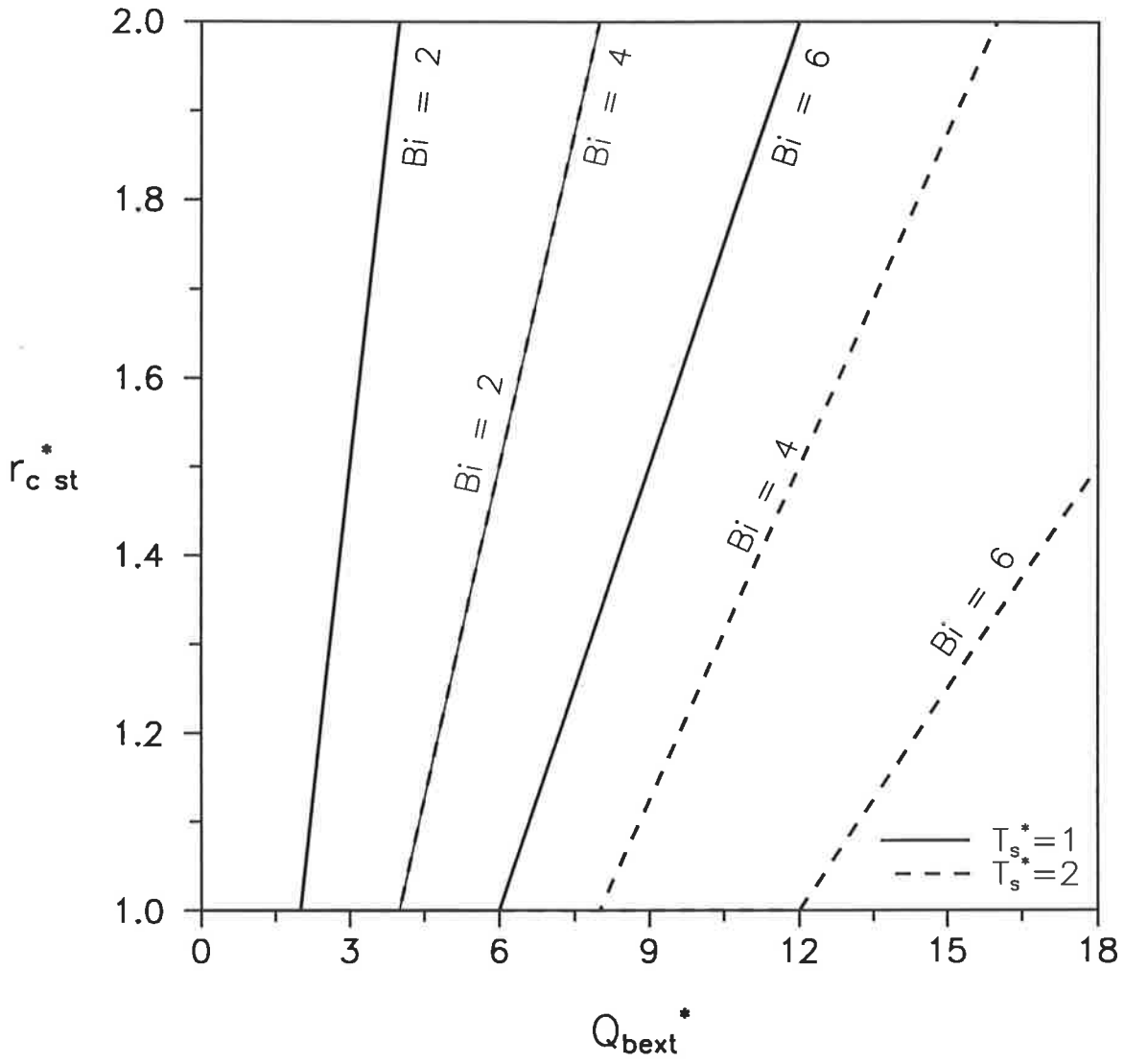

Figure 4.2b: Influence of the power supplied on the steady state coating radius for several values of the sintering temperature and Biot number.

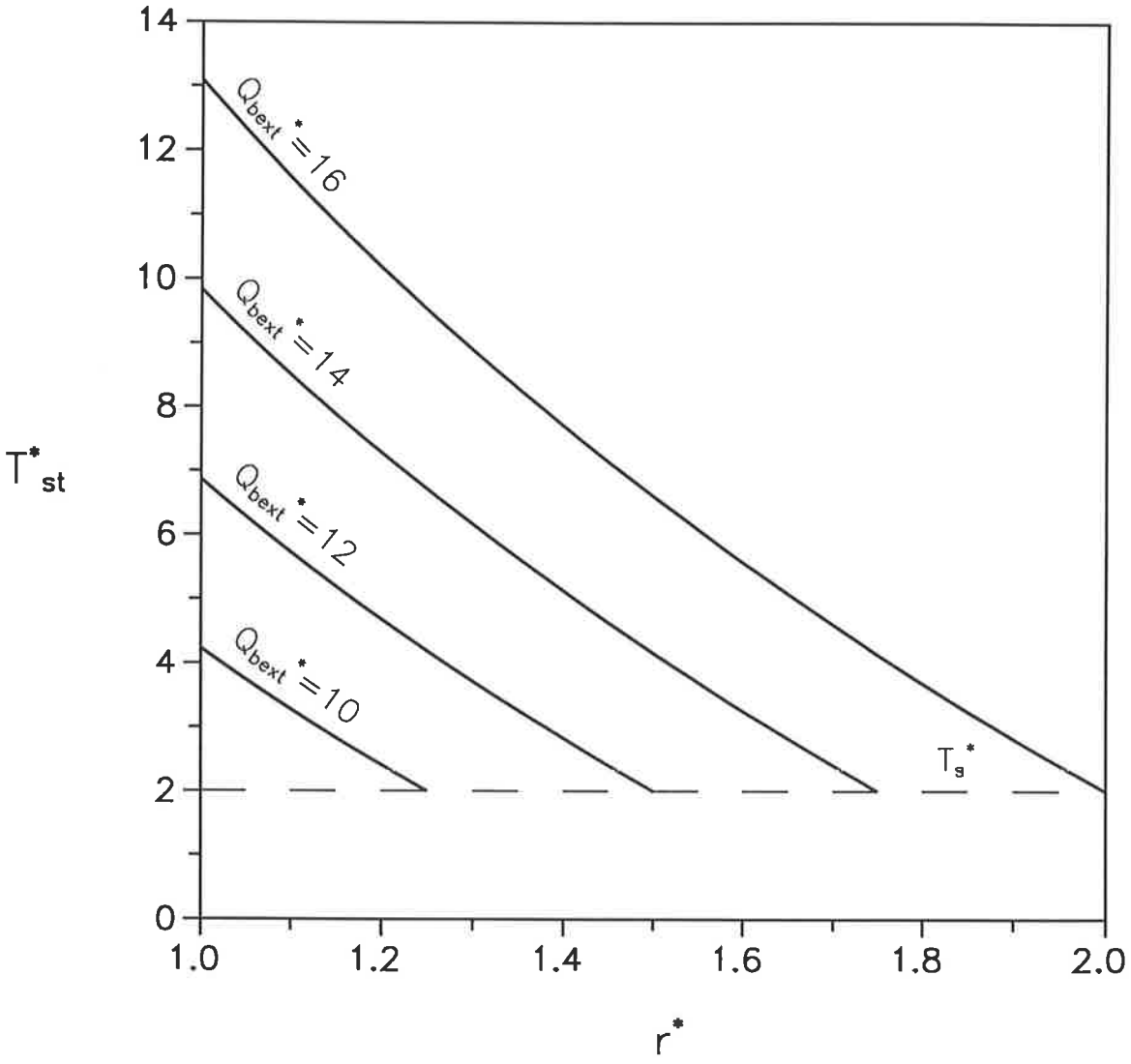

Figure 4.3: Temperature profile in the coating at steady state for various levels of power supplied to the immersed body (Bi = 4, $T_s^* = 2$).

several methods for solving these problems. Perhaps the clearer, to one inexperienced in the field, are the *front-tracking methods*. Here, the conduction equation and the energy balance at the moving interface are solved virtually as they appear on paper; no spatial transformations of the Landau type nor any integral transformations of the temperature are used. Based on this technique, two simulation programs were written. They will be discussed next.

The first simulation program involved the use of an initial value problem ordinary differential equation (ODE) solver, available from a commercial numerical subroutine library. It was necessary to convert the partial differential equation (4.13) of the coating-erosion model to ODE form. This was achieved by discretising the radial coordinate, r, to create a series of nodes; node i in the coating layer had position r_i and temperature T_i. Thus, equation (4.13) was replaced by a set of ordinary differential equations of the form:

$$\frac{d\left(c_p(T_i).T_i\right)}{dt} = fn\left(c_p(T_1).T_1, \ldots, c_p(T_N).T_N, t\right), \qquad i=1,..,N \qquad (4.58)$$

- one for each of the N nodes. Note that time remains a continuous variable. To implement this solution method, a subroutine has to be written which will calculate all the time-derivatives given the current time and the values of the time-differentiated variables. The ODE solver is invoked to march the system of equations forward in time. This technique has significant advantages. Firstly, the library code has already been written and is unlikely to contain errors. Secondly, these solvers employ computationally efficient algorithms, probably including adaptive step size control - which can cut program execution times by factors of tens or hundreds (Press et al., 1989, p607). Finally, the solver would guarantee that the answers meet the accuracy requirements of the user. **ODEINT** by Press et al. (1989, Chapter 15) is a good example of an ODE solver

with these features. It can use either the fourth order Runge-Kutta technique or the Bulirsch-Stoer method as its basic solution strategy.

Unfortunately, this approach failed. Despite lengthy efforts, the simulation could not advance the solution over the discontinuities caused by swapping between alternative equations in the coating-erosion model. It was decided to adopt a more robust technique.

The SIMPLE and SIMPLER algorithms for solving combined heat transfer and fluid flow problems were presented in Patankar (1980). Both space and time coordinates are discretised. The discretisation technique that was developed has "*the* appearance *of a finite-difference method, but employs many ideas that are typical of the finite-element methodology*". In particular, for conduction in solids, Patankar advocates a fully implicit first-order-in-time, first-order-in-space scheme. Patankar also gives advice on the positioning of control volumes, the handling of non-linearities and methods for solving the discretised equations. Sparrow et al. (1977) used the above approach to investigate a Stefan problem which also involved motion in the fluid. In that work, the placement of nodes; interpolation of temperature and velocity; and the movement of the solid-liquid interface were discussed in the context of Patankar's methods.

A second version of the simulation program for the coating-erosion model was written which embraced many of the principles outlined in Patankar (1980) and Sparrow et al. (1977). This version has proved to be quite robust, probably because of its fully implicit, low-order nature. Key computational aspects of the program are described in the following.

Program Structure:

The program can operate in two modes: *fixed time step mode* and *extrapolation mode*. The first of these is used for tentative calculations - it is fast in relative terms, but may be

inaccurate. As shown in Figure 4.4, it simply involves solving the model equations over a (small) fixed time step, Δt, updating the temperatures and coating radius, then repeating this process. No checking is performed on the adequacy of the answers as affected by the size of the time step. The second mode under which the program may run does consider the time-accuracy of the calculations. In essence, over a "large" time step Δt, it performs a number of sub-simulations with successively smaller time step sizes, $\Delta t_{substep}$, then attempts to extrapolate the results to the limit of $\Delta t_{substep} = 0$. If consecutive extrapolations agree within a certain tolerance, then the latter of these serves as the solution over Δt, otherwise, another simulation run (with a still smaller $\Delta t_{substep}$) and extrapolation is performed. A flow diagram is provided in Figure 4.5. This general idea is known as *Richardson's Deferred Approach to the Limit*. It is used in Romberg integration and the Bulirsch-Stoer method for solving ordinary differential equations (Press et al., 1989, Sections 4.3 and 15.4). Extrapolation mode was used to obtain all of the results shown in this thesis.

Advancing the Solution by Δt:

In a time interval Δt, four events may occur in the immersed body / fluidized bed system:

- **Event A:** the body, when a layer of coating is not present, may convect heat directly to the fluidized bed;
- **Event B:** a layer of coating may just have formed on the immersed body;
- **Event C:** heat may be transferred from the body through a layer of coating to the bed, with net erosion of the layer;
- **Event D:** the coating layer may continue to build up while heat is being transferred from the body, through the coating, into the fluidized bed.

At the beginning of the time step, it is not known which of these situations will take place. It is necessary to perform some speculative calculations, then correct them if needed. If a coating layer is present at the end of these calculations, then the control

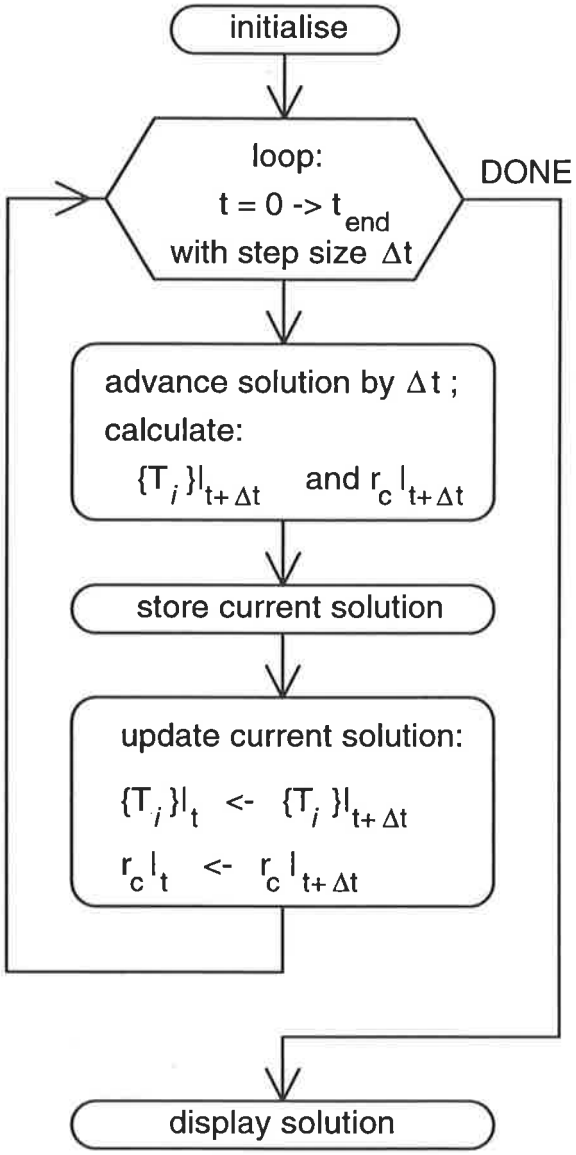

Figure 4.4: Structure of the simulation program when running in fixed time step mode.

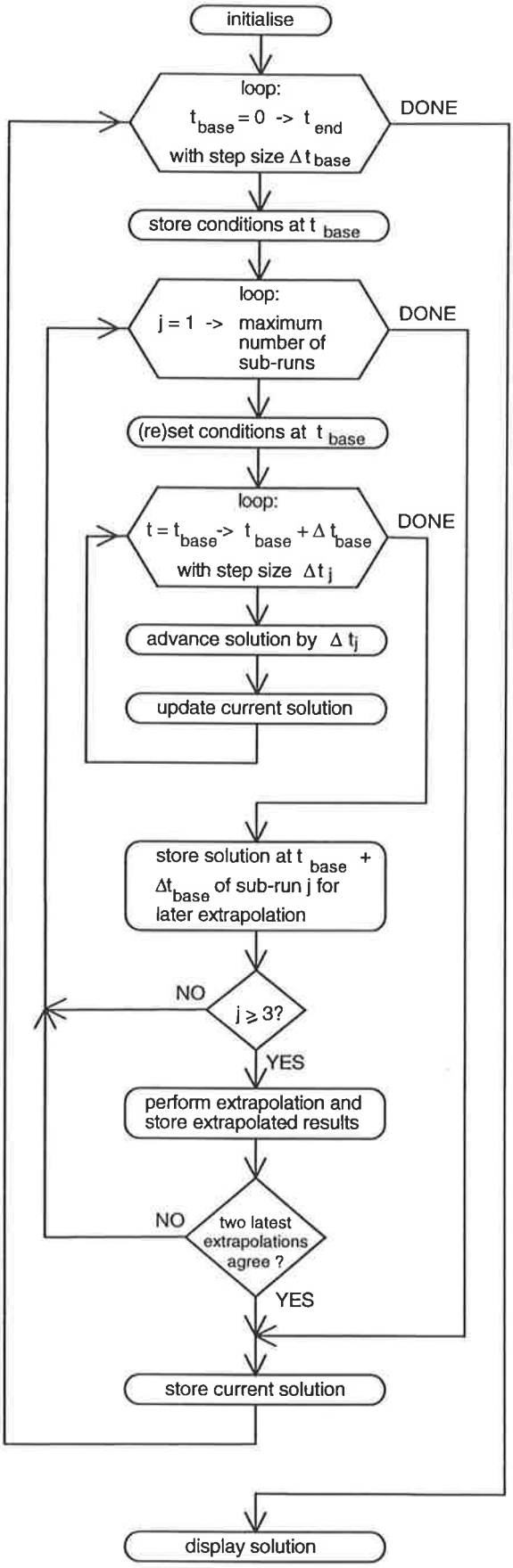

Figure 4.5: Structure of the simulation program when running in extrapolation mode.

volumes are repositioned and the nodal temperatures are interpolated by the enthalpy integral method mentioned in Sparrow et al. (1977). Note that the number of control volumes is constant and that their size changes. The method is summarised in Figure 4.6.

Solving the Energy Balance in the Coating:

When the model equations are discretised, the coating becomes divided into a series of control volumes, each containing one node. There are control volumes of zero width on each of the boundaries of the coating; those inside have equal size. The nodes are located according to Patankar's *Practice B* - that is, at the centres of their control volumes (Patankar, 1980, Section 4.6-1). Equation (4.13), the energy balance in the coating layer, becomes a tridiagonal system of equations which may be solved efficiently with the routine **TRIDAG** (Press et al., 1989, Section 2.6).

Variable System Properties:

Built into the structure of the program is the ability to deal with properties of the system that may change with time or temperature. The thermal conductivity of the coating and the specific heat of the immersed body, for example, may be functions of temperature. Likewise, the temperature of the fluidized bed and the power supplied to the heater can be time dependant. Special care has to be taken with the coating thermal conductivity; see Appendix D.

The erosion rate may also vary. In this case, equation (2.14) by Zhu et al. (1991) and the results of Nieh et al. (1991) are used to calculate local erosion rates. These must be averaged to obtain the effective erosion rate experienced by the immersed body (Appendix C). Supporting calculations are required to determine the bubble size and frequency. The simplest approach (as indicated in Section 2.3.2) was taken - the use of correlations developed for fluidized beds without immersed objects.

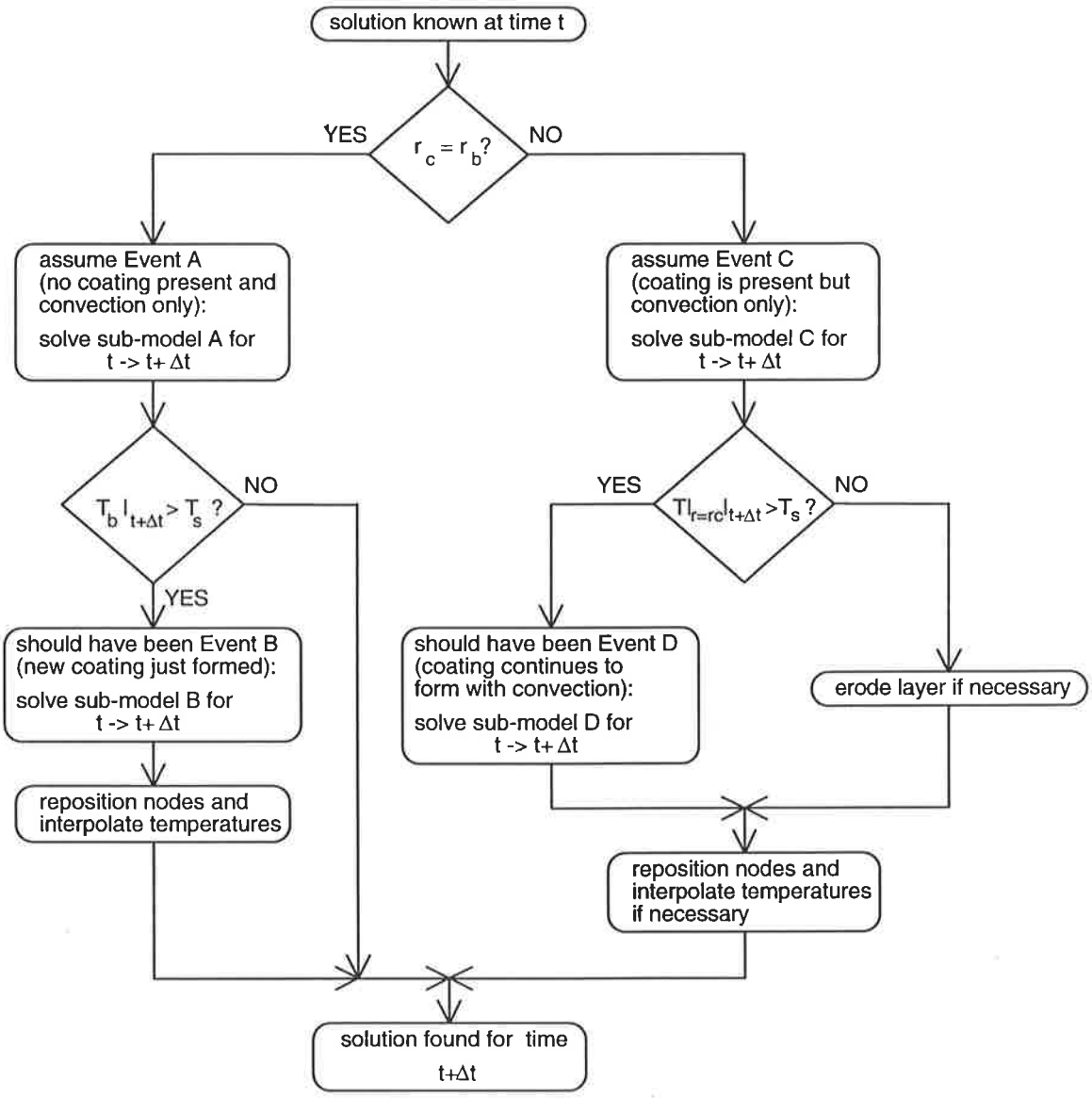

Figure 4.6: Method for advancing the solution of the coating-erosion model over a small time step Δt.

While the simulation can perform variable-property calculations, a separate constant-property mode is also available. Because of the iterative nature of the calculations involved for variable properties, a constant mode calculation will run considerably faster - at least twice the speed.

Further mathematical details of the program appear in Appendix D.

Other Features of the Simulation Program:

- it is interactive and menu driven for ease of use (a "batch mode" version has also been implemented);
- results are presented in both dimensional and dimensionless formats (dimensionless results are applicable only for constant properties);
- graphs of the results are displayed on-screen along with the analytical steady state solutions (constant property case);
- time-dependant experimental data, such as, the power supplied to the heater, bed temperature and the superficial gas velocity, may be used in the calculations;
- steady state behaviour may be obtained for a system with variable properties (note that the steady state solutions given in Section 2.3.1 apply only for constant properties);
- powder coating problems (no erosion effect) may also be investigated.

Appendix E contains a full listing of the source code of **CEMODEL**, the simulation program.

All simulations were performed on an IBM-compatible personal computer with a 486DX central processing unit running at 33MHz. The execution times for the simulations

presented in Section 4.4 ranged from a few seconds to about half an hour each, depending on the values of the input variables.

4.4 PARAMETRIC STUDY

To investigate the behaviour of the coating-erosion model, a parametric study was conducted. The dimensionless form of the model was used, so the results apply only when all of the system's properties are constant. **CEMODEL** was run in extrapolation mode to ensure the accuracy of the solutions.

In the study, the transient behaviour of the system is revealed by plotting the key variables - the dimensionless coating radius, r_c^*, and the immersed body temperature, T_b^* - against t^*, the dimensionless time. The nature of the steady state solution - Case I or II of Section 4.3.1 - provides a convenient way of classifying the transient solution. Firstly, a base case is established. Further results are obtained by varying each parameter separately about its base value.

4.4.1 Base Case

The base case was analysed to display the representative behaviour of the system and to verify the solution method. The parameter values chosen reflect typical conditions experienced in the experimental work; they are:

- Z, heat capacity parameter: 1;
- T_{bo}^*, dimensionless initial body temperature: 0;
- $Q_{b\,ext}^*$, dimensionless power supplied to the immersed body: 9, 14;
- Bi, Biot number: 6;
- T_s^*, dimensionless sintering temperature: 2;
- $\mathcal{R}_e^*$, dimensionless potential erosion rate: 0.5.

Note that two distinct values of $Q_{b\,ext}^*$ were chosen - they correspond to the two cases of the steady state solution. Calculations continued until steady conditions prevailed.

The temperature history of the immersed body is reported in Figure 4.7a for the two values of $Q_{b\,ext}^*$. Figure 4.7b shows the corresponding results for the coating radius. In the low power situation (Case I), no coating layer forms and the final temperature of the body is below the sintering temperature ($T_s^* = 2$). In Case II, a coating layer builds up and the temperature of the immersed body consequently rises above T_s^*. Note that the coating layer does not form until the body has reached the sintering temperature - that is, there is a clearly-defined lag time in the r_c^* plot. The response of the system is initially rapid, but slows down with time. Steady conditions are reached much earlier in the low power case (at $t^* \approx 1$) than in the high power one ($t^* \approx 8$ is needed). Also shown in Figures 4.7a and 4.7b, are the analytical steady state solutions from Section 4.3.1. The dynamic, numerical results agree with the expected steady values at long times, lending credence to the simulation. Finally, Figure 4.8 reveals how the temperature profile in the coating evolves in the Case II problem. The temperature profiles appear quite linear and have very similar slopes. Equation (4.55c), the analytical temperature profile at steady state agrees very well with the simulation at $t^* = 8$. This suggests that heat transfer in the coating layer behaves in a "pseudo- steady state" manner, at least for the base case parameters.

It was decided to check whether **CEMODEL**'s numerical solutions are independent of the calculational parameters, such as the number of nodes in the coating layer and the size of the time step (for fixed time step mode). There was little difference in the base case solutions for N = 7, 12, 22 and 32 nodes in the coating. It is thought that this is because of the very nearly linear temperature profile that exists in the coating layer. However, if the coating's thermal properties were temperature dependant, it is likely that the temperature profile would be non-linear and N would be of more importance. Any reasonable fixed time step (such as $\Delta t^* = 0.001$) yields a transient solution close to that

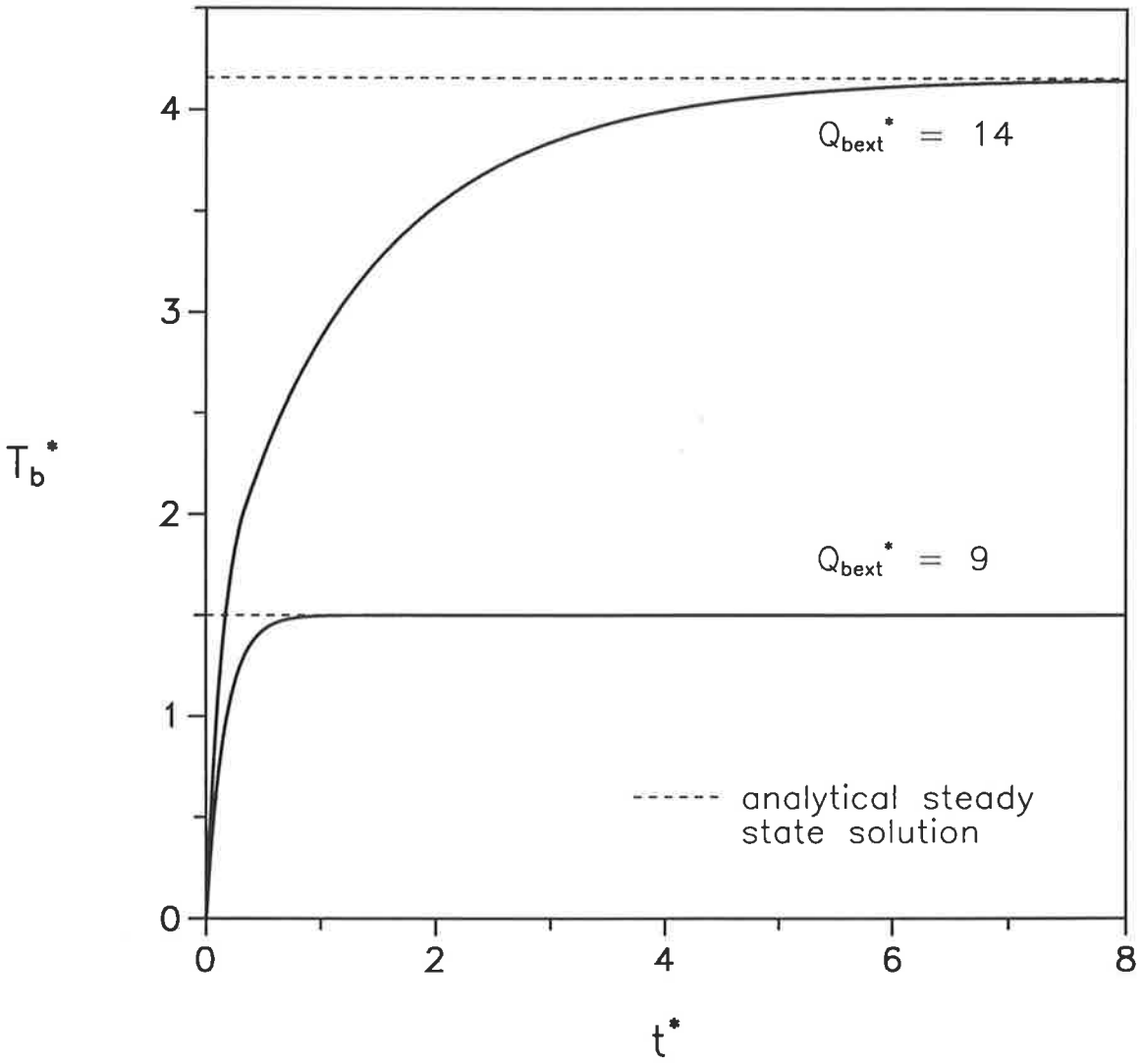

Figure 4.7a: Temperature history of the immersed body for the base case (Z = 1, $T_{bo}^* = 0$, $Q_{b\,ext}^* = 9$ & 14, Bi = 6, $T_s^* = 2$, $\mathcal{R}_e^* = 0.5$).

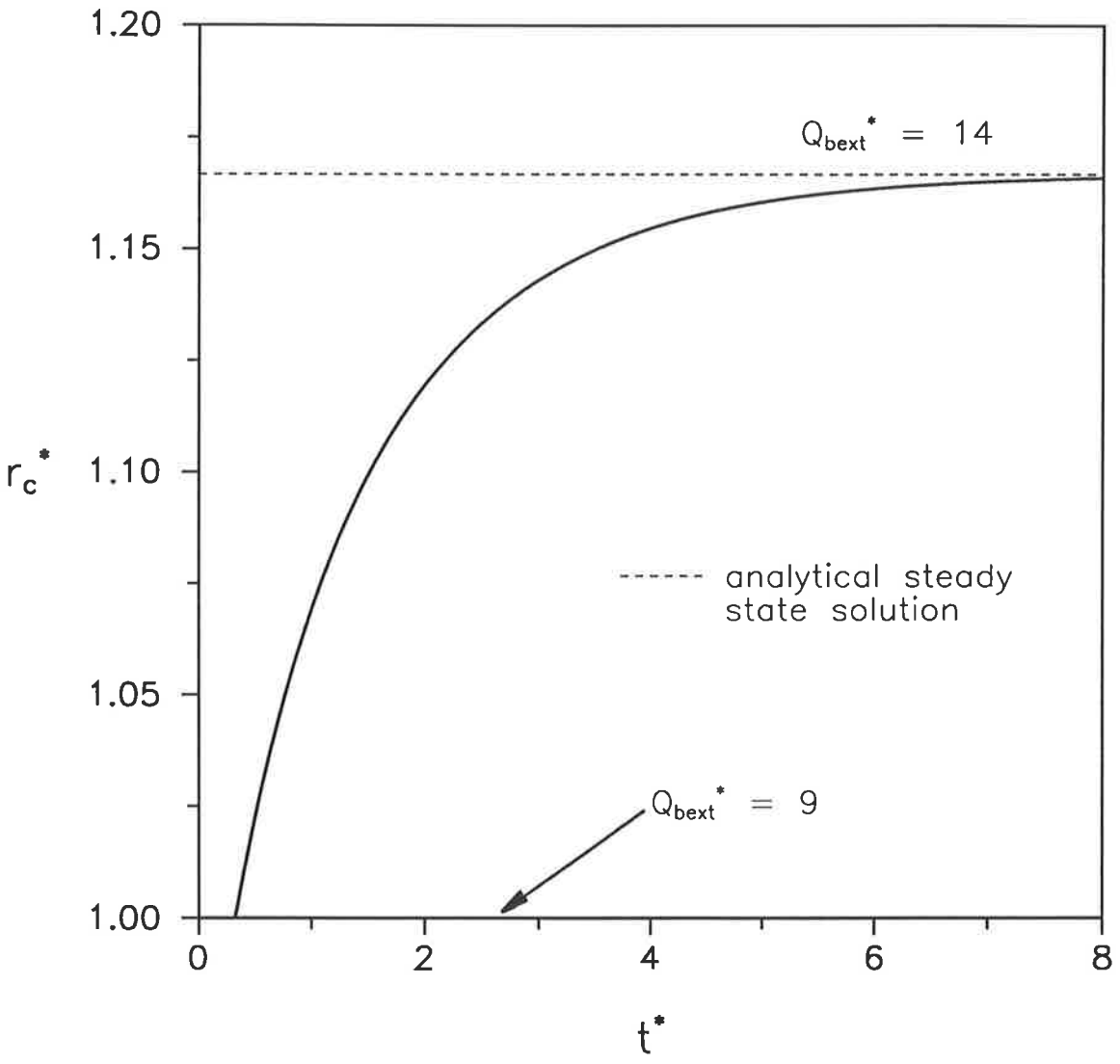

Figure 4.7b: History of the coating radius for the base case (Z = 1, $T_{bo}^* = 0$, $Q_{b\,ext}^* = 9$ & 14, Bi = 6, $T_s^* = 2$, $\mathcal{R}_e^* = 0.5$).

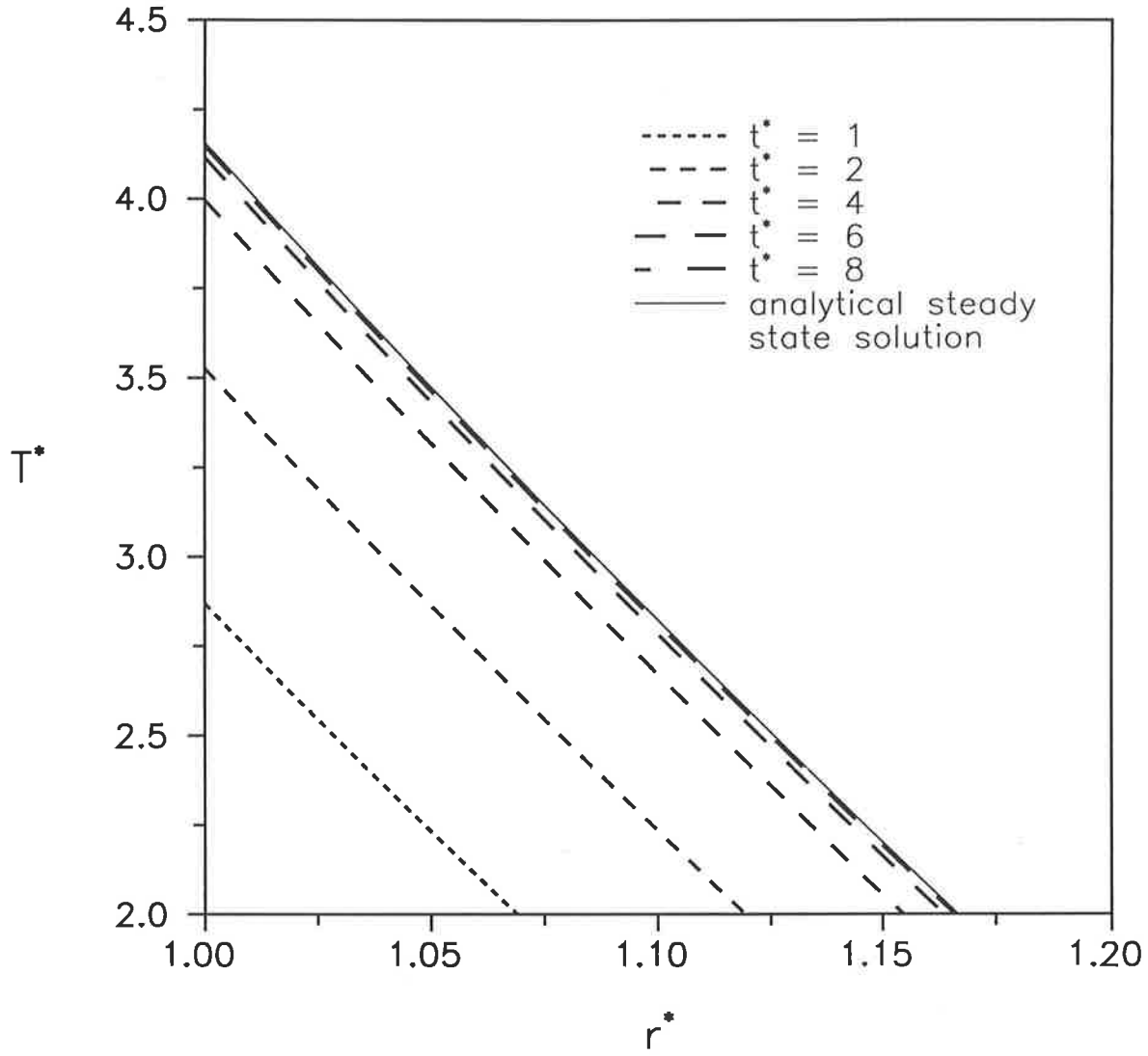

Figure 4.8: Evolution of the temperature profile in the coating for the basic Case II problem ($Z = 1$, $T_{bo}^* = 0$, $Q_{b\,ext}^* = 14$, $Bi = 6$, $T_s^* = 2$, $\mathcal{R}_e^* = 0.5$).

obtained with extrapolation mode. Fixed-Δt calculations always lag a little behind the extrapolation mode solutions, but still reach the same steady state value. The numerical scheme of Patankar (1980), which was used in **CEMODEL**, will attain the correct steady state solution, regardless of the size of the time step.

4.4.2 Further Results

After characterising the base case, a study was performed in which each parameter was varied separately about its base value. Table 4.1 summarises the range of the parameters used.

Table 4.1: Range of values used in the parametric study.

Parameter	Values[1]
Z	0.1, 0.5, **1**, 5, 10 ,50
T_{bo}^*	-4, -2, **0**, 1, 2, 3, 4, 5, 6
$Q_{b\,ext}^*$ [2]	6, **9**, 12, 13, **14**, 15, 16
Bi	3, 4, 5, **6**, 7, 8
T_s^*	1, 1.25, 1.5, 1.75, **2**, 2.25
$\mathcal{R}_e^*$ [3]	0, 0.01, 0.05, 0.1, 0.2, 0.3, **0.5** (Case I) 0, 0.005, 0.01, 0.02, 0.03, **0.5** (Case II)

Notes:

1. The base case values appear in bold type.
2. $Q_{b\,ext}^* = 9$ and 14 are Case I and II solutions, respectively.
3. The base $\mathcal{R}_e^*$ value yields a limiting behaviour - see later discussion.

The values chosen reflect extreme experimental conditions. It is thought that the gamut of behaviour of the system is covered in this study; nothing which has not been presented here should occur by choosing combinations of extreme parameter values. The

exception to this statement is the limit of $\mathcal{R}_e^* = 0$ - that is, no erosion. Substantially different behaviour will arise in this case - however, it is then purely a powder coating problem and therefore not the central interest of the thesis. The results for each parameter are discussed next.

The Heat Capacity Parameter, Z:

The effect of Z on the system for both types of steady state behaviour is shown in Figures 4.9a to 4.9c. In agreement with Section 4.3.1, Z does not influence the steady state values of the immersed body temperature and the coating radius. Nor does it change the basic way in which the system reaches steady conditions. However, the time taken to achieve steady state is strongly dependent on the heat capacity parameter. Small values of Z produce a fast response and the final state of the system is reached quickly. The speed of the response is different in the two basic cases. For a given Z, a Case I situation (in which no coating layer forms) reaches steady state much more quickly than a Case II problem. Note also that in Case II, the time lag before the formation of the coating layer increases with Z, as it takes longer for the body to exceed the sintering temperature.

Essentially, Z reflects the immersed body's resistance to changes in temperature - its "thermal inertia". It strongly affects the time taken to reach steady state, but not the kind of path taken, nor the final state of the system itself.

Dimensionless Initial Temperature of the Immersed Body, T_{bo}^*:

Perhaps the richest behaviour of the system is brought out by varying T_{bo}^*. Similar to Z and as expected from Section 4.3.1, the dimensionless initial body temperature does not alter the final values of r_c^* and T_b^*. Its influence on the path taken to reach steady state and the time involved is significant, nonetheless.

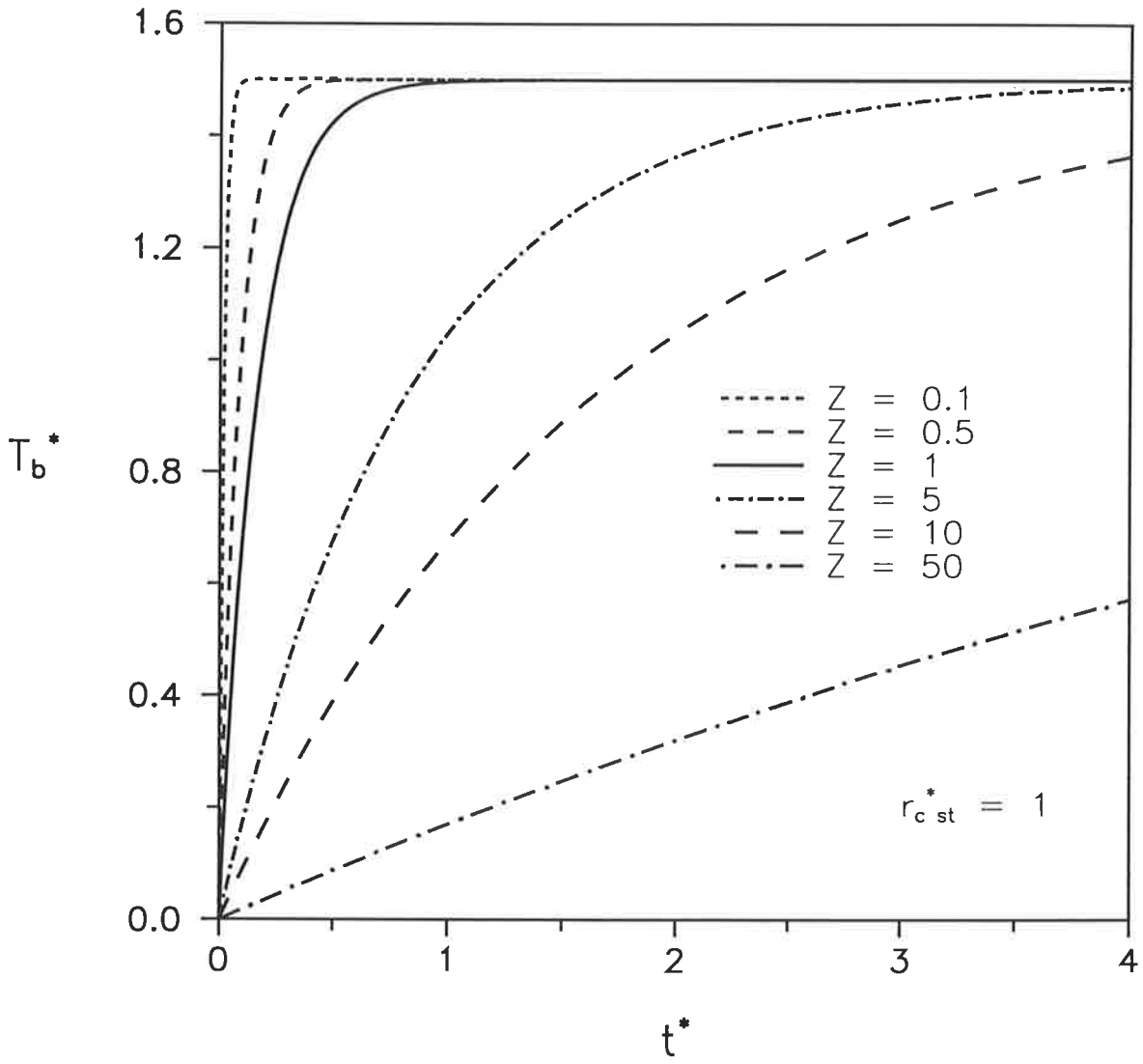

Figure 4.9a: Effect of Z on the temperature history of the immersed body for a Case I problem ($T_{bo}^* = 0$, $Q_{b\,ext}^* = 9$, Bi = 6, $T_s^* = 2$, $\mathcal{R}_e^* = 0.5$).

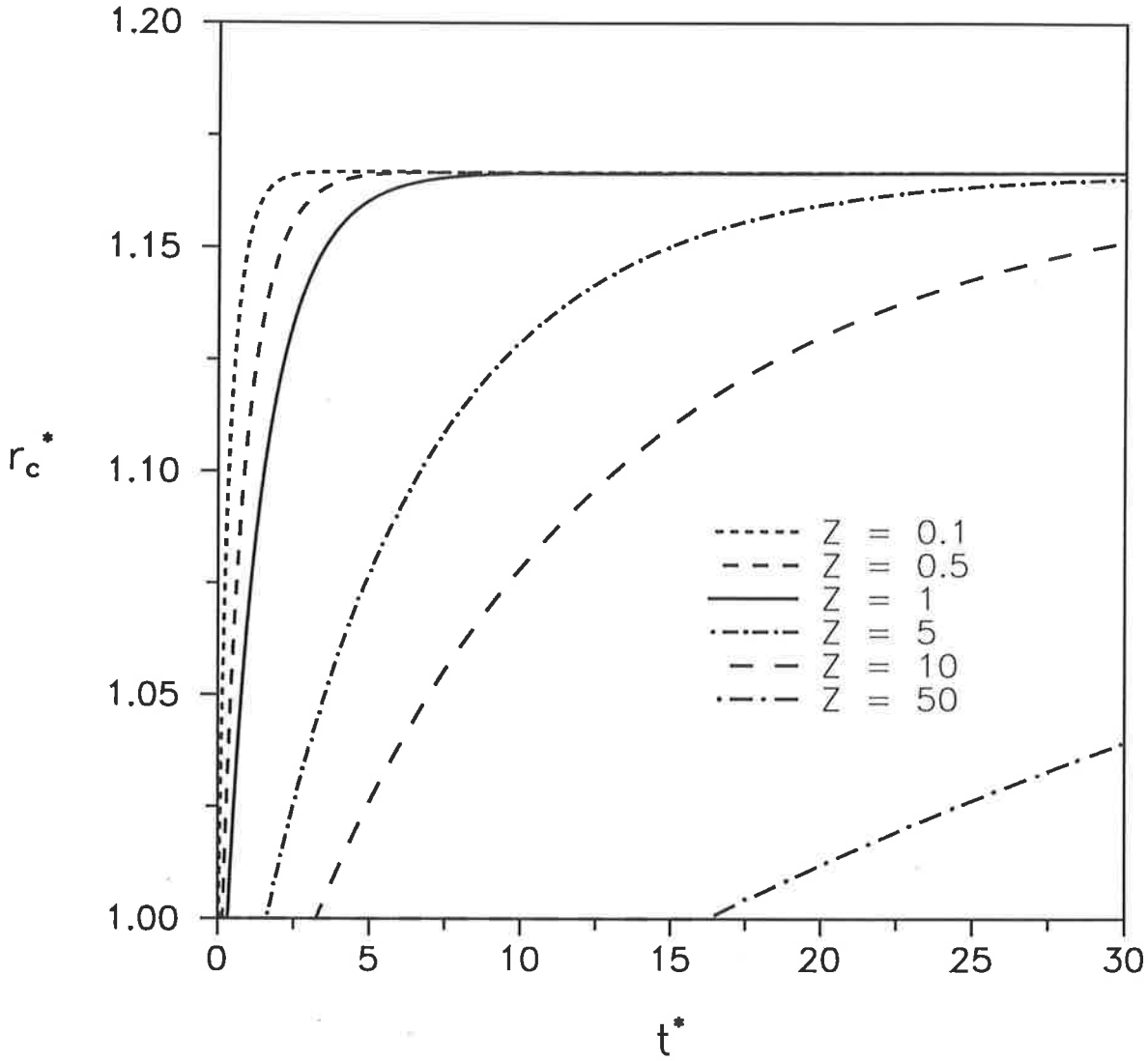

Figure 4.9c: Effect of Z on the history of the coating radius for a Case II problem ($T_{bo}^* = 0$, $Q_{b\,ext}^* = 14$, Bi = 6, $T_s^* = 2$, $\mathcal{R}_e^* = 0.5$).

The Case I (low power) situation is revealed in Figures 4.10a and 4.10b. When T_{bo}^* is low (less than $T_b^*{}_{st}$, which is 1.5 here), the body heats up, but does not exceed the sintering temperature of the particles. When $T_b^*{}_{st} < T_{bo}^* < T_s^*$ (= 2), the body cools down, so still, it remains below the sintering temperature. No coating is formed in either case. For a high initial body temperature ($T_{bo}^* > T_s^*$), the body cools down on exposure to the bed, but some coating is formed transiently. Figure 4.10b indicates that the coating builds up rapidly in the beginning, but soon growth slows, the coating reaches a maximum thickness, and then erodes away completely. Clearly, the rapidly-formed coating layer cannot be sustained by the given level of power supplied to the body. Note that the coating radius reaches its steady state value ($r_c^*{}_{st} = 1$) suddenly, and *before* the immersed body's temperature is steady. The situation where $T_{bo}^* > T_s^*$, $Q_{b\,ext}^* = 0$ and $\mathcal{R}_e^* \approx 0$ corresponds to a powder coating operation in which the immersed body is preheated (Section 2.2). Figure 4.10b shows what might happen to the coating if erosion is significant or the immersion time is too long.

Under high power, the system behaves in a more complex manner, as seen in Figures 4.10c and 4.10d. As in Case I, when T_{bo}^* is above or equal to the sintering temperature, some coating forms immediately. Again, the rate of coating is initially high but then slows. For the higher initial temperatures ($T_{bo}^* = 5$ & 6 here), a maximum coating thickness is obtained, then it begins eroding, to level out at the final value; the body's temperature falls monotonically. For somewhat lower T_{bo}^* (but still above T_s^*), the steady state thickness is approached monotonically from below. The temperature of the immersed body falls rapidly at first, then rises slowly to reach $T_b^*{}_{st}$ from below, mirroring the behaviour of r_c^*. If $T_{bo}^* < T_s^*$, there is a delay before the immersed body reaches the sintering temperature and so no coating forms until then. Thereafter, the coating builds up monotonically.

In summary, the initial temperature of the body does not affect the final state of the system. If the body is initially hotter than the sintering temperature, some coating will

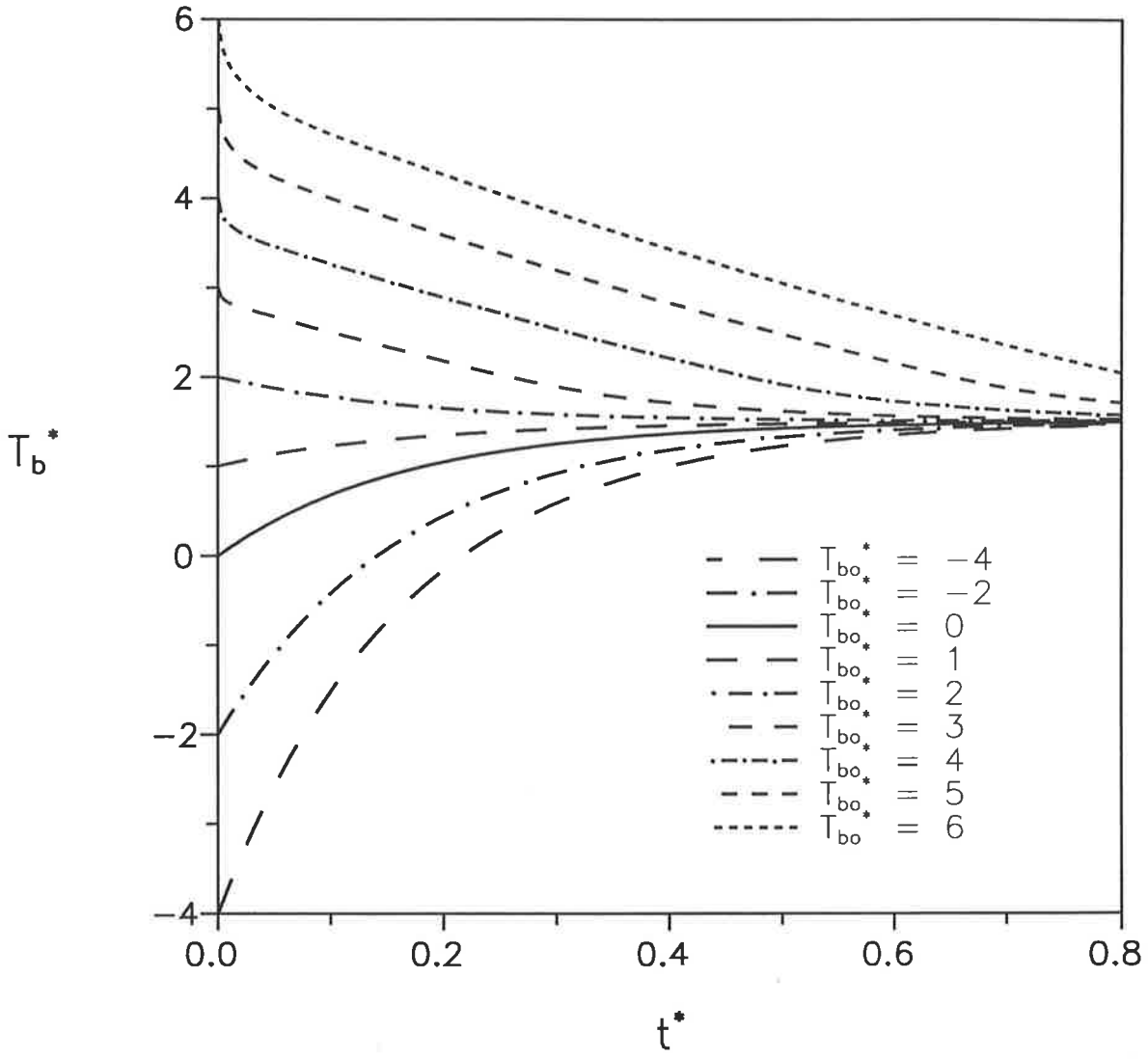

Figure 4.10a: Effect of T_{bo}^* on the temperature history of the immersed body for a Case I problem ($Z = 1$, $Q_{b\,ext}^* = 9$, $Bi = 6$, $T_s^* = 2$, $\mathcal{R}_e^* = 0.5$).

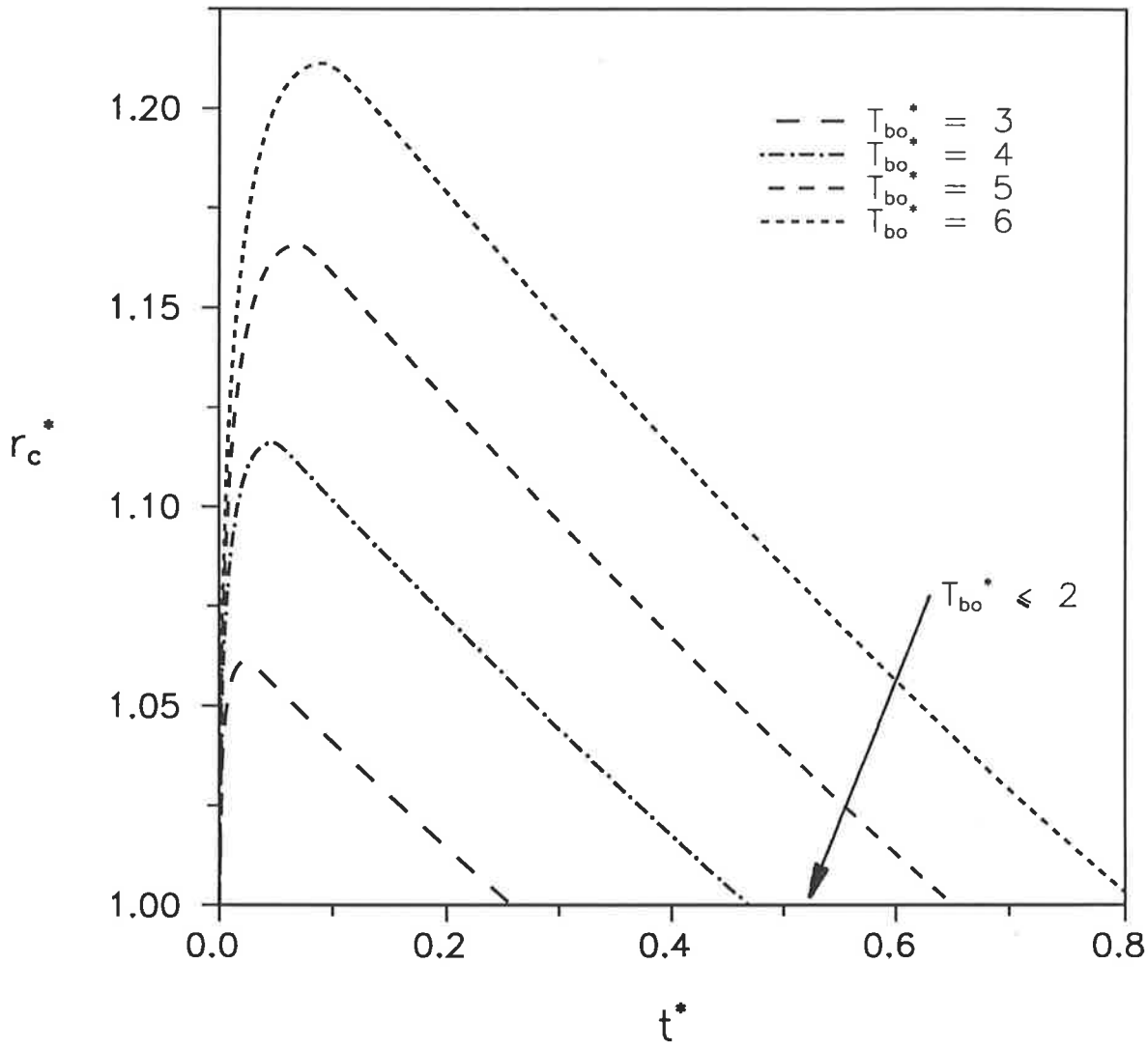

Figure 4.10b: Effect of T_{bo}^* on the history of the coating radius for a Case I problem ($Z = 1$, $Q_{b\,ext}^* = 9$, $Bi = 6$, $T_s^* = 2$, $\mathcal{R}_e^* = 0.5$).

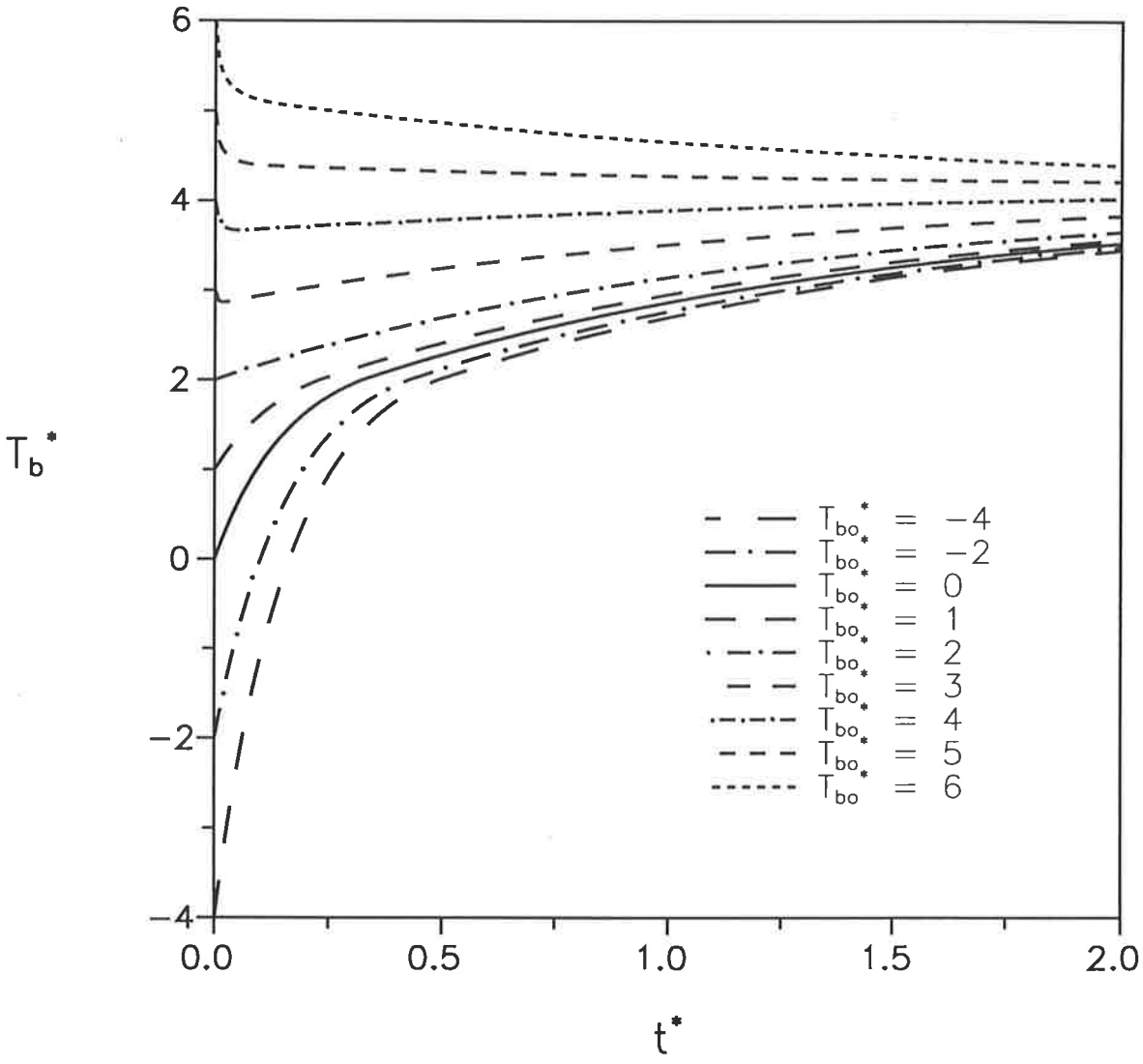

Figure 4.10c: Effect of T_{bo}^* on the temperature history of the immersed body for a Case II problem ($Z = 1$, $Q_{b\,ext}^* = 14$, $Bi = 6$, $T_s^* = 2$, $\mathcal{R}_e^* = 0.5$).

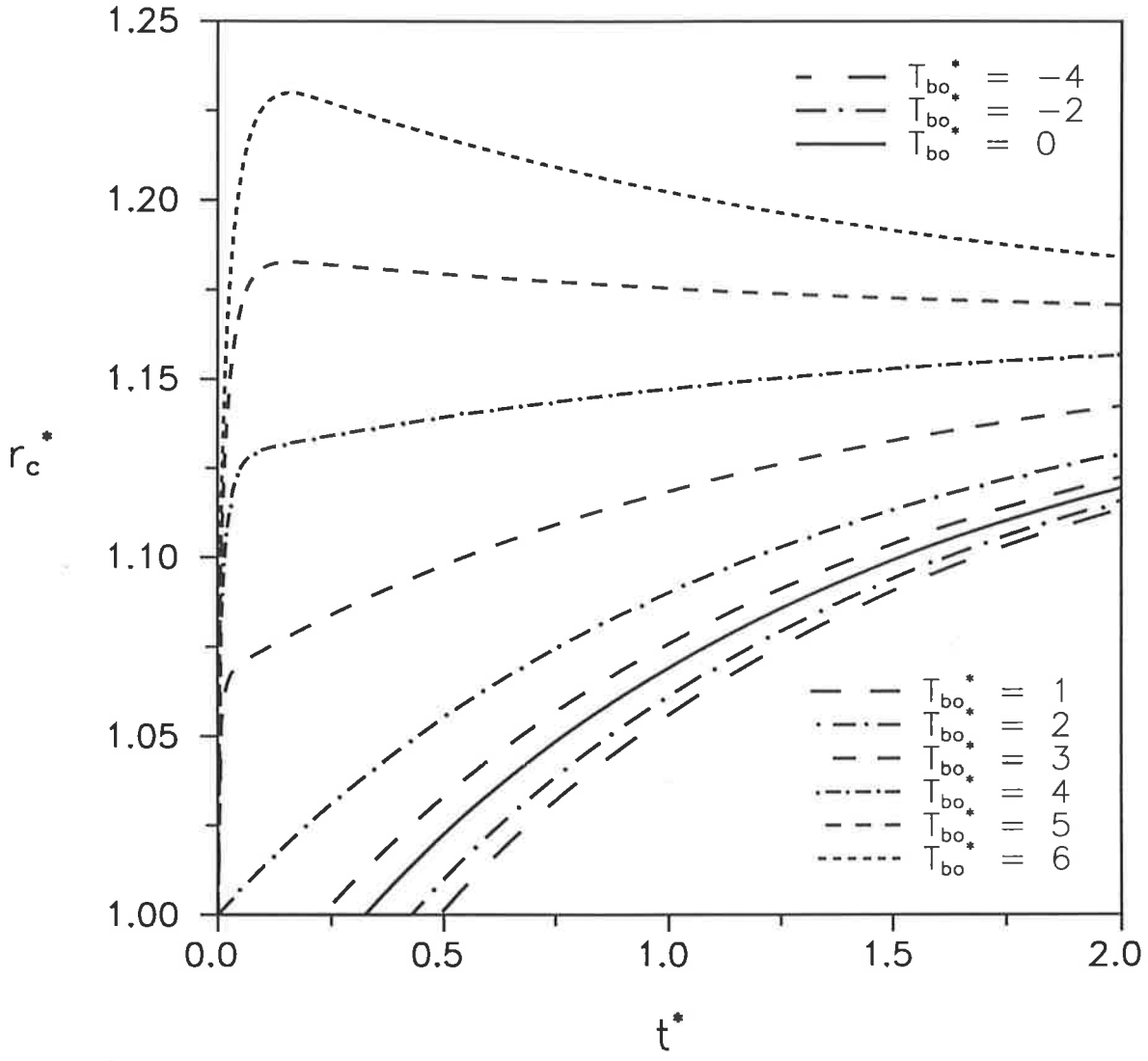

Figure 4.10d: Effect of T_{bo}^* on the history of the coating radius for a Case II problem ($Z = 1$, $Q_{b\,ext}^* = 14$, $Bi = 6$, $T_s^* = 2$, $\mathcal{R}_e^* = 0.5$).

appear immediately, regardless of the potential rate of erosion. Whether the coating persists or erodes away completely depends on the relative power supplied to the body. If the body is below T_s^* initially and the power is high, there will be a time lag before the coating starts to form.

Dimensionless Power Supplied to the Immersed Body, $Q_{b\,ext}^*$:

The effect of the power supplied to the body has already been discussed a little in Section 4.4.1. In Figures 4.11a and 4.11b, results for several more values of $Q_{b\,ext}^*$ are presented. Included is $Q_{b\,ext}^* = 12$ which marks the steady state Case I / II transition. As the power is increased, the initial response of the system becomes quicker, the temperature of the immersed body rises, and steady state is achieved later.

Biot Number, Bi:

Figures 4.12a to 4.12d demonstrate the effect of the Biot number on the coating radius and body temperature. Clearly, Bi influences the nature of the solution. When $Q_{b\,ext}^* = 9$, the Case I / II transition occurs at Bi = 4.5; for $Q_{b\,ext}^* = 14$, it is at Bi = 7 ($T_s^* = 2$ in both).

The Biot number reflects the ease by which the immersed body / coating system loses energy to the fluidized bed. If Bi is high, energy is readily transferred to the bed and the body's temperature will be relatively low - so, little or no coating will form. The initial response of the system is rapid if the Biot number is low (as energy is more easily accumulated in the body than released to the bed). However, steady conditions are attained more quickly when Bi is high.

Dimensionless Sintering Temperature, T_s^*:

The dimensionless sintering temperature, like $Q_{b\,ext}^*$ and Bi, affects the nature of the solution as seen in Figures 4.13a to 4.13d. For $Q_{b\,ext}^* = 9$, the Case I / II transition occurs at $T_s^* = 1\ ^1/_2$, while for $Q_{b\,ext}^* = 14$, the boundary is $T_s^* = 2\ ^1/_3$ (since Bi = 6).

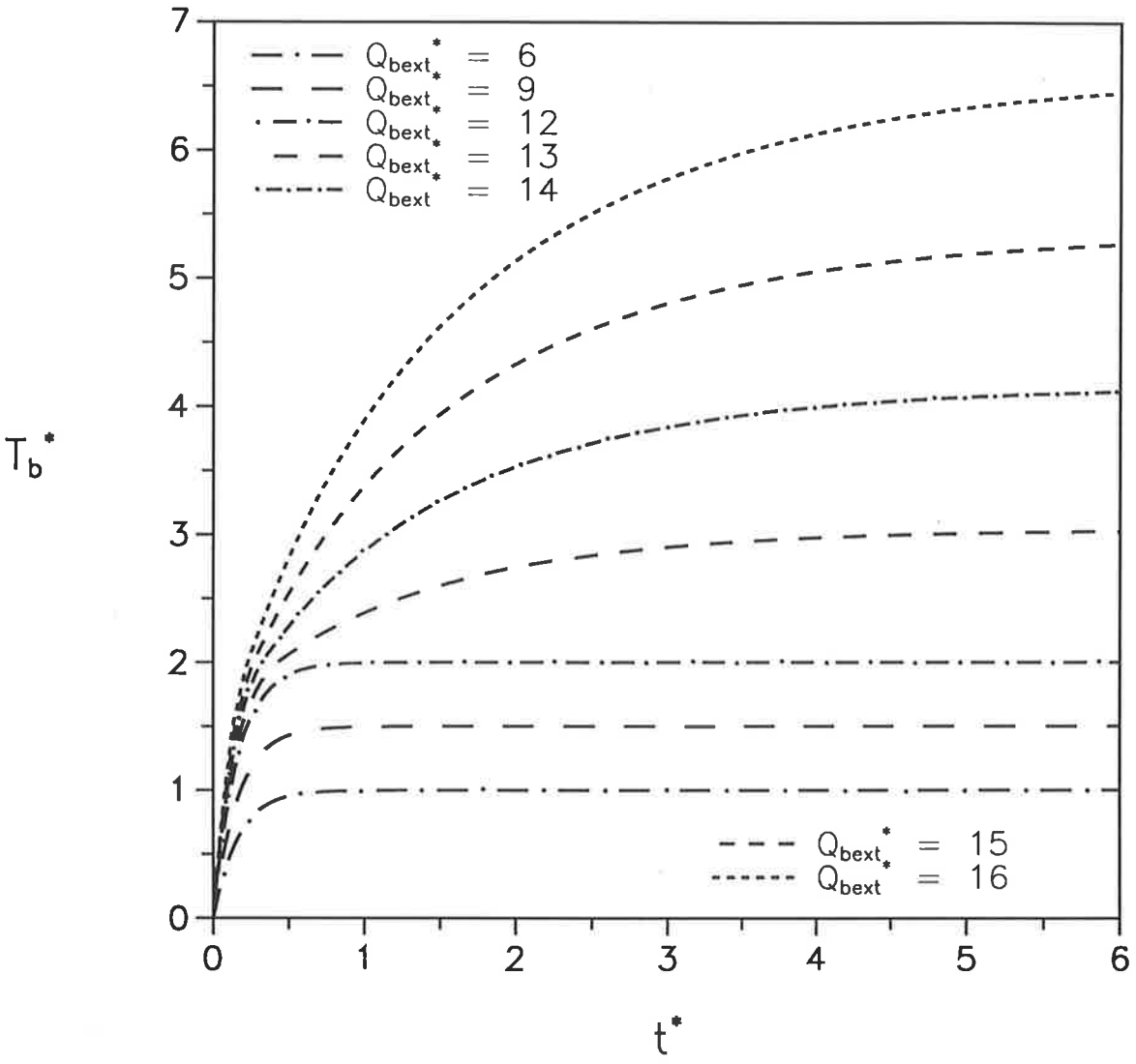

Figure 4.11a: Effect of $Q_{b\,ext}^*$ on the temperature history of the immersed body (Z = 1, $T_{bo}^* = 0$, Bi = 6, $T_s^* = 2$, $\mathcal{R}_e^* = 0.5$).

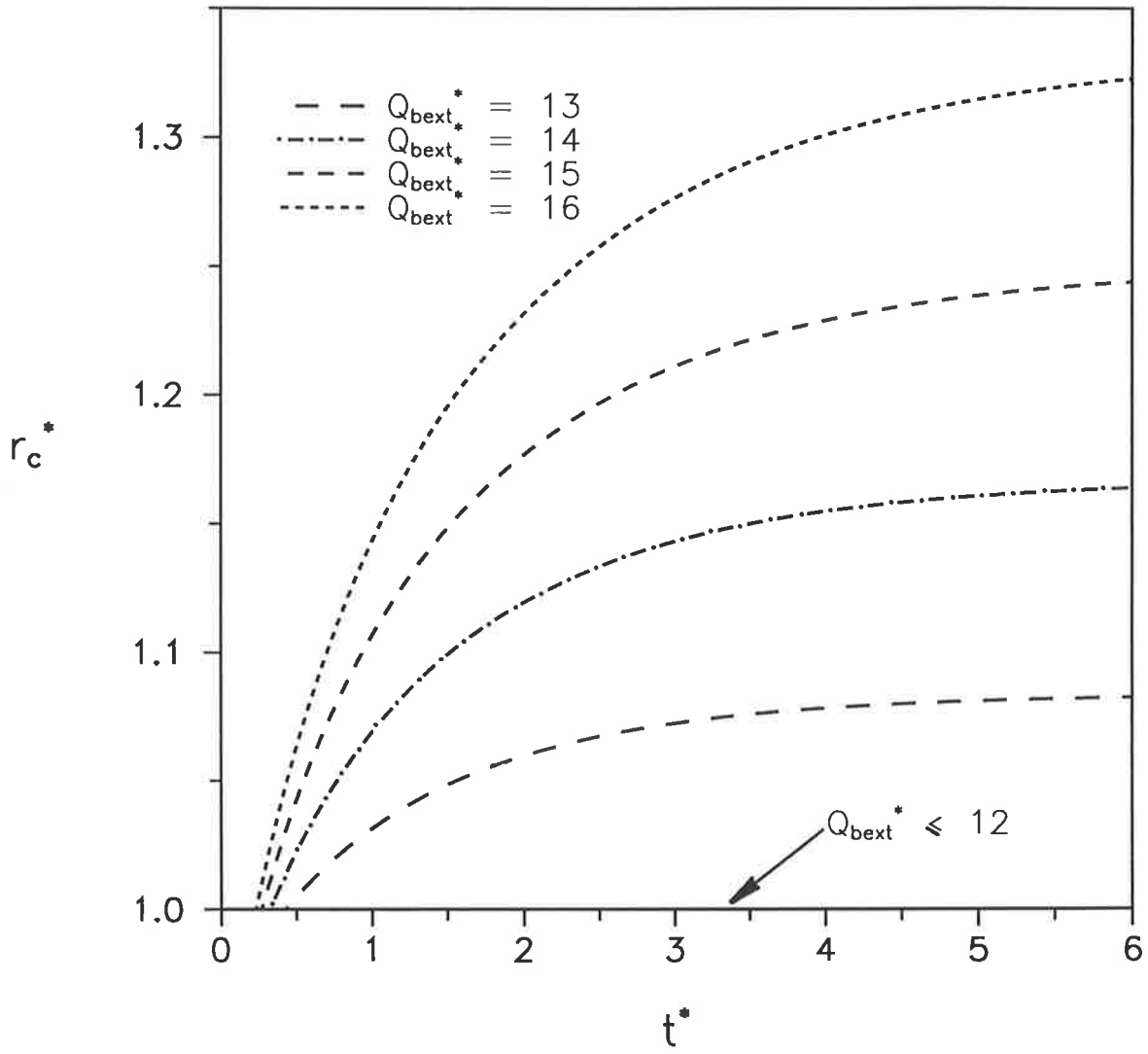

Figure 4.11b: Effect of $Q_{b\,ext}^*$ on the history of the coating radius (Z = 1, T_{bo}^* = 0, Bi = 6, T_s^* = 2, $\mathcal{R}_e^*$ = 0.5).

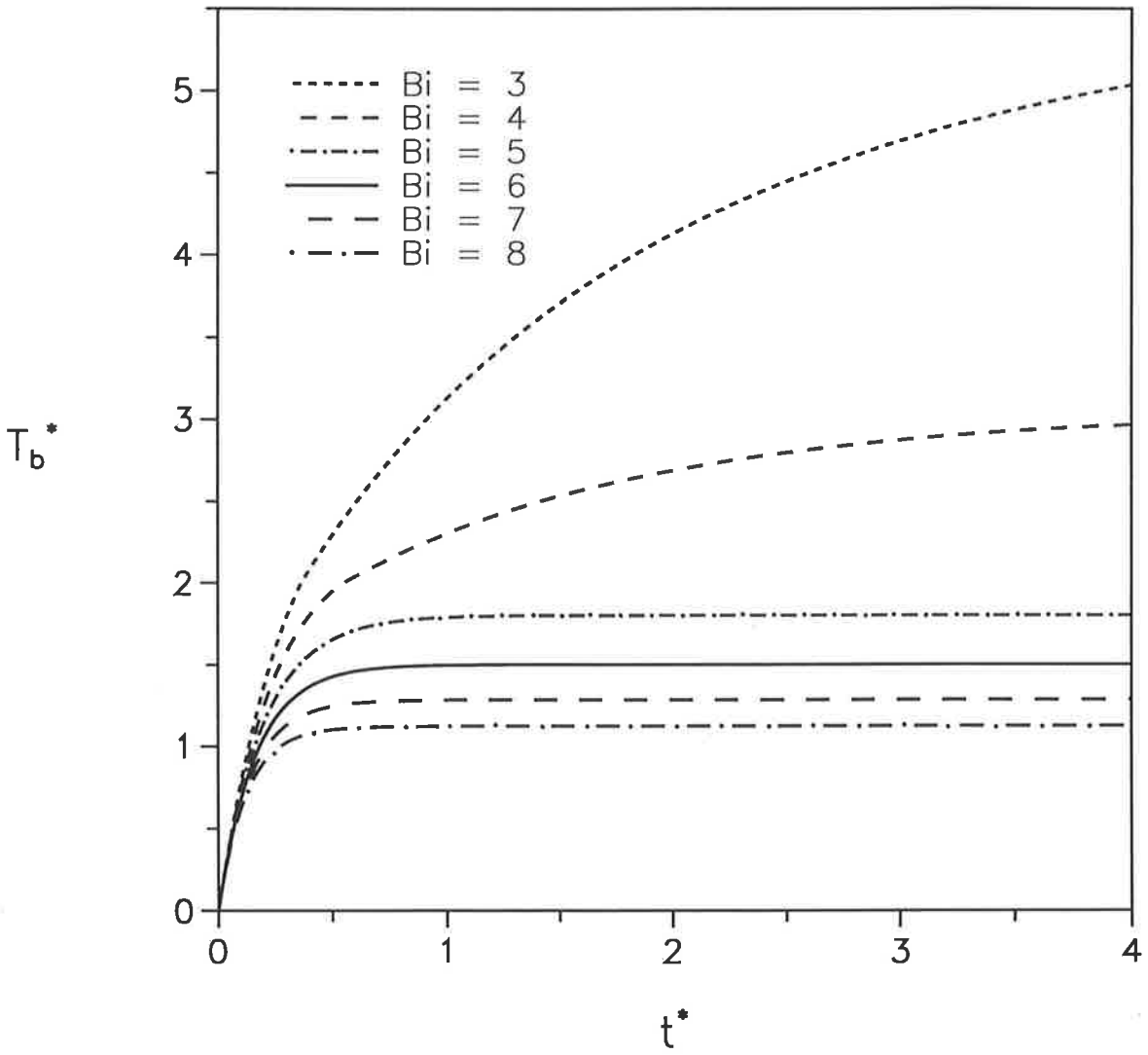

Figure 4.12a: Effect of Bi on the temperature history of the immersed body for $Q_{b\,ext}^* = 9$ ($Z = 1$, $T_{bo}^* = 0$, $T_s^* = 2$, $\mathcal{R}_e^* = 0.5$).

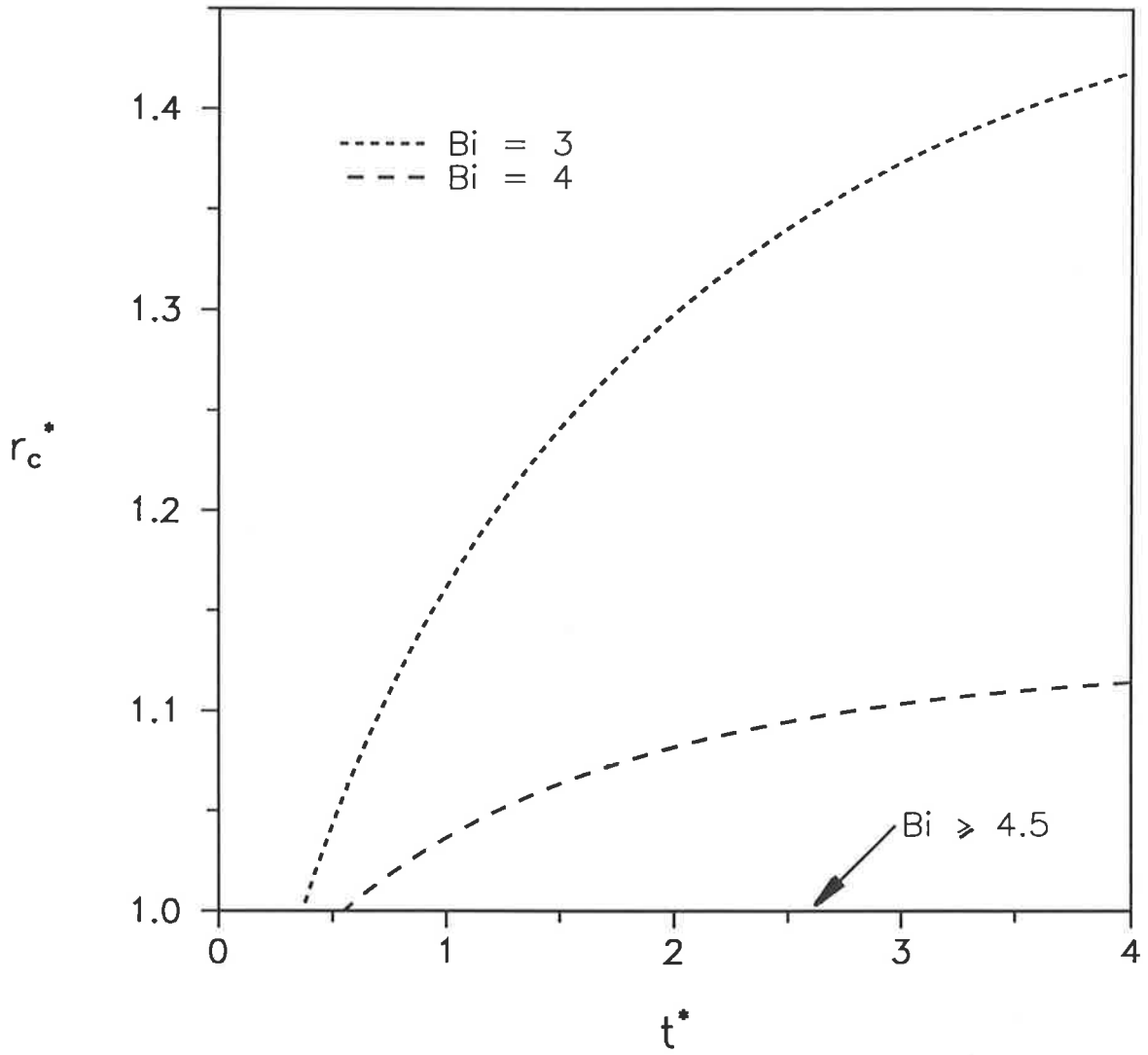

Figure 4.12b: Effect of Bi on the history of the coating radius for $Q_{b\,ext}^* = 9$ (Z = 1, $T_{bo}^* = 0$, $T_s^* = 2$, $\mathcal{R}_e^* = 0.5$).

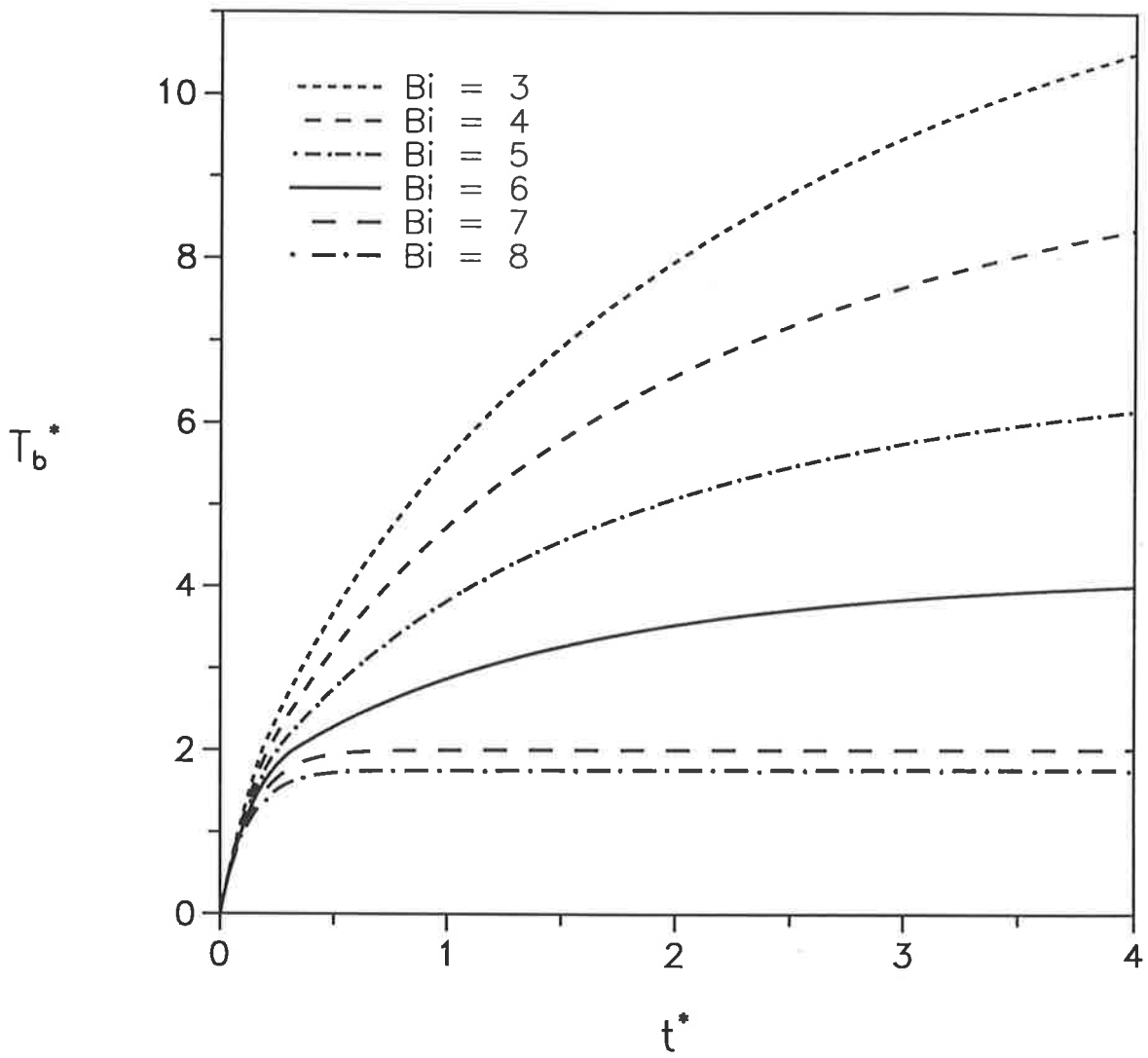

Figure 4.12c: Effect of Bi on the temperature history of the immersed body for $Q_{b\,ext}{}^* = 14$ ($Z = 1$, $T_{bo}{}^* = 0$, $T_s{}^* = 2$, $\mathcal{R}_e{}^* = 0.5$).

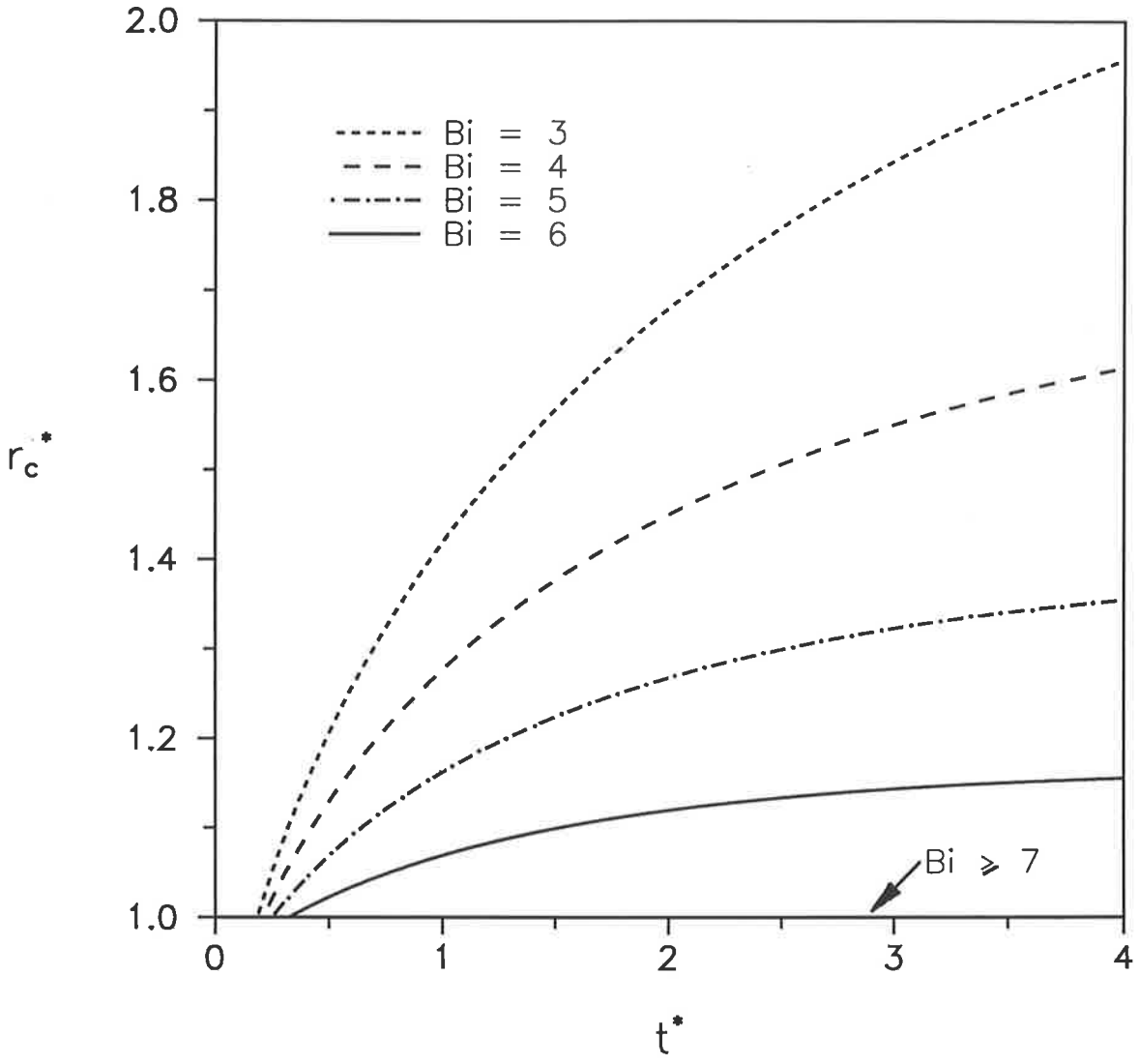

Figure 4.12d: Effect of Bi on the history of the coating radius for $Q_{b\,ext}^* = 14$ ($Z = 1$, $T_{bo}^* = 0$, $T_s^* = 2$, $\mathcal{R}_e^* = 0.5$).

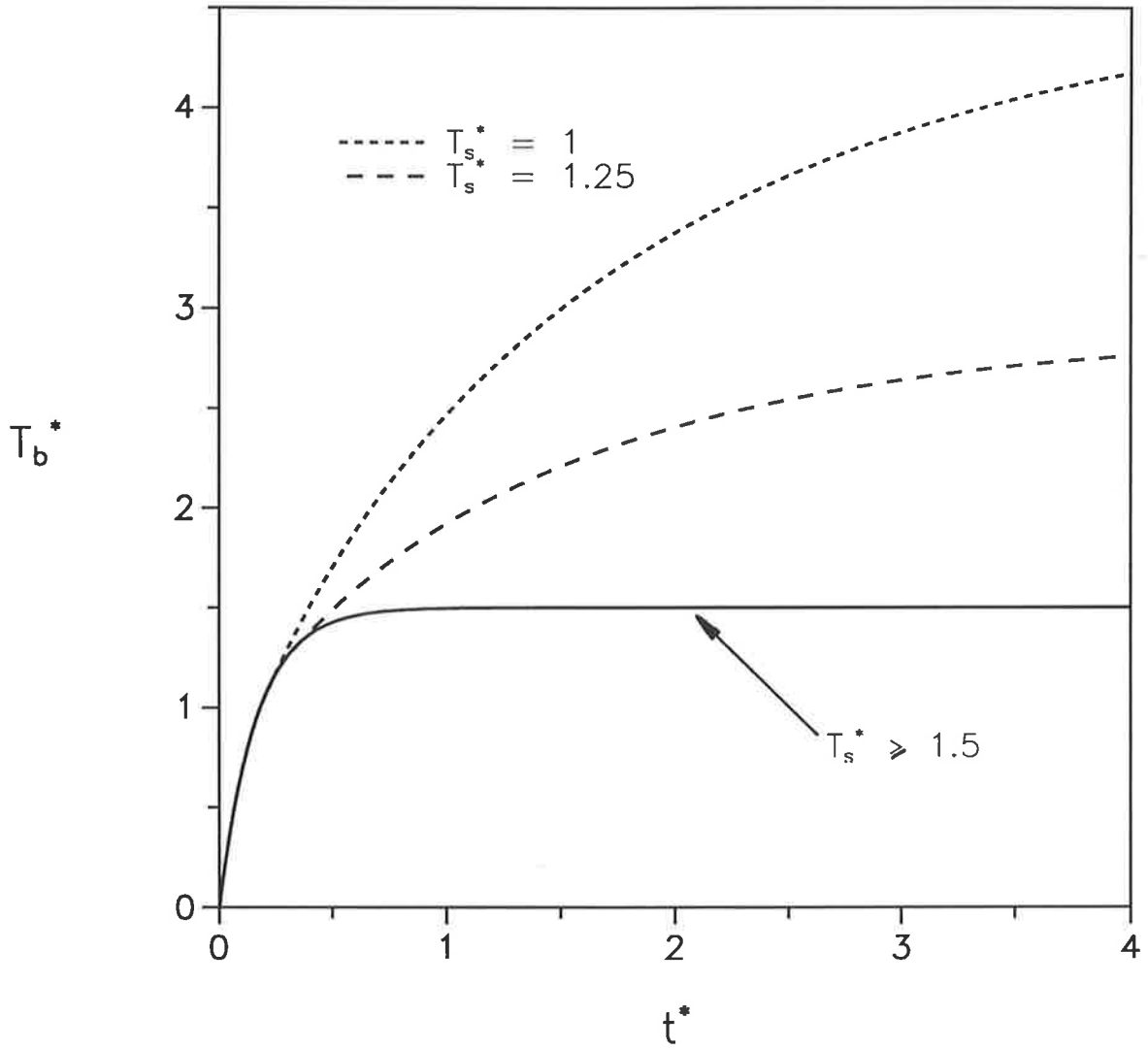

Figure 4.13a: Effect of T_s^* on the temperature history of the immersed body for $Q_{b\,ext}^* = 9$ ($Z = 1$, $T_{bo}^* = 0$, $Bi = 6$, $\mathcal{R}_e^* = 0.5$).

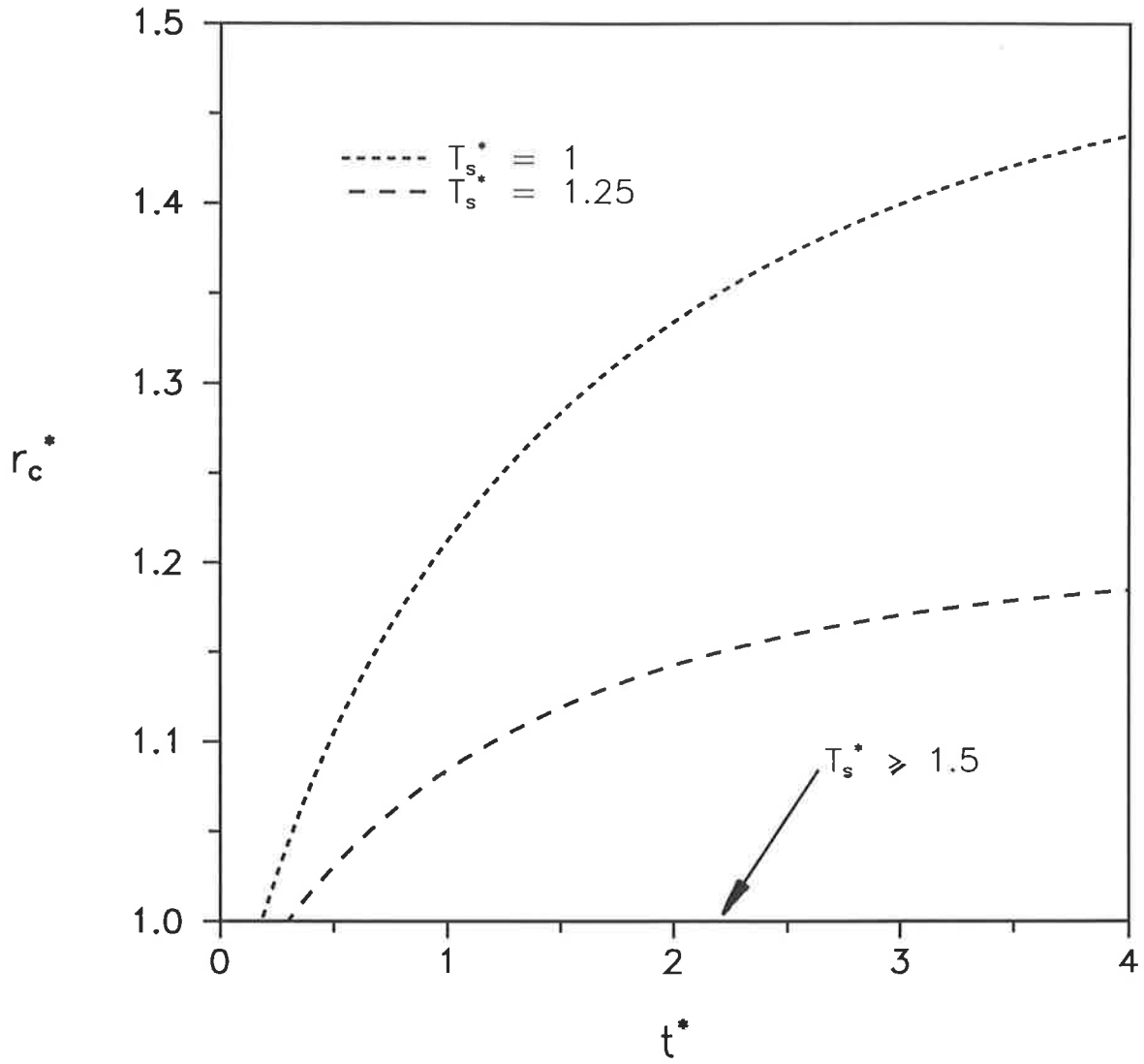

Figure 4.13b: Effect of T_s^* on the history of the coating radius for $Q_{b\,ext}^* = 9$ (Z = 1, $T_{bo}^* = 0$, Bi = 6, $\mathcal{R}_e^* = 0.5$).

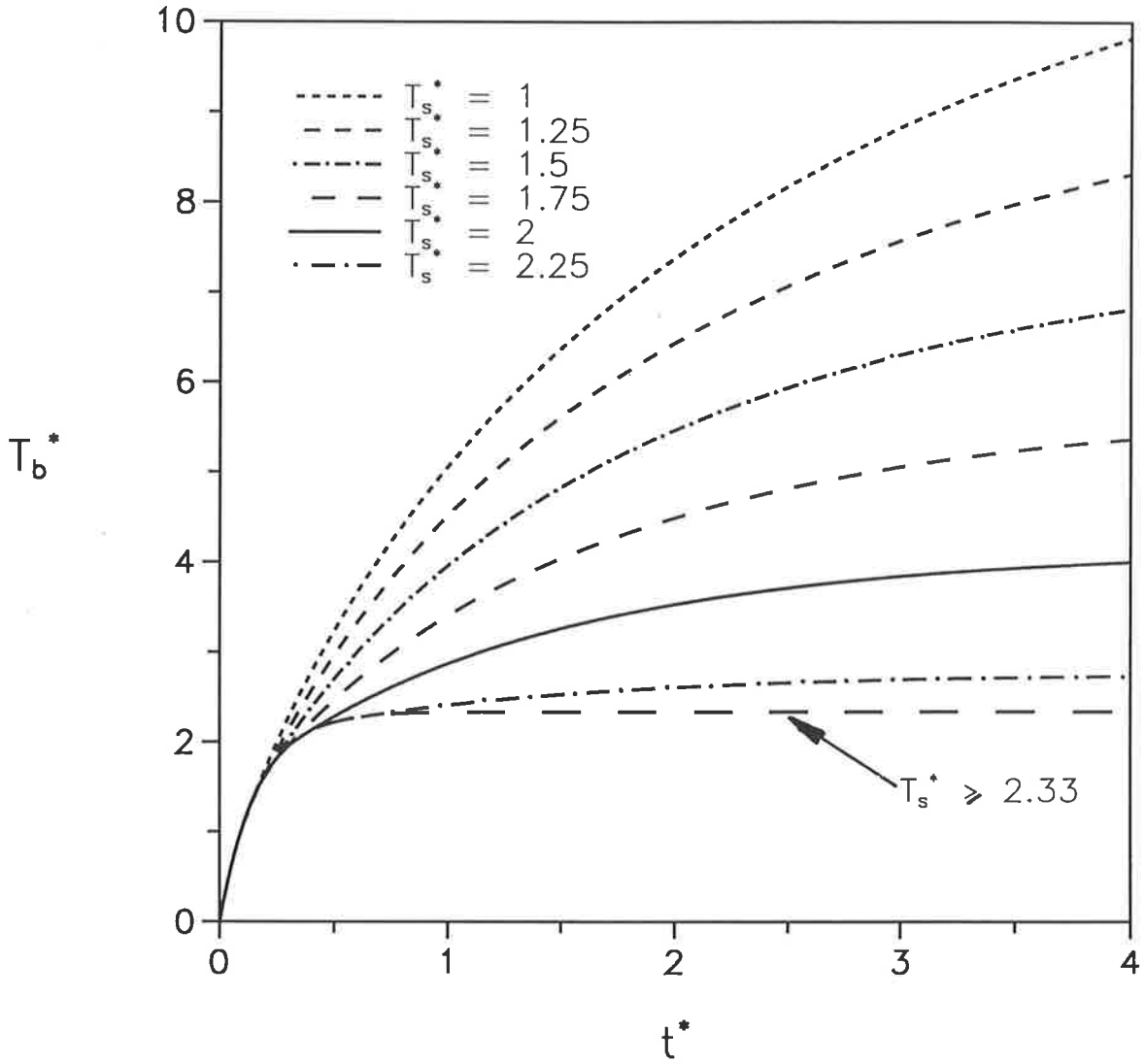

Figure 4.13c: Effect of T_s^* on the temperature history of the immersed body for $Q_{b\,ext}^* = 14$ ($Z = 1$, $T_{bo}^* = 0$, $Bi = 6$, $\mathcal{R}_e^* = 0.5$).

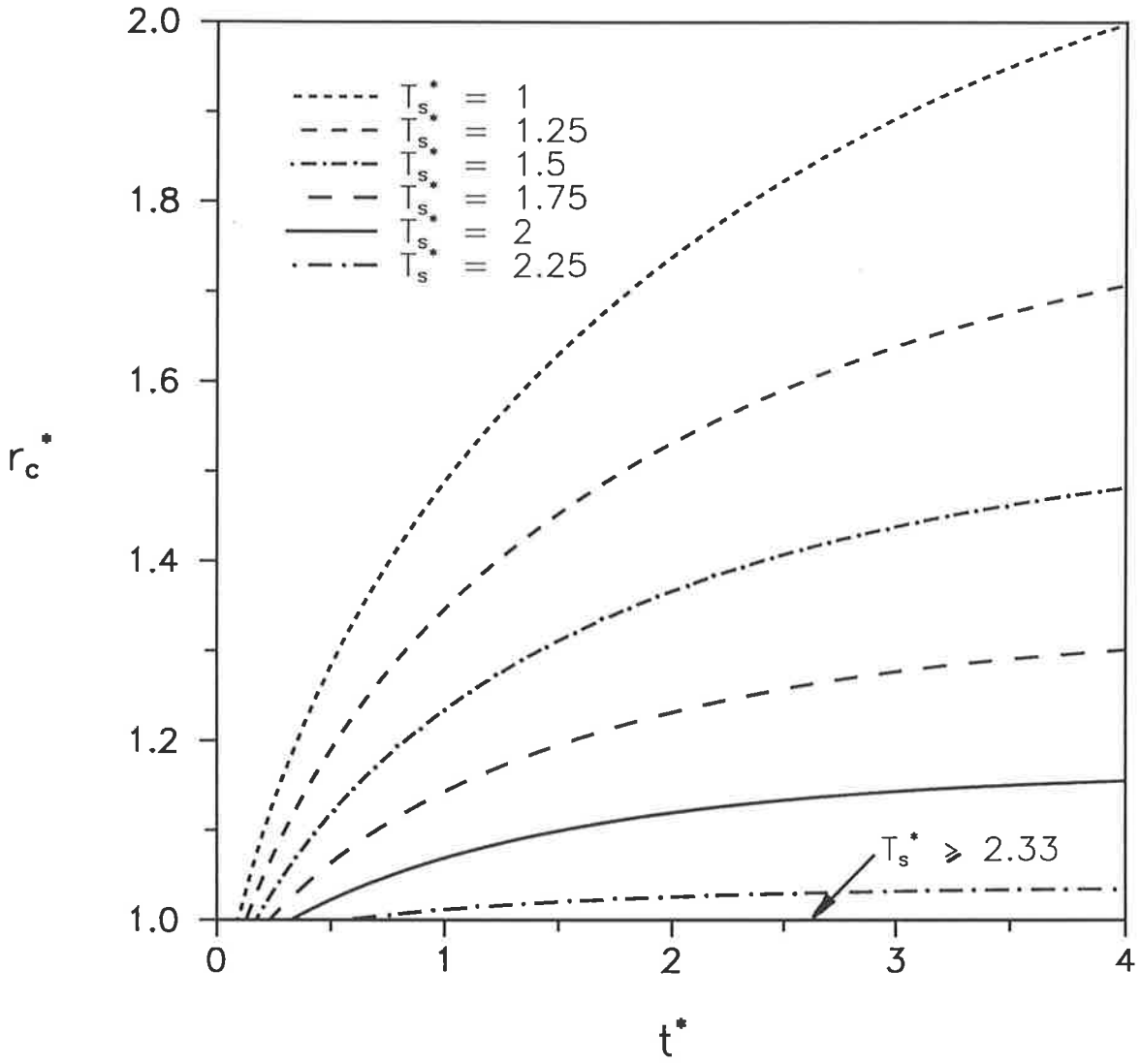

Figure 4.13d: Effect of T_s^* on the history of the coating radius for $Q_{b\,ext}^* = 14$ ($Z = 1$, $T_{bo}^* = 0$, $Bi = 6$, $\mathcal{R}_e^* = 0.5$).

Note that while T_s^* determines the boundary, it does not affect the behaviour of a Case I system. If it is known that the system is always below the sintering temperature, then it does not matter what the sintering temperature is, since convection is the sole mechanism by which the body looses energy - no coating process is involved. However, in Case II problems, where the body is hotter than the sintering temperature, T_s^* determines the transient and steady state values of T_b^* and r_c^*. In this case, if T_s^* is high, the initial response of the system is slow, little coating is formed and steady state conditions are attained quickly.

Dimensionless Potential Erosion Rate, $\mathcal{R}_e^*$:

As long as it is non-zero, the actual value of $\mathcal{R}_e^*$ is only important in a certain situation.† This is when a coating layer forms that is too thick to be maintained by the current level of power supplied to the immersed body, so that the layer suffers net erosion. For example, this may occur if the power to the body is cut after being at a high (Case II) level for some time. Alternatively, if the initial temperature of the immersed body is above the sintering temperature, a coating will form immediately - and if $Q_{b\,ext}^*$ is not high enough, the layer will erode until it reaches a sustainable thickness. The latter approach (with $T_{bo}^* = 6$) was used to investigate the effect of $\mathcal{R}_e^*$ on the system. Further, as seen in Figures 4.14a to 4.14d, the potential erosion rate produces different behaviour in the system only up to a limiting value, $\mathcal{R}_e^*{}_\infty$ ($\mathcal{R}_e^*{}_\infty \approx 0.34$ for $Q_{b\,ext}^* = 9$; $\mathcal{R}_e^*{}_\infty \approx 0.042$ for $Q_{b\,ext}^* = 14$). The potential erosion rate affects the time taken to reach steady conditions, but not the steady state itself (provided $\mathcal{R}_e^*$ is non-zero). Also shown in Figures 4.14a to 4.14d is the no-erosion situation, in which the steady state r_c^* and T_b^* are different from the corresponding steady values obtained for $\mathcal{R}_e^* > 0$.

In both low and high power cases, the system reaches steady state quickly if the potential erosion rate is high. In the initial, linear part of eroding phase of the r_c^* plots, the coating radius decreases at the given erosion rate, for $\mathcal{R}_e^* < \mathcal{R}_e^*{}_\infty$. The limiting erosion rate, $\mathcal{R}_e^*{}_\infty$, exists because the coating layer cannot be eroded beyond the $T^*(r^*) = T_s^*$

† Note that $\mathcal{R}_e^*$, the (linear) potential erosion rate in ms^{-1}, is constant in each simulation run of the parametric study, and in particular, is independent of the coating thickness.

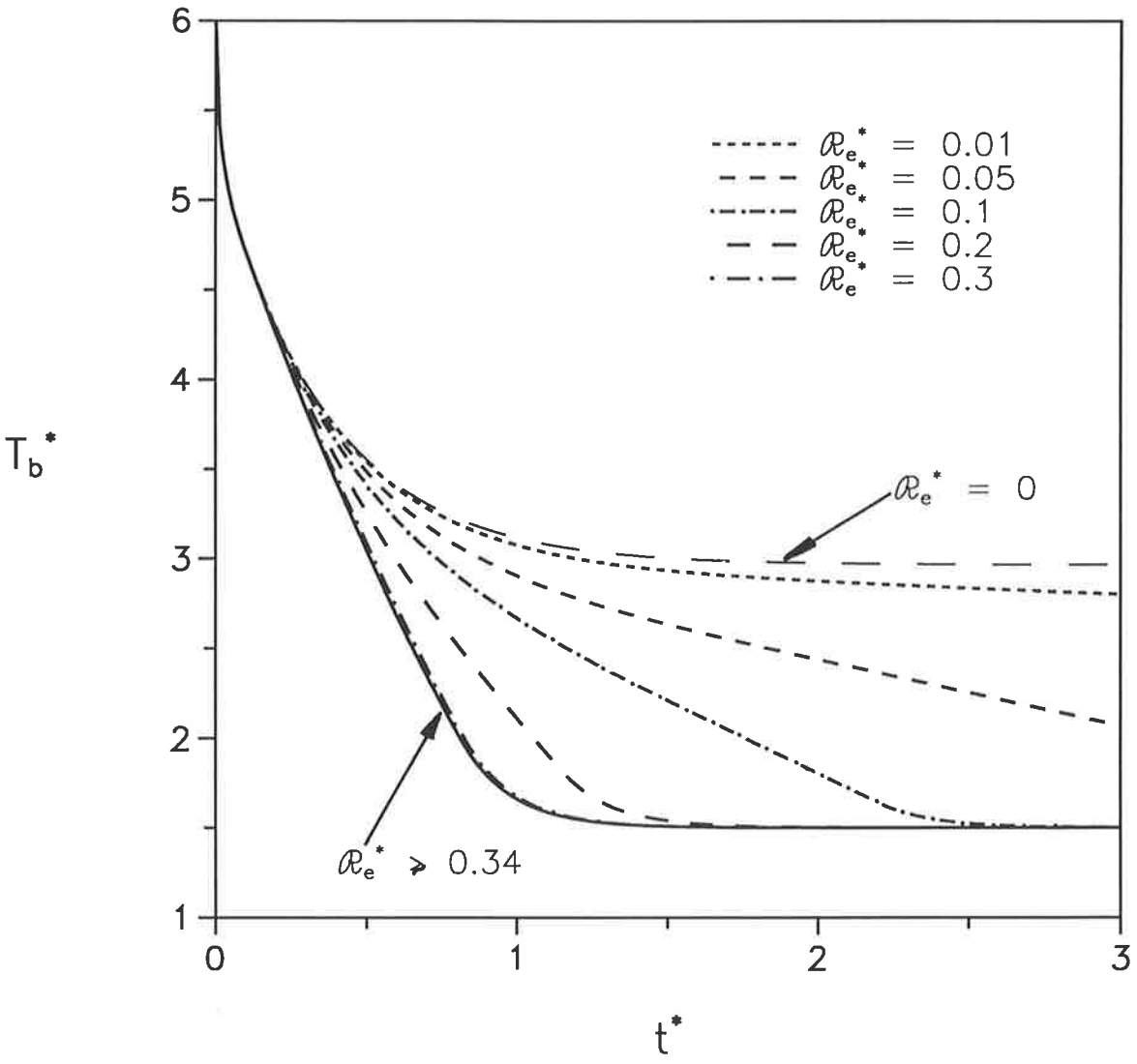

Figure 4.14a: Effect of $\mathcal{R}_e^*$ on the temperature history of the immersed body for a Case I problem ($Z = 1$, $T_{bo}^* = 6$, $Q_{b\,ext}^* = 9$, $Bi = 6$, $T_s^* = 2$).

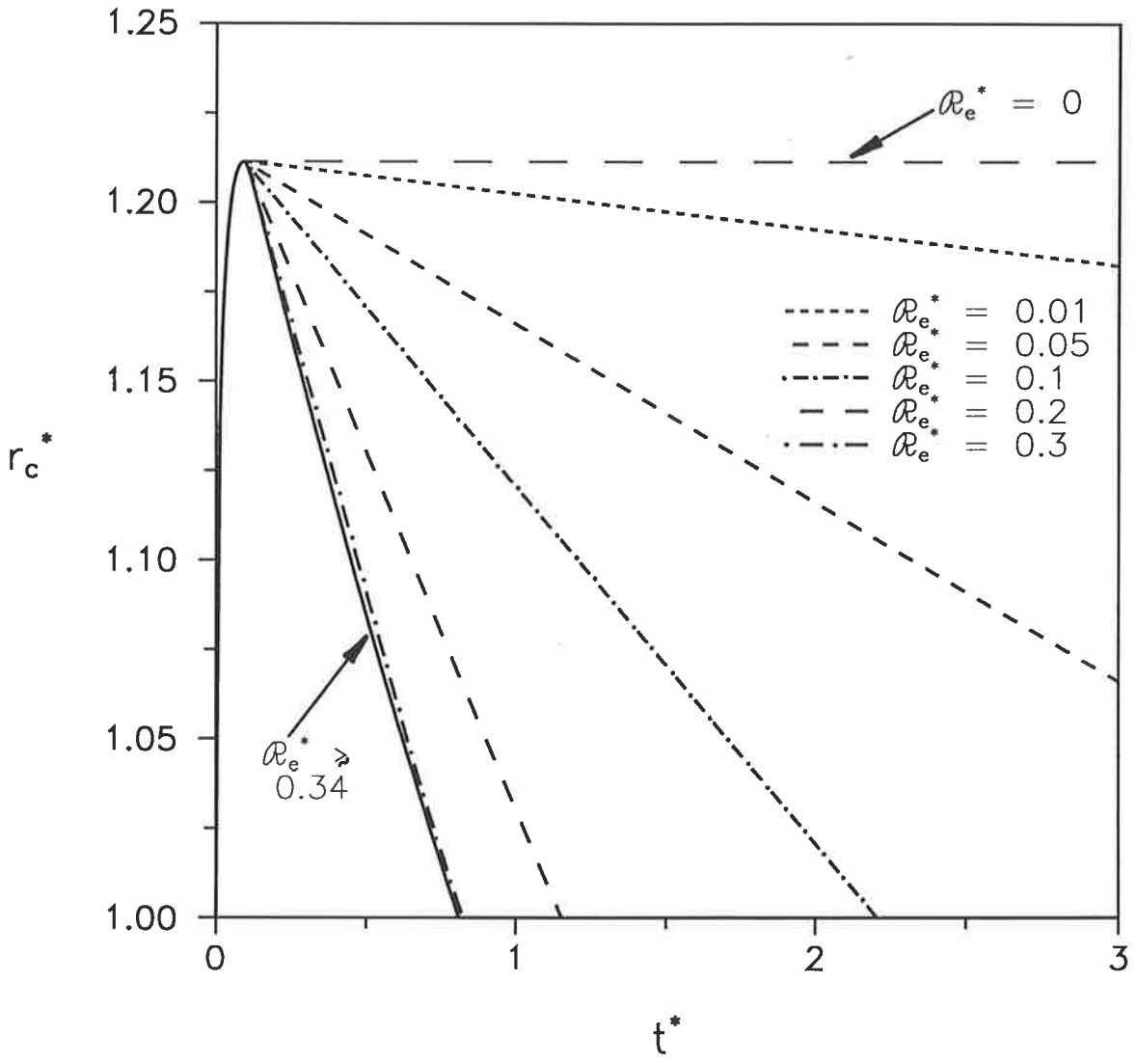

Figure 4.14b: Effect of $\mathcal{R}_e^*$ on the history of the coating radius for a Case I problem ($Z = 1$, $T_{bo}^* = 6$, $Q_{b\,ext}^* = 9$, $Bi = 6$, $T_s^* = 2$).

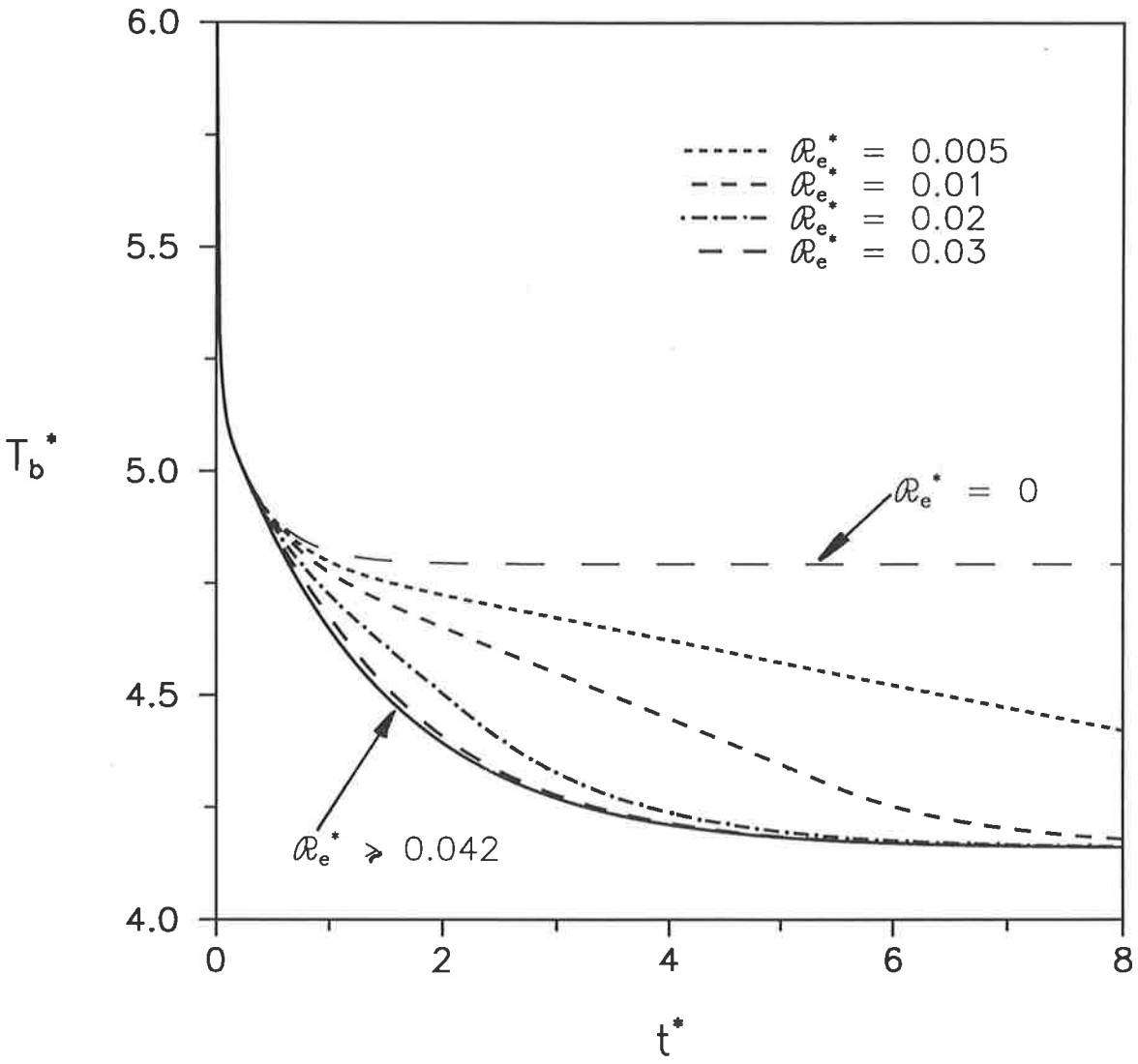

Figure 4.14c: Effect of $\mathcal{R}_e^*$ on the temperature history of the immersed body for a Case II problem ($Z = 1$, $T_{bo}^* = 6$, $Q_{b\,ext}^* = 14$, $Bi = 6$, $T_s^* = 2$).

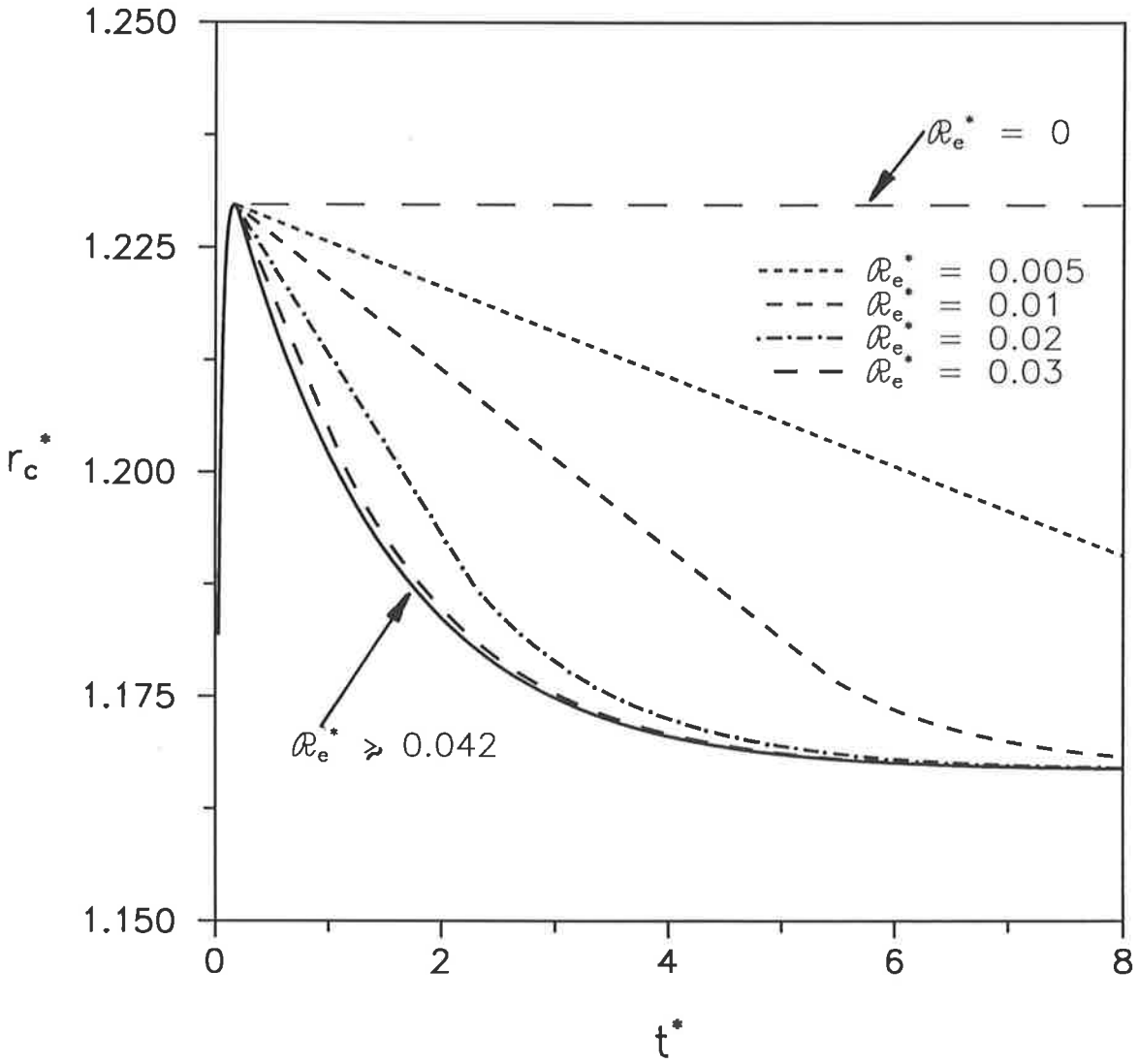

Figure 4.14d: Effect of $\mathcal{R}_e^*$ on the history of the coating radius for a Case II problem ($Z = 1$, $T_{bo}^* = 6$, $Q_{b\,ext}^* = 14$, $Bi = 6$, $T_s^* = 2$).

front as it recedes through the layer. Net erosion can only take place while the outer surface of the coating is cooler than the sintering temperature. $\mathcal{R}_e^*{}_\infty$ is higher for the low power case than the high power one since the T_s^* front inside the coating recedes more quickly.

In the normal case, the absolute value of the potential erosion rate is unimportant - only the difference between it and the potential coating rate is relevant. However, when a situation arises in which net erosion of the coating layer occurs, the absolute value of $\mathcal{R}_e^*$ (up to $\mathcal{R}_e^*{}_\infty$) determines uniquely how quickly the system will achieve steady state. In this event, a high $\mathcal{R}_e^*$ yields a fast initial response and steady state prevails in a short time.

Summary:

- It has been verified that only $Q_{b\,ext}^*$, Bi and T_s^* determine the steady state values of r_c^* and T_b^*.
- Steady state is achieved in a short time if the conditions in Table 4.2 are satisfied.

Table 4.2: Trends in the parameters that cause the immersed body / coating system to reach steady state quickly.

Parameter	Trend
Z	low
T_{bo}^*	near $T_b^*{}_{st}$
$Q_{b\,ext}^*$	low
Bi	high
T_s^*	no effect (Case I) high (Case II)
$\mathcal{R}_e^*$	no effect (no net erosion) high (if net erosion occurs)

- T_{bo}^* has a significant influence on the path taken by the system in reaching its final state as seen in Table 4.3.

Table 4.3: Influence of T_{bo}^* on the general transient behaviour of the immersed body / coating system.

T_{bo}^*	Case	
	I	II
low	$T_{bo}^* < T_b^*{}_{st}$: body heats up; no coating	$T_{bo}^* < T_s^*$: body heats up; delay in coating growth
intermediate	$T_b^*{}_{st} < T_{bo}^* < T_s^*$: body cools; no coating	$T_s^* < T_{bo}^* < T_b^*{}_{st}$: body cools, reaches minimum, heats up; coating forms instantly then rate slows
high	$T_{bo}^* > T_s^*$: body cools; coating forms instantly, reaches maximum, then erodes completely	$T_{bo}^* > T_b^*{}_{st}$: body cools; coating forms instantly, reaches maximum, then erodes to steady thickness

4.5 COMPARISON WITH THE NON-SINTERING SYSTEM

It is interesting to compare the behaviour of two immersed body systems which are in every way identical except one - in one of the systems, the particles do not become adhesive. The following discussion is restricted to the difference in the steady state temperature of the immersed body that is obtained with sintering as opposed to non-sintering particles. Both systems are assumed to have constant physical and thermal properties, and non-zero potential erosion rates.

When particles do not sinter, no coating layer is formed and heat transfer from the immersed body occurs only by direct convection to the fluidized bed. Thus, it is a Case I (low power) situation according to Section 4.3.1. Let $T_{b'st}$ be the steady state immersed body temperature in this alternative system in which the particles do not sinter. Define:

$$T_{b'st}^{*} = \frac{T_{b'st} - T_{\infty}}{T_m - T_{\infty}} \tag{4.59}$$

where T_m is the melting temperature of the particles in the original system. From equation (4.54b), it is clear that:

$$T_{b'st}^{*} = \frac{Q_{b\,ext}^{*}}{Bi} \tag{4.60}$$

regardless of the power supplied to the immersed body.

In Figure 4.15, the steady state temperatures of the immersed body in the sintering and non-sintering systems are compared for a range of $Q_{b\,ext}^{*}$ and three values of T_s^{*}. The adhesive and non-adhesive systems behave identically for $Q_{b\,ext}^{*} < Bi.T_s^{*}$. When the power is higher, it is clear that the insulating effect of coating formation significantly increases the temperature of the immersed body.

Finally, it is productive to relate formally the behaviour of the coating-erosion model to an important engineering problem - the fouling of heat transfer surfaces. After a heat exchanger has been in operation for some time, deposits may build up on its heat transfer surfaces. These deposits restrict the flow of heat and are usually characterised by a fouling factor, R_f, which is included as an additional resistance term in the overall heat transfer equation. The fouling factor may be defined as:

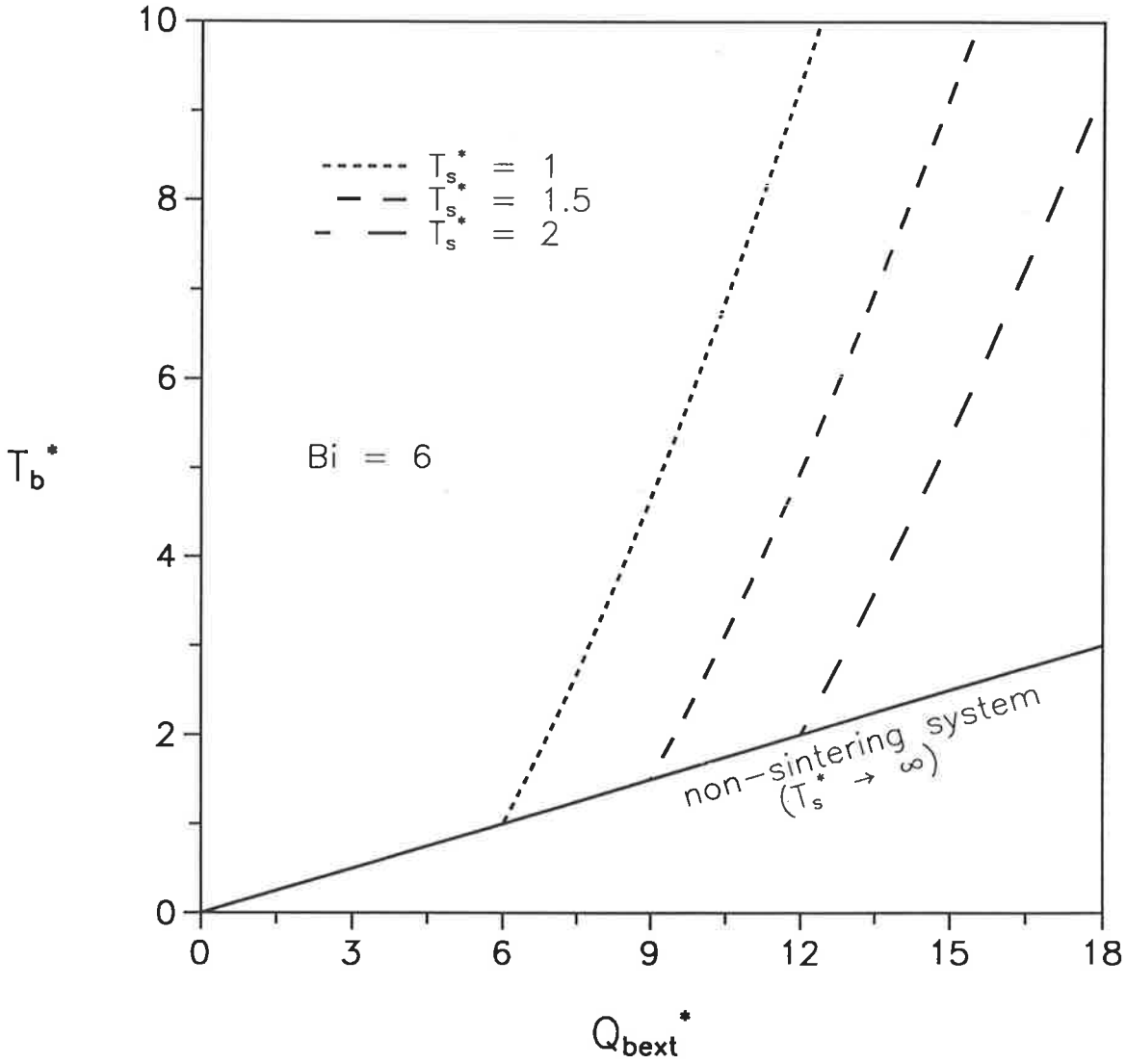

Figure 4.15: Comparison of the steady state temperature of an immersed body when the particles do and do not sinter.

$$R_f = \frac{1}{h_{fouled}} - \frac{1}{h_{clean}} \tag{4.61}$$

which, for the purposes of this thesis, may be non-dimensionalised to yield:

$$R_f^* = \frac{k R_f}{r_b} = \frac{1}{Bi_{fouled}} - \frac{1}{Bi_{clean}} \tag{4.62}$$

Now, Bi_{clean} characterises heat transfer in the absence of coating formation - this corresponds to the non-adhesive particle case considered above. Bi_{fouled} is an effective Biot number defined by:

$$Q_{b\,ext}^* = Bi_{fouled} \cdot T_b^*{}_{st} \tag{4.63}$$

where $T_b^*{}_{st}$ is given by equation (4.54b) or (4.55b). The effects of both modes of heat removal - convection and coating formation - are lumped together in Bi_{fouled}. On combining the expressions for $T_b^*{}_{st}$ with equations (4.62) and (4.63), we find that:

$$R_f^* = \begin{cases} 0 , & Q_{b\,ext}^* \le Bi . T_s^* \quad (4.64a) \\ \dfrac{T_s^*}{Q_{b\,ext}^*} - \dfrac{1}{Bi} + \ln\left(\dfrac{Q_{b\,ext}^*}{Bi \, . \, T_s^*}\right) , & Q_{b\,ext}^* \ge Bi . T_s^* \quad (4.64b) \end{cases}$$

Figure 4.16 illustrates how the dimensionless fouling factor varies with the power supplied to the body for three values of the sintering temperature.

An alternative quantity that characterises the extent of fouling is the percentage reduction in the overall heat transfer coefficient. In this case:

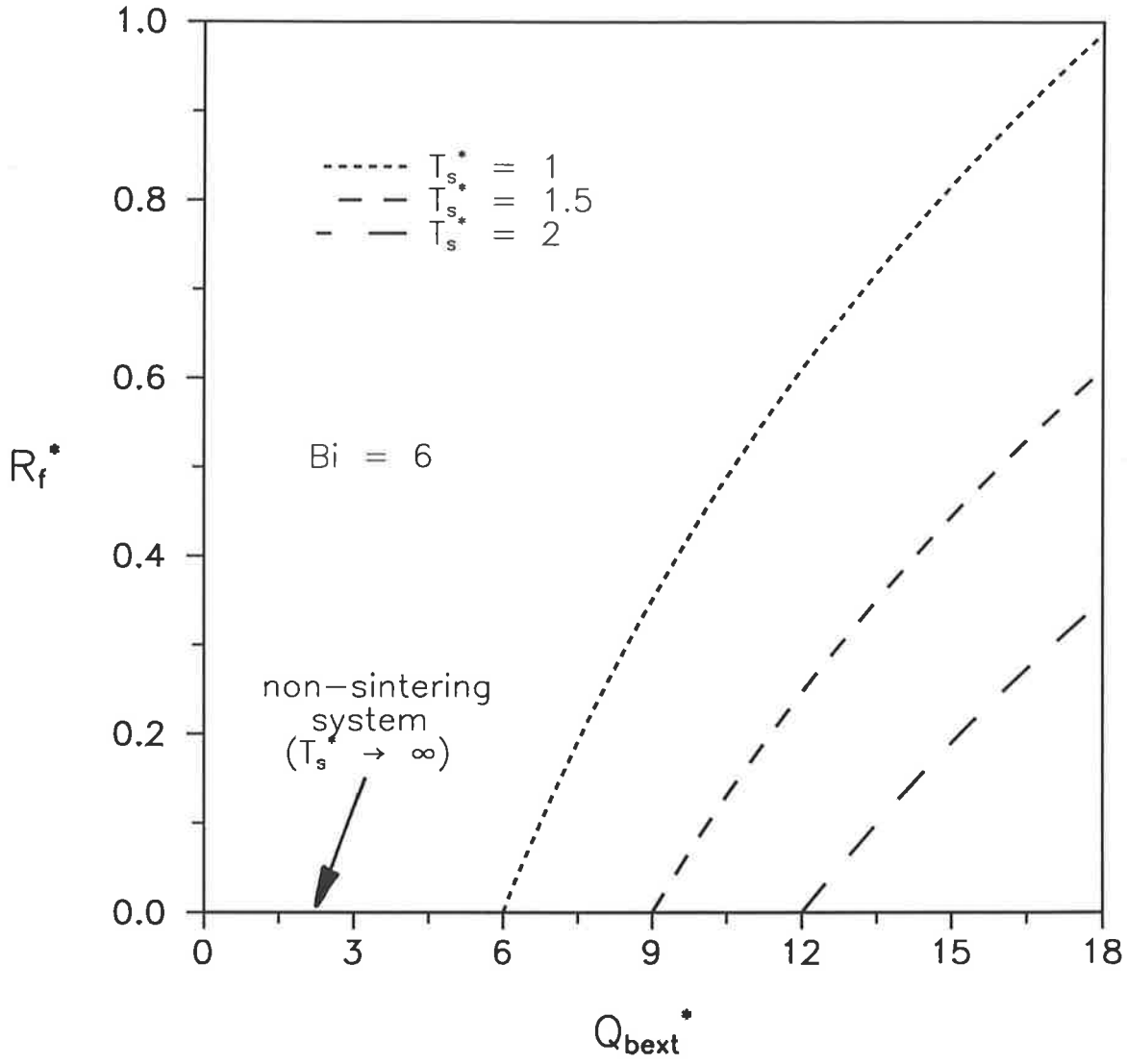

Figure 4.16: Effect of $Q_{b\,ext}^*$ and T_s^* on the dimensionless fouling factor, R_f^*, according to equation (4.64).

$$\begin{pmatrix} \text{reduction in overall} \\ \text{heat transfer coefficient} \end{pmatrix} = \frac{Bi_{clean} - Bi_{fouled}}{Bi_{clean}} \times 100\%$$

$$= \begin{cases} 0\% , & Q_{bext}^* \le Bi.T_s^* \quad (4.65a) \\ \left(1 - \dfrac{Q_{bext}^*/Bi}{T_s^* + Q_{bext}^*.ln\left(Q_{bext}^*/(Bi.T_s^*)\right)}\right) \times 100\% , & Q_{bext}^* \ge Bi.T_s^* \quad (4.65b) \end{cases}$$

The percentage reduction in heat transfer coefficient is displayed in Figure 4.17 as a function of the power supplied to the body and the sintering temperature.

When $Q_{b\,ext}^*$ is low, no coating forms, so R_f^* is zero and there is no reduction in the overall heat transfer coefficient. At high powers, R_f^* increases and the overall heat transfer coefficient decreases, demonstrating that heat transfer may be significantly impeded by the presence of the coating layer. It is important to note that the resistance to heat transfer at the Case I / II boundary increases very suddenly. If the system were just below the transition point, marked by $Q_{b\,ext}^* = Bi.T_s^*$, and the power increased slightly, then heat flow would be substantially reduced, causing the temperature of the immersed body to increase rapidly. This situation may be dangerous or otherwise undesirable. If it is to be avoided, then the system should be operated far enough below the Case I / II boundary so that process fluctuations do not drive the system into the coating formation regime.

4.6 SUMMARY

A mathematical model of the coating-erosion phenomenon was developed from a mass balance which combines fluidized bed powder coating theory with studies of the erosion of tubes in a fluidized bed. The model predicts how the thickness (or mass) of the deposit and the temperature of the immersed body change with time. Non-dimensionalisation reveals that the system's behaviour is governed by seven

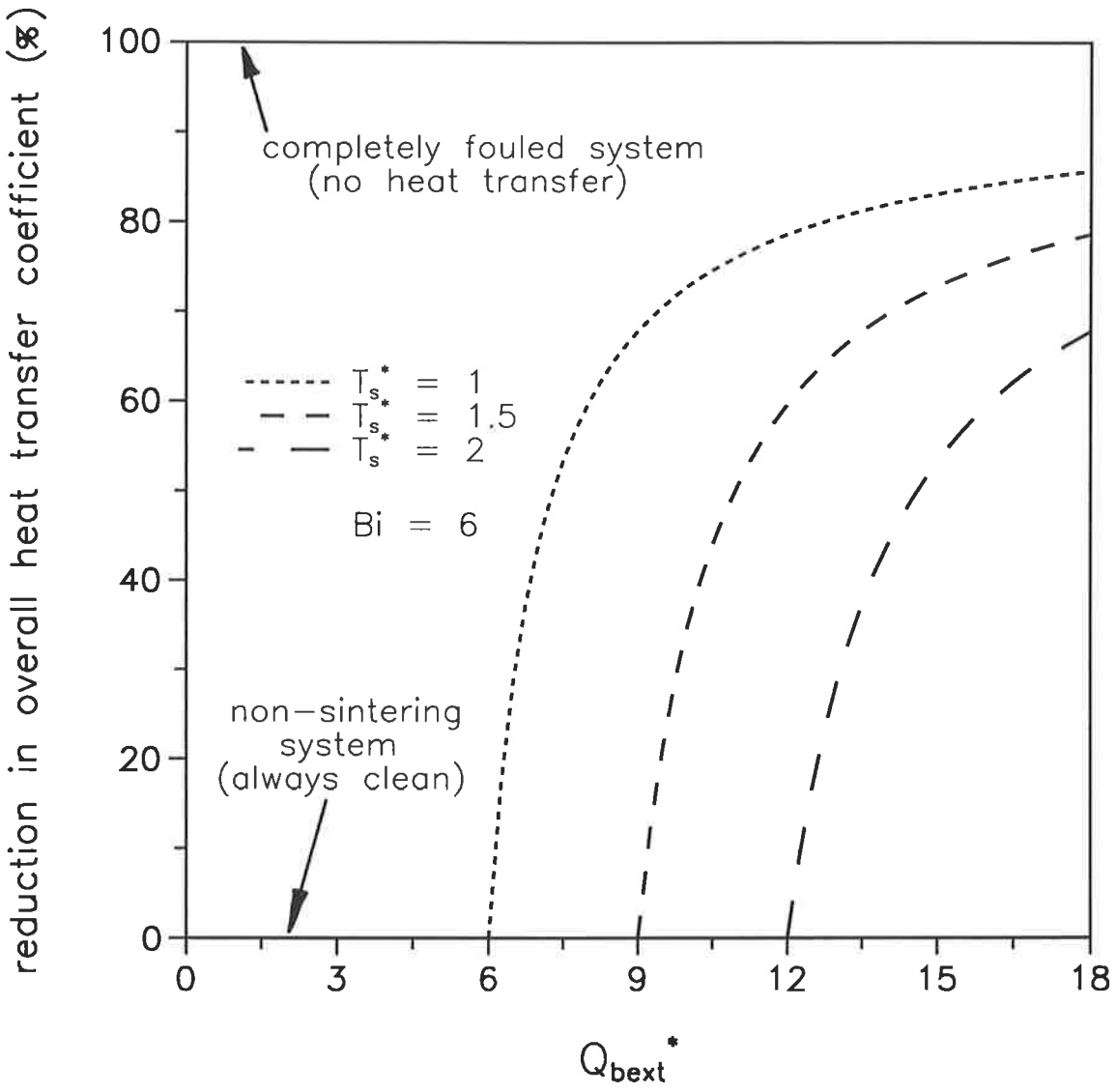

Figure 4.17: Effect of $Q_{b\,ext}^*$ and T_s^* on the overall heat transfer coefficient according to equation (4.65).

dimensionless groups: Z, T_{bo}^*, $Q_{b\,ext}^*$, Bi, T_s^*, $\mathcal{R}_e^*$ and the dimensionless time, t^*. The model was formulated for a cylindrical immersed body and it is assumed that the deposit forms with uniform thickness over its surface.

Steady State Solutions:

The model has simple analytical steady state solutions, equations (4.54) and (4.55), which depend on only three of the dimensionless groups: $Q_{b\,ext}^*$, Bi and T_s^*. There are two regimes of behaviour:

- **Case I** - Low Power: in which the body remains cooler than the sintering temperature and no coating layer forms;
- **Case II** - High Power: in which the immersed body is above the sintering temperature and an insulating layer of coating is present.

The body temperature and amount of coating increase with $Q_{b\,ext}^*$, while they decrease with Bi and T_s^*.

Dynamic Solutions:

A flexible simulation program was written to obtain dynamic solutions of the coating-erosion model. Z, T_{bo}^* and $\mathcal{R}_e^*$ may significantly influence the path and time taken to reach steady conditions, but they do not affect the final state of the system. The time taken to reach steady state decreases with $\mathcal{R}_e^*$ and increases with Z and $|T_{bo}^* - T_{b\,st}^*|$. $\mathcal{R}_e^*$ only affects the solution if net erosion of the coating occurs.

Comparison with the Non-Sintering System:

The formation of a deposit on a heat transfer surface is an additional resistance to heat flow and is known as *fouling*. The results of the coating-erosion model were recast in the form of two parameters used to characterise fouling - the fouling factor and the percentage reduction in the overall heat transfer coefficient, equations (4.64) and (4.65). With a slight shift in operating conditions, the system can change from being deposit-free to heavily fouled, causing a large and possibly dangerous temperature rise.

Chapter 5:

RESULTS AND DISCUSSION

In this chapter, the results of the coating-erosion experiments are compared with the model predictions. A correlation for the sintering temperature is developed in terms of the operating conditions. Finally, the results of this thesis are related to the pulse-enhanced, indirectly-heated fluidized bed gasifier.

5.1 INTRODUCTION

Before comparing the coating-erosion theory and experiments, the extent of the experimental study described in Chapter 3 is outlined. Next, the input variables of the model developed in Chapter 4 are discussed; several important variables need estimation or parameter fitting. The experimental results themselves consist of: the temperature history of the immersed body, the mass, spatial distribution and internal structure (cross-section) of the coating present at the end of an experiment. The method of comparison of the experiments and the theory is explained, then the comparison is made. Extensions to the simple, one-dimensional formulation of the coating-erosion model are discussed in the light of the experimental results. An important aspect of this thesis is the identification and preliminary correlation of the sintering temperature, a key system property. Lastly, the current study is related to two other systems - a bed subject to defluidization, and the pulse-enhanced, indirectly-heated fluidized bed gasifier of MTCI and ThermoChem Inc. which was introduced in Chapter 1.

5.2 EXPERIMENTAL OVERVIEW

The coating-erosion experiments were performed according to the procedure set out in Section 3.4.4. Although 45 such experiments were conducted, only 37 of them were selected for further analysis. The unsuccessful experiments were rejected because of partial equipment failure or erratic bed operation. The complete data of all of the successful experiments are tabulated in Appendix G.

As indicated in Chapter 3, the principal experimental variables involved in these experiments were: the superficial gas velocity and the temperature of the fluidized bed, the power supplied to the immersed body, and the duration of the experiment. Table 5.1 presents the range of the main experimental variables covered in this study.

Table 5.1: Range of the principal experimental variables covered in the coating-erosion experiments.

Variable	Range
Power supplied to the immersed body[1]	440 - 760 W
Superficial gas velocity[1,2]	0.26 - 0.57 ms^{-1} at T_∞,p ($\approx$ 1.2 - 2.8 u_{mf})
Fluidized bed temperature[1]	490 - 590 °C
Duration	120 - 1740 s

Note:

1. Averaged over an experimental run.

2. The u_0 used herein were generally below those suggested by Chandran and Chen (1986, *Encyclopedia of Fluid Mechanics*, Vol.4, Ch.30, p994, Gulf Publishing) for fluidized beds with immersed heat transfer tubes. However, to satisfy the aim of this study (Chapter 1), a range of conditions - from pro-deposition to pro-erosion - was traversed. For the current bed material, this meant that most experiments were conducted below the superficial velocities recommended by Chandran and Chen.

5.3 INPUTS TO THE MODEL

To compare the experimental data with a dynamic simulation of the system based on the coating-erosion model, it is necessary to assign correct values to the *input variables* used by the model. These inputs include the thermal and physical property information needed to evaluate all of the independent variables appearing in Section 4.2. The main experimental variables are considered separately from the other information.

5.3.1 Principal Experimental Variables

The power supplied to the immersed body, the superficial gas velocity and the bed temperature were measured as a group at reasonably regular intervals throughout each experimental run. Because of the experimental set-up, it was difficult to maintain these variables at fixed values - they tended to deviate (sometimes strongly) as a run progressed. Instead of using time-averaged values, it was decided to employ piece-wise linear histories of these variables as the inputs to the simulation program. Figure 5.1 is a plot of the heater power, bed temperature and gas velocity with time for a typical experiment. The principal variables are now discussed briefly in turn:

Power supplied to the immersed body, $Q_{b\ ext}$:

The power remained reasonably constant - in most experiments it did not vary by more than ±2% from the beginning of a run to the end. The greatest deviation was -3.4% in experiment 21.

Temperature of the fluidized bed, T_∞:

Consistent with the practice of Chapter 3, the temperature of the fluidized bed at any time was assumed to be the average of the TC2, TC3 and TC4 readings. Sometimes, the fluidized bed's temperature was quite uniform (within a few degrees), but often, there were significant temperature gradients in the lower portion of the bed between TC2 and

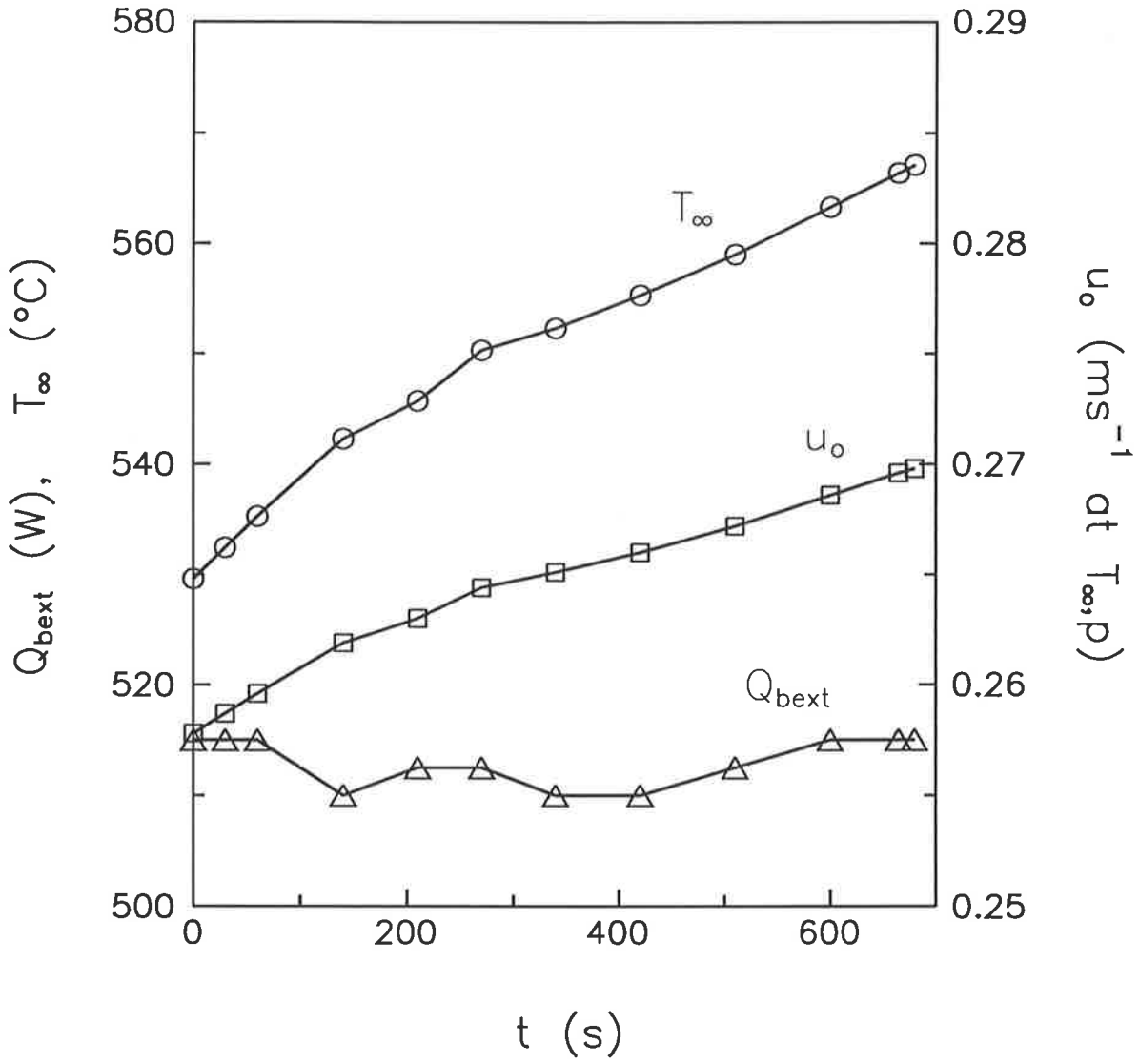

Figure 5.1: Variation of the power supplied to the immersed body ($Q_{b\,ext}$), temperature of the fluidized bed (T_∞) and superficial gas velocity (u_o) with time for a typical coating-erosion experiment (number 34).

TC3. At the beginning of an experiment, the gradients were small, but, with time, the agreement worsened. At the end of experiments 9 and 10, which experienced the greatest temperature gradients, TC3 was approximately 65 °C hotter than TC2. Over all the experiments, the mean disparity at the end of a run was about 30 °C.† In all cases, the differences between TC3 and TC4 were insignificant by comparison.

During an experiment, T_∞ tended to rise almost linearly with time. The rate of rise ranged from about 2 to 11 °C/minute, depending upon the experimental conditions. A low fluidizing velocity combined with a high heater power caused the most rapid increases. The average rate was about 5 °C/minute. So, for the purposes of data entry into the simulation program, the fluidized bed's temperature was averaged spatially, but permitted to vary with time. Of course, ideally, T_∞ should have been uniform and constant in each experiment.

Superficial gas velocity, u_o:

The superficial gas velocity generally mirrored the temperature of the fluidized bed - and so, it increased in an approximately linear manner with time. This was expected, as the mass flowrate of the air entering the apparatus was nearly constant and the density of the gas is proportional to its absolute temperature. The gas velocity increased from between 0.001 to 0.004 (ms^{-1} at T_∞,p)/minute in line with T_∞.

Duration of the experiment, t_{end}:

An experiment was continued until either a desired time had elapsed or the U-tube heater had reached its high temperature operating limit of about 750 °C.

In addition, the initial temperature of the immersed body, T_{bo}, is a key parameter of the model, but it was not varied explicitly in the experimental study. In all the experiments, the body and the fluidized bed were very nearly in thermal equilibrium before the power was supplied to the body, so, $T_{bo} = T_\infty|_{t=0}$ within a few degrees.

† While calculations based on TC2 and equation (3.2) reveal that the whole bed remained fluidized in all experiments, the large temperature differences suggest poor quality fluidization. Note the use of temperature probes to detect high-temperature defluidization (Siegell 1976, p35; Lau and Whalley 1981, *Fuel Proc. Tech.* **4**(2+3), p101-115; Atakül and Ekìncí 1989, *J. Inst. Energy* **LXII**(450), p56-61 & 1990, *Powder Technol.* **60**(2), p77-82; Dawson and Brown 1992, *Fuel* **71**(5), p585-592).

5.3.2 Other Model Inputs

These may be classified into five groups - those dealing with: the immersed body, the coating that forms on the body, estimation of the potential erosion rate, the quantities determined in the preliminary experiments of Chapter 3, and finally, the sintering temperature.

Properties of the immersed body:

Forming this category are: the mass of the immersed body, m_b, its specific heat capacity, c_{pb}, and the body's radius and length, r_b and L, respectively. (Note that, for the purposes of modelling as outlined in Section 4.2, the immersed body is assumed to be cylindrical.) The mass of the immersed body was assumed to be the mass of the heated zone (see Section 3.2.1) which was estimated by:

$$\begin{pmatrix}\text{mass of}\\ \text{heated zone}\end{pmatrix} = \begin{pmatrix}\text{mass of U}-\\ \text{tube heater}\end{pmatrix} \times \frac{(\text{length of heated zone along tube axis})}{(\text{length of U}-\text{tube along tube axis})} \qquad (5.1)$$

Its specific heat capacity was calculated as the mass-fraction-weighted-average of the specific heat capacities of the Incoloy 800 tube and the MgO insulation that form the bulk of the heater (the existence of the resistance wire was ignored in this calculation). Literature values for the individual c_ps were used: $c_{p\ \text{Incoloy 800}} \approx 500\ \text{Jkg}^{-1}\text{K}^{-1}$ at room temperature and $c_{p\ \text{MgO}} \approx 1280\ \text{Jkg}^{-1}\text{K}^{-1}$ over the range 20 - 750 °C. The mass fraction of the metal tube was about 0.24. The radius and the length of the body were deduced from measurements made in Chapter 3 and by the following expressions:

$$r_b = d_h / 2 \qquad (5.2)$$

$$L = 2.L_h - d_h + (\pi/2 - 1).D_h. \qquad (5.3)$$

Properties of the coating:

The density (ρ), specific heat capacity (c_p) and thermal conductivity (k) of the coating need to be known. The coating forms when particles heat up, become sticky, and adhere to the surface of the immersed body. The layer grows as further particles stick onto those already there. Now, if the particles do not melt completely on deposition, but only lightly sinter, the coating will be at least partly porous. This porosity must be taken into account in the determination of the physical and thermal properties of the coating mentioned above.

It is a simple matter to relate the bulk density and specific heat capacity of a porous medium to the properties of the solid and fluid that comprise it:

$$\rho = \varepsilon.\rho_f + (1-\varepsilon).\rho_s \tag{5.4}$$

$$c_p = \frac{\varepsilon.\rho_f.c_{pf} + (1-\varepsilon).\rho_s.c_{ps}}{\varepsilon.\rho_f + (1-\varepsilon).\rho_s} \tag{5.5}$$

In the present system, $\rho_s >> \rho_f$, so, the above expressions are well approximated as:

$$\rho = (1-\varepsilon).\rho_s \tag{5.6}$$

$$c_p = c_{ps} \tag{5.7}$$

Calculation of the effective thermal conductivity of a porous medium with a motionless fluid, however, is more complex. Xavier and Davidson (1985) cite several experimental and theoretical studies. The correlation of Gelperin et al. (Gelperin and Einstein, 1971, p487-488):

$$\frac{k}{k_f} = 1 + \frac{(1-\varepsilon)(1-[k_f/k_s])}{[k_f/k_s] + 0.28\,\varepsilon^{0.63[k_f/k_s]^{-0.18}}} \tag{5.8}$$

was used in this thesis, partly because it has the correct asymptotic limits of $k \rightarrow k_s$ as $\varepsilon \rightarrow 0$ and $k \rightarrow k_f$ as $\varepsilon \rightarrow 1$. Figure 5.2 displays the effect of the porosity on the properties of the coating layer at 700 °C. The values of ρ_f, c_{pf}, c_{ps}, k_f and k_s were obtained from the literature; ρ_s was measured by the author. Clearly, ρ and k vary significantly with ε over the range $0 \leq \varepsilon \leq 0.42$ (the upper limit corresponds to the approximate porosity of a randomly-packed bed of equally-sized spheres). Now, what porosity should be used in the above equations to make the experiment / theory comparison?

Although there are good reasons to expect that the porosity of the coating should change with time and position in the layer, it was decided to use a constant value of $\varepsilon = 0.21$ for all of the experiments in the present study. The reason behind this choice and a discussion of the model modifications needed to allow properly for variable-porosity behaviour may be found in Appendix H.

Potential erosion rate:

Calculation of the potential one-dimensional erosion rate experienced by the immersed body ($\mathcal{R}_e$) requires the averaging of the local erosion rate over the heated surface of the U-tube. This procedure is discussed in Appendix C. The correlation of Zhu et al. (1991), equation (2.14), was used to estimate the local erosion rate of a horizontal tube. For a tube inclined at an angle of θ radians to the horizontal, regression of the data of Nieh et al. (1991) suggests that the local erosion rate is $(1 - 0.354\ \theta)$ times the local erosion rate of a horizontal tube in the same position ($0 \leq \theta \leq \pi/2$). The models of Darton et al. (1977) and Agarwal (1985) were used to calculate, respectively, the bubble diameter and point frequency, which are required by equation (2.14). Also needed is an empirical constant, k_e (= k_{ZR}), which depends on the physical properties of the particles and the target surface of the particular eroding system. The assignment of a value to k_e is discussed briefly in Section 5.4.

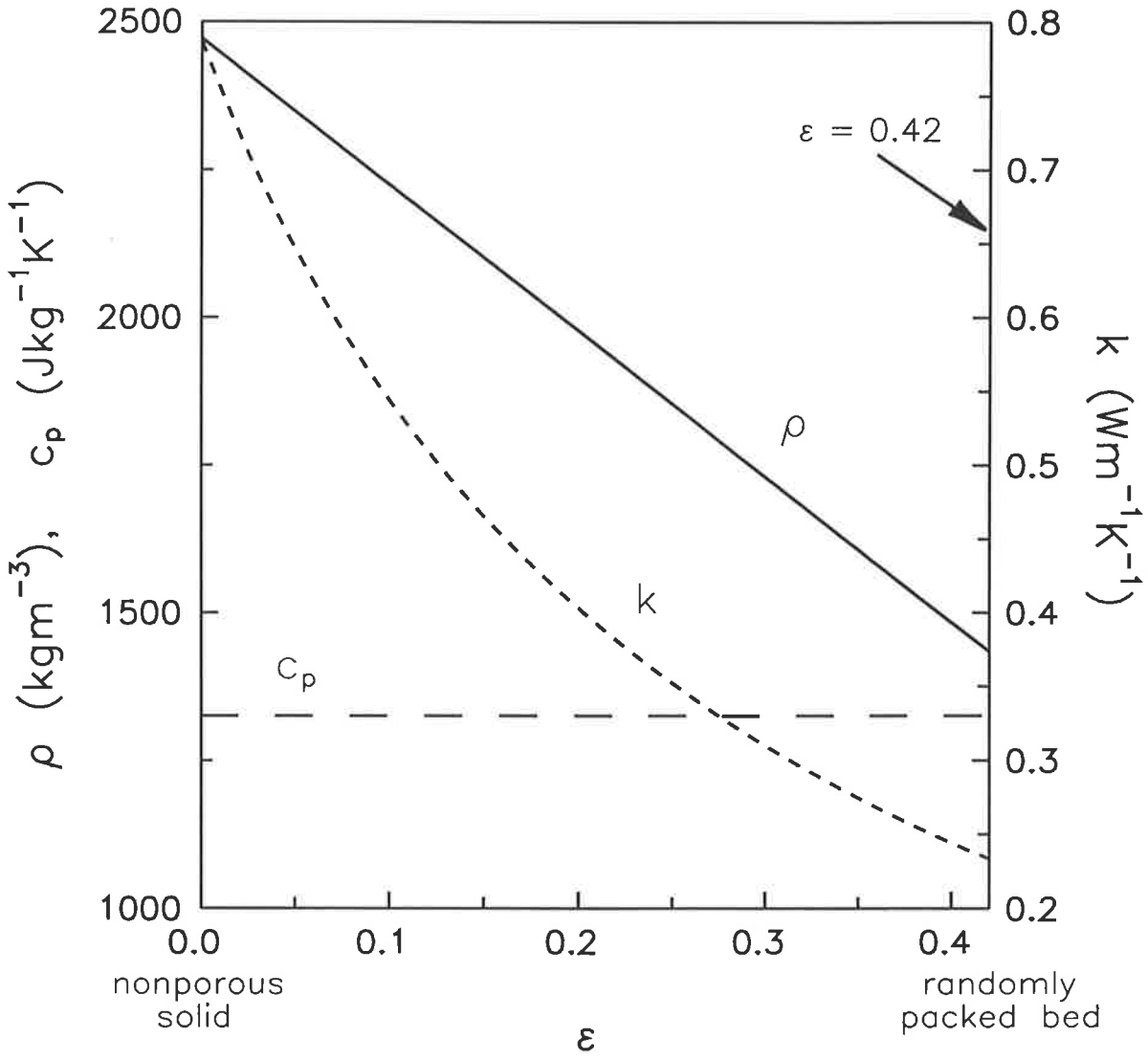

Figure 5.2: Effect of porosity on the density, specific heat capacity and thermal conductivity of a packed bed of glass ballotini at 700 °C as calculated by equations (5.4), (5.5) and (5.8), respectively.

Quantities determined in the preliminary experiments:

Values for the effective melting temperature of the glass ballotini, T_m, the minimum fluidization velocity, u_{mf}, and the immersed body-to-bed heat transfer coefficient, h, were obtained from the author's own preliminary experiments (Chapter 3).

Sintering temperature:

The sintering temperature (T_s) of the particles in a particular environment is *a priori* unknown. T_s had to be determined by regression of the experimental data as discussed in Section 5.4.

The values of all the input variables of the coating-erosion model and their sources are listed in Table 5.2.

5.4 Experimental Results and Model Comparison

Experimental Results:

The experimental results comprise the temperature history of the immersed body, and the mass and geometry of the coating layer at the end of the experiment. Data from a typical experiment are shown in Figures 5.3 and 5.4. Appendix G contains the complete set of results.

Method of Comparison:

Given the input variables (Section 5.3) and the various calculational parameters (such as the number of nodes in the coating and error tolerances), the simulation program **CEMODEL** can predict the temperature of the immersed body and the coating mass as functions of time. Unfortunately, a key input variable, the sintering temperature, T_s, is unknown. T_s is expected to vary with the system's operating parameters, but in an as-yet unquantified manner. For the purposes of comparison, T_s was used as an adjustable parameter, different but constant for each experiment, which was varied so that the

Table 5.2: Summary of the input variables of the coating-erosion model.

Input Variable	Value / Equation and Source
c_p	Equation (5.5)
c_{pb}	1094 $Jkg^{-1}K^{-1}$; calculated from data in Liley et al. (1985, p3-16, p3-132) and Smithells and Brandes (1976)
c_{pf}	Coulson et al. (1989, p765)
c_{ps}	Equation (24) of Sharp and Ginther (1951) for code 0080 glass
d_h	Equation (10) of Darton et al. (1977)
d_h	0.0107 m; measured
d_{holes}	0.4 $x10^{-3}$ m; specified
d_p	645 $x10^{-6}$ m; measured
D_{bed}	0.1027 m; measured
D_h	0.0504 m; measured
h	Equation (3.10); measured - see Section 3.5.3
k	Equation (5.8)
k_e	0 for experiment 9; see Section 5.4
k_f	Ried et al. (1987)
k_s	0.787 $Wm^{-1}K^{-1}$; Liley et al. (1985, p3-260)
L	0.226 m; equation (5.3)
L_h	0.104 m; measured
m_h	0.0948 kg; measurements + equation (5.1)
n_{holes}	121; counted
$Q_{h\,ext}$	Piece-wise linear history from experimental data
r_h	5.36 $x10^{-3}$ m; equation (5.2)
t_{end}	Experimental data
T_{ho}	Initial experimental T_h data point
T_m	625 °C; measured - see Section 3.5.1
T_s	To be determined by regression - see Section 5.4
T_∞	Piece-wise linear history from experimental data
u_{mf}	Equation (3.2); measured - see Section 3.5.2
u_o	Piece-wise linear history from experimental data
z_h	0.0505 m; measured
ε	0.21; see Appendix H
ρ	Equation (5.4)
ρ_f	Ideal gas law
ρ_s, ρ_p	2472 kgm^{-3}; measured
ψ	$\approx$ 1.0; estimated

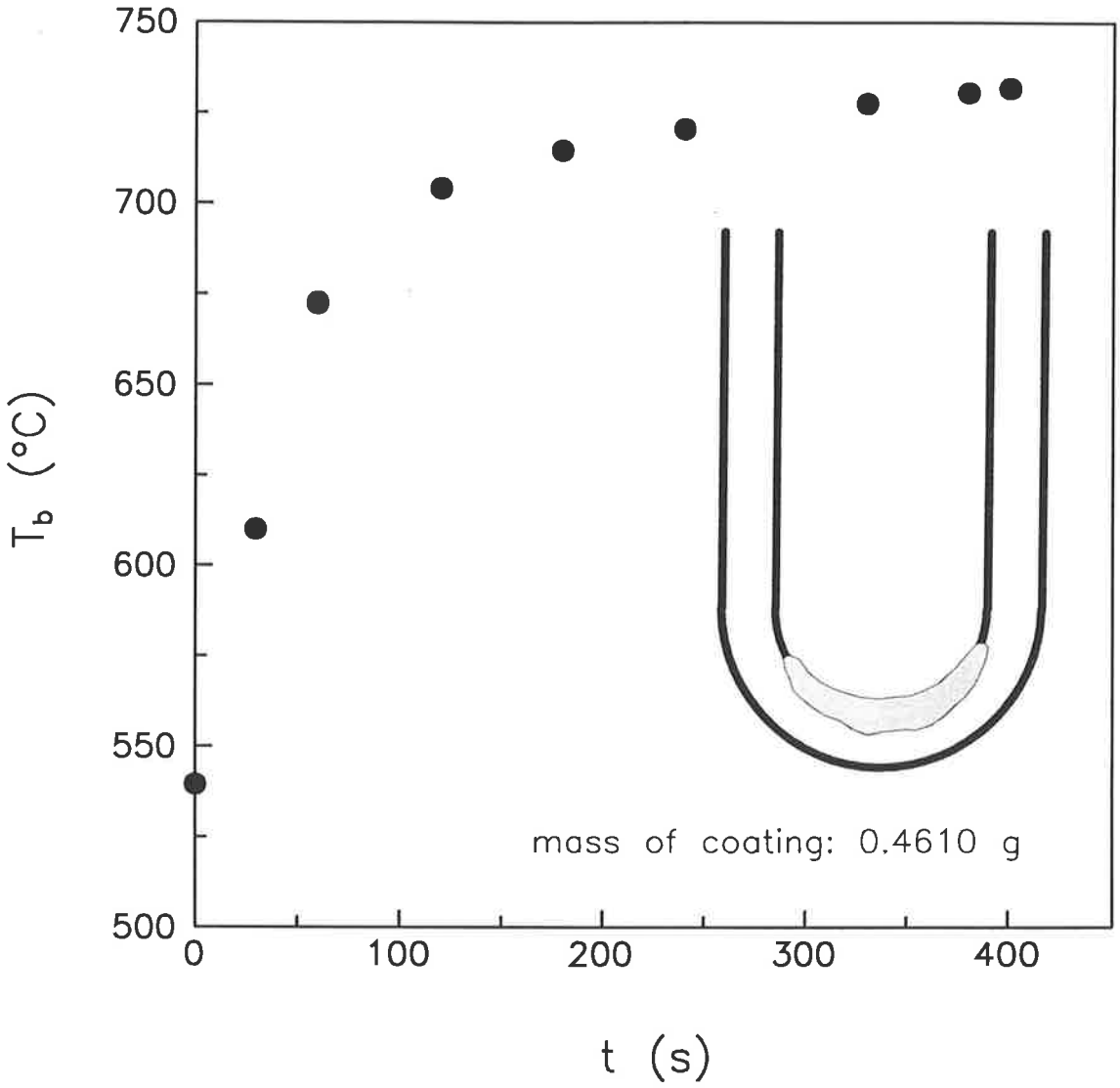

Figure 5.3: Data from experiment 7.

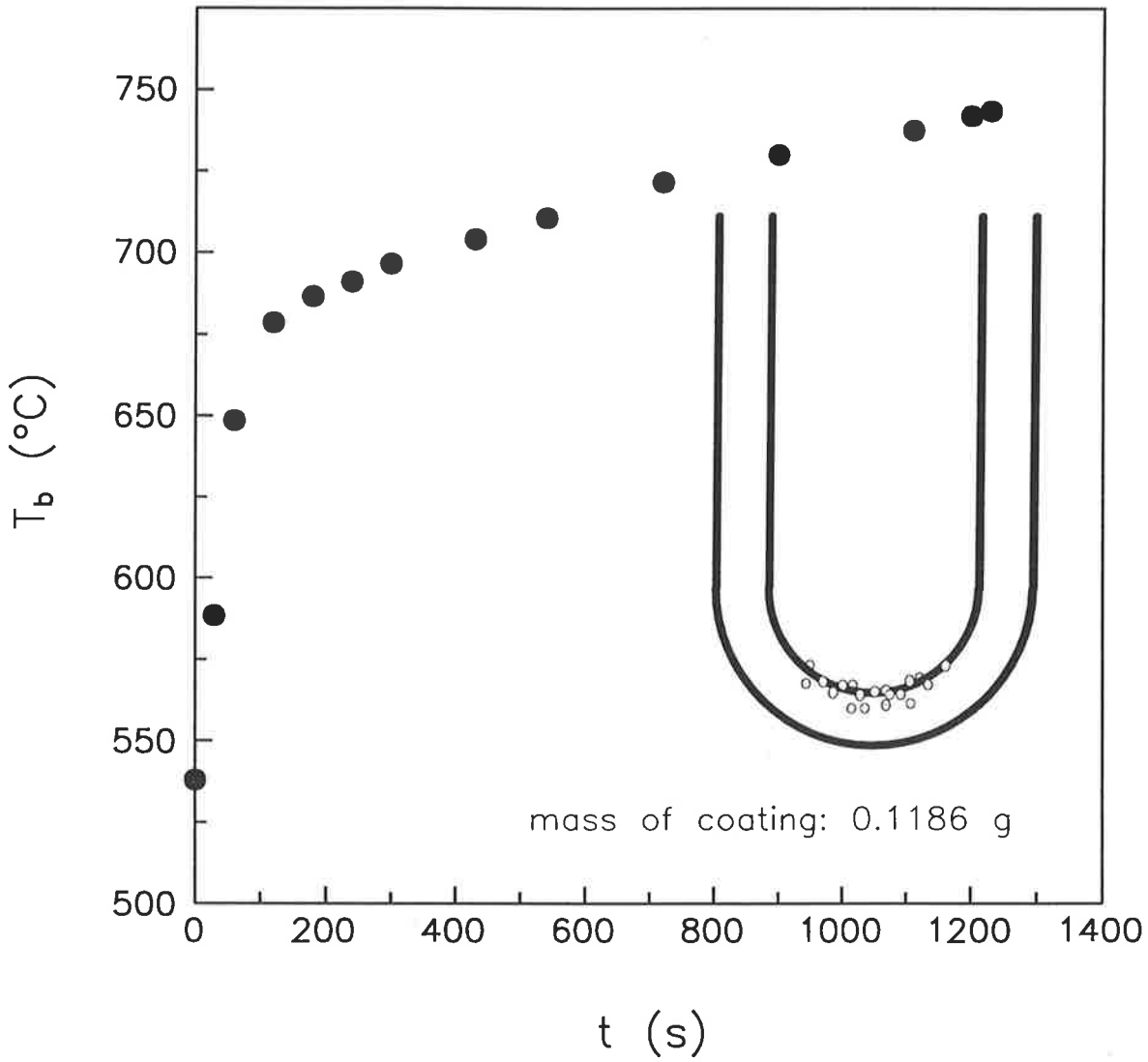

Figure 5.4: Data from experiment 13.

experimental and simulated masses of coating at the end of an experiment were equal. (A batch version of **CEMODEL** incorporating an automatic routine to perform the data fitting was written.) Through the appropriate choice of T_s, the experimental and predicted masses could always be made to agree exactly. The predicted and experimental temperature histories of the immersed body were then compared.

An additional adjustable parameter is k_e, the erosion rate constant. It is only important if a coating has formed on the immersed body, and then there is a change in the operating conditions so that the potential coating rate falls below the potential erosion rate, causing net erosion of the layer. This situation arose in only one experiment, number 9, which had the smallest mass of coating, less than 0.01 g. For simplicity, k_e was set to zero (meaning no erosion) and T_s was determined as normal. The T_s value obtained in experiment 9 must be treated with extra caution. A far better approach would be to determine k_e from a series of separate erosion-only experiments, similar to those in Zhu et al. (1991). This is a possible area for future research. Zhu et al. (1991) found that k_e increases with decreasing Young's modulus of the target and increasing hardness of the particles. In the present situation, it is important to consider the effect of temperature on these material properties.

In summary, although **CEMODEL** is a fully predictive simulation program, a key input variable, T_s, is unknown. The experimental and predicted coating masses were made to agree through parameter fitting with T_s for each experiment. On this basis, a comparison was made of the simulated and experimental temperature histories of the immersed body.

5.4.1 Body Temperature and Coating Mass

Results:

In all the experiments, the immersed body is initially at the temperature of the fluidized bed. When the power is supplied to the body, T_b rises rapidly - through 150 - 200 °C in

100 - 150 s. A reasonably sudden transition follows, after which the body's temperature increases at a much slower rate. The rates in the fast and slow rise periods depend on the operating parameters (such as the power and the superficial gas velocity).

The mass of coating that formed on the immersed body ranged from 0.01 to 3.70 g, again depending on the experimental conditions.

Comparison:

For each experiment, the predicted temperature history of the immersed body and the experimental data are plotted together in Appendix G. Figures 5.5 and 5.6 are two of these comparative plots which have typical features.

Initial Rise: For all of the experiments, the simulation program overpredicts T_b in the initial part of the immersed body's response - that is, it expects the temperature to rise too rapidly. The most likely cause of this error is the underestimation of the specific heat capacity of the immersed body and the mass of the heated zone. Neither of these quantities was measured directly. Better agreement could be obtained if an effective value of $(m_b.c_{pb})$ were determined through fitting the experimental and predicted T_b-histories in the initial rise period. This approach has some legitimacy since the extent of the heated zone of the present experimental apparatus is not well defined - there is some conduction up the legs of the U-tube heater. If another immersed body, more effectively insulated against conduction, were constructed, these ambiguities could be avoided.

The rapid initial response of the immersed body is caused by a temporary, large difference in the amount of energy entering and leaving the body. Energy enters at a rate of $Q_{b\,ext} > 0$ Watts and leaves at $hA(T_b-T_\infty)$ Watts - the difference is accumulated in the body, causing T_b to rise. As T_b increases, the rate of energy dissipation increases, and so, the response slows.

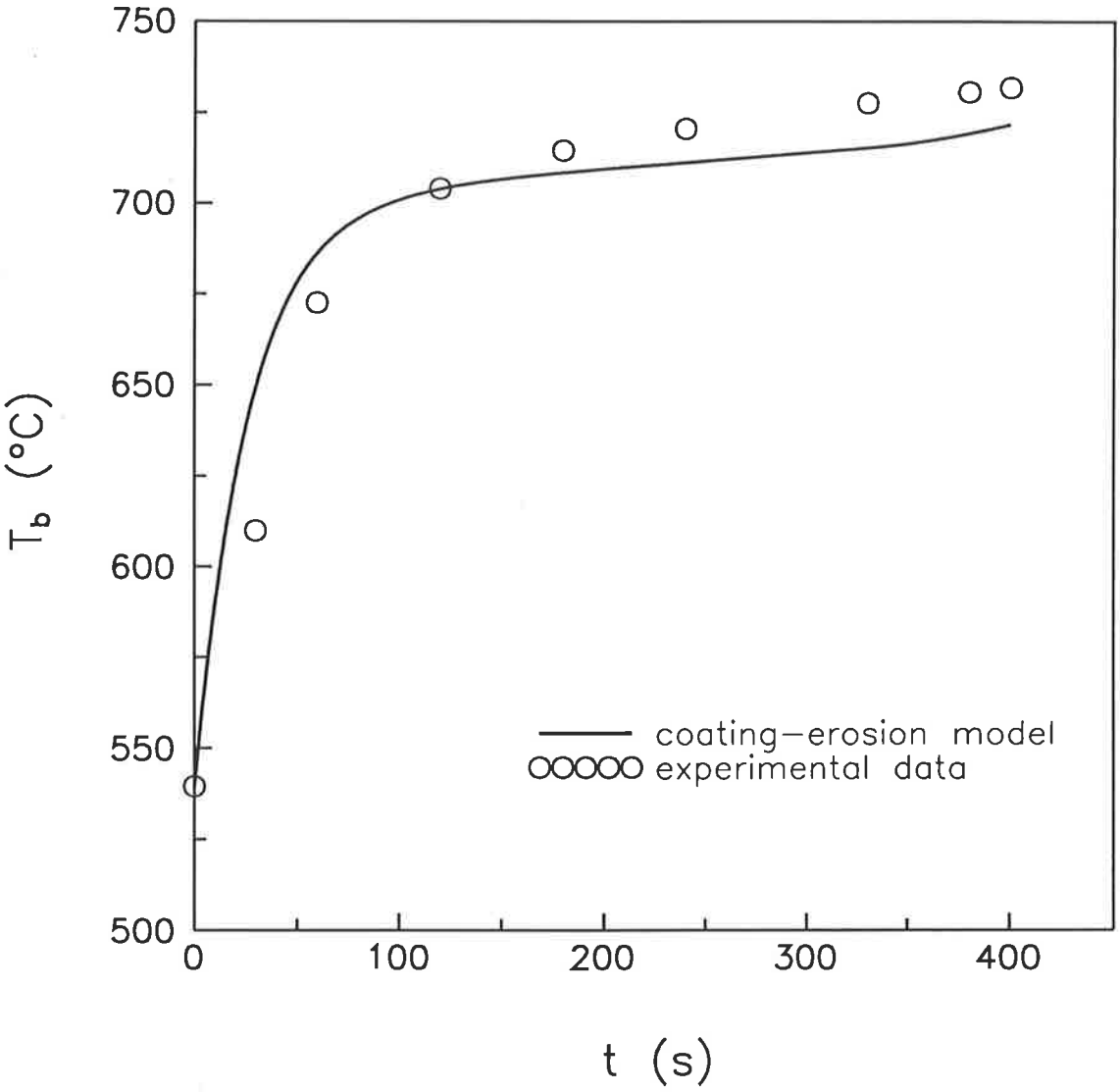

Figure 5.5: Comparison of the predicted and experimental temperature histories of the immersed body for experiment 7.

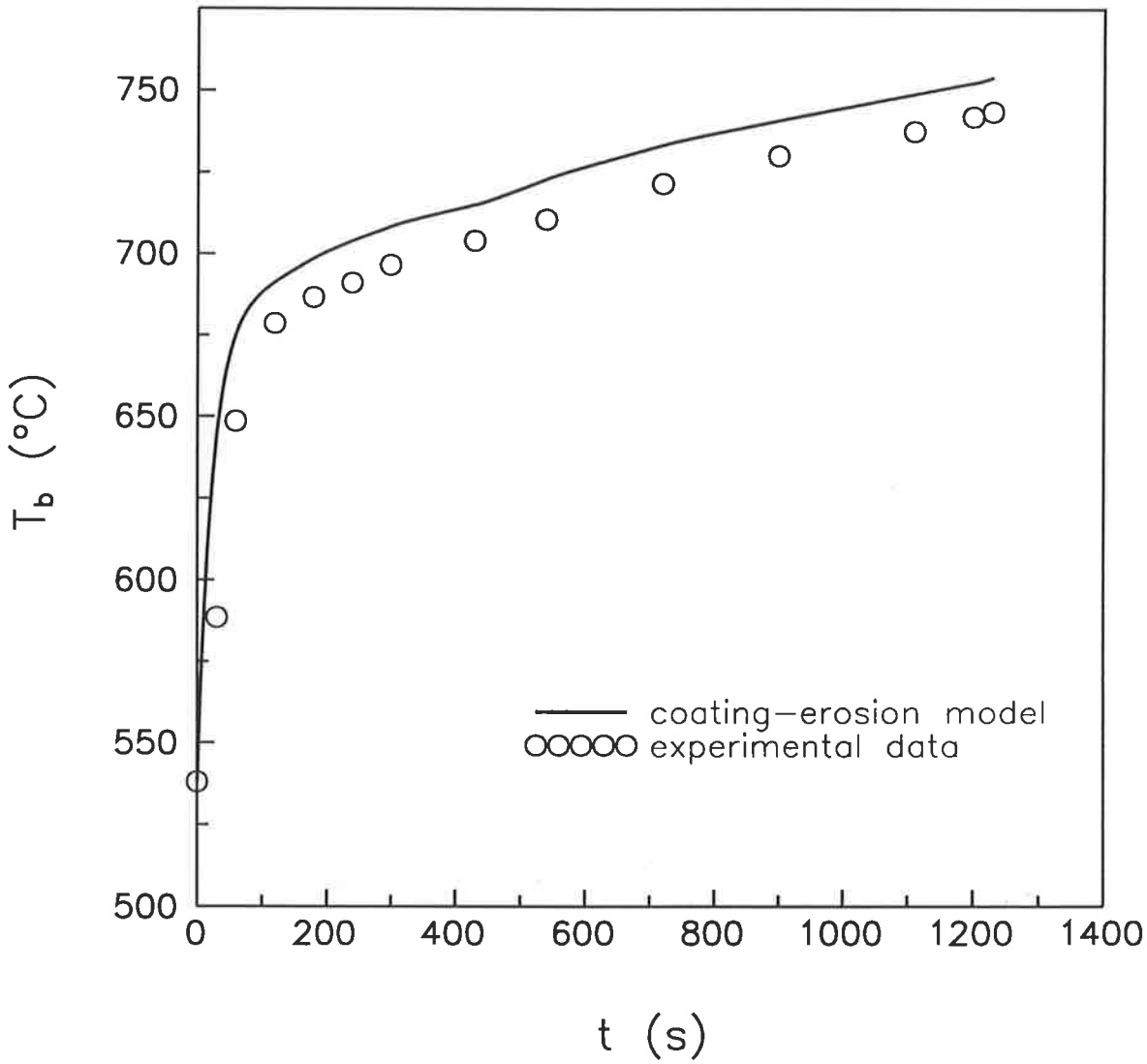

Figure 5.6: Comparison of the predicted and experimental temperature histories of the immersed body for experiment 13.

Transition: After the initial rise, the predicted temperature history undergoes a fairly sudden transition - in good agreement with the experimental data. The transition marks the point where a close balance between the body's energy input and output has been achieved.

Long-Time Behaviour: In agreement with the experimental data, the body temperature rises more slowly and almost linearly with time after the transition. In some experiments, the simulation consistently overpredicted the long-time temperature of the immersed body; in others T_b was consistently underpredicted. Overestimation occurred about twice as often as underestimation in the present study. The slow rise of T_b with time that was experienced in the experiments is partly due to the increasing bed temperature. As T_∞ rises, the rate of energy dissipation from the body falls, so the body heats up until the energy input and output balance at some new, higher T_b.

Most of the predicted T_b versus time plots are not perfectly smooth, but have small "bumps" in them. Fluctuations in the experimental input variables - T_∞, u_o and $Q_{b\,ext}$ (see Figure 5.1, for example) - were carried through the simulation program's calculations, causing the bumps seen in the predicted T_b history plots.

Of much greater significance is the onset of coating formation as predicted by the simulation using the "best fit" values of the sintering temperature for each experiment. According to the model, when the immersed body exceeds T_s, particles will begin to deposit permanently on the surface. The point is marked by an increase in the rate of change of the simulated temperature of the body. In most experiments, the formation of a coating layer is predicted to occur very near the end of the run. In experiment 7 (see Figure 5.5), for example, T_s was found to be 715 °C - a temperature predicted to be reached after 328 s of operation, 82% of the duration of the experiment. For experiment 13 (Figure 5.6), T_s = 752 °C was obtained nearly 98% of the way through the run. (The T_s values for all of the experiments appear in Appendix G.) Thus, it appears that, under

the present range of experimental conditions, the system is just on the verge of the "coating formation" regime. Most of the time, the model suggests, the immersed body looses heat solely by direct convection to the fluidized bed. The high temperature operating limit of the U-tube heater prevented experiments of longer duration.

Effect of Porosity:

Section 5.3.2 described how the properties of a porous medium (ρ, c_p and k) are influenced by the medium's porosity. It is not immediately clear from the parametric study of Section 4.4 how the immersed body's temperature history and mass of coating are affected by the voidage of the coating layer. Figure 5.7a is a plot of the body temperature versus time for three values of the coating porosity under typical conditions. The corresponding information on the mass of the coating appears in Figure 5.7b.

As the porosity of the coating is increased:

- the temperature of the immersed body rises;
- the mass of the coating layer decreases;
- the system responds more slowly.

Note that the thickness of the coating layer is unaffected by ε. In the current example, changing the porosity from 0 to 0.42 causes the steady state temperature of the immersed body to increase by over 100 °C. The corresponding mass of the coating falls by about 40%.

Consequently, if it is important that the immersed body remain cool, a solid rather than porous coating is preferred. Alternatively, if deposits on the body are not wanted, a porous coating is better as it has a lower mass than a solid one and is mechanically weaker, making it easier to clean off. Finally, with time and high temperatures, sintering

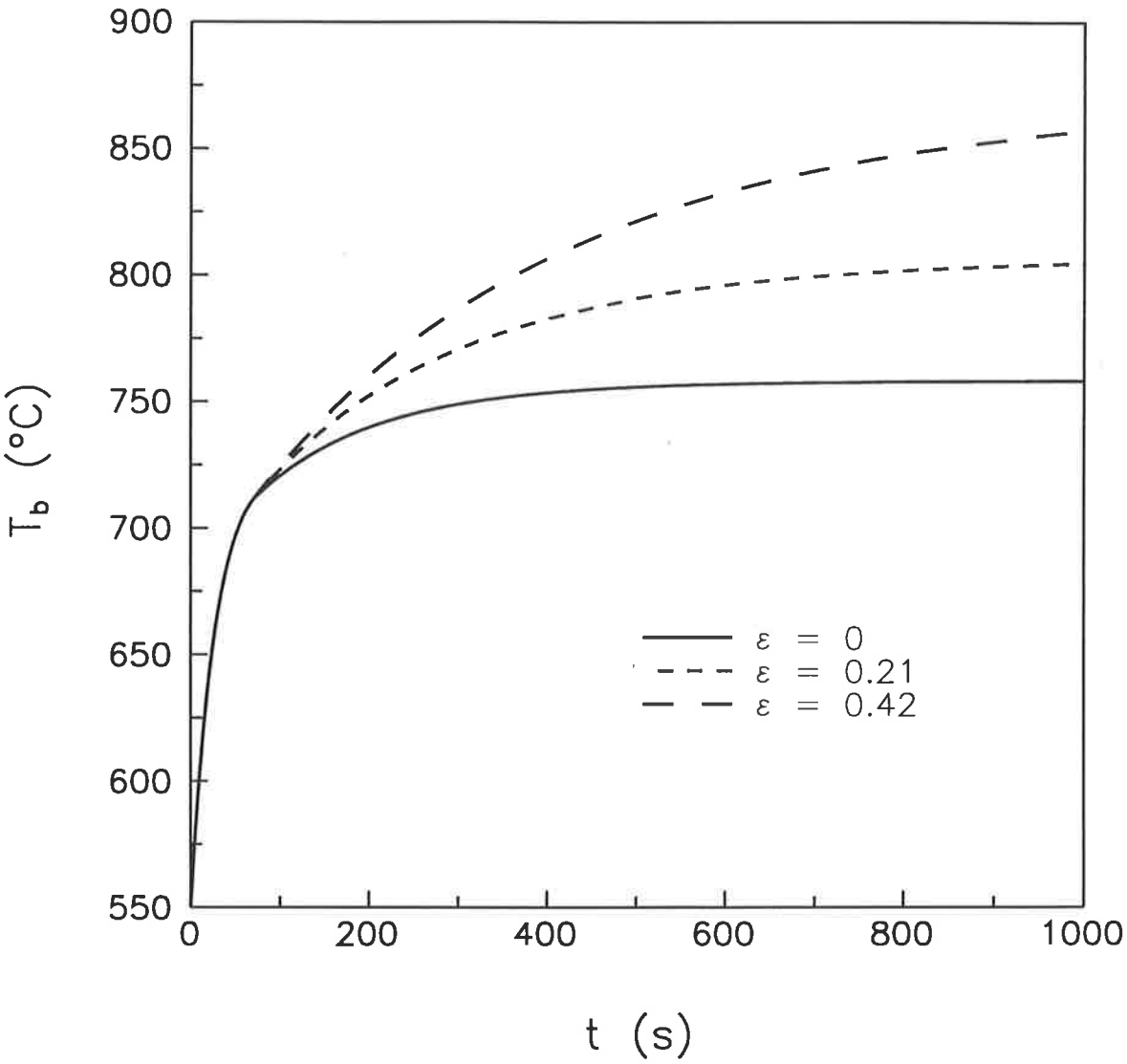

Figure 5.7a: Effect of the porosity of the coating layer on the temperature history of the immersed body ($Q_{b\,ext}$ = 650 W, u_o = 0.28 ms^{-1}, T_∞ = 550 °C, T_s = 711 °C).

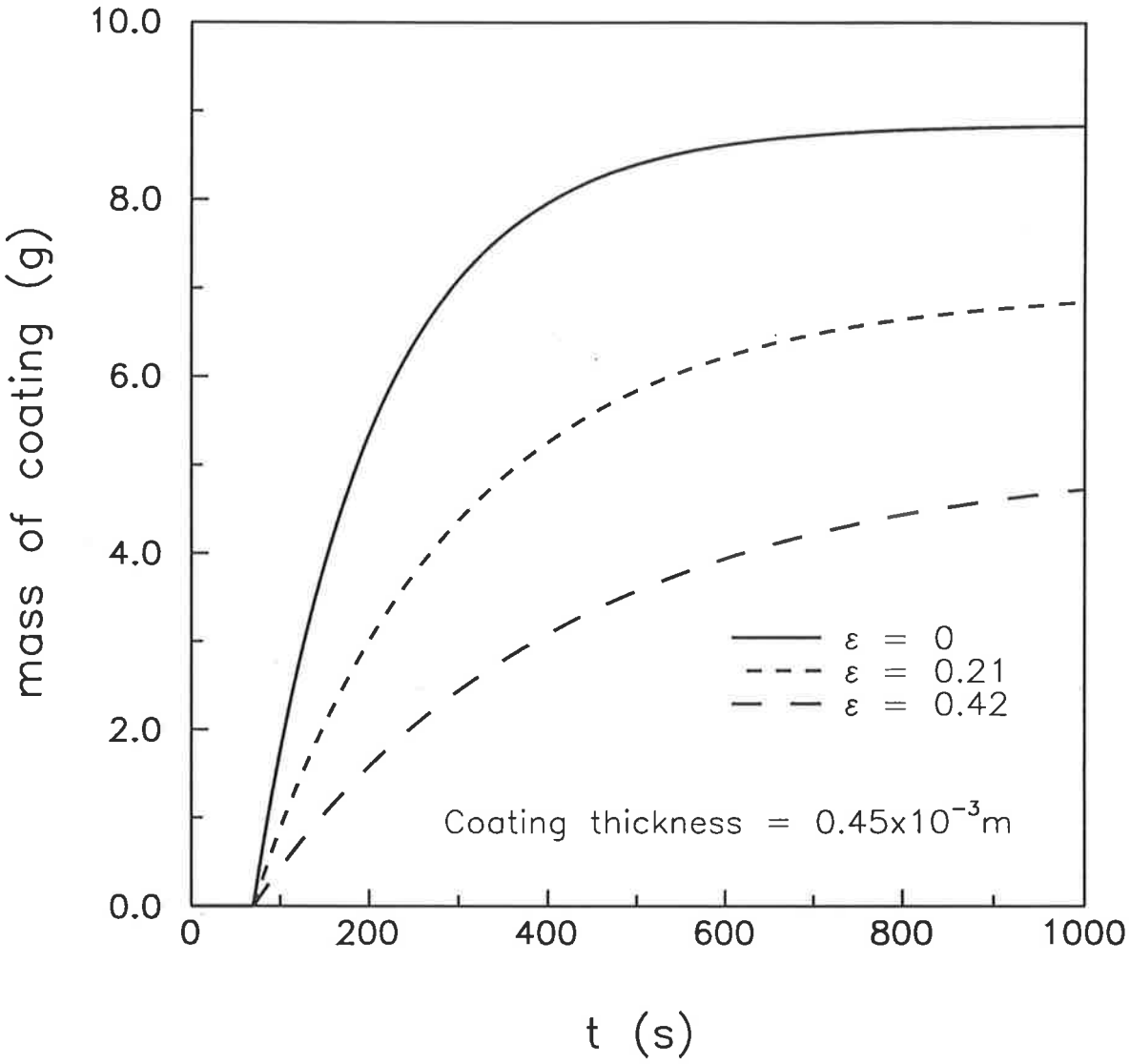

Figure 5.7b: Effect of the porosity of the coating layer on the history of the mass of the coating ($Q_{b\,ext}$ = 650 W, u_o = 0.28 ms^{-1}, T_∞ = 550 °C, T_s = 711 °C).

will continue inside a porous coating layer, causing its voidage to fall. Thus, real, variable-porosity systems are expected to approach non-porous behaviour at long times.

5.4.2 Spatial Distribution of the Coating

The coating-erosion model assumes that a coating layer forms evenly over the surface of a cylindrical immersed body. In the current experiments, however, a U-shaped immersed body was used and the deposits that appeared were not uniform. Figure 5.8 shows the approximate shape of two deposits that were obtained in the experimental study. Figure 5.9 is a photograph of a fragment of the coating that formed on top of the bend of the U-tube heater in experiment 22. (Appendix G contains the spatial distribution information for all of the experiments.)

The deposit shown in Figure 5.8a is typical of many in the experiments - a patch located on the top of the bend of the U-tube. As the mass of the coating increases, the deposit tends to become thicker and to spread over more of the bend. In experiments with a large mass of coating, the deposit covers the bend and continues up the leg of the heater that has the hotspot (Figure 5.8b). The coating on the leg may extend up to around 80 mm above the bottom of the U-tube. At a given height on the U-tube leg, the coating can be quite uniform in thickness about the tube's perimeter.

The experimentally observed spatial distribution of the coating cannot be explained by the current, one-dimensional theory. A three-dimensional formulation is necessary, and this needs *local* (rather than spatially averaged) information about the immersed body / fluidized bed system. It is thought that the heat flux, heat transfer coefficient and sintering temperature are the key variables that determine the coating's spatial distribution. The present (one-dimensional) theory indicates that the local rate of mass deposition should increase with increasing local heat flux from the immersed body and decrease with increasing local heat transfer coefficient and sintering temperature. The

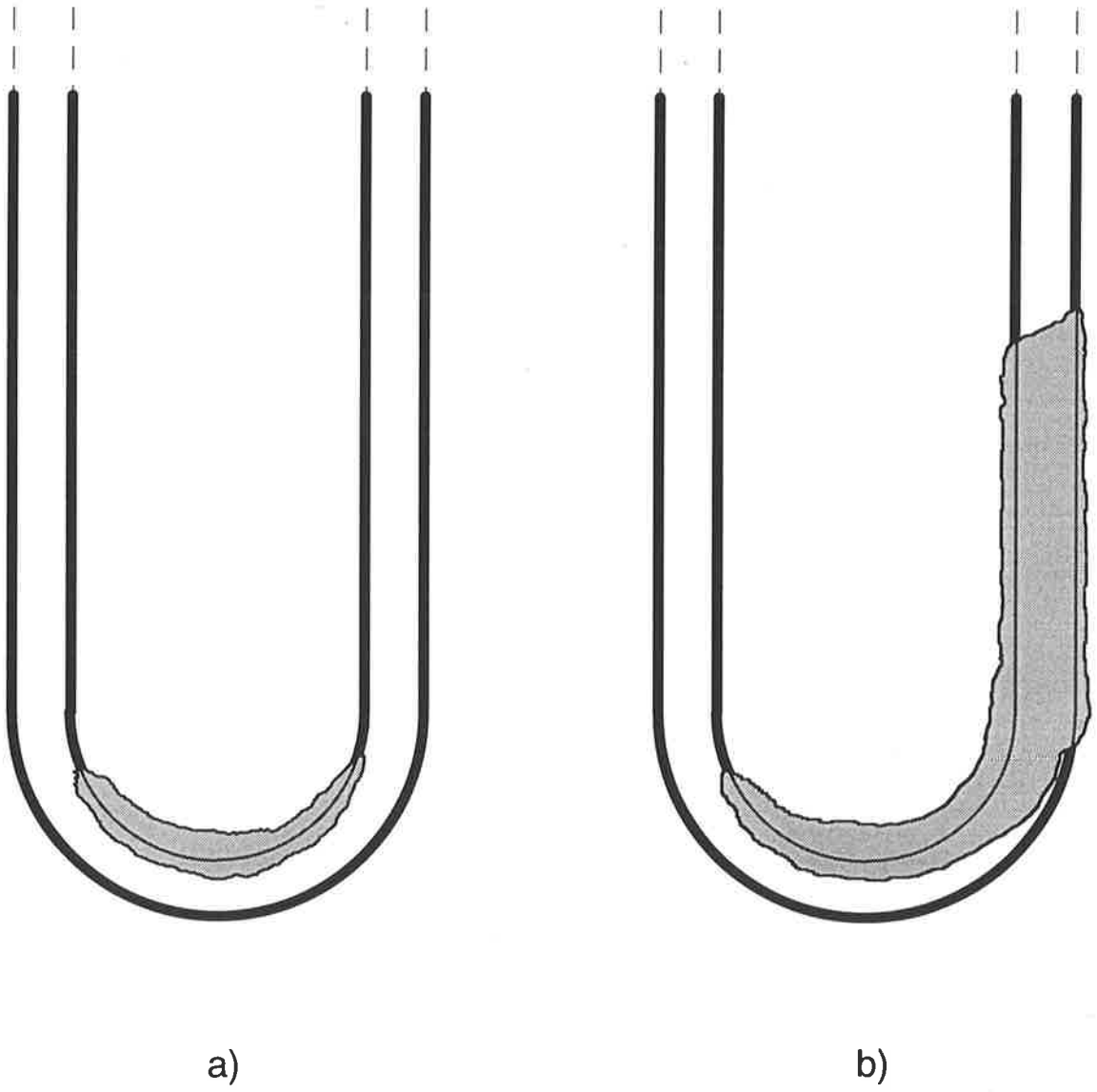

Figure 5.8: Sketch of two deposits that formed on the U-tube heater - a) experiment 34, b) experiment 35.

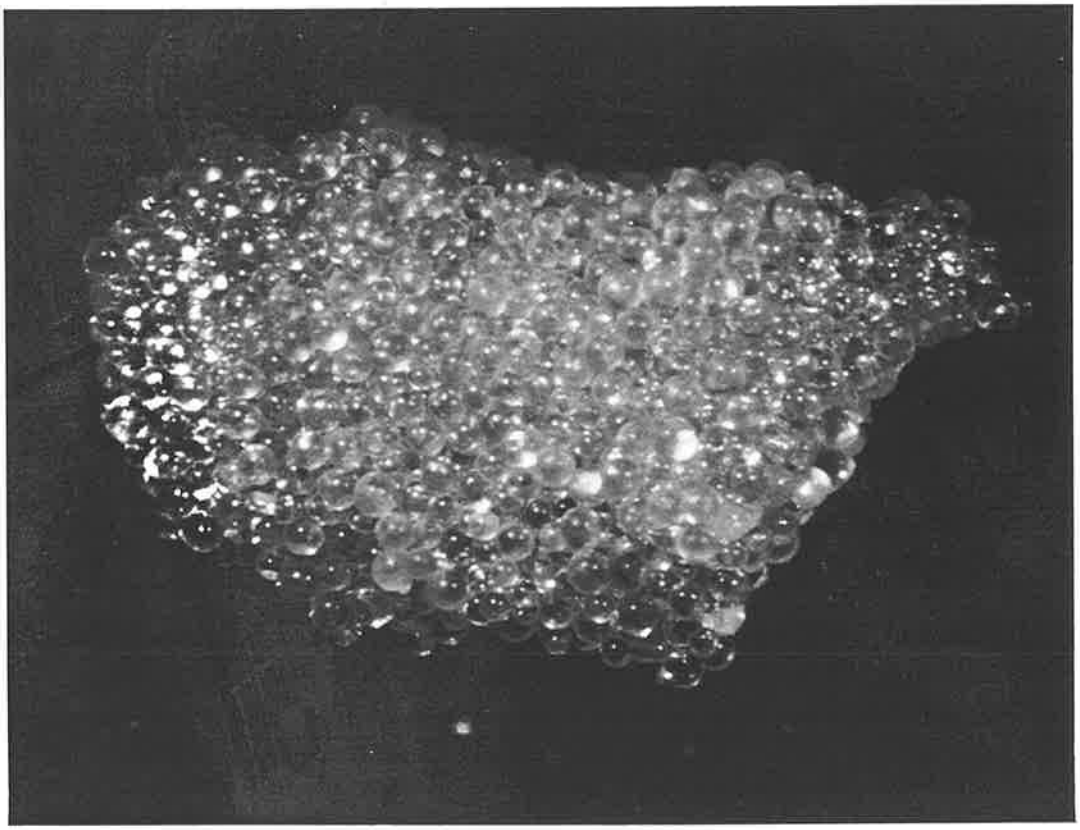

[Magnification: 11 times]

Figure 5.9: Photograph of a fragment of the coating that formed on the top of the bend of the U-tube heater in experiment 22.

local sintering temperature is expected to be strongly dependent on the local potential erosion rate. Hence consideration of the local heat transfer coefficient, potential erosion rate and heat flux in the light of the one-dimensional theory may explain the location of the deposits formed in the experiments.

Local Heat Flux:

The local heat flux of the immersed body used in the current study is proportional to the density of the internal resistance wire coils at a given point. To a first approximation, the heat flux is uniform over the legs of the U-tube, except at the hotspot. There, the heat flux is higher as the resistance wire coils were bunched up during manufacture (Section 3.2.1). Around the bend of the U-tube, the coils may be more closely spaced along the inner part (top) of the tube than on the outer part (bottom of the tube). Hence, the heat flux may be higher on the top of the tube's bend.

The author can find no studies of the local variations in the heat transfer coefficient or potential erosion rate for vertical U-tubes. However, such investigations have been conducted on horizontal, inclined and vertical cylinders. The results of these studies will be summarised, then they will be related to the U-tube case of interest here.

Local Heat Transfer Coefficient - Horizontal Tubes:

Saxena et al. (1978), in a review of several heat transfer studies on horizontal tubes, concluded that:

- at low superficial gas velocities (but above u_{mf}), the local heat transfer coefficient is low directly above and below the tube and reaches a maximum at an angle slightly above the tube's equator;
- as u_o increases, h_{local} increases for all angles; the increase is rapid above the tube and slow around the equator;

- around u_{opt} (the velocity of the maximum in the *average* h - u_o curve), the heat transfer coefficient at the equator and the top of the tube either coincide or differ by less than 25%;
- with further increases in the gas velocity, h_{local} at the top of the tube and the equator either remain the same or gradually decrease. The maximum local heat transfer coefficient occurs at the top of the tube.

These trends are well demonstrated in the study of Noack (1970), whose experimental conditions were similar to the present ones (glass beads fluidized by air, d_p = 600 μm, d_h = 25 mm). The angular distribution of h_{local} becomes more uniform as the diameter of the tube decreases.

All of the above behaviour can be well explained by the motion of the bed particles in the neighbourhood of the immersed tube (Noack, 1970; Saxena et al., 1978; Kurosaki et al., 1988). Although not directly relevant here, Adams (1982) presented a theory for the angular variation of the *bubble phase* local heat transfer coefficient in a two-dimensional fluidized bed.

Local Heat Transfer Coefficient - Inclined Tubes:

According to Gelperin and Einstein (1972, p509-512), as the orientation of a tube is changed from horizontal to vertical, the angular variation of the local heat transfer coefficient about the tube's axis decreases (the local heat transfer coefficient is uniform about the perimeter of a vertical tube).

- At low superficial gas velocities, h_{local} at the bottom of the tube increases rapidly as the inclination angle of the tube increases (that is, as the tube becomes more vertical). The heat transfer coefficient at the sides and top of the tube increases quite slowly.

- At high u_o, the angle of inclination does not significantly affect the heat transfer coefficient on the top or sides of the tube. At the bottom of the tube, h_{local} increases slightly with an increase in the tube's angle of inclination.

Local Heat Transfer Coefficient - Vertical Tubes:

While there is no variation of the local heat transfer coefficient about a vertical tube's perimeter, h_{local} can vary along the tube's length. Two key factors affecting h_{local} for vertical tubes are:

- the fraction of time that the position of interest on the tube is in contact with the bubble phase of the fluidized bed. In part, this fraction depends on the height of the point above the distributor and the geometry of the tube / bed system.
- the distribution of the ages of the packets of emulsion (Mickley and Fairbanks, 1955) that contact the point of interest on the tube. (The age of an emulsion packet is the length of time that it has been in contact with *any part* of the heat transfer surface.) Hence, the age distribution depends on the pattern of solids movement, the shape and size of the heat transfer surface and the position of the point of interest on the surface.

Clearly, the local gas and solid motion determines the local heat transfer behaviour. In turn, the local hydrodynamics depend on the motion of bubbles and emulsion throughout the fluidized bed. Bubbles coalesce with height (Clift and Grace, 1985) and are influenced by immersed tubes (Rowe and Everett, 1972; Hager and Thomson, 1973; Yates et al., 1984; Sitnai and Whitehead, 1985). Solids move around the bed in vortices (several can exist in a bed simultaneously) which may be replaced by vortices of different size and direction with changes in the superficial gas velocity (Lin et al., 1985; Kunii and Levenspiel, 1991, p137-141). There is also a thermal stabilisation zone close to the gas distributor which leads to high values of h that increase with height in the zone (Gelperin et al., 1964). Consequently, the variation of h_{local} along a vertical tube can be quite

complex. For example, refer to the data of Berg et al. (1974) and Ozkaynak and Chen (1980). In their review, Saxena et al. (1978) drew no more general conclusions than the above about the local heat transfer coefficient for a vertical tube.

Deffenbaugh and Green (1987) performed an experimental local transient heat transfer / flow visualisation study on a vertical 50 mm diameter tube in a fluidized bed of 800 μm glass beads. They concluded that the heat transfer process was much more complex than any of the then-extant models allowed. Recently, two fundamental hydrodynamic models for fluidized beds have been extended by the inclusion of energy balances to allow the calculation of local instantaneous heat transfer coefficients experienced by the walls of the bed (Kılkış, 1991; Kuipers et al., 1992).

Tentatively, based on the literature cited above, it is thought that:

- at low u_o (say, $u_o \lesssim 2.5\ u_{mf}$), the local heat transfer coefficient will increase with increasing vertical position on the tube;
- at high u_o ($u_o \gtrsim 2.5\ u_{mf}$), h_{local} will decrease with vertical position;

for a vertical tube / bed system approximating the apparatus used in the experimental work of the present study.

Local Erosion Rate - Horizontal Tubes:

The local erosion rate is high somewhere near the bottom of the tube, decreases around the sides, and is a minimum on the top. Indeed, Zhu et al. (1990) found that more than 95% of the material loss occurs on the bottom half of the tube. The angular position of the maximum local erosion rate has been variously reported as: 40-50° (Zhu et al., 1990), 25° (Liu and Levy, 1991) and 0° (Nieh et al., 1991) displaced from the bottom of the tube. Little data is available on the variation of the angular erosion profile with superficial gas velocity. The results of Nieh et al. (1991) suggest that the local erosion

rate increases for all angles as u_o is increased, but that the rate of increase is significantly higher below the equator than above.

Local Erosion Rate - Inclined Tubes:

The author can find no information on the local erosion behaviour of inclined tubes. Average erosion rate studies suggest that there is a smooth transition between the horizontal and vertical states (Nieh et al., 1991).

Local Erosion Rate - Vertical Tubes:

Although the average erosion rate of a vertical tube is lower than that of a horizontal tube (Nieh et al., 1991), there is little information on the local erosion behaviour of vertical tubes. Zhu et al. (1990) found that the erosion rate of a horizontal tube of square cross-section was about ten times higher on the bottom of the tube than on the vertical sides. This result suggested that most erosion is caused by approximately normal particle impacts; abrasion (in which particles slide over the surface) is comparatively unimportant. Bubble motion studies (Hager and Thomson, 1973; Rowe and Everett, 1972; Gunn and Al-Doori, 1985; Lim, 1992, p155-160) suggest that near normal particle impacts would not be very common on a vertical tube. The author suspects that the erosion rate would be high close to the bottom of the tube and would quickly stabilise around a constant low value with increasing distance along the tube. Of course, the behaviour could be considerably more complex - experimental or simulation (Ding and Lyczkowski, 1992; Ding et al., 1992) studies are needed.

Now, having briefly reviewed the behaviour of horizontal, vertical and inclined tubes, it is possible to postulate how the local heat transfer coefficient and erosion rate will vary on the U-tube heater used in the experimental study of this thesis. These conjectures, along with the local heat flux information are presented in Figure 5.10.

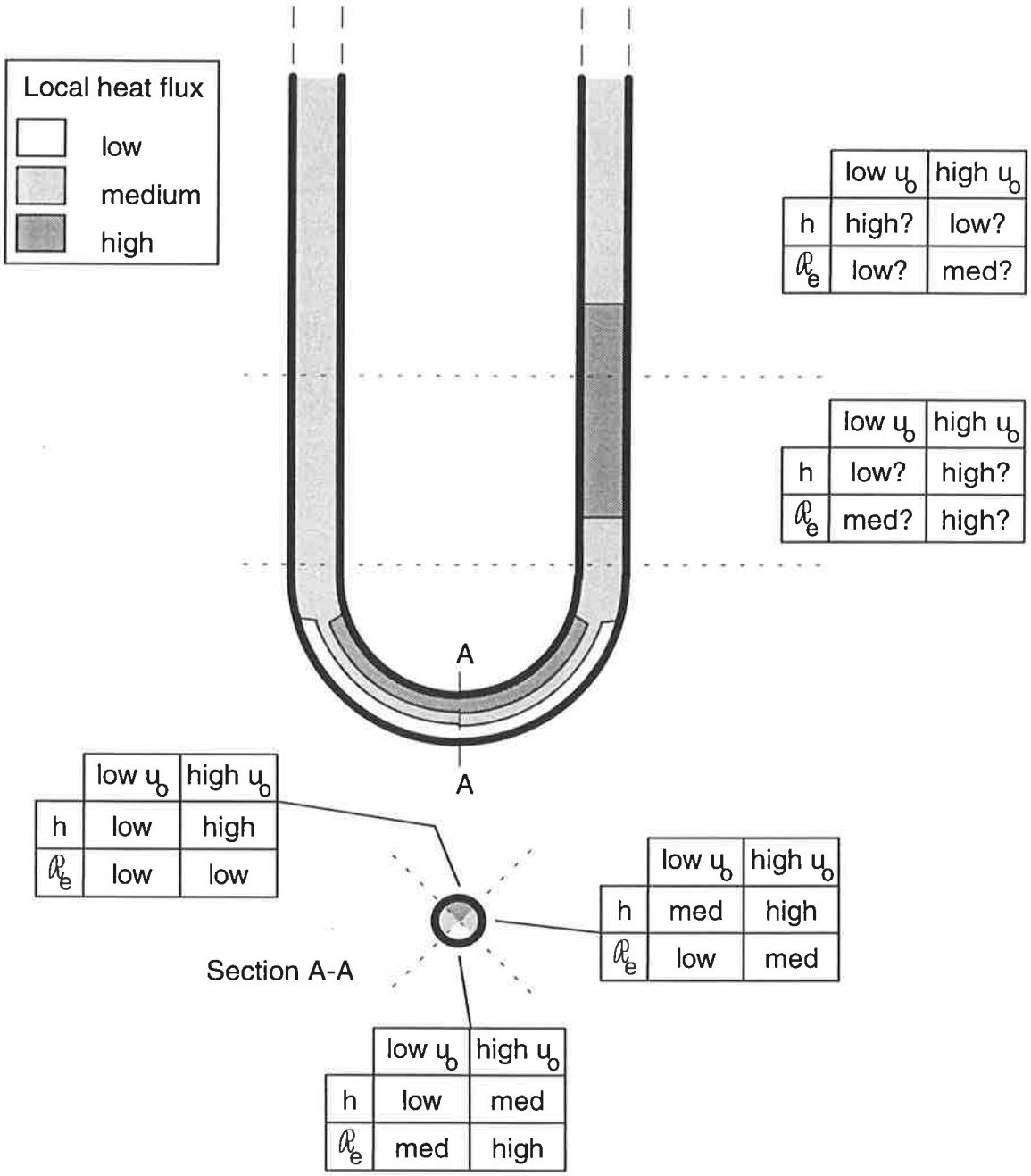

Figure 5.10: Postulated approximate variation of the relative local heat transfer coefficient, erosion rate and heat flux on the immersed U-tube heater at low and high superficial gas velocities.

According to the current coating-erosion model, deposits should form where the heat flux is high, and the heat transfer coefficient and potential erosion rate (related to T_s) are low. This situation arises on the top of the bend of the U-tube at low gas velocities. In every experiment, some - if not all - of the coating was deposited in this position. At low u_o, Figure 5.10 also suggests that coating may form on the bottom or sides of the U-tube's bend, but this was not observed experimentally. Finally, based on the postulated local behaviour, coating could occur around the hotspot at both low and high gas velocities. The experimental study revealed that a deposit did form over the hotspot, but only at low u_o.

The preceding discussion shows that a three-dimensional version of the coating-erosion model incorporating local information could likely predict the spatial distribution of the coating on the U-tube heater that was observed in the experiments. However, the detailed local information needed to make quantitative predictions is apparently unavailable at present. It may be difficult to perform experiments for the local h and $\mathcal{R}_e$ data that are appropriate to the present study, since the diameter of the tube used here (10 mm) is substantially smaller than that used in other heat transfer and erosion studies (the smallest are 20-30 mm). A future alternative may be to use detailed simulation tools, such as those being developed by Kuipers et al. (1992), Kılkış (1991) and Ding and Lyczkowski (1992). It would be comparatively easy to insert a U-tube heater into one of these models and extract the local information as required.

5.4.3 The Coating in Cross-Section

The previous section discussed the spatial distribution of the coating formed on the U-tube heater in the experimental study. In this section, another geometrical aspect of the coating layer - its internal structure - will be briefly examined.

Figure 5.11 is a view of the coating formed in experiment 30, showing the layer of particles which was attached to the heater's surface. The bond necks between adjacent particles and the random nature of the particle locations are clearly visible. Fracture sites, produced when the particle- heater surface bond necks were broken, can also be seen.

A cross-sectional view of the coating layer from experiment 22 appears in Figure 5.12. Once again, the particle-particle and particle- heater surface bonds can be seen. Although the coating is relatively thick (about six particle layers), it is difficult to observe any variation in the local porosity through the cross-section. As discussed in Section 5.3.2, the local porosity of the coating is expected to increase with increasing distance from the heater surface, due to differences in the local time and temperature for sintering.

However, a very clear variation in the local porosity is apparent in Figure 5.13, which was obtained with a different coating material and heater. Adjacent to the heater surface is a layer of non-porous material about one particle diameter thick. On top of the solid layer, the particles are only lightly sintered together, much as in Figure 5.12. This coating was obtained in a fluidized bed of spherical polystyrene beads (d_p = 840 x10^{-6} m) at $u_o/u_{mf} \approx 1.2$, T_∞ = 80 °C with an immersed heater (axially-centred vertical cylinder with insulated top, d_h = 0.02 m, L = 0.05 m, z_h = 0.1 m) operating at 13 W for 160 minutes. Although the glass ballotini and polystyrene bead experiments are different in several ways, it is thought that the presence of a non-porous layer is due to the comparatively long duration of the latter experiments. In modelling the coating-erosion behaviour experienced in the polystyrene system, there is a definite need to take into account the porosity variations of the coating layer. In the glass system, the use of an average coating porosity is probably adequate for the conditions covered in the current experimental study.

[Magnification: 26 times]

Figure 5.11: Photograph of the coating that formed in experiment 30 showing the layer of particles that was in contact with the surface of the U-tube heater.

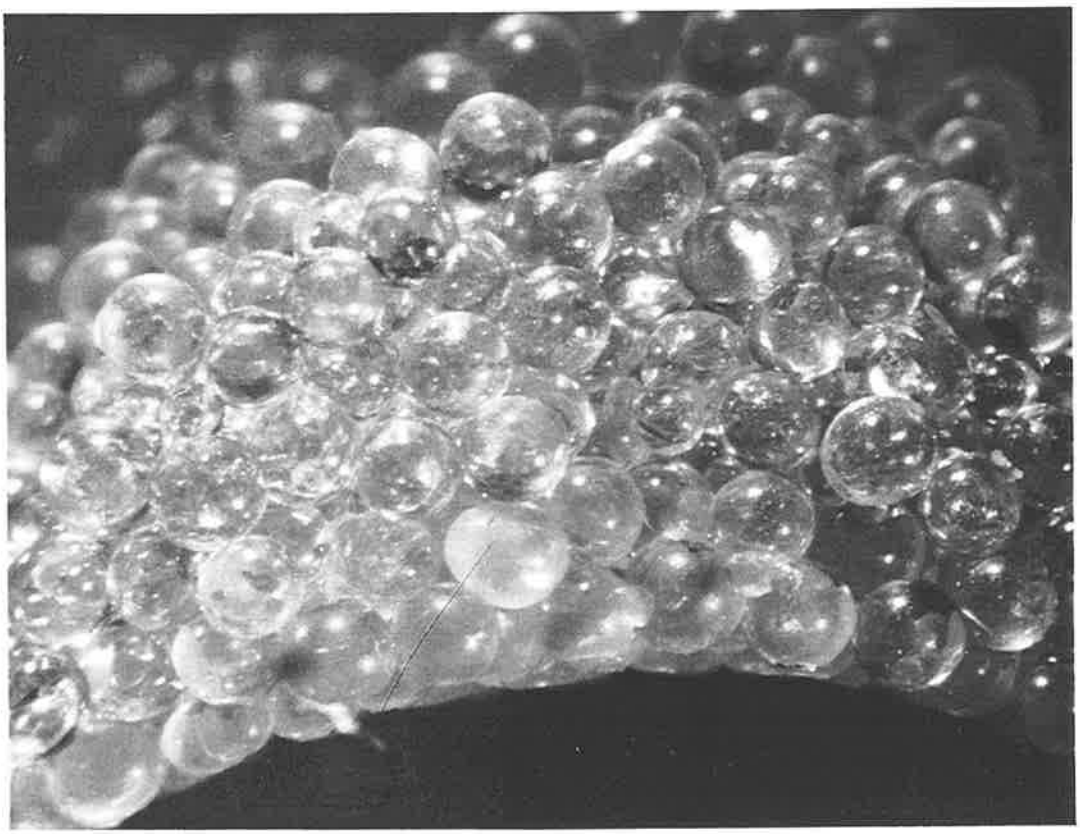

[Magnification: 22 times]

Figure 5.12: Photograph of the cross-section of the coating that formed in experiment 22.

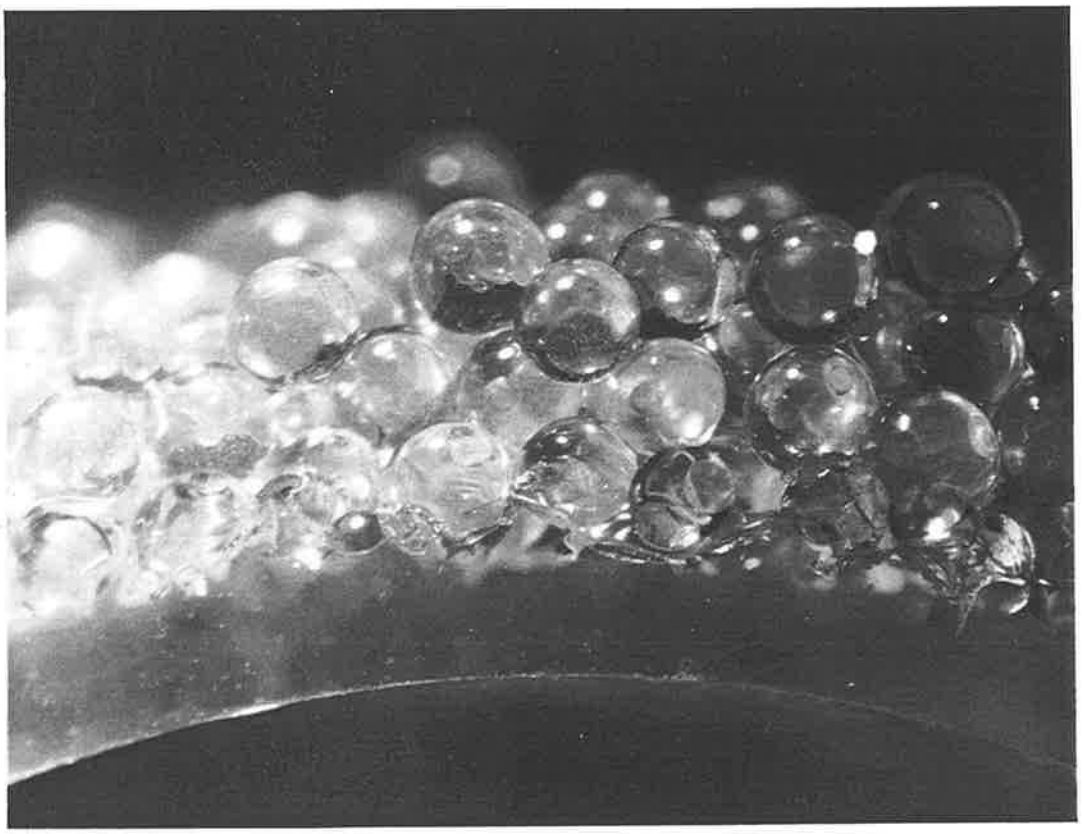

[Magnification: 20 times]

Figure 5.13: Photograph of the cross-section a coating composed of polystyrene beads.

Future research may lie in quantifying the porosity variations in the coating layer. A possible experimental technique may involve thoroughly impregnating samples of the coating with an opaque resin, different in colour to the particles. When the resin has hardened, the resin / coating block could be sectioned and photographed. A three-dimensional picture of the internal structure of the coating layer could be built up with the aid of a computer. (A digital image analysis system would be a very useful tool for this process.) In this way, detailed quantitative information on the porosity of the coating may be obtained.

5.4.4 Sintering Temperature

As indicated in Section 5.4, a key input variable of the coating-erosion model, the sintering temperature (T_s), is unknown *a priori*. T_s is the temperature of a surface immersed in a fluidized bed at which particles will adhere to the surface for a given set of operating conditions and materials. Individual values of T_s were determined for each experiment by parameter fitting (the values are tabulated in Appendix G). The author sought to determine how the T_s values varied with the operating conditions in the current experimental system.†

Figure 5.14 shows that T_s varies strongly with the dimensionless excess gas velocity (recall T_m = constant = 625 °C). T_s increases rapidly with u_o for $1.25\ u_{mf} \lesssim u_o \lesssim 2\ u_{mf}$; beyond $u_o \approx 2\ u_{mf}$, T_s is virtually constant. Extrapolation of the data suggests that $T_s \approx T_m$ at $u_o \approx u_{mf}$, which is expected from the definition of the effective melting temperature used in this study (see Sections 3.4.1 and 3.5.1).

Whether a particle sticks to a surface depends on the balance between the adhesive and erosive processes. Since the potential erosion rate (a measure of the erosive process) is a strong function of the superficial gas velocity, it is reasonable to expect a strong relationship between T_s and $\mathcal{R}_e$. Figure 5.15 is a plot of the potential erosion rate versus

† The following interpretation of the T_s results is tentative in view of the model assumptions, U-tube geometry, bed temperature gradients and other factors as discussed in preceding sections of Chapters 3 and 5.

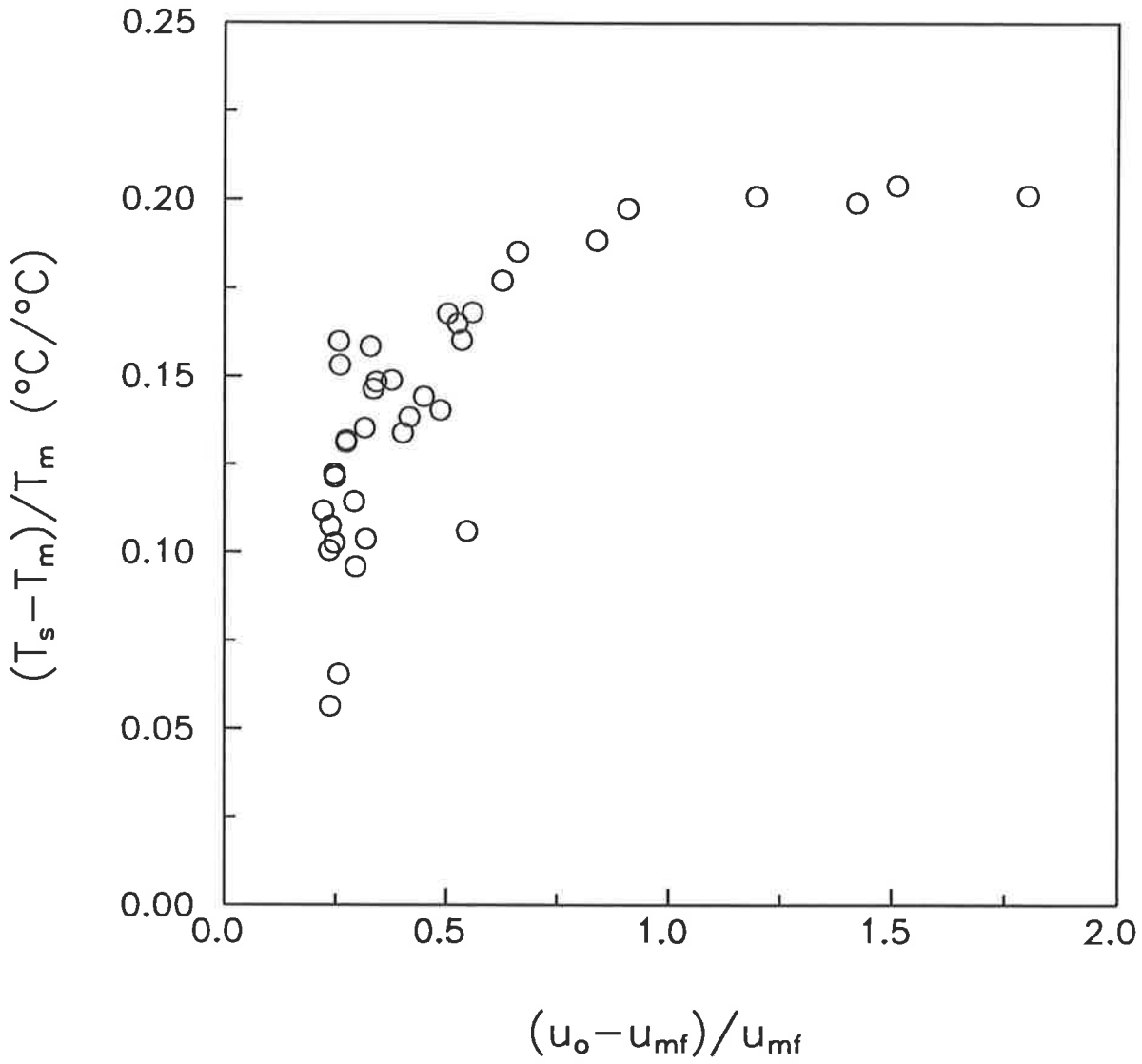

Figure 5.14: Variation of the sintering temperature with the superficial gas velocity.

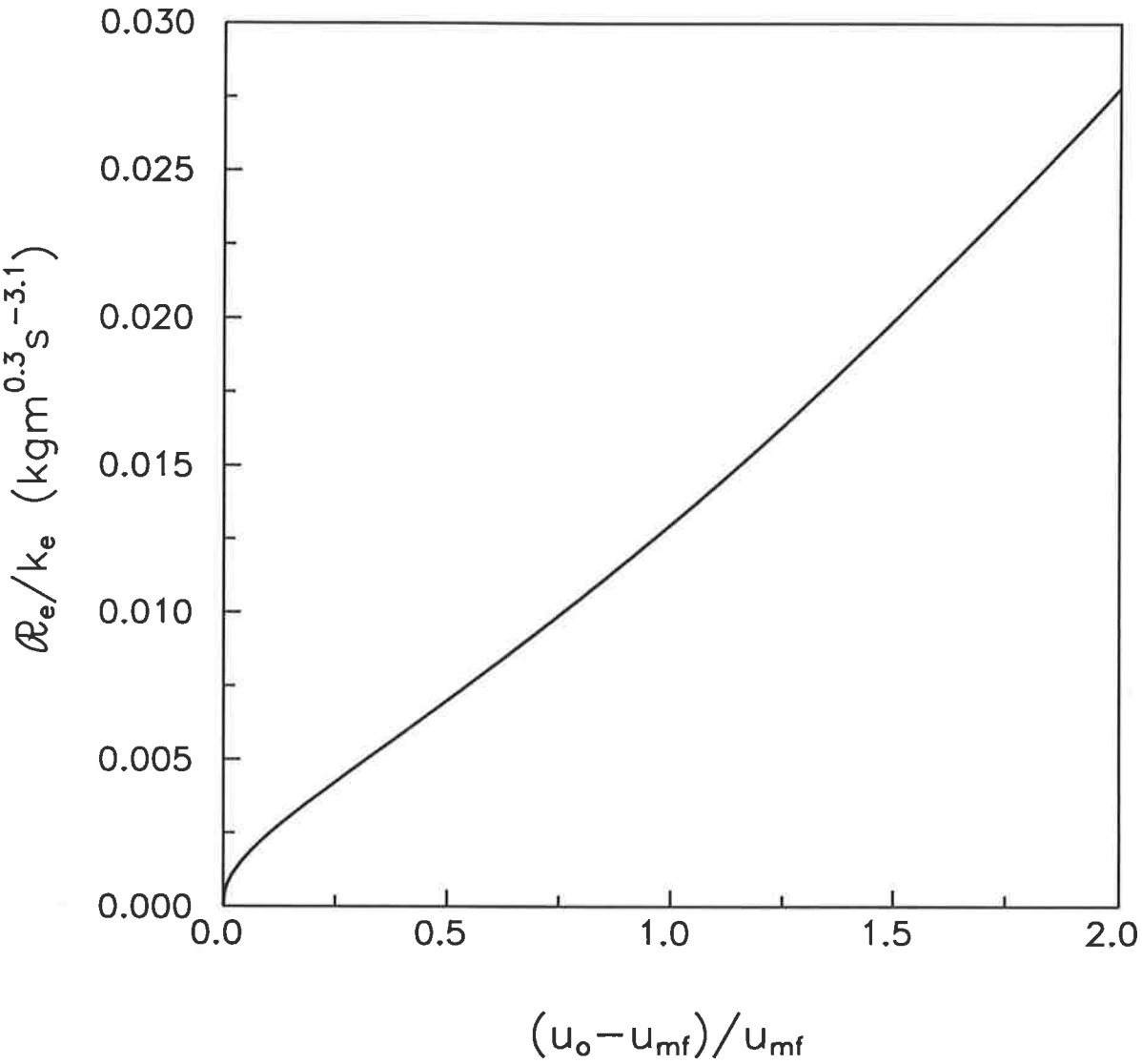

Figure 5.15: Relationship between the superficial gas velocity and the potential erosion rate.

the gas velocity, and Figure 5.16 shows directly the variation of T_s with $\mathcal{R}_e/k_e$ = $f_b\rho_p d_p^{1.2} u_b^{2.1}(1.04-\psi)$. (It was assumed that k_e is a material constant, independent of the operating conditions in the range traversed in this study.)

With the aid of Figure 5.16, it is now clear that the value of the potential erosion rate may affect a coating-erosion system in two ways:

- through equation (4.16) *when net erosion of the coating is taking place*. In "normal" circumstances, when there is net coating, it is only the *difference* between the potential coating and erosion rates that is important;
- through its influence on the sintering temperature.

However, if the potential erosion rate is high enough, the sintering temperature appears to be independent of $\mathcal{R}_e$ for the range of conditions covered in this work. Even when net erosion occurs, different behaviour results only for $\mathcal{R}_e \leq \mathcal{R}_{e\infty}$ (Section 4.4.2).

As a first attempt, the data in Figures 5.14 and 5.16 were correlated by the expression:

$$\frac{T_s - T_m}{T_m} = k_1\left(1-e^{-k_2 X}\right) \tag{5.9}$$

where X is either $(u_o-u_{mf})/u_{mf}$ or $\mathcal{R}_e/k_e$. To reduce the scatter of this correlation, a term including the temperature of the fluidized bed was added. It was found that the sintering temperature increased slightly with increasing T_∞. The final correlation for T_s is:

$$\frac{T_s - T_m}{T_m} = k_1\left(1-e^{-k_2 X}\right)\left(k_3 T_\infty - 1\right) \tag{5.10}$$

where X may be either $(u_o-u_{mf})/u_{mf}$ or $\mathcal{R}_e/k_e$, as before. Some statistical information and the values of k_1 - k_3, as found by regression, are presented in Table 5.3. Parity plots of

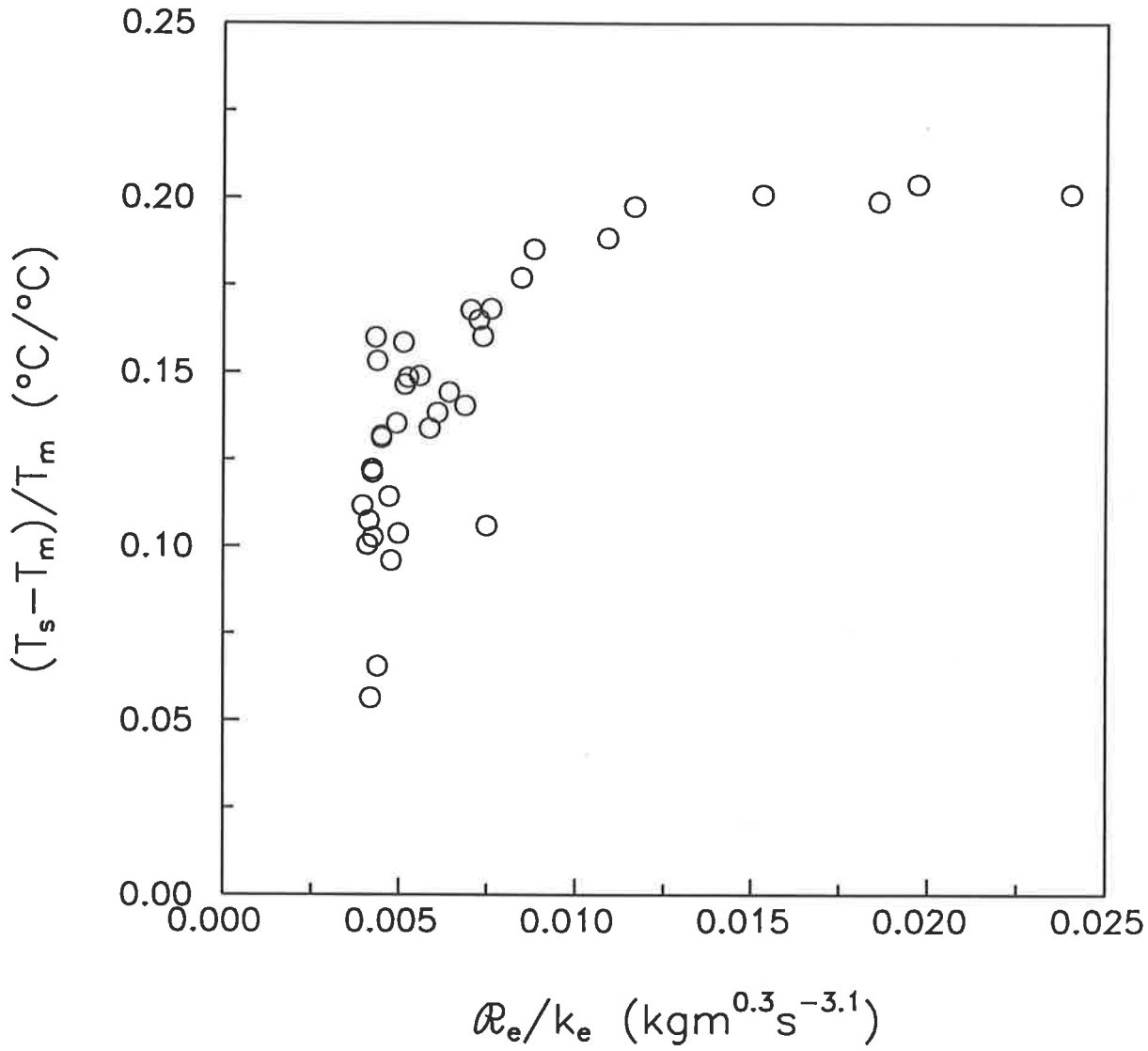

Figure 5.16: Variation of the sintering temperature with the potential erosion rate.

the correlation appear in Figures 5.17 and 5.18. While the $\mathcal{R}_e/k_e$ form of equation (5.10) has a slightly better fit, the u_o-based form is preferred since $\mathcal{R}_e/k_e$ is relatively difficult to evaluate.

Table 5.3: Best-fit parameters and statistics for the sintering temperature correlation, equation (5.10).

Parameter	$X = (u_o-u_{mf})/u_{mf}$	$X = \mathcal{R}_e/k_e$
k_1	0.225	0.268
k_2	4.58	278
k_3	3.22×10^{-3}	3.02×10^{-3}
RMS Error (°C)	12.4	12.0
Average Error (%)	1.2	1.2
Maximum Error (%)	5.8	5.4

Note that these parameters apply when the following units are used in equation (5.10):

T_s, T_m: °C;
u_o, u_{mf}: ms^{-1} at T_∞, p;
$(\mathcal{R}_e/k_e)$: $kgm^{0.3}s^{-3.1}$.

Clearly, the above correlations are quite tentative and apply only to the current experimental system over a relatively small range of operating conditions. However, they are valuable since they indicate how other systems might behave and they demonstrate that T_s varies in a systematic way. Ultimately, a theoretically-based explanation of the variation of T_s with the operating conditions is desired. Vatistas (1992) has developed a theoretical framework for the sticking probability of particles subject to adhesion, erosion and surface rolling events. The "efficiencies" of these events (which are input variables of Vatistas' theory) may be calculated from models based on

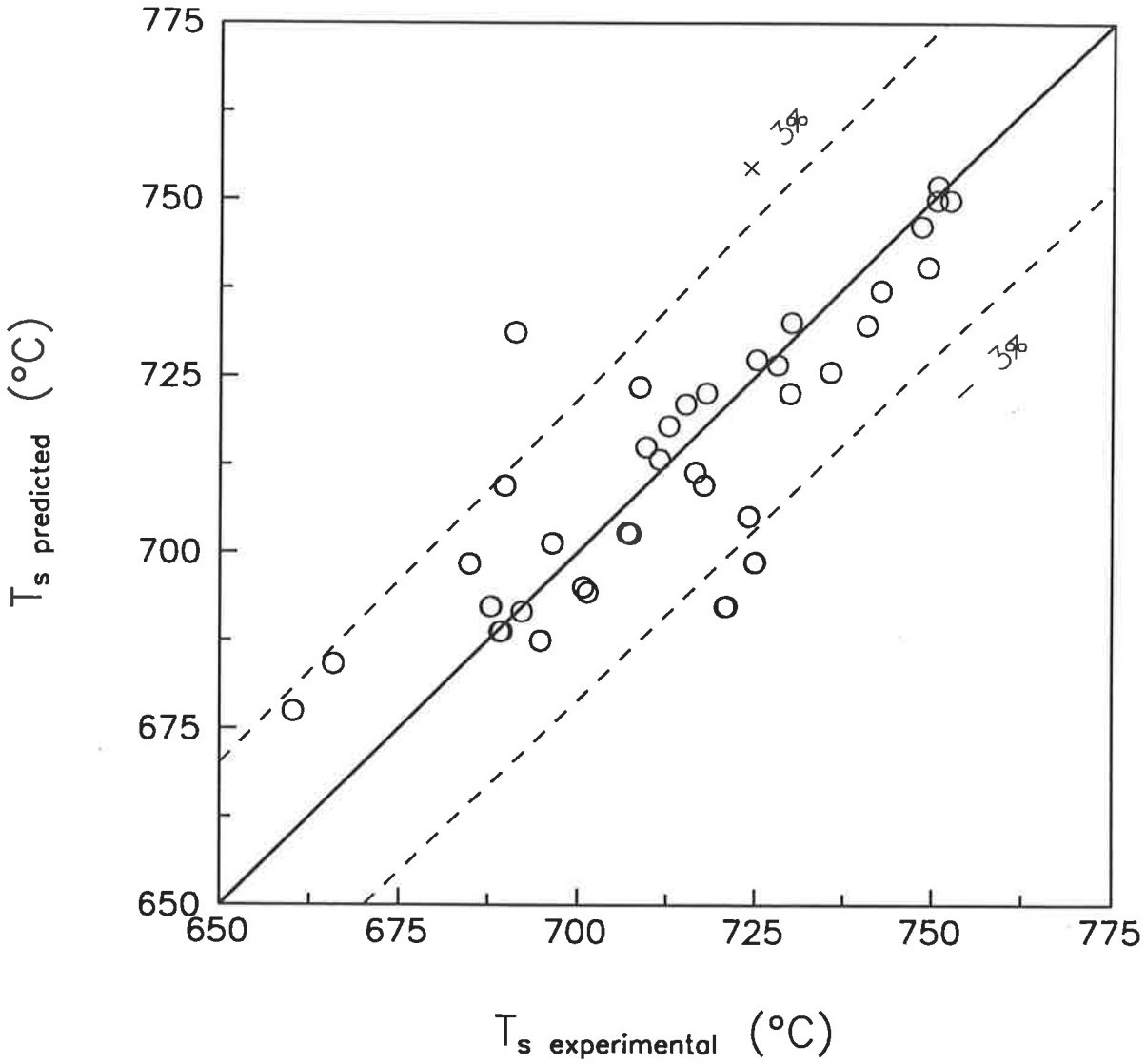

Figure 5.17: Parity plot for the u_o-based form of the sintering temperature correlation, equation (5.10).

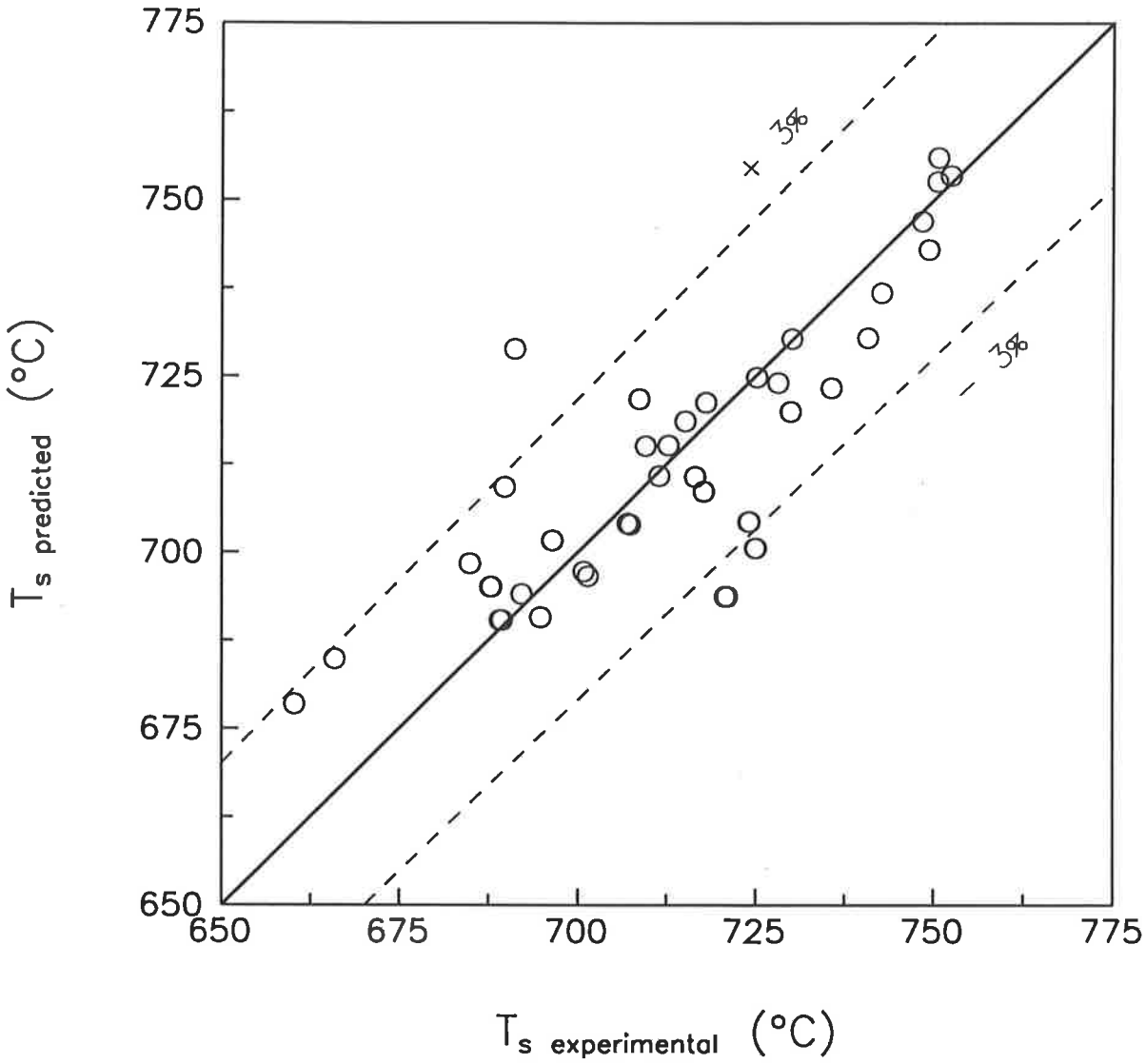

Figure 5.18: Parity plot for the $\mathcal{R}_e$-based form of the sintering temperature correlation, equation (5.10).

the behaviour of individual particles. For example, Jen and Tsao (1980), Tsao et al. (1982), Huang (1985), Huang (1986), Mazzone (1986) and Ennis et al. (1990) have studied the adhesion of single particles to other particles and to flat surfaces arising from surface tension and viscous forces under isothermal conditions. The analysis of these events is complicated by the existence of significant temporal and spatial temperature gradients close to an immersed heat transfer surface in a fluidized bed (Flamant et al., 1992, 1993; Lu et al., 1993).

The identification and attempted correlation of the sintering temperature is one of the main features of this thesis. For glass ballotini at least, the temperature of an immersed surface at which particles begin to deposit changes with the operating conditions of the fluidized bed. It remains to be seen whether other amorphous substances and crystalline materials behave in the same way.

Finally, it is interesting to draw some parallels between particle- immersed surface and particle-particle sintering behaviour in fluidized beds. Siegell (1976) was the first to investigate systematically the phenomenon of *high-temperature defluidization*. Above a critical temperature, T_{ms}, a fluidized bed may loose fluidization due to *almost instantaneous interparticle sintering*, despite being operated at a gas velocity above the (traditionally) expected value of u_{mf}. Fluidization may be maintained only by increasing the gas flowrate. The velocity required to avoid defluidization has been found to increase approximately linearly (Siegell, 1976) and superlinearly (Mazzone, 1986) with the temperature of the fluidized bed. The above behaviour is depicted in Figure 5.19. It has been observed for a wide range of substances, including: metals, polymers, ionic salts, FCC catalysts and coal ashes (Siegell, 1976; Mazzone, 1986; Compo, 1989).

Whether the bed is fluidized or defluidized depends on the relative strengths of the interparticle binding and breaking forces. The binding forces increase with T_∞; the breaking forces with u_o. T_{ms}, Siegell's minimum sintering temperature, and the "high

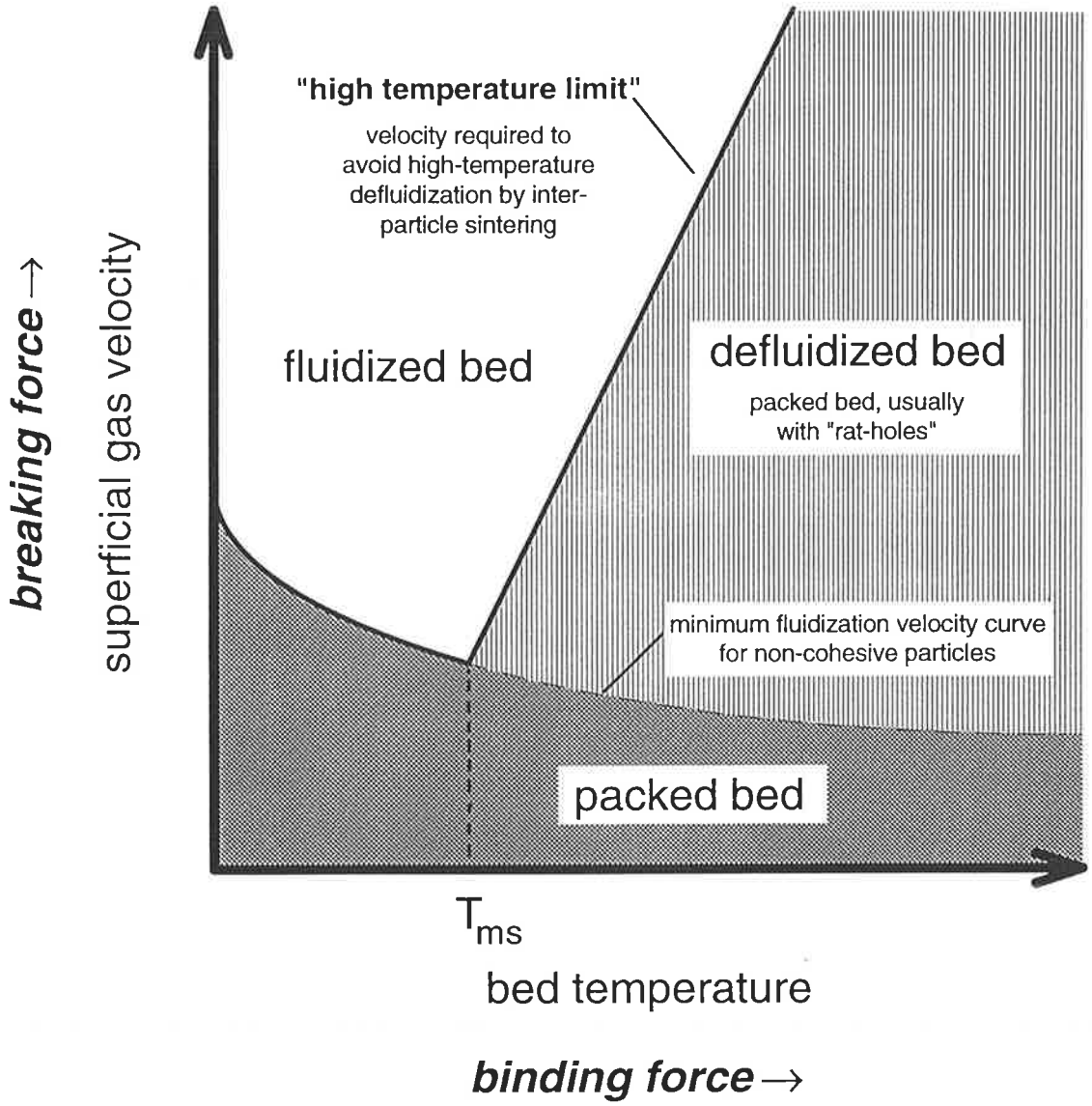

Figure 5.19: Operating regimes of a fluidized bed at high temperature.

temperature limit" are the manifestations of this force balance. These quantities depend primarily upon the material forming the particles, but also upon the particle size and the height to diameter ratio of the fluidized bed. The relative minimum sintering temperature of substances with a definite melting point, T_{ms}/T_{mpt}, has been found to range from 0.40 K/K (molybdenum powder) to 0.98 K/K (polyethylene beads, polyethylene granules). Note that T_{ms} is always lower than the melting temperature. The minimum sintering temperatures of materials without a well defined melting point, such as glass, have also been measured. For these materials, T_{ms}/T_m is rather ambiguous. Perhaps coincidentally, as noted in Section 3.5.1, the effective melting temperature of the glass ballotini used in the experimental study is very similar to the minimum sintering temperature determined by Compo (1989). Models of defluidization and particle agglomeration in fluidized beds have been proposed by several workers; they are critically reviewed by Compo (1989, p9-20, p135-146). In an interesting and relevant study, Ennis et al. (1991) developed a model of a fluidized bed granulator and considered its defluidization.

Now, compare these findings with the sintering behaviour of particles and immersed surfaces, as investigated in this thesis (Figure 5.20). Deposit formation on a surface which is at a given high temperature *may* be avoided if the fluidizing gas velocity is raised. The velocity needed to overcome coating varies with the temperature of the immersed surface as reported in equation (5.10). However, the present experiments (Figure 5.14) suggest that at sufficiently high immersed surface temperatures, a deposit will form regardless of the superficial velocity. In line with the particle-particle case, deposit formation depends upon the balance of the particle- immersed surface binding and breaking processes. The binding (coating) force increases with the immersed surface temperature; the breaking (erosive) force increases with u_o. Future work in modelling the behaviour of the sintering temperature may benefit from a thorough study of the literature on the theory of fluidized bed agglomeration and defluidization. However, first priority should be given to conducting an extensive experimental program covering a

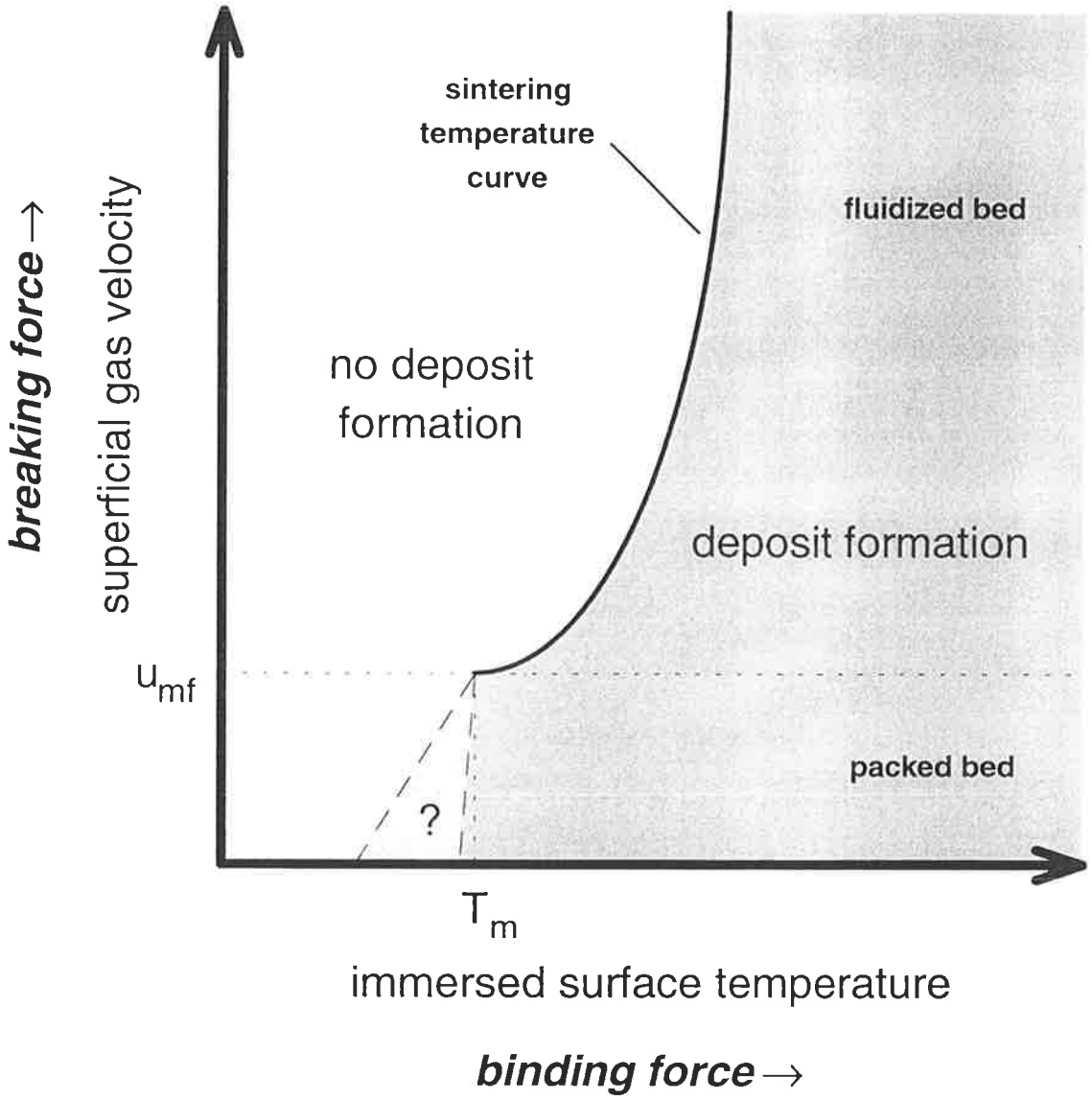

Figure 5.20: Deposit / no deposit regimes for a heated surface immersed in a fluidized bed at a given bed temperature.

wide range of materials, particle sizes, fluidization velocities and immersed objects. It is important to bear in mind that the conclusions of this thesis are drawn from a study of particles of only one material and size, and with an immersed body of a particular shape.

5.5 IMPLICATIONS FOR THE MTCI / THERMOCHEM GASIFIER

Before discussing the implications for a different system, the scope and findings of the current study will be summarised. The aim of the study was to investigate the effect of particle deposition and removal on an object immersed in a fluidized bed. Many combinations of deposition and removal mechanisms, bed materials and shapes of the object are possible. The particular combination considered in this thesis is set out in Table 5.4. The behaviour of the immersed surface was characterised mainly by its temperature history (as deposition was thermally-driven in this study) and the thickness or mass of the deposit that formed on the surface. The spatial distribution of the deposit on the object and the internal structure of the deposit were subsidiary features.

Table 5.4: General characteristics of the system considered in the current study.

Environment:	Bubbling, gas-solid fluidized bed
Deposition process:	Sintering onto a high-temperature surface
Removal process:	Erosion by impact of particles from passing bubbles
Bed material:	Spherical, soda-lime glass beads of narrow size range
Fluidizing agent:	Heated dry air
Immersed surface:	Experiment: electrically-heated vertical U-tube
	Theory: constant heat flux cylinder[1]

Note:
1: one-dimensional analysis - only radial variation considered.

Fouling, the formation of an insulating deposit on a heat transfer surface, reduces the overall heat transfer coefficient, causing a decrease in heat flow or an increase in the temperature of the surface. A deposit will form on an object immersed in a fluidized bed if the object's surface is above the sintering temperature. If the power supplied to the immersed object is low, its surface will be cooler than the sintering temperature, so no deposit will form. However, if the supplied power is high, the object will be above the sintering temperature and an insulating layer of coating will be present. The transition between low and high power behaviour is sudden, so, near the boundary, small changes in the operating conditions can significantly alter the state of the system. The sintering temperature, itself a function of the operating conditions, characterises the single-particle adhesion and removal processes. In this study, the sintering temperature was found to increase with the superficial gas velocity and the temperature of the fluidized bed. However, if the surface is hot enough, deposition will occur regardless of the gas velocity. Figure 5.21 shows qualitatively how the temperature of the immersed body and the thickness of the deposit vary with the main operating variables.

When particles adhere to the deposit, they do not melt completely on contact; hence at least part of the deposit is porous. A highly porous (low density) coating is highly insulating, leading to a high immersed body temperature and a small mass of deposit. The coating porosity also affects the ease of mechanical cleaning of the heat transfer surface and the surface's corrosion resistance. The porosity will decrease with time through interparticle sintering, which depends on the coating's age, temperature and any external forces.

The operating principles and commercial motivation behind the pulse-enhanced, indirectly-heated fluidized bed gasifier of MTCI and ThermoChem Inc. (ThermoChem, 1993), have been described briefly in Chapter 1. Further details of specific applications may be found in Black (1991), Durai-Swamy et al. (1991), and Aghamohammadi and Durai-Swamy (1993). Essentially, it is a fluidized bed gasifier operated without oxygen,

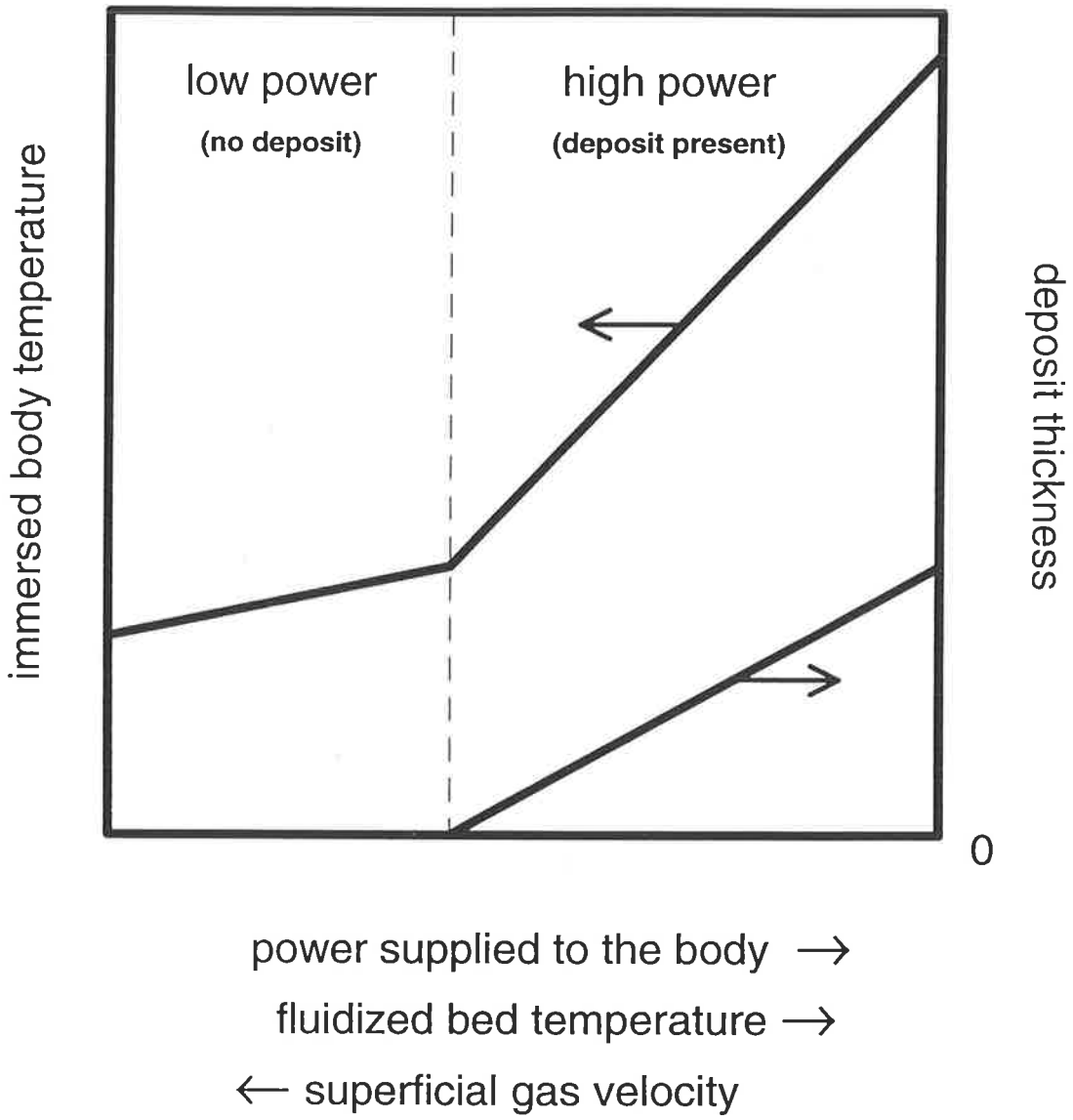

Figure 5.21: Qualitative variation of the immersed body system with the main operating variables.

in which the energy needed to drive the gasification reactions is provided by a bundle of immersed heat transfer tubes. The tubes are heated by hot gases from the pulse-combustion of part of the gasifier product gas. Conventional gasifiers use a steam/oxygen or steam/air mixture to fluidize the bed, so the combustion and gasification reactions compete in the same process vessel; immersed tubes are not needed. Physical separation of the combustion and gasification reactions leads to many advantages. However, it introduces into the fluidized bed a hot surface - the immersed tube bundle - which may suffer from fouling.

Table 5.5 outlines the key features of the indirectly-heated gasifier for comparison with Table 5.4. Several coating deposition and removal mechanisms are postulated. There do not appear to be any reports of fouling in the indirectly-heated gasifier, so the system may be operating below its sintering temperature. Like the model system studied in this thesis, a small change in the operating conditions (a slight decrease in the superficial gas velocity, for example) could push the system into the coating formation regime, and so, markedly change its operation. If an insulating deposit forms on the heat transfer tubes, the overall heat transfer coefficient will decrease, so the temperature of the gasifier may drop, causing a loss in gas production. Further, prolonged exposure of the heat transfer tubes to higher-than-expected temperatures may force the premature replacement of the tubes to avoid burnout or mechanical failure.

Conversely, deposit formation may be beneficial, if some decrease in heat transfer is tolerable. Direct erosive attack of the tube metal by the bed particles may be prevented by a tenacious deposit. In fluidized bed combustors, the wastage of immersed heat transfer surfaces is a major limitation to their commercial acceptance (Bouillard and Lyczkowski, 1991). Since the tubes of the indirectly-heated gasifier are hotter than those in fluidized bed combustors, the avoidance of direct metal erosion is likely to be an even more important issue.

Table 5.5: General characteristics of the pulse-enhanced, indirectly-heated fluidized bed gasifier.

Environment:	Gas-solid fluidized bed
Deposition processes[1] :	• Sintering onto high-temperature surface • Particle capture by partially molten phase present on surface • Evaporation of volatiles, leaving solid deposit on surface • Chemical reaction producing solid/liquid product on surface
Removal processes[1] :	• Erosion by impact of particles from passing bubbles • Consumption of coating by chemical reaction
Bed material:	Varies depending on the application, for example: • Black liquor recovery in the paper industry: Na_2SO_4 particles + black liquor spray (65% fibre residue) • Disposal of sludge waste from recycle paper mill: Sand particles + sludge spray (50-80% solids) • Solid biomass gasification: Limestone particles + biomass (pistachio shells, wood chips, rice hulls, etc.)
Fluidizing agent:	Superheated steam
Immersed surface:	Horizontal tube bundle heated internally by hot combustion gases

Note:
1: postulated.

A deposit changes the chemical and physical environment of a tube's surface, and hence may lower the corrosion resistance of the tube. The chemical nature of the coating is important. The deposit's porosity influences the rate of diffusion of the reactants and products of the corrosion reactions.

The erosion, corrosion and fouling processes are interrelated. Mann et al. (1991) have examined these processes experimentally in an atmospheric fluidized bed combustor for several coals and different heat transfer tube materials. They described the worst-case scenario for the synergistic action of the three processes - *"if a deposit/scale were to build up and readily spall off in repeated cycles... [this] would greatly increase both the corrosive and erosive mechanisms of tube metal wastage"* (Mann et al., 1991, p28).

In summary, it is clear that the deposition and erosion mechanisms conceivably present in the pulse-enhanced, indirectly-heated fluidized bed gasifier are much more complex than those considered in the development of the coating-erosion model. Even so, it is reasonable to suggest that this gasifier may suffer from fouling of its immersed heat transfer surfaces.

5.5 SUMMARY

Although the coating-erosion model is fully predictive, a key input variable, the sintering temperature, is an unknown function of the operating conditions. For each of the 37 coating-erosion experiments analysed, the sintering temperature was obtained by data fitting so that the experimental and theoretical masses of coating at the end of the experiment agreed. The experimental and predicted temperature histories were then compared.

Comparison:

Both the simulated and experimental temperature histories exhibited the same behaviour - a fast initial temperature rise, with a sudden transition to the slow rise phase which continued to the end of the experiment. In general, the temperature histories agreed well. The analysis showed that the experimental system operated in the low power regime for much of an experiment's duration. Only near the end of a run was deposition predicted to take place. Experiments could not be performed over longer times as there was a high-temperature operating limit on the immersed U-tube heater.

Porosity of the Deposit:

The deposits formed in the experiments were porous - that is, the particles had sintered together, but were not completely fused. The porosity of a deposit affects its density and thermal conductivity, and hence the behaviour predicted by the coating-erosion model. A constant porosity of 0.21 was assumed for the model calculations. A sensitivity analysis revealed that a high coating porosity leads to a high immersed body temperature, low coating mass and slow response; the coating thickness is porosity-independent. In reality, the coating porosity will decrease with time and temperature through interparticle sintering. A preliminary effort towards the inclusion of sintering effects in the model appears in Appendix H.

Spatial Distribution of the Coating:

The experiments showed that the deposits on the U-tube heater tended to form in patches, mostly on the top of the U-tube bend, but also over the hotspot on one of the heater's legs. In contrast, the present coating-erosion model assumes that the deposit forms with uniform thickness over the entire surface of a cylindrical immersed body. This conflict between the model's assumptions and the experimental reality is the main cause for caution in the acceptance of the results of this work. However, consideration of the *local* heat transfer coefficient, potential erosion rate and heat flux suggests that a

three-dimensional version of the coating-erosion model using local information is likely to predict correctly the experimentally observed pattern of deposition.

Sintering Temperature:

The sintering temperature data (obtained by parameter fitting as explained earlier) were correlated with the superficial gas velocity or potential erosion rate, and the temperature of the fluidized bed. Equation (5.10) represents the data with an average error of about 1%. Much more experimental work with a wide range of materials is needed to verify the functional dependence of the sintering temperature on the operating conditions which was observed in this study. Further, the relationship between the sintering temperature, the (effective) melting temperature and the minimum sintering temperature for defluidization should be investigated.

MTCI / ThermoChem Gasifier:

Fouling of the heat transfer tubes of the pulse-enhanced, indirectly-heated fluidized bed gasifier is a distinct possibility. A deposit will reduce heat transfer, possibly causing the loss of export gas production or premature tube replacement. Conversely, a tenacious deposit may protect a heat transfer surface from direct particle impact erosion. Moreover, the presence of a deposit influences the tube's corrosion resistance. This gasifier is a complex, multicomponent system in which chemical and physical processes act together to determine the coating-erosion behaviour. Clearly, a great deal of research would be needed to quantify all of these deposition and removal mechanisms.

Chapter 6:

CONCLUSIONS AND RECOMMENDATIONS

The aim of this study was to investigate the behaviour of an immersed surface that is subject to both particle deposition and removal processes in a fluidized bed. For the particular system studied here, in which the immersed surface was heated, high-temperature sintering caused deposition that was opposed by particle impact erosion arising from the bubbling action of the bed. Experiments were performed on an electrically heated U-tube immersed in a high-temperature fluidized bed of glass ballotini. The results were analysed by a one-dimensional, radial-cylindrical mathematical model that combined fluidized bed powder coating theory with studies of the erosion of tubes in a fluidized bed.

The main conclusions of this study and some recommendations appear below.

Mathematical Model:

A dynamic model of the system, which predicts the temperature of the immersed body and the coating mass, is characterised by seven dimensionless groups: Z, T_{bo}^*, $Q_{b\,ext}^*$, Bi, T_s^*, ℓ_e^* and t^*. Only $Q_{b\,ext}^*$, Bi and T_s^* determine the steady state solution. T_{bo}^* may strongly affect the path taken in reaching steady conditions. Two regimes of steady state behaviour exist: (i) ***low power*** in which no coating forms, and (ii) ***high power*** in which an insulating coating layer is present. The low/high power transition is sudden; near the boundary, a small change in the operating conditions may substantially alter the

state of the system. Future work should involve extending the model to two or three dimensions, and relaxing the assumption of constant-density coating.

Porosity of the Coating:

Particles do not have to melt completely to adhere to a surface - they may just be lightly sintered, hence a deposit may not be completely solid. The porosity of the deposit in the current system strongly affects the model's predictions. Interparticle sintering will cause the average deposit porosity to decrease with time. Further, local variations in the porosity through the thickness of the coating are expected. Experimental work, possibly involving microscopic digital image analysis of deposits in cross-section, should be undertaken to measure the deposit porosity for comparison with the predictions of sintering theory as outlined in this study.

Spatial Distribution of the Coating on the Immersed Object:

Deposits tended to form in patches, mainly on top of the U-tube's bend and over the hotspot on one of the heater's legs. While the current theory assumes uniform deposition, a three-dimensional version incorporating local information is likely to predict these experimental observations. Further work is needed to characterise the local heat flux, heat transfer coefficient and sintering temperature.

Sintering Temperature:

The sintering temperature, a key system parameter, varies with the operating conditions of the fluidized bed. A tentative sintering temperature correlation for the current system was developed in terms of the superficial gas velocity and the temperature of the fluidized bed. Further experiments to determine the sintering temperature function should be performed on a range of amorphous and crystalline particles of different sizes for several immersed object shapes. A theoretical explanation of the sintering temperature may be based on studies of single-particle adhesion and removal. The

relationship between the sintering temperature, the melting temperature and the minimum sintering temperature for defluidization should be investigated.

Implications for the MTCI / ThermoChem Gasifier:

The pulse-enhanced, indirectly-heated fluidized bed gasifier developed by MTCI may experience deposit formation on its immersed heat transfer tubes, although this behaviour - **fouling** - has not been reported in the open literature. Tube burnout, a fall in gas production, *decreased* tube erosion and altered corrosion resistance of the tubes are possible outcomes. Consequently, further laboratory-scale experiments should be performed on equipment and with materials that more closely resemble those in the commercial system so that these conjectures may be verified. Further theoretical work would be needed to characterise the additional chemical and physical mechanisms of deposition and removal operating in this complex, multicomponent system.

The present study may be viewed as an extension of fluidized bed powder coating theory to allow for erosion effects that appear at high superficial gas velocities. Perhaps more importantly, the study contributes to the understanding of the fouling of firetube heat exchange surfaces immersed in a fluidized bed.

NOMENCLATURE

a	first diameter of a torus, Figure C.2, [m]
A	area, [m^2]
A	composition-dependent parameter in equation (H.5), [Pas]
A	convenience variable, Appendix D, [K]
A_b	surface area of the immersed body, [m^2]
Ar	$d_p^3 g\rho_g(\rho_p-\rho_g)/\mu_g^2$, Archimedes number (also called Galileo number), [-]
b	second diameter of a torus, Figure C.2, [m]
B	composition-dependent parameter in equation (H.5), [K]
B	convenience variable, Appendix D, [Km^{-1}]
Bi	hr_b/k, Biot number, [-]
Bi_b	$h(V_b/A_b)/k_b$, Biot number of an immersed body without a coating, [-]
Bi_{clean}	$h_{clean}\, r_b/k$, Biot number for an immersed body when clean, [-]
Bi_{fouled}	$h_{fouled}\, r_b/k$, Biot number for an immersed body with fouling, [-]
c_p	specific heat capacity of the coating, [$Jkg^{-1}K^{-1}$]
c_p'	effective specific heat capacity of the coating used when the enthalpy of fusion is significant, [$Jkg^{-1}K^{-1}$]
$\hat{c}_p'$	specific heat capacity of the coating at the temperature $(T_N' + T_s)/2$, [$Jkg^{-1}K^{-1}$]
c_{pb}	specific heat capacity of the immersed body, [$Jkg^{-1}K^{-1}$]
c_{pf}	specific heat capacity of a fluid, [$Jkg^{-1}K^{-1}$]
c_{pg}	specific heat capacity of the fluidizing gas, [$Jkg^{-1}K^{-1}$]

c_{pi}	specific heat capacity of node *i*, [$Jkg^{-1}K^{-1}$]
c_{pmf}	effective specific heat capacity of the fluidized bed at minimum fluidization conditions, [$Jkg^{-1}K^{-1}$]
c_{pp}	specific heat capacity of the bed particles, [$Jkg^{-1}K^{-1}$]
c_{ps}	specific heat capacity of a solid, [$Jkg^{-1}K^{-1}$]
c_{pX}	specific heat capacity of substance X, [$Jkg^{-1}K^{-1}$]
C	composition-dependent parameter in equation (H.5), [K]
C_D	isolated-sphere drag coefficient, [-]
C_R	factor in equation (3.6) to allow for non-axial tube location, [-]
$\mathcal{CL}$	indicates that a layer of coating is present, equation (4.8), [logical]
$\overline{\mathcal{CL}}$	indicates that a layer of coating is not present, equation (4.8), [logical]
$\mathcal{CT}$	indicates that coating may proceed, equation (4.9), [logical]
$\overline{\mathcal{CT}}$	indicates that coating will not proceed, equation (4.9), [logical]
d_b	equivalent bubble diameter (diameter of a sphere having the same volume as the bubble), [m]
d_h	diameter of a tube or of the tube of the U-tube heater, [m]
d_{holes}	diameter of the holes of a perforated plate distributor, [m]
d_p	diameter of the particles, [m]
D_{bed}	internal diameter of the fluidized bed, [m]
D_h	diameter of the bend of the U-tube heater, Figure C.1, [m]
E_{coat}	energy consumed in the formation of new coating in the time Δt, [J]
E_{cond}	energy conducted into the new part of the coating in the time Δt, [J]
E_{conv}	energy convected to the bed from the new part of the coating in the time Δt, [J]
E_v	kinetic energy dissipation rate per unit volume of a gas-solid mixture that leads to the erosion of an immersed surface, [Wm^{-3}]
f_b	void (bubble or slug) point frequency, [Hz]
fn	a particular function

F_p	applied compressive force between two particles, [N]
g	gravitational acceleration, [ms^{-2}]
Ga	$d_p^3 g\rho_g(\rho_p-\rho_g)/\mu_g^2$, Galileo number (also called Archimedes number), [-]
h	heat transfer coefficient between the {immersed body or outer surface of the coating} and the fluidized bed, [$Wm^{-2}K^{-1}$]
h_{clean}	heat transfer coefficient for a clean surface, [$Wm^{-2}K^{-1}$]
h_f	heat transfer coefficient for the gas film in the model of Xavier and Davidson (1981, 1985), [$Wm^{-2}K^{-1}$]
h_{fouled}	heat transfer coefficient for a surface with fouling, [$Wm^{-2}K^{-1}$]
h_{gc}	gas convective component of heat transfer coefficient in the model of Xavier and Davidson (1981, 1985), [$Wm^{-2}K^{-1}$]
h_p	average heat transfer coefficient between the emulsion and a surface when there is no gas film heat transfer resistance, model of Xavier and Davidson (1981, 1985), [$Wm^{-2}K^{-1}$]
h_{pc}	particle convective component of heat transfer coefficient in the model of Xavier and Davidson (1981, 1985), [$Wm^{-2}K^{-1}$]
H_t	hardness of an eroding surface, [Pa]
i	number of an experimental data point, Appendix F, [ordinal]
i	number of a node, [ordinal]
j	substep number in the integration of the coating-erosion model equations, [ordinal]
k	thermal conductivity of the coating, [$Wm^{-1}K^{-1}$]
k	a constant: $0 < k < 1$, Figure A.1, [-]
$\hat{k}'$	thermal conductivity of the coating at the temperature $(T_N' + T_s)/2$, [$Wm^{-1}K^{-1}$]
$k_1,\ldots k_6$	constants, [various units]
k_b	thermal conductivity of the immersed body, [$Wm^{-1}K^{-1}$]
k_{BT}	theoretical erosion rate coefficient of Bouillard et al. (1989), equation (2.13), [-]
k_e	erosion rate coefficient, [$kg^{-1}m^{0.7}s^{2.1}$]

k_e^o	effective thermal conductivity of a packed bed with stagnant fluid, [$Wm^{-1}K^{-1}$]
k_f	thermal conductivity of a fluid, [$Wm^{-1}K^{-1}$]
k_g	thermal conductivity of the fluidizing gas, [$Wm^{-1}K^{-1}$]
k_i	constant number i, [various units]
k_{ii}	thermal conductivity at the inner interface of control volume *i*, [$Wm^{-1}K^{-1}$]
k_i	thermal conductivity of node *i*, [$Wm^{-1}K^{-1}$]
k_{mf}	effective thermal conductivity of the fluidized bed at minimum fluidization conditions, [$Wm^{-1}K^{-1}$]
k_{oi}	thermal conductivity at the outer interface of control volume *i*, [$Wm^{-1}K^{-1}$]
k_s	thermal conductivity of a solid, [$Wm^{-1}K^{-1}$]
k_{ZE}	experimental erosion rate coefficient of Zhu et al. (1991), equation (2.9), [$kg^{-1}m^{-0.8}s^{2.3}$]
$k_{ZE'}$	experimental erosion rate coefficient of Zhu et al. (1991), equation (2.10), [$kg^{-1}m^{0.2}s^{1.3}$]
k_{ZR}	experimental erosion rate coefficient of Zhu et al. (1991), equation (2.14), [$kg^{-1}m^{0.7}s^{2.1}$]
k_{ZT}	theoretical erosion rate coefficient of Zhu et al. (1991), equation (2.11), [$m^{-1}s^{-1}$]
ℓ_d	maximum depth of deformation of a surface caused by the impact of a particle, [m]
L	length of the immersed body, [m]
L	characteristic vertical dimension of an immersed surface in the heat transfer model of Xavier and Davidson (1981, 1985), [m]
L_b	half thickness of a flat plate, [m]
L_h	height of the heated zone of the U-tube heater, Figure C.1, [m]
L_o	initial length of a linear particle chain, [m]
m_b	mass of the immersed body, [kg]
M	mass flux of particles striking a surface, [$kgm^{-2}s^{-1}$]
n_{holes}	number of holes in a perforated plate distributor, [-]

N	number of nodes in the coating, including boundary nodes, [-]
N	number of data points, Appendix F, [-]
N_p	number of particles striking a surface, [-]
Nu_h	hd_h/k_g, Nusselt number based on the diameter of the immersed body, [-]
Nu_p	hd_p/k_g, Nusselt number based on the particle diameter, [-]
O	order of magnitude
p	atmospheric pressure, [Pa]
p	any property of a polymer, [various units]
$\overline{p}$	averaged polymer property, [various units]
P_k	pitch of the knurling on a surface - the distance between adjacent knurls as measured along a non-curved part of the surface, [m]
Pr	$c_{pg}\mu_g/k_g$, Prandtl number, [-]
P_t	"material pressure" of an eroding surface, [Pa]
q	rate of heat flow, [W]
q_{ii}	rate of energy transfer across the inner interface of control volume *i*, [W]
$Q_{b\,ext}$	external power supplied to the immersed body, [W]
$\overline{Q}_{b\,ext}$	external power supplied to the immersed body at time $(t + \Delta t/2)$, [W]
$Q_{b\,ext}^*$	$Q_{b\,ext}/(2\pi kL(T_m-T_\infty))$, dimensionless external power supplied to the immersed body, [-]
r	radial position, [m]
r'	variable of integration, equation (H.9), [m]
$\mathbf{r}$	normal vector to a surface in Cartesian coordinates, [{m, m, m}]
r^*	r/r_b, dimensionless radial position, [-]
r_b	radius of the immersed body, [m]
r_c	radius of the coating, [m]
r_c^*	r_c/r_b, dimensionless radius of the coating, [-]
r_{ii}	radial position of the inner interface of control volume *i*, [m]

r_i	radial position of node *i*, [m]
r_{oi}	radial position of the outer interface of control volume *i*, [m]
Re	$d_p u_o \rho_g / \mu_g$, Reynolds number, [-]
Re_{mf}	$d_p u_{mf} \rho_g / \mu_g$, Reynolds number at minimum fluidization conditions, [-]
R_f	fouling factor, [$W^{-1}m^2K$]
R_f^*	kR_f/r_b, dimensionless fouling factor, [-]
$\mathcal{R}_c$	potential coating rate, [ms^{-1}]
$\mathcal{R}_c^*$	$r_b\mathcal{R}_c/\alpha$, dimensionless potential coating rate, [-]
$\mathcal{R}_e$	potential erosion rate, [ms^{-1}]
$\mathcal{R}_e'$	erosion rate which is only a function of z and θ, [ms^{-1}]
$\overline{\mathcal{R}}_e$	effective one-dimensional erosion rate, [ms^{-1}]
$\mathcal{R}_{e\infty}$	limiting potential erosion rate (for $\mathcal{R}_e > \mathcal{R}_{e\infty}$, the behaviour of the immersed body is not influenced by $\mathcal{R}_e$), [ms^{-1}]
$\mathcal{R}_e^*$	$r_b\mathcal{R}_e/\alpha$, dimensionless potential erosion rate, [-]
$\mathcal{R}_{e\infty}^*$	$r_b\mathcal{R}_{e\infty}/\alpha$, dimensionless limiting potential erosion rate (see $\mathcal{R}_{e\infty}$), [-]
$\mathcal{R}_{eBT}$	theoretical erosion rate of Bouillard et al. (1989), [ms^{-1}]
$\mathcal{R}_{eZE}$	experimental erosion rate of Zhu et al. (1991) as determined from single particle experiments, [ms^{-1}]
$\mathcal{R}_{eZE'}$	experimental erosion rate of Zhu et al. (1991) as determined from single particle experiments (alternative version), [ms^{-1}]
$\mathcal{R}_{eZR}$	experimental erosion rate of Zhu et al. (1991) as determined from fluidized bed experiments, [ms^{-1}]
$\mathcal{R}_{eZT}$	theoretical erosion rate of Zhu et al. (1991), [ms^{-1}]
SSE	Sum of the Square Error, equation (F.1), [various units]
s	vector that defines any point on the surface of the immersed body relative to the centre of the distributor in Cartesian coordinates, [{m, m, m}]
$\mathcal{S}$	represents the surface of an immersed body

$\mathcal{S}_{\mathbf{I}}$	represents region I of the surface of the U-tube heater, Figure C.1
$\mathcal{S}_{\mathbf{II}}$	represents region II of the surface of the U-tube heater, Figure C.1
$\nabla \mathbf{s_o}$	outward normal vector of the surface of the immersed body in Cartesian coordinates, [{m, m, m}]
t	time, [s]
t^*	$\alpha t/r_b^2$, dimensionless time, [-]
t_o	time at which the coating formed, [s]
t_1, t_2, t_3	different times: $t_1 < t_2 < t_3$, Figure A.1, [s]
t_{base}	time at the start of a base time step, [s]
t_{end}	duration of a simulation or an experiment, [s]
T	temperature, [K, unless other units stated]
T^*	$(T-T_\infty)/(T_m-T_\infty)$, dimensionless temperature, [-]
T_1,... T_N	nodal temperatures, [K]
T_b	temperature of the immersed body, [K]
T_b^*	$(T_b-T_\infty)/(T_m-T_\infty)$, dimensionless temperature of the immersed body, [-]
T_b'	temperature of an immersed body in a non-sintering particle system, [K]
$T_b'^*$	$(T_b'-T_\infty)/(T_m-T_\infty)$, dimensionless temperature of an immersed body in a non-sintering particle system, [-]
T_{bo}	initial temperature of the immersed body, [K]
T_{bo}^*	$(T_{bo}-T_\infty)/(T_m-T_\infty)$, dimensionless initial temperature of the immersed body, [-]
T_f	$(T_b+T_\infty)/2$, film temperature, [K, except °C in equation (3.10)]
T_i	interface temperature (if $\overline{\mathcal{CL}}$ $T_i = T_b$, else $T_i = T\|_{r=r_c}$), [K]
T_i	temperature of node i, [K]
T_i^*	$(T_i-T_\infty)/(T_m-T_\infty)$, dimensionless interface temperature (see T_i), [-]
T_m	(effective) melting temperature of the particles, [K, except °C in equation (5.10)]

T_{mpt}	melting temperature of a substance with a definite melting point, [K]
T_{ms}	minimum sintering temperature for defluidization, [K]
T_s	sintering temperature of the particles, [K, except °C in equation (5.10)]
T_s^*	$(T_s-T_\infty)/(T_m-T_\infty)$, dimensionless sintering temperature of the particles, [-]
T_∞	temperature of the bulk of the fluidized bed, [K, except °C in equations (3.2) and (5.10)]
$\overline{T}_\infty$	temperature of the fluidized bed at time $(t + \Delta t/2)$, [K]
u_b	void (bubble or slug) rise velocity, [ms^{-1}]
u_{mb}	minimum bubbling velocity, [ms^{-1}]
u_{mf}	minimum fluidization velocity, [ms^{-1}, ms^{-1} at T_∞,p in equations (3.2) and (5.10)]
u_o	superficial gas velocity, [ms^{-1}, ms^{-1} at T_∞,p in equation (5.10)]
u_{opt}	superficial gas velocity that brings about the maximum heat transfer coefficient, [ms^{-1}]
u_x	(u_o-u_{mf}), excess superficial gas velocity, [ms^{-1}, ms^{-1} at T_∞,p in equation (3.10)]
v	velocity of material flowing past a point, [ms^{-1}]
v_p	speed of particles striking a surface, [ms^{-1}]
v_r	velocity of material flowing past a point in the radial direction, [ms^{-1}]
V_b	volume of the immersed body, [m^3]
x	linear position, [m]
x	diameter of the bond neck between two sintering spheres, [m]
x	position of a point relative to the centre of the distributor in Cartesian coordinates, [{m, m, m}]
x^*	x/δ, dimensionless linear position, [-]
$x_{expt\ i}$	experimental data point i, Appendix F, [various units]
$x_{pred\ i}$	predicted value corresponding to data point i, Appendix F, [various units]
X	$(u_o-u_{mf})/u_{mf}$ or $(\mathcal{R}_e/k_e)$, equation (5.10), [-] or [$kgm^{0.3}s^{-3.1}$], respectively

X coefficient of nodal equations, Appendix D, [various units]

Y coefficient of nodal equations, Appendix D, [various units]

Y_m Youngs modulus of an eroding surface, [Pa]

z vertical position, [m]

z_h height of the bottom of the U-tube heater above the distributor, [m]

Z $\rho_b c_{pb}/(2\rho c_p)$, heat capacity parameter, [-]

Z coefficient of nodal equations, Appendix D, [$Wm^{-1}K^{-1}$]

ZY $\left(\frac{\rho c_p}{\rho c_{pb}}\right)\left(\frac{k}{hL_b}\right)\left(\frac{T_{bo}-T_m}{T_m-T_\infty}\right)$, parameter of Abuaf and Gutfinger (1973), [-]

Greek Symbols

α thermal diffusivity of the coating, [m^2s^{-1}]

α_e effective thermal diffusivity of the fluidized bed, [m^2s^{-1}]

α_g thermal diffusivity of the fluidizing gas, [m^2s^{-1}]

γ surface tension, [Nm^{-1}]

δ thickness of the coating on a flat plate, [m]

δ average thickness of the gas lens between a particle and an immersed surface in the model of Xavier and Davidson (1981, 1985), [m]

δ_s steady state thickness of the coating on a flat plate that would be obtained if the plate were to remain at its initial temperature, [m]

ε bulk porosity of a fluidized bed (includes emulsion voids + bubbles), [-]

ε porosity of the coating layer, [-]

ε_o initial porosity, [-]

ε_b bubble fraction (fraction of bed volume occupied by bubbles), [-]

ΔL change in length of a linear particle chain, [m]

ΔH	enthalpy of fusion of the coating, [Jkg^{-1}]
ΔP_{bed}	pressure drop over the fluidized bed, Figure 3.3, [cm of H_2O]
Δt	integration time step, [s]
Δt^*	$\alpha \Delta t / r_b^2$, dimensionless integration time step, [-]
Δt_{base}	base time step of the integration, [s]
Δt_j	time step for substep j of the integration, [s]
$\Delta t_{substep}$	time step for a substep of the integration, [s]
θ	impact angle of particles striking a surface ($\theta = \pi/2$ indicates normal impact), [radians]
θ	inclination angle of a tube ($\theta = 0$ indicates that the tube is horizontal), [radians]
θ	local inclination angle of the U-tube heater ($\theta = 0$ indicates that the tube is locally horizontal), [radians]
μ	viscosity, [Pas]
μ_g	viscosity of the fluidizing gas, [Pas]
ρ	density of the coating, [kgm^{-3}]
ρ_b	density of the immersed body, [kgm^{-3}]
ρ_f	density of a fluid, [kgm^{-3}]
ρ_g	density of the fluidizing gas, [kgm^{-3}]
ρ_{mf}	bulk density of a fluidized bed at minimum fluidization conditions, [kgm^{-3}]
ρ_p	density of the particles, [kgm^{-3}]
ρ_p	density of a solid, [kgm^{-3}]
τ	age of the coating, [s]
ψ	approximate sphericity of the particles, [-]

Superscripts

+	just above
-	just below
'	value at the end of the time step, Appendix D

Subscripts

1	lower limit
2	upper limit
1, 2,...	various values forming a group
st	steady state conditions

REFERENCES

Abuaf, N. and Gutfinger, C., 1973, Heat Transfer with a Moving Boundary: Application to Fluidized-Bed Coating of Thin Plates, *Int. J. Heat Mass Transfer* **16**, 213-216.

Adams, R.L., 1982, An Approximate Model of Bubble Phase Convective Heat Transfer to a Horizontal Tube in a Large Particle Fluid Bed, *J. Heat Transfer - Trans. ASME* **104**, 565-567.

Agarwal, P.K., 1985, Bubble Characteristics in Gas Fluidized Beds, *Chem. Eng. Res. Des.* **63**, 323-337.

Agarwal, P.K. and O'Neill, B.K., 1988, Transport Phenomena in Multi-Particle Systems - I. Pressure Drop and Friction Factors: Unifying the Hydraulic-Radius and Submerged-Object Approaches, *Chem. Engng Sci.* **43**(9), 2487-2499.

Aghamohammadi, B. and Durai-Swamy, K., 1993, A Disposal Alternative for Sludge Waste from Recycled Paper and Cardboard, Paper presented at the 1993 TAPPI Engineering Conference, Orlando, Florida, September 1993.

Ahmed, S., 1989, Fluidized Bed Coating, *J. Inst. Eng. (India) Part T3* **69**, 87-92.

Askeland, D.R., 1990, *The Science and Engineering of Materials*, 2nd SI Edition, p134-136, Chapman and Hall, London.

Bankoff, S.G., 1964, Heat Conduction or Diffusion with Change of Phase, in *Advances in Chemical Engineering* **5**, p75-150, Academic Press, New York.

Bayat, F., Levy, E.K. and Alkan, I., 1990, Analysis of the Effects of Bubble Coalescence on Tube Wastage, *AIChE Symp. Ser.* **86**(276), 1-9.

Bellman Jnr, R. and Levy, A., 1981, Erosion Mechanism in Ductile Metals, *Wear* **70**(1), 1-27.

Berg, B.V., Baskakov, A.P. and Seréétériin, B., 1974, Local Heat Transfer between a Vertical Cylinder and a Fluidized Bed, *J. Eng. Phys.* **21**(6), 1484-1488. [English Translation of Russian *Inzhenerno-Fizicheskii Zhurnal* **21**(6), p985-991]

Bird, R.B., Stewart, W.E. and Lightfoot, E.N., 1960, *Transport Phenomena*, John Wiley & Sons, New York.

Bitter, J.G.A., 1963a, A Study of Erosion Phenomena: Part I, *Wear* **6**(1), 5-21.

Bitter, J.G.A., 1963b, A Study of Erosion Phenomena: Part II, *Wear* **6**(3), 169-190.

Black, N.P., 1991, Biomass Gasification Project Gets Funding to Solve Black Liquor Safety and Landfill Problems, *Tappi J.* **74**(2), 65-68.

Bouillard, J.X. and Lyczkowski, R.W., 1991, On the Erosion of Heat Exchanger Tube Banks in Fluidized-Bed Combustors, *Powder Technol.* **68**, 37-51.

Bouillard, J.X., Lyczkowski, R.W., Folga, S., Gidaspow, D. and Berry, G.F., 1989, Hydrodynamics of Erosion of Heat Exchanger Tubes in Fluidized Bed Combustors, *Can. J. Chem. Eng.* **67**, 218-229.

Carslaw, H.S. and Jaeger, J.C., 1959, *Conduction of Heat in Solids*, 2nd Edition, Ch. 11, Oxford University Press, Oxford.

Clift, R., 1993, An Occamist Review of Fluidized Bed Modelling, *AIChE Symp. Ser.* **89**(296), 1-17.

Clift, R. and Grace, J.R., 1985, Continuous Bubbling and Slugging, in *Fluidization*, 2nd Edition (Edited by Davidson, J.F., Clift, R. and Harrison, D.), p73-132, Academic Press, London.

Coble, R.L. and Burke, J.E., 1963, Sintering in Ceramics, in *Progress in Ceramic Science* (Edited by Burke, J.E.), Vol. 3, p197-251, Pergamon Press, Oxford.

Compo, P.C., 1989, *Thermally-Induced Agglomeration in Fluidized Beds*, Ph.D. Thesis, The City University of New York.

Coulson, J.M., Richardson, J.F. and Sinnott, R.K., 1989, *Chemical Engineering*, Vol. 6 (An Introduction to Chemical Engineering Design), Pergamon Press, Oxford.

Crank, J., 1984, *Free and Moving Boundary Problems*, Clarendon Press, Oxford.

Darton, R.C., LaNauze, R.D., Davidson, J.F. and Harrison, D., 1977, Bubble Growth due to Coalescence in Fluidised Beds, *Trans. Instn Chem. Engrs* **55**, 274-280.

Deffenbaugh, D.M. and Green, S.T., 1987, Transient Heat Transfer and Bubble Dynamics in a Pressurized Fluidized Bed, *Int. J. Heat Mass Transfer* **30**(10), 2151-2160.

de Jong, B.H.W.S, 1989, Glass, in *Ullmann's Encyclopedia of Industrial Chemistry* (Edited by Elvers, B., Hawkins, S., Ravenscroft, M., Rounsaville, J.F. and Schulz, G.) 5th Edition, Vol. A.12, p364-432, VCH Verlagsgesellschaft mbH, Weinheim, F.R.G.

Ding, J. and Lyczkowski, R.W., 1992, Three-Dimensional Kinetic Theory Modeling of Hydrodynamics and Erosion in Fluidized Beds, *Powder Technol.* **73**, 127-138.

Ding, J., Lyczkowski, R.W., Burge, S.W. and Gidaspow, D., 1992, Three-Dimensional Models of Hydrodynamics and Erosion in Fluidized-Bed Combustors, *AIChE Symp. Ser.* **88**(289), 85-98.

Ducamp, V.C. and Raj, R., 1989, Shear and Densification of Glass Powder Compacts, *J. Am. Ceram. Soc.* **72**(5), 798-804.

Dullien, F.A.L., 1979, *Porous Media - Fluid Transport and Pore Structure*, Academic Press, New York.

Durai-Swamy, K., Warren, D.W. and Mansour, M.N., 1991, Indirect Steam Gasification of Paper Mill Sludge Waste, *Tappi J.* **74**(10), 137-143.

Elmas, M., 1970, On Heat Transfer with Moving Boundary, *Int. J. Heat Mass Transfer* **13**, 1625-1627.

Elmas, M., 1973, *Fluidised Bed Powder Coating,* Power Technology Publication Series No. 5, Dorset Press, Dorchester, U.K.

Ennis, B.J., Li, J., Tardos, G.I. and Pfeffer, R., 1990, The Influence of Viscosity on the Strength of an Axially Strained Pendular Liquid Bridge, *Chem. Engng Sci.* **45**(10), 3071-3088.

Ennis, B.J., Tardos, G.I. and Pfeffer, R., 1991, A Microlevel-Based Characterization of Granulation Phenomena, *Powder Technol.* **65**, 257-272.

Exner, H.E. and Petzow, G., 1975, Shrinkage and Rearrangement during Sintering of Glass Spheres, in *Sintering and Catalysis* (Edited by Kuczynski, G.C.), *Mater. Sci. Res.* Vol. 10, p279-293, Plenum Press, New York.

Exner, H.E. and Petzow, G., 1980, A Critical Evaluation of Shrinkage Equations, in *Sintering Processes* (Edited by Kuczynski, G.C.), *Mater. Sci. Res.* Vol. 13, p107-120, Plenum Press, New York.

Finnie, I., 1960, Erosion of Surfaces by Solid Particles, *Wear* **3**, 87-103.

Flamant, G., Fatah, N., Olalde, G. and Hernandez, D., 1992, Temperature Distribution near a Heat Exchanger Wall Immersed in High-Temperature Packed and Fluidized Beds, *J. Heat Transfer - Trans. ASME* **114**, 50-55.

Flamant, G., Lu, J.D. and Variot, B., 1993, Towards a Generalized Model for Vertical Walls to Gas-Solid Fluidized Beds Heat Transfer - II. Radiative Transfer and Temperature Effects, *Chem. Engng Sci.* **48**(13), 2493-2503.

Gelperin, N.I., Ainshtein, V.G. and Romanova, N.A., 1964, On the Effect of the Height of the Heat-Exchange Surface on the Heat-Transfer Coefficient in a Fluidized Bed, *Int. Chem. Engng* **4**(3), 502-505.

Gelperin, N.I. and Einstein, V.G., 1971, Heat Transfer in Fluidized Beds, in *Fluidization* (Edited by Davidson, J.F. and Harrison, D.), p471-540, Academic Press, London.

German, R.M., 1984, *Powder Metallurgy Science*, p145-200, Metal Powder Industries Federation, Princeton.

Gidaspow, D. and Ettehadieh, B., 1983, Fluidization in Two-Dimensional Beds with a Jet. 2. Hydrodynamic Modeling, *Ind. Eng. Chem. Fundam.* **22**(2), 193-201.

Grewal, N.S. and Saxena, S.C., 1979, Effect of Surface Roughness on Heat Transfer from Horizontal Immersed Tubes in a Fluidized Bed, *J. Heat Transfer - Trans. ASME* **101**, 397-403.

Grewal, N.S. and Saxena, S.C., 1980, Heat Transfer between a Horizontal Tube and a Gas-Solid Fluidized Bed, *Int. J. Heat Mass Transfer* **23**(11), 1505-1519.

Gunn, D.J. and Al-Doori, H.H., 1985, The Measurement of Bubble Flows in Fluidized Beds by Electrical Probe, *Int. J. Multiphase Flow* **11**(4), 535-551.

Gururajan, V.S., Agarwal, P.K. and Agnew, J.B., 1992, Mathematical Modelling of Fluidized Bed Coal Gasifiers, *Trans. Instn Chem. Engrs Part A* **70**, 211-238.

Gutfinger, C. and Chen, W.H., 1969, Heat Transfer with a Moving Boundary - Application to Fluidized-Bed Coating, *Int. J. Heat Mass Transfer* **12**, 1097-1108.

Gutfinger, C. and Chen, W.H., 1970, An Approximate Theory of Fluidized-Bed Coating, *Chem. Engng Prog. Symp. Ser.* **66**(101), 91-100.

Hager, W.R. and Thomson, W.J., 1973, Bubble Behaviour around Immersed Tubes in a Fluidized Bed, *AIChE Symp. Ser.* **69**(128), 68-77.

Holman, J.P., 1989, *Heat Transfer*, SI Metric Edition, p134-135, McGraw-Hill, Singapore.

Hosny, N. and Grace, J.R., 1984, Forces on a Tube Immersed within a Fluidized Bed, in *Fluidization IV* (Edited by Kunii, D. and Toei, R.), p111-120, Engineering Foundation, New York.

Huang, C.-C., 1986, *The Granulation and Rehydration of Alumina Powders*, Ph.D. Thesis, West Virginia University.

Huang, C.-S., 1985, *Fundamentals of Agglomeration in a Fluidized Bed*, Ph.D. Thesis, Illinois Institute of Technology.

Hutchings, I.M., 1987, Wear by Particulates, *Chem. Engng Sci.* **42**(4), 869-878.

Jagota, A., Mikeska, K.R. and Bordia, R.K., 1990, Isotropic Constitutive Model for Sintering Particle Packings, *J. Am. Ceram. Soc.* **73**(8), 2266-2273.

Jen, C.O. and Tsao, K.C., 1980, Coal-Ash Agglomeration Mechanism and Its Application in High Temperature Cyclones, *Sep. Sci. Technol.* **15**(3), 263-276.

Kılkış, B., 1991, Computer-Aided Analysis of Fluidized Bed to External Wall Local Heat Transfer, *Chem. Engng J.* **46**, 47-60.

Kingery, W.D., 1965, *Introduction to Ceramics*, John Wiley & Sons, New York.

Klose, W. and Lent, M., 1985, Agglomeration Kinetics of Coking Coal Particles during the Softening Phase, *Fuel* **64**, 193-199.

Kreyszig, E., 1983, *Advanced Engineering Mathematics*, 5th Edition, p830-832, John Wiley & Sons, New York.

Kuczynski, G.C., 1972, Physics and Chemistry of Sintering, *Advan. Colloid Interface Sci.* **3**, 275-330.

Kuczynski, G.C., 1975, Statistical Approach to the Theory of Sintering, in *Sintering and Catalysis* (Edited by Kuczynski, G.C.), *Mater. Sci. Res.* Vol. 10, p325-337, Plenum Press, New York.

Kuipers, J.A.M., Prins, W. and van Swaaij, W.P.M., 1992, Numerical Calculation of Wall-to-Bed Heat-Transfer Coefficients in Gas-Fluidized Beds, *AIChE J.* **38**(7), 1079-1091.

Kunii, D. and Levenspiel, O., 1991, *Fluidization Engineering*, 2nd Edition, Butterworth-Heinemann, Boston.

Kurosaki, Y., Ishiguro, H. and Takahashi, K., 1988, Fluidization and Heat-Transfer Characteristics around a Horizontal Heated Circular Cylinder Immersed in a Gas Fluidized Bed, *Int. J. Heat Mass Transfer* **31**(2), 349-358.

Landau, H.G., 1950, Heat Conduction in a Melting Solid, *Q. Appl. Math.* **8**(1), 81-94.

Landrock, A.H., 1965, Fluidized-Bed Coating, in *Encyclopedia of Polymer Science and Technology*, Vol. 3, p808-830, John Wiley & Sons, New York.

Levy, E., Wagh, M., Sethu, H. and Pinarbasi, A., 1992, Pattern Recognition Analysis of Bubbles Impacting on Tubes, *Powder Technol.* **70**, 175-181.

Liley, P.E., Reid, R.C. and Buck, E., 1985, Physical and Chemical Data, in *Perry's Chemical Engineers' Handbook* (Edited by Perry, R.H., Green, D.W. and Maloney, J.O.), 6th Edition, Ch.3, McGraw-Hill, Singapore.

Lim, K.S., 1992, *Digital Image Analysis Study of Bubbling, Solids Mixing and Segregation in Fluidized Beds*, Ph.D. Thesis, The University of Adelaide.

Lin, J.S., Chen, M.M. and Chao, B.T., 1985, A Novel Radioactive Particle Tracking Facility for Measurement of Solids Motion in Gas Fluidized Beds, *AIChE J.* **31**(3), 465-473.

Liu, Y. and Levy, A.V., 1991, The Influence of Test Parameters on Material Wastage in a Fluidized Bed Wear Test Rig, *Wear* **151**, 365-379.

Livshits, Yu. Ye., Tamarin, A.I. and Zabrodskiy, S.S., 1978, Maximum Forces Acting on a Body Immersed in a Fluidized Bed, *Fluid Mech. - Soviet Res.* **7**(3), 30-36.

Lu, J.D., Flamant, G. and Snabre, P., 1993, Towards a Generalized Model for Vertical Walls to Gas-Solid Fluidized Beds Heat Transfer - I. Particle Convection and Gas Convection, *Chem. Engng Sci.* **48**(13), 2479-2492.

Mackenzie, J.K. and Shuttleworth, R., 1949, A Phenomenological Theory of Sintering, *Proc. Phys. Soc., London Part B* **62**(12), 833-852

Mann, M.D., Kalmanovitch, D.P. and Hajicek, D.R., 1987, Boiler Tube Corrosion/Erosion/Deposition Resulting from Fluidized Bed Combustion, Paper presented at the Joint ASME/IEEE Power Generation Conference, Miami Beach, Florida, Oct. 4-8, 1987, ASME paper: 87-JPGC-FACT-9.

Mann, M.D., Kalmanovitch, D.P. and Hajicek, D.R., 1991, *Topical Report: Corrosion, Erosion and Deposition of AFBC Boiler Tube Surfaces,* Energy & Environmental Research Center, University of North Dakota.

Mazzone, D.N., 1986, *Agglomeration of Particles in Fluidized Beds*, Ph.D. Thesis, The City University of New York.

Meijer, J.A.M., 1983, Prevention of Calcium Sulfate Scale Deposition by a Fluidized Bed, *Desalination* **47/IV**, 3-15.

Meirmanov, A.M., 1992, *The Stefan Problem,* de Gruyter Expositions in Mathematics 3, Walter de Gruyter, Berlin.

Mickley, H.S. and Fairbanks, D.F., 1955, Mechanism of Heat Transfer to Fluidized Beds, *AIChE J.* **1**(3), 374-384.

Neilson, J.H. and Gilchrist, A., 1968, Erosion by a Stream of Solid Particles, *Wear* **11**(2), 111-122.

Nguyen, T.H. and Grace, J.R., 1978, Forces on Objects Immersed in Fluidized Beds, *Powder Technol.* **19**, 255-264.

Nieh, S., Lee, S.W. and Fu, T.T., 1991, Effects of Tube Orientation and Gas Velocity on the Erosion of a Tube Inserted into a Fluidized Bed, *Powder Technol.* **67**, 229-235.

Noack, R., 1970, Lokaler Wärmeübergang an horizontalen Rohren in Wirbelschichten, *Chemie-Ing.-Techn.* **42**(6), 371-376. [In German]

Ozkaynak, T.F. and Chen, J.C., 1980, Emulsion Phase Residence Time and Its Use in Heat Transfer Models in Fluidized Beds, *AIChE J.* **26**(4), 544-550.

Patankar, S.V., 1980, *Numerical Heat Transfer and Fluid Flow*, Hemisphere, Washington.

Press, W.H., Flannery, B.P., Teukolsky, S.A., and Vetterling, W.T., 1989, *Numerical Recipes in Pascal*, Cambridge University Press, Cambridge.

Rabinovich, E.M., 1985, Preparation of Glass by Sintering, *J. Mater. Sci.* **20**(11), 4259-4297.

Rafailidis, S.V., Clift, R., Addis, E.J., Bagshaw, W., Cheesman, D.J. and Yates, J.G., 1992, The Effect of Horizontal Tubes on Bubble Motion, in *Fluidization VII*, (Edited by Potter, O.E. and Nicklin, D.J.), p875-883, Engineering Foundation, New York.

Rahaman, M.N., De Jonghe, L.C., Scherer, G.W. and Brook, R.J., 1987, Creep and Densification during Sintering of Glass Powder Compacts, *J. Am. Ceram. Soc.* **70**(10), 766-774.

Rehmat, A., Huang, C., Carty, R., Hariri, H. and Arastoopour, H., 1988, *ACS Div. Fuel Chem.* **33**(2), 176-187.

Reid, R.C., Prausnitz, J.M. and Poling, B.E., 1987, *The Properties of Gases and Liquids*, 4th Edition, p530-535, McGraw-Hill, New York.

Richart, D.S., 1985, Powder Coating, in *Encyclopedia of Polymer Science and Engineering*, 2nd Edition, Vol. 3, p575-601, John Wiley & Sons, New York.

Rowe, P.N. and Everett, D.J., 1972, Fluidised Bed Bubbles Viewed by X-Rays Part I - Experimental Details and the Interaction of Bubbles with Solid Surfaces, *Trans. Instn Chem. Engrs* **50**(1), 42-48.

Rumpf, H., Sommer, K. and Steier, K., 1978, The Effect of Plastic Deformation, Sintering, and Viscoelastic Flow on Particle Adhesion, *Int. Chem. Engng* **18**(4), 558-565.

Saxena, S.C. and Vogel, G.J., 1977, The Measurement of Incipient Fluidisation Velocities in a Bed of Coarse Dolomite at Temperature and Pressure, *Trans. Instn Chem. Engrs* **55**(3), 184-189.

Saxena, S.C., Grewal, N.S., Gabor, J.D., Zabrodsky, S.S. and Galershtein, D.M., 1978, Heat Transfer between a Gas Fluidized Bed and Immersed Tubes, in *Advances in Heat Transfer* **14**, p149-247, Academic Press, New York.

Saxena, S.C., 1989, Heat Transfer between Immersed Surfaces and Gas-Fluidized Beds, in *Advances in Heat Transfer* **19**, p97-190, Academic Press, San Diego.

Scherer, G.W., 1977, Sintering of Low-Density Glasses: I, Theory, *J. Am. Ceram. Soc.* **60**(5-6), 236-239.

Schofield, P.A., Minchener, A.J., Sutcliffe, P.T. and Stringer, J., 1990, The Effect of Deposit Build-Up on Surface Oxygen Levels of AFBC Heat-Exchangers, *J. Inst. Energy* **LXIII**(455), 61-69.

Sharp, D.E. and Ginther, L.B., 1951, Effect of Composition and Temperature on the Specific Heat of Glass, *J. Am. Ceram. Soc.* **34**(9), 260-271.

Siegell, J.H., 1976, *Defluidization Phenomena in Fluidized Beds of Sticky Particles at High Temperatures*, Ph.D. Thesis, The City University of New York.

Sitnai, O. and Whitehead, A.B., 1985, Immersed Tubes and Other Internals, in *Fluidization*, 2nd Edition (Edited by Davidson, J.F., Clift, R. and Harrison, D.), p473-493, Academic Press, London.

Smithells, C.J. and Brandes, E.A. (Editors), 1976, *Metals Reference Book*, 5th Edition, p957, Butterworths, London.

Sparrow, E.M., Patankar, S.V. and Ramadhyani, S., 1977, Analysis of Melting in the Presence of Natural Convection in the Melt Region, *J. Heat Transfer - Trans. ASME* **99**, 520-526.

Szekely, J, 1983, Some Mathematical Physical and Engineering Aspects of Melting and Solidification Problems, in *Free Boundary Problems: Theory and Applications* (Edited by Fasano, A. and Primicerio, M.), Vol. I, p283-292, Research Notes in Mathematics 78, Pitman Books, London.

Szekely, J. and Jassal, A.S., 1978, An Experimental and Analytical Study of the Solidification of a Binary Dendritic System, *Met. Trans.* **9B**, 389-398

ThermoChem, 1993 - Publicity material available from ThermoChem Inc., Santa Fe Springs, California, U.S.A.

Thimsen, D.P., Steen, D., Welte, A., Raatikka, L., Osthus, D. and Stallings, J.W., 1991, Fireside Tube Fouling in Two Utility Bubbling AFBC Boilers, in *Clean Energy for the World: Proceedings of the 11th International Conference on Fluidized-Bed Combustion,* Vol. 2, p631-638, ASME, New York.

Tsao, K.C., Tabrizi, H., Rehmat, A. and Mason, D.M., 1982, Coal-Ash Agglomeration Mechanism in a High Temperature Cyclone, ASME paper: 82-WA/HT-29.

Vatistas, N.T., 1992, Effect of Adhesion Time on Particle Deposition: Reentrainment and Rolling, *Ind. Eng. Chem. Res.* **31**(6), 1549-1554.

Wen, C.Y. and Yu, Y.H., 1966, Mechanics of Fluidization, *Chem. Engng Prog. Symp. Ser.* **62**(62), 100-111.

Wender, L. and Cooper, G.T., 1958, Heat Transfer Between Fluidized-solids Beds and Boundary Surfaces - Correlation of Data, *AIChE J.* **4**(1), 15-23.

Weyl, W.A. and Marboe, E.C., 1964, *The Constitution of Glasses: A Dynamic Interpretation*, Vol. II, Part One, p731-733, John Wiley & Sons, New York.

Xavier, A.M. and Davidson, J.F., 1981, Heat Transfer to Surfaces Immersed in Fluidised Beds and in the Freeboard Region, *AIChE Symp. Ser.* **77**(208), 368-373.

Xavier, A.M. and Davidson, J.F., 1985, Heat Transfer in Fluidized Beds: Convective Heat Transfer in Fluidized Beds, in *Fluidization*, 2nd Edition (Edited by Davidson, J.F., Clift, R. and Harrison, D.), p437-464, Academic Press, London.

Yates, J.G., 1987, On the Erosion of Metal Tubes in Fluidized Beds, *Chem. Engng Sci.* **42**(2), 379-380.

Yates, J.G., Cheesman, D.J., Mashingaidze, T.A., Howe, C. and Jefferis, G., 1984, The Effect of Vertical Rods on Bubbles in Gas Fluidized Beds, in *Fluidization IV* (Edited by Kunii, D. and Toei, R.), p103-110, Engineering Foundation, New York.

Zhu, J., Grace, J.R. and Lim, C.J., 1990, Tube Wear in Gas Fluidized Beds - I. Experimental Findings, *Chem. Engng Sci.* **45**(4), 1003-1015.

Zhu, J., Lim, C.J., Grace, J.R. and Lund, J.A., 1991, Tube Wear in Gas Fluidized Beds - II. Low Velocity Impact Erosion and Semi-Empirical Model for Bubbling and Slugging Fluidized Beds, *Chem. Engng Sci.* **46**(4), 1151-1156.

Appendix A:

THE IMPLEMENTATION OF LANDAU-LIKE TRANSFORMATIONS

Situations involving heat transfer to a boundary that moves because of a phase change are termed Stefan Problems. They are generally of a nonlinear nature since the position of the moving boundary is *a priori* unknown. One method of simplifying their solution is to transform the position variable so that the boundaries of the material become fixed with respect to the transformed variable. Landau (1950) is first credited with using a transformation of this type; several variations appear in Bankoff (1964). Use of any of these transformations apparently causes an "extra term" to appear in the transformed version of the energy conservation equation. By using physical arguments, the appearance of this "extra term" is explained below.

The one-dimensional energy conservation equation for a solid in rectangular coordinates is usually written as:

$$\rho c_p \frac{\partial T}{\partial t} = \frac{\partial}{\partial x}\left(k \frac{\partial T}{\partial x}\right) \tag{A.1}$$

In Stefan problems, equation (A.1) applies over a region such as $0 < x < \delta(t)$, where $\delta(t)$ is the position of the moving boundary. Frequently, a Landau-like transformation is used to make the boundaries of the solid become fixed with respect to a transformed position variable. Here, let such a variable, x^*, be defined as:

$$x^* = x / \delta(t) \qquad (A.2)$$

so that $x^* = 0$ represents the stationary boundary of the solid and $x^* = 1$ represents the moving boundary. Thus, the conservation equation is valid for $0 < x^* < 1$.

Now, with time, as $\delta(t)$ changes, the physical position in the solid represented by constant x^* changes, as illustrated in Figure A.1.

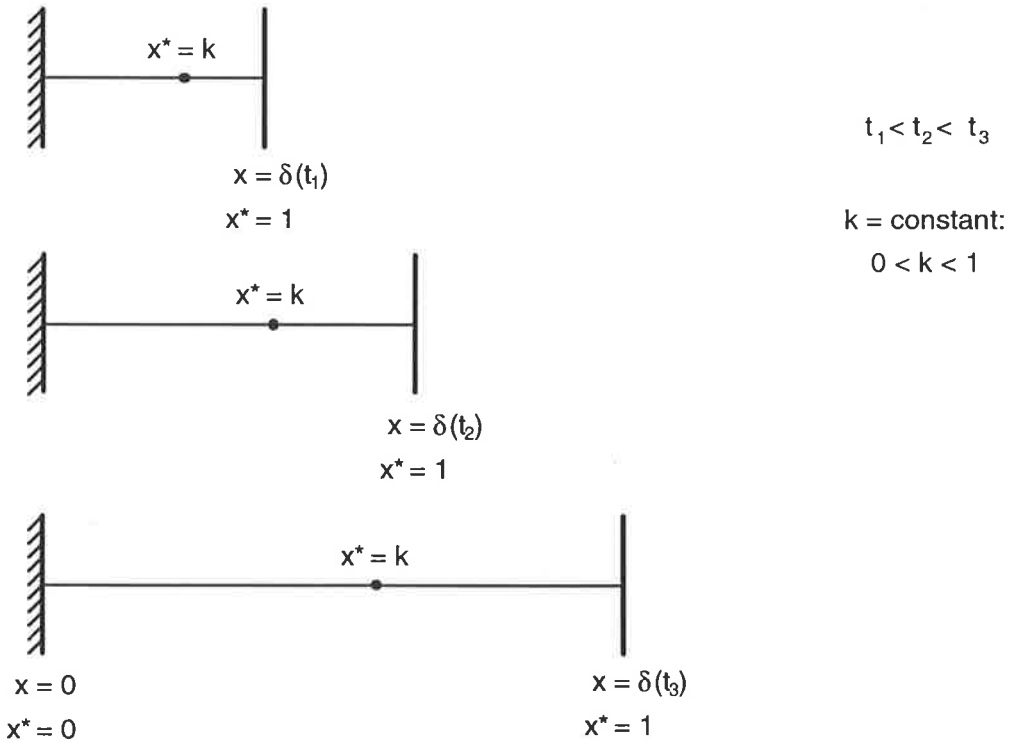

Figure A.1: Comparison of transformed and untransformed coordinates.

It can be seen that x^* = constant moves with time. Alternatively, there is a "flow" of solid material through the plane at x^* = constant. This apparent convective movement of material must be accounted for in writing the energy balance in terms of the transformed coordinate, x^*. (Recall that $\partial T/\partial t$ is the rate of change of temperature with respect to time *at a fixed point in space*.)

On including a convective component, the energy balance, equation (A.1), becomes:

$$\rho c_p \frac{\partial T}{\partial t} = \frac{\partial}{\partial x}\left(k\frac{\partial T}{\partial x}\right) - \frac{\partial}{\partial x}\left(\rho c_p T v\right) \tag{A.3}$$

where v is the velocity of the material flowing past a point. The product ρv is constant, so:

$$\rho c_p\left[\frac{\partial T}{\partial t} + v\frac{\partial T}{\partial x}\right] = \frac{\partial}{\partial x}\left(k\frac{\partial T}{\partial x}\right) \tag{A.4}$$

or:

$$\rho c_p \frac{DT}{Dt} = \frac{\partial}{\partial x}\left(k\frac{\partial T}{\partial x}\right) \tag{A.5}$$

where DT/Dt is a substantial derivative (Bird et al., 1960, p73). Indeed, equation (A.5) is the one-dimensional energy balance for an incompressible fluid which undergoes heat transfer by a combination of bulk flow and conduction (Bird et al., 1960, p316, eqn 10.1-25)

For the untransformed variable x, v = 0, so equation (A.5) reduces to equation (A.1), the usual conduction equation. However, for x^*,

$$v = -x^* \cdot \frac{d\delta}{dt} \tag{A.6}$$

With the aid of Figure A.1, it can be seen why the negative sign appears in equation (A.6): $x^* = k$ is moving to the right, so from the frame of reference of x^*, the material is moving to the left. It should be noted that at $x^* = 0$, $v = 0$ and at $x^* = 1$, $v = -d\delta/dt$ as expected.

Finally, using $dx^* = (1/\delta)dx$, we may write the transformed version of the energy conservation equation:

$$\rho c_p \left[\frac{\partial T}{\partial t} - \frac{x^*}{\delta} \cdot \frac{d\delta}{dt} \cdot \frac{\partial T}{\partial x^*} \right] = \frac{1}{\delta^2} \cdot \frac{\partial}{\partial x^*} \left(k \frac{\partial T}{\partial x^*} \right) \qquad \text{(A.7)}$$

The second term in the square brackets of equation (A.7) is the "extra term" referred to earlier.

A very concise mathematical derivation of equation (A.7) is given in Crank (1984, p187).

Appendix B:

TRANSFORMATION OF THE ENERGY BALANCE IN THE COATED LAYER BY EQUATION (4.20)

The one-dimensional radial heat conduction equation for a solid is usually written as:

$$\rho c_p \frac{\partial T}{\partial t} = \frac{1}{r} \frac{\partial}{\partial r}\left(k\, r \frac{\partial T}{\partial r}\right), \qquad r_b < r < r_c(t) \tag{B.1}$$

If one wishes to apply a Landau-like transformation to the problem, a convective term must be added (Appendix A), so that:

$$\rho c_p \frac{DT}{Dt} = \frac{1}{r} \frac{\partial}{\partial r}\left(k\, r \frac{\partial T}{\partial r}\right) \tag{B.2}$$

or

$$\rho c_p \left[\frac{\partial T}{\partial t} + v_r \frac{\partial T}{\partial r}\right] = \frac{1}{r} \frac{\partial}{\partial r}\left(k\, r \frac{\partial T}{\partial r}\right) \tag{B.3}$$

If the transformation equation (4.20), $r^* = r / r_b$, is used, then for r^* = constant,

$$v_r = \frac{dr}{dt} = r^* . \frac{dr_b}{dt} = r^* . 0,$$

that is, $v_r = 0$. Hence there is no "convective" term in the transformed version of the energy balance and (B.2) reduces to (B.1). This apparent inconsistency with the

conclusion of Appendix A is easy to reconcile. Equation (4.20) is not a transformation of the Landau type - it is based on the inner fixed radius of the coated layer, not the outer moving one, thus it does not anchor the outer boundary at a fixed value.

Appendix C:

EFFECTIVE EROSION RATE EXPERIENCED BY THE U-TUBE HEATER

The rate of erosion of a surface in a fluidized bed varies with its position and orientation. Clearly, the U-tube heater used in the experimental work is a three-dimensional object that will suffer different amounts of erosion in different places. However, the coating erosion model developed here is only one-dimensional. Thus, to compare the experimental data with the model, an effective one-dimensional erosion rate experienced by the heater must be estimated.

From a tube erosion model or experimental data, a local erosion rate, $\mathcal{R}_e(\mathbf{x},\mathbf{r})$, can be estimated. The point of interest relative to the centre of the distributor is $\mathbf{x}$, and the desired orientation is represented by $\mathbf{r}$, a vector normal to the imaginary surface at the point. It is assumed that the local erosion rate is unaffected by adjacent parts of the immersed body. This is true only to a first approximation. Under these conditions, the effective one-dimensional erosion rate, $\overline{\mathcal{R}}_e$, is given by:

$$\overline{\mathcal{R}}_e = \frac{\int_S \mathcal{R}_e(\mathbf{s},\ \nabla \mathbf{s_o})\,dA}{\int_S dA} \qquad (C.1)$$

where:

$\mathcal{S}$ represents the surface of the heater;

$\mathbf{s}$ is a vector function that defines any point on the surface of the heater with respect to an origin located on the bed's axis at the level of the distributor;

$\nabla \mathbf{s_o}$ is the outward normal vector function of the heater surface;

dA is a surface element of the heater.

Tube erosion models do not usually provide very detailed information. In this study, only the variation of the local erosion rate with height above the distributor and inclination angle of the immersed tube is available. Consequently, the calculation of $\overline{\mathcal{R}}_e$ is much simplified. The local erosion rate is now modified to become:

$$\mathcal{R}_e' = \text{fn}\,(z,\theta)$$

where z is the height above the distributor and θ is the local angle of inclination of the heater to the horizontal. The geometry of the U-tube heater is given in Figure C.1. It is convenient to consider regions I and II separately. Further, the problem is symmetrical about the line A-A, so only half of the heater will be considered in the following derivation.

Region I:

The surface area of a torus is $\pi^2 ab$ where a and b are diameters as defined in Figure C.2. Thus, over half of the heater (that is, for one quarter of a torus),

$$\int_{\mathcal{S}_I} dA = \frac{\pi^2 d_h D_h}{4} \qquad \text{(C.2)}$$

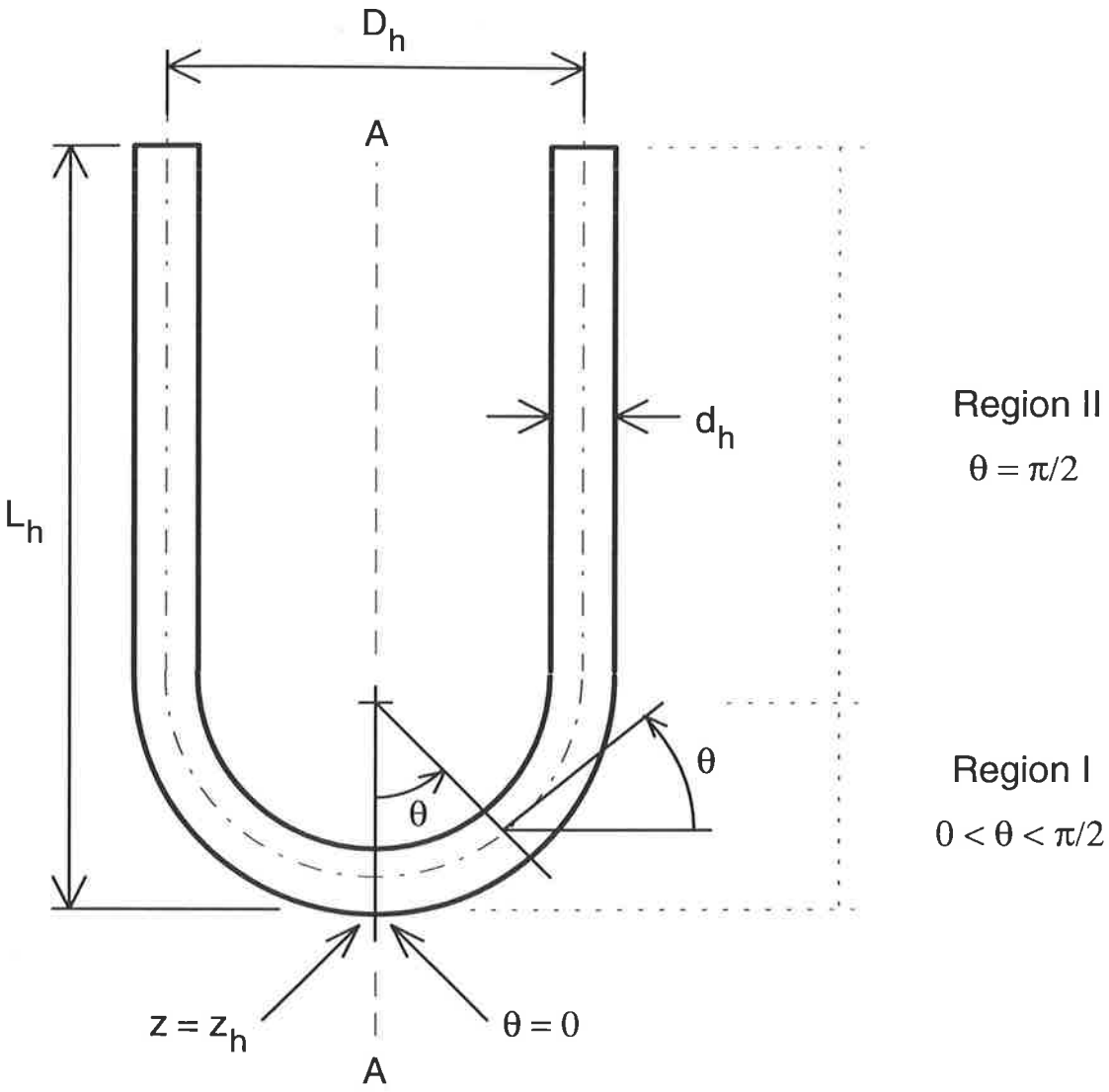

Figure C.1: Geometry of the U-tube heater defined.

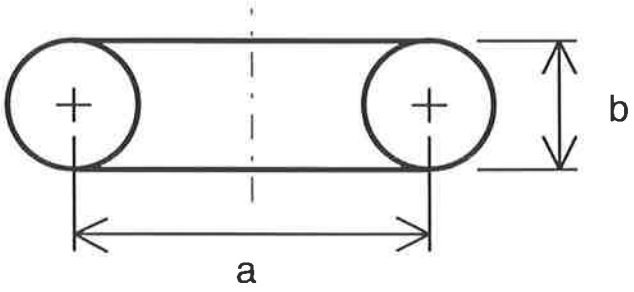

Figure C.2: Cross-section of a torus showing the definitions of diameters a and b.

and for a differential slice,

$$dA = \pi^2 d_h D_h \frac{d\theta}{2\pi} = \frac{\pi d_h D_h}{2} d\theta$$

Thus, over half of the heater,

$$\int_{\mathcal{A}_I} \mathcal{R}_e(\mathbf{s}, \nabla \mathbf{s_o}) dA = \frac{\pi d_h D_h}{2} \int_0^{\pi/2} \mathcal{R}_e'(z(\theta), \theta) d\theta \qquad \text{(C.3a)}$$

where the height above the distributor, z, is related to θ by simple geometry as:

$$z(\theta) = z_h + \frac{d_h}{2} + \frac{D_h}{2}(1-\cos\theta) \qquad \text{(C.3b)}$$

Region II

The length of the legs of the heater is (L_h - D_h/2 - d_h/2), so the surface area of one leg is:

$$\int_{\mathcal{A}_{II}} dA = \pi d_h (L_h - D_h/2 - d_h/2) \qquad \text{(C.4)}$$

and the area of a differential element is:

$$dA = \pi d_h dz$$

So, for one leg of the heater,

$$\int_{\mathcal{A}_{II}} \mathcal{R}_e(\mathbf{s}, \nabla \mathbf{s_o}) dA = \pi d_h \int_{z_1}^{z_2} \mathcal{R}_e'(z, \frac{\pi}{2}) dz \qquad \text{(C.5a)}$$

where:

$$z_1 = z_h + D_h/2 + d_h/2 \tag{C.5b}$$

$$z_2 = z_h + L_h \tag{C.5c}$$

Now, the average erosion rate may be calculated by:

$$\overline{\mathcal{R}}_e = \frac{\int_{\mathcal{S}_I} \mathcal{R}_e\,(\mathbf{s}, \nabla \mathbf{s_o})\,dA + \int_{\mathcal{S}_{II}} \mathcal{R}_e\,(\mathbf{s}, \nabla \mathbf{s_o})\,dA}{\int_{\mathcal{S}_I} dA + \int_{\mathcal{S}_{II}} dA} \tag{C.6}$$

with the individual integrals given by equations (C.2) - (C.5). The local erosion rate models are likely to involve complex functions of z and θ since they involve bed hydrodynamics. Even so, it is a reasonably straightforward matter to numerically evaluate equations (C.3a) and (C.5a).

Appendix D:

DISCRETISATION OF THE MODEL EQUATIONS

The numerical solution of the coating-erosion equations, as implemented in **CEMODEL**, was heavily based on the techniques of Patankar (1980).

Discretisation Procedure:

Spatial Discretisation:

The coating layer was discretised according to *Practice B* of Patankar (1980, Section 4.6-1); see Figure D.1. Note that the boundary control volumes (numbers *1* and *N*) have zero width.

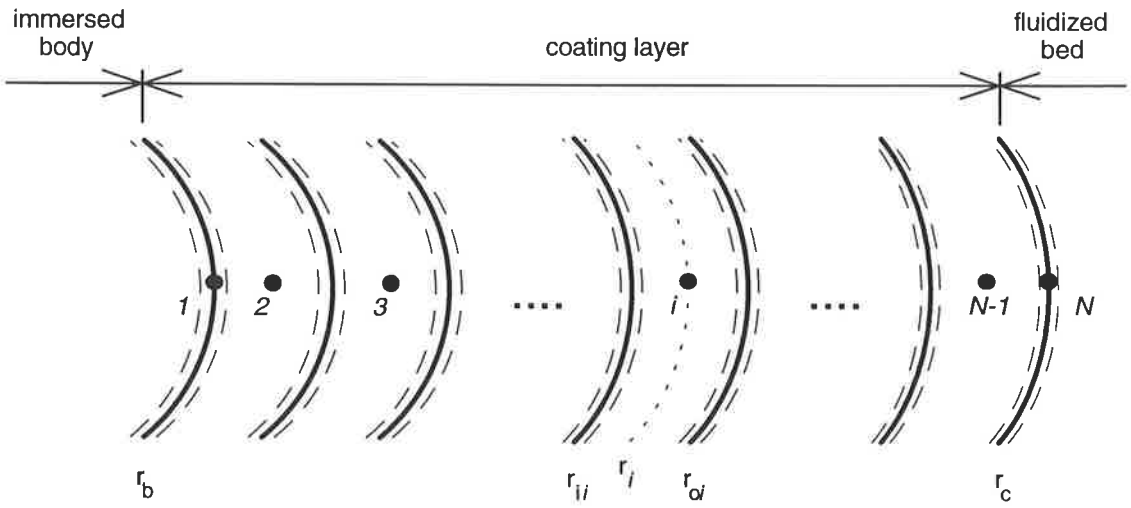

Figure D.1: Discretisation of the coating layer into control volumes.

Temporal Discretisation:

The coating-erosion model is an initial value problem, so the purpose of discretisation is to allow the calculation of "new" values of the dependant variables from their "old" values at the beginning of the time step. Patankar (1980, Section 4.3) supports the use of a first order, fully implicit scheme, in which the new values are assumed to hold over the entire time step. One advantage of this approach is that the discretised equations will reach the correct steady state even when relatively large time steps are used.

Energy Balance over the Coating Layer:

Equation (4.13) was integrated twice, with respect to time and position:

$$\int_{r_{ii}}^{r_{oi}} \int_{t}^{t+\Delta t} r\rho \frac{\partial (c_p T)}{\partial t} \, dt \, dr \quad = \quad \int_{t}^{t+\Delta t} \int_{r_{ii}}^{r_{oi}} \frac{\partial}{\partial r}\left(k\, r \frac{\partial T}{\partial r} \right) dr \, dt$$

$$\Rightarrow \quad \frac{\rho}{2}\left(r_{oi}^{\,2} - r_{ii}^{\,2}\right)\left(c_{pi}'.T_i' - c_{pi}.T_i\right)$$

$$= \int_{t}^{t+\Delta t} \left[k_{oi} r_{oi} \left(\frac{T_{i+1} - T_i}{r_{i+1} - r_i} \right) - k_{ii} r_{ii} \left(\frac{T_i - T_{i-1}}{r_i - r_{i-1}} \right) \right] dt$$

$$= \left[k_{oi}' \, r_{oi} \left(\frac{T_{i+1}' - T_i'}{r_{i+1} - r_i} \right) - k_{ii}' \, r_{ii} \left(\frac{T_i' - T_{i-1}'}{r_i - r_{i-1}} \right) \right] \Delta t$$

where the unprimed variables denote values at the beginning of the time step and primed quantities indicate values at the end of the step. Collecting like temperature terms yields the discretised equation for an *internal node* ($i = 2,\ldots N\text{-}1$) in the coating layer:

$$-ZT_{i-1}' + (X'+Y+Z)T_i' - YT_{i+1}' = XT_i \qquad \text{(D.1)}$$

where, for this equation:

$$X = \frac{\rho c_{pi}\left(r_{oi}^2 - r_{ii}^2\right)}{2\Delta t}; \qquad X' = \frac{\rho c_{pi}'\left(r_{oi}^2 - r_{ii}^2\right)}{2\Delta t};$$

$$Y = \frac{k_{oi}' r_{oi}}{r_{i+1} - r_i}; \qquad Z = \frac{k_{ii}' r_{ii}}{r_i - r_{i-1}}.$$

This procedure was performed for all of the equations that needed discretisation.

Interface Conductivity:

When the thermal conductivity of the coating is constant, the interface conductivities, k_{ii} and k_{oi} in equation (D.1), naturally obey: $k_{ii} = k_{oi} = k$. However, when the conductivity is variable, k_{ii} and k_{oi} must be some average of the thermal conductivities of the adjacent nodes. Patankar (1980, p44-47) argues that the appropriate average is one that leads to the correct prediction of the amount of energy transferred between the control volumes. It is easy to show that the energy, q, conducted between two points, $\{r_1,T_1\}$ and $\{r_2,T_2\}$, in a cylindrical system is:

$$q = \frac{T_2 - T_1}{\left[\frac{\ell n(r_1 / r_2)}{2\pi k L}\right]}$$

So, the energy transferred across the inner interface of control volume *i* based on the interface conductivity is:

$$q_{ii} = \frac{T_i - T_{i-1}}{\left[\frac{\ell n(r_{i-1} / r_i)}{2\pi k_{ii} L}\right]} \qquad \text{(D.2)}$$

Equivalently, q_{ii} may be expressed in terms of the conductivities of the adjacent control volumes as:

$$q_{ii} = \frac{T_i - T_{i-1}}{\left[\frac{\ell n(r_{ii}/r_i)}{2\pi k_i L}\right] + \left[\frac{\ell n(r_{i-1}/r_{ii})}{2\pi k_{i-1} L}\right]} \qquad \text{(D.3)}$$

So, equating (D.2) and (D.3) yields:

$$k_{ii} = \frac{\ell n(r_{i-1}/r_i)}{\left[\frac{\ell n(r_{ii}/r_i)}{k_i}\right] + \left[\frac{\ell n(r_{i-1}/r_{ii})}{k_{i-1}}\right]} \qquad \text{(D.4)}$$

and, by inspection:

$$k_{oi} = \frac{\ell n(r_i/r_{i+1})}{\left[\frac{\ell n(r_{oi}/r_{i+1})}{k_{i+1}}\right] + \left[\frac{\ell n(r_i/r_{oi})}{k_i}\right]} \qquad \text{(D.5)}$$

Patankar shows that the above averaging technique yields expressions with the correct asymptotic behaviour and which can deal with sudden changes in thermal conductivity.

Energy Balance over the Body when a Coating Layer Is Not Present:

Equation (4.10a) was discretised as follows:

$$\int_t^{t+\Delta t} m_b \frac{\partial(c_{pb} T_1)}{\partial t}\, dt = \int_t^{t+\Delta t} \left[Q_{b\,ext} - h.2\pi r_b L(T_1 - T_\infty)\right] dt$$

which implicitly uses equation (4.12), $T_b = T|_{r=r_b} = T_1$.

$$\Rightarrow \quad m_b\left(c_{pb}'.T_1' - c_{pb}.T_1\right) = \left[\overline{Q}_{b\,ext} - h'.2\pi r_b L\left(T_1' - \overline{T}_\infty\right)\right]\Delta t$$

where the quantities with overbars are evaluated at time $(t + \Delta t/2)$. Rearrangement yields the explicit relation:

$$T_1' = \frac{\overline{Q}_{b\,ext} + Y\overline{T}_\infty + XT_1}{X' + Y} \qquad \text{(D.6)}$$

where, for this equation:

$$X = \frac{m_b c_{pb}}{\Delta t}\ ; \qquad X' = \frac{m_b c_{pb}'}{\Delta t}\ ; \qquad Y = h'.2\pi r_b L\ .$$

Energy Balance over the Body when a Coating Layer Is Present:

Equation (4.10b) may be discretised as:

$$\int_t^{t+\Delta t} m_b \frac{\partial (c_{pb} T_1)}{\partial t} dt = \int_t^{t+\Delta t} \left[Q_{b\,ext} - \left(-k.2\pi r_b L \frac{\partial T}{\partial r}\bigg|_{r=r_b} \right) \right] dt \qquad (D.7)$$

again by using equation (4.12).

$$\Rightarrow \quad m_b \left(c_{pb}'.T_1' - c_{pb}.T_1 \right) = \left[\overline{Q}_{b\,ext} + k_2'.2\pi r_b L \left(\frac{T_2' - T_1'}{r_2 - r_1} \right) \right] \Delta t$$

Note that the thermal conductivity of the second node appears in the above equation since the first control volume has zero width. As before, like terms are collected, so:

$$(X'+Y)T_1' - YT_2' = \overline{Q}_{b\,ext} + XT_i \qquad (D.8)$$

where, for this equation:

$$X = \frac{m_b c_{pb}}{\Delta t}\ ; \qquad X' = \frac{m_b c_{pb}'}{\Delta t}\ ; \qquad Y = \frac{k_2' 2\pi r_b L}{r_2 - r_1}\ .$$

Energy Balance over the Coating/Bed Interface when Coating Formation Does Not Take Place:

Equation (4.15a) may be discretised as:

$$\int_t^{t+\Delta t} -k.2\pi r_c L \frac{\partial T}{\partial r}\bigg|_{r=r_c} dt = \int_t^{t+\Delta t} h.2\pi r_c L \left(T|_{r=r_c} - T_\infty \right) dt$$

$$\Rightarrow \quad -k_{N-1}'\left(\frac{T_N'-T_{N-1}'}{r_N-r_{N-1}}\right)\Delta t \;=\; h'\left(T_N'-\overline{T}_\infty\right)\Delta t$$

As above, the thermal conductivity of the (N-1)th node appears in the expression since the Nth control volume has zero width. Collecting like terms gives:

$$-XT_{N-1}' + (X+1)T_N' \;=\; \overline{T}_\infty \qquad \text{(D.9)}$$

where, for this equation:

$$X \;=\; \frac{k_{N-1}'}{h'\left(r_N-r_{N-1}\right)}\,.$$

Energy Balance over the Coating/Bed Interface when Coating Formation Takes Place. I. Existing Coating Layer:

In line with the fully implicit approach that was adopted for the discretisation, it was assumed that the new coating that forms in a time step appears in full at the beginning of the step. However, the control volumes are not repositioned until the end of the time step. Consequently, when coating formation is active, node *N* is not on the coating/bed interface in the current time step, but remains in its position from the previous time step. The situation is clarified in Figure D.2.

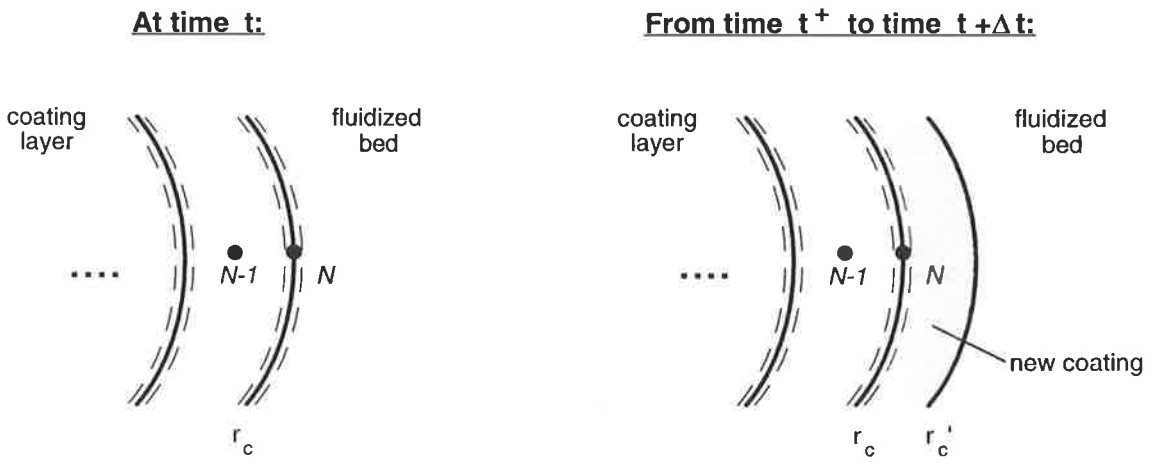

Figure D.2: Discretisation used for new coating formation.

During the time step, at node N, heat is transferred solely by conduction:

$$-k.2\pi r_c L\left.\frac{\partial T}{\partial r}\right|_{r=r_c^-} = -k.2\pi r_c L\left.\frac{\partial T}{\partial r}\right|_{r=r_c^+} \qquad (D.10)$$

$$\Rightarrow \quad k_{N-1}'\left(\frac{T_N'-T_{N-1}'}{r_N-r_{N-1}}\right) = \hat{k}'\left(\frac{T_s-T_{N-1}'}{r_c'-r_N}\right)$$

since the temperature profile in the new part of the coating is assumed to be linear. In equation (D.10), $\hat{k}'$ is the thermal conductivity of the coating evaluated at the temperature $(T_N'+T_s)/2$. Once again, like terms are collected:

$$-XT_{N-1}' + (X+Y)T_N' = YT_s \qquad (D.11)$$

where, for this equation:

$$X = k_{N-1}'(r_c'-r_N); \qquad Y = \hat{k}'(r_N-r_{N-1}).$$

An energy balance over the newly-formed part of the coating allows the simultaneous solution of r_c' and the nodal temperatures, $T_1,\ldots T_N$. Note that the mass balance over the coating layer, equation (4.16), is included implicitly in these discretised equations. Over a time interval Δt, the amount of energy conducted into the new coating is:

$$E_{cond} = -\hat{k}'.2\pi r_N L.B.\Delta t \qquad (D.12)$$

and the amount lost to the bed by convection is:

$$E_{conv} = h'.2\pi r_c' L(T_s-\overline{T}_\infty)\Delta t \qquad (D.13)$$

The amount of energy required to form the new part of the coating is:

$$E_{coat} = \int_{r_N}^{r_c'} \rho c_p(T(r)-T_\infty).2\pi rL\,dr$$

and, if it is assumed that the temperature profile in this region is linear, then it can be shown that:

$$E_{coat} = \rho \hat{c}_p' 2\pi L\left[\frac{A}{2}\left(r_c'^2 - r_N^2\right) + \frac{B}{3}\left(r_c'^3 - r_N^3\right)\right] \qquad (D.14)$$

where, for these equations:

$$A = T_N' - \overline{T}_\infty - B.r_N; \qquad B = \left(\frac{T_s - T_N'}{r_c' - r_N}\right).$$

Energy Balance over the Coating/Bed Interface when Coating Formation Takes Place. II. No Initial Coating Layer:

Using arguments similar to those above, the discretisation of equation (D.7) becomes in this case:

$$m_b\left(c_{pb}'.T_I' - c_{pb}.T_I\right) = \left[\overline{Q}_{b\,ext} + \hat{k}'.2\pi r_b L\left(\frac{T_s - T_I'}{r_c' - r_b}\right)\right]\Delta t$$

$$\Rightarrow \quad T_I' = \frac{\overline{Q}_{b\,ext} + YT_s + XT_I}{X' + Y} \qquad (D.15)$$

where, for this equation:

$$X = \frac{m_b c_{pb}}{\Delta t}; \qquad X' = \frac{m_b c_{pb}'}{\Delta t}; \qquad Y = \frac{\hat{k}'.2\pi r_b L}{r_c' - r_b}.$$

Again, over Δt:

$$E_{cond} = -\hat{k}'.2\pi r_b L.B.\Delta t \qquad (D.16)$$

$$E_{conv} = h'.2\pi r_c' L\left(T_s - \overline{T}_\infty\right)\Delta t \qquad (D.17)$$

$$E_{coat} = \rho \hat{c}_p' 2\pi L\left[\frac{A}{2}\left(r_c'^2 - r_b^2\right) + \frac{B}{3}\left(r_c'^3 - r_b^3\right)\right] \qquad (D.18)$$

where, for these equations:

$$A = T_I' - \overline{T}_\infty - B.r_b; \qquad B = \left(\frac{T_s - T_I'}{r_c' - r_b} \right).$$

Appendix E:

LISTING OF COMPUTER PROGRAM CEMODEL

The simulation program was written on an IBM-compatible personal computer in Borland International's Turbo Pascal Version 6.0. It comprises a main program, **CEMODEL**, and eight specially-written units. An EGA or VGA video adapter is required for graphical presentation of the results.

Units form the basis of modular programming in Turbo Pascal. They are collections of: constants, data-types, variables, procedures and functions. Each unit is compiled separately and its contents may be accessed by other units and programs through a **uses** clause. The **interface** section of a unit determines which parts of the unit are visible to other units and programs - it defines what is "public". In contrast, the **implementation** part contains "private" information which is only available to the particular unit in which it is defined. Functions and procedures are declared in the interface portion, but their "bodies" appear in the implementation section. If necessary, initialisation statements may be included at the end of a unit.

The contents of each unit are outlined below.

CRT *	is a unit supplied with Turbo Pascal that controls basic keyboard and text screen operation;
GRAPH *	is another predefined unit that handles the graphics screen;
VARDEFNS	includes definitions of various shared data-types, constants and variables;
EXTRAS *	contains extra maths functions and short utility routines;
PROPCOND	is used to calculate thermal and physical properties, and the bed conditions at a given time;
GETDATA *	introduces the program and allows the user to vary the model parameters;
RECIPES *	includes several numerical routines given in Press et al. (1989);
CESOLVE	contains the routines for calculating the average erosion rate, implementing the coating-erosion model and guiding its solution;
GRAPHER *	contains general graphing routines;
DISPLAY *	graphs the model predictions and writes them to a file.

In any computer program, there is a trade-off between the speed of execution and the clarity of the program's source code. It is hoped that the many comments and the use of meaningful variable names will offset much of the obscurity created in seeking fast execution times.

Note that several versions of the simulation program were developed; the one presented here is interactive and does not explicitly account for the porosity of the coating.

Due to space limitations, complete listings of all of the units could not be included.

---

* Listing not included.

CEMODEL

```
program cemodel;

{ Coating Erosion Simulation Program }

uses
  vardefns,getdata,cesolve,display;

begin

  startup;

  repeat
    setup;
    if quitprogram then
      exit;
    solve;
    savesolution;
    displaysolution
  until false

end.
```

VARDEFNS

```
unit vardefns;

{ in this unit, various shared types, constants and variables are defined }

{$N+}    { use extension of standard Pascal floating point types }


{ NB:  The program uses two symbols differently from the rest of the
thesis:
       Tm is the SINTERING TEMPERATURE of the particles
       Tmpt is the EFFECTIVE MELTING TEMPERATURE of the
particles }

interface

const
  title : string = 'Coating-Erosion Simulation Program: 4.0b
Gordon Ingram, 1993.';

  { sometimes used in place of true and false }
  no = 0;
  yes = 1;

  { types for umfmodel, dbmodel, distributor and Rerosioncalc }
  agarwal = 2;
  saxena = 3;
  wen = 4;
  expt = 5;
  darton = 6;
  porous = 7;
  perforated = 8;
  fast = 9;
  slow = 10;

  { definitions for Recipes }
  nvar = 32;     { maximum number of equations for TRIDAG }

  { other array lengths }
  nexpt = 22;     { maximum no. of experimental data points }
  ngraph = 201;    { maximum number of solution points allowed for
graphing }

type
  reallyreal = real;     { save the default definition of real }

  real = double;     { change the definition of real }

  { definitions for Recipes }
  realfntype = function(x:real):real;
  realarraynvar = array[1..nvar] of real;

  { other arrays for experimental data and graphing }
  realarraynexpt = array[1..nexpt] of real;
  RRarrayngraph = array[1..ngraph] of reallyreal;
  RRarraynvar = array[1..nvar] of reallyreal;

var

uoconst,Qbextconst,Tinfconst,cpbconst,kconst,cpconst,hconst,umfconst,
  Rerosionconst : real;
  uo_is_const,Qbext_is_const,Tinf_is_const,cpb_is_const,k_is_const,
  cp_is_const,h_is_const,umf_is_const,Rerosion_is_const,all_are_const :
byte;

  N : byte;     { number of nodes }

  umfmodel,dbmodel,distributor,Rerosioncalc : byte;


Dbed,nholes,dholes,p,Dbend,Dtube,ztube,Ltube,mb,Ab,Tbinit,Tm,Tmpt
,rhop,dp,psi,
  rho,t_end,Abeddivnh,rb,C_Zhu : real;


  Ntsteps_is_const : byte;
  Ntsteps : longint;     { number of time steps for solving the equations }

  ndata : byte;     { number of experimental data points }

  mass_expt : real;
  t_expt,Tinf_expt,Tb_expt,uo_expt,Qbext_expt : realarraynexpt;
  comment1_expt,comment2_expt : string[80];

  { variables for graphing routine }
  Gtime,Grc,GTb,GTrc : RRarrayngraph;
  nGpts : word;
  GT1,GT2,Gr1,Gr2 : RRarraynvar;
  Gtime1,Gtime2 : reallyreal;
  gotGT1,gotGT2 : boolean;

  outputfile : string;

  driver,mode : integer;     { for graphics }
  quitprogram : boolean;

  mass_pred,Tbend : real;
  exptdatafile : string;

implementation
  { nothing private here }


  { no initialisation needed for unit }
end.
```

PROPCOND

```
unit propcond;

{ this unit contains routines to determine:
   a) thermal and physical properties of the body, particles, gas and bed
   b) bed conditions at a given time }

{$N+}    { use extension of standard Pascal floating point types }

interface

uses
 vardefns;

{ procedures and functions }

 function  uo(t:real):real;
 function  Qbext(t:real):real;
 function  Tinf(t:real):real;
 function  cpb(T:real):real;
 function  k(T:real):real;
 function  cp(T:real):real;
 function  umf(Tbed,pbed:real):real;
 procedure getbubprops(var z,t,ub,fb:real);
 function  h(Tb,time:real):real;

implementation

uses
 extras,recipes;

const

 g = 9.81;     { gravitational acceleration (m.s^-2) }

 { parameters for air }
 MW = 28.96;          { molecular weight in g/gmol }
 epsoverk = 78.6;     { Leonard-Jones parameters: }
 sigma = 3.711;       {  epsoverk in K, sigma in Angstroms }

var
 Ga : real;

function uo(t:real):real;
{ returns the superficial gas velocity in the bed at time t }
var
 i:byte;
begin
 if uo_is_const = yes then
  uo := uoconst
 else
  begin
   i:=0;
   repeat
    inc(i)
   until ((t >= t_expt[i]) and (t <= t_expt[i+1])) or (i=ndata-1);
   uo := uo_expt[i] + (t-t_expt[i])/(t_expt[i+1]-t_expt[i])
                    *(uo_expt[i+1]-uo_expt[i])
  end
end;

function Qbext(t:real):real;
{ returns the rate at which energy is transferred to the immersed body
(W)
 from an external source at time t }
var
 i:byte;
begin
 if Qbext_is_const = yes then
  Qbext := Qbextconst
 else
  begin
   i:=0;
   repeat
    inc(i)
   until ((t >= t_expt[i]) and (t <= t_expt[i+1])) or (i=ndata-1);
   Qbext := Qbext_expt[i] + (t-t_expt[i])/(t_expt[i+1]-t_expt[i])
                    * (Qbext_expt[i+1]-Qbext_expt[i])
  end
end;

function Tinf(t:real):real;
{ returns the bed temperature at time t }
var
 i:byte;
begin
 if Tinf_is_const = yes then
  Tinf := Tinfconst
 else
  begin
   i:=0;
   repeat
    inc(i)
   until ((t >= t_expt[i]) and (t <= t_expt[i+1])) or (i=ndata-1);
   Tinf := Tinf_expt[i] + (t-t_expt[i])/(t_expt[i+1]-t_expt[i])
                    * (Tinf_expt[i+1]-Tinf_expt[i])
  end
end;

function rhog(T,p:real):real;
{ returns the ideal gas density at temperature T (degC) & pressure p (Pa)
}
begin
 rhog := MW*p/(8314*(T+273.15))
end;

function mu(T:real):real;
{ returns the gas viscosity at temperature T (degC) }
{ uses Chapman-Enskog theory & collision integral of Neufeld et al. as
given
 in Reid et al. (1987), eqns (9-3.9), (9-4.3) - requires
 Leonard-Jones parameters (given in Appendix B of reference). }
var
 Tstar,omegav:real;
begin
 Tstar := (T+273.15)/epsoverk;
 omegav := 1.16145*pow(Tstar,-0.14874) + 0.52487*gexp(-
0.77320*Tstar)
        + 2.16178*gexp(-2.43787*Tstar);
 mu := 26.69*sqrt(MW*(T+273.15)) / (sqr(sigma)*omegav)*1e-7
end;

function cpb(T:real):real;
{ returns the specific heat capacity of the immersed body at temperature
T }
begin
 if cpb_is_const = yes then
  cpb := cpbconst
 else
  { put variable property expression here }
  error('in CPB: variable property not implememented.')
end;

function k(T:real):real;
{ returns the thermal conductivity of the coating material at temperature
T }
```

```
begin
 if k_is_const = yes then
  k := kconst
 else
  { put variable property expression here }
  error('in K: variable property not implememented.')
end;

function cp(T:real):real;
{ returns the specific heat capacity of the coating material at temperature
T }
begin
 if cp_is_const = yes then
  cp := cpconst
 else
  { use "true specific heat" as fn(temperature) expression of Sharp &
   Ginther (1951) with composition of code 0080 glass, after unit
   conversion }
  cp := (0.00322634*sqr(T) + 4.41964*T + 743.6) / sqr(0.00146*T +
1)
end;

{$F+}
function fRemfag(Re:real):real;
{ returns zero when the correct value of Remf is given as input
according
 to the correlation of Agarwal & O'Neill (1988), eqn(35a) }
var
 phi,CD:real;
begin
 { use single sphere drag coefficient of Flemmer & Banks (1986) }
 phi := 0.261*pow(Re,0.369) - 0.105*pow(Re,0.431) -
0.124/(1+sqr(log(Re)));
 CD := 24/Re * pow(10,phi);

 fRemfag := Ga - 513*Re - 37.5*CD*sqr(Re)
end;
{$F-}

function umf(Tbed,pbed:real):real;
{ returns the minimum fluidization velocity at temperature Tbed and
 pressure pbed }
var
 rhogas,mugas,Remf:real;
begin
 if umf_is_const = yes then
  umf := umfconst
 else
  begin
   rhogas := rhog(Tbed,pbed);
   mugas := mu(Tbed);
   Ga := rhogas*(rhop-rhogas)*g*pow(dp,3)/sqr(mugas);

   if umfmodel <> expt then     { use literature correlation }
    begin
     case umfmodel of
      agarwal:
       begin     { Agarwal & O'Neill (1988) }
        Remf := sqrt(sqr(42.81)+0.061*Ga)-42.81;     { approx soln }
        Remf := zbrent(fRemfag,Remf*0.5,Remf*1.5,1e-5,0);  {
improved }
       end;
      saxena:     { Saxena & Vogel (1977)}
       Remf := sqrt(sqr(25.28)+0.0571*Ga)-25.28;
      wen:        { Wen & Yu (1966) }
       Remf := sqrt(sqr(33.7)+0.0408*Ga)-33.7;
     end;
     umf := Remf*mugas/(rhogas*dp)
    end
   else
    umf := 0.333934 + ( -0.00042227 +
                (4.67242e-7 - 2.109e-10*Tbed)*Tbed )*Tbed
  end
end;

procedure getbubprops(var z,t,ub,fb:real);
{ calculates the bubble rise velocity and bubble point frequency at time t
 and height z in the bed }
const
 k = 0.711;     { velocity rise coefficient for 3D bubbles }
var
 uexcess,dbo,zo,db,Ao:real;
begin

 uexcess := uo(t) - umf(Tinf(t),p);

 if uexcess < 0 then
  error('in GETBUBPROPS: Bed is not fluidized.');

 case dbmodel of

  agarwal:
   begin
    case distributor of
     porous:
      begin
       dbo := 0.376*sqr(uexcess);
       zo := 0
      end;
     perforated:
      begin
       dbo := 0.871624592*pow(Abeddivnh*uexcess,0.4);
       zo := dholes * 5.2 * pow( rhog(Tinf(t),p)*dholes/(rhop*dp),
0.3)
                  * ( 1.3*pow( sqr(uo(t))/(g*dholes), 0.2) - 1 )
      end;
    end;
    db := dbo + 0.467*pow(z-zo,0.4)*sqrt(dbo) + 0.0597*pow(z-
zo,0.8)
   end;

  darton:
   begin
    case distributor of
     porous:     Ao := 0;
     perforated:  Ao := Abeddivnh;
    end;
    db := 0.54 * pow(uexcess,0.4) * pow(z+4*sqrt(Ao),0.8) * pow(g,-
0.2)
   end;

 end;

 ub := k*sqrt(g*db) + uexcess;

 if dbmodel <> agarwal then
  { Darton doesn't calculate zo which is needed for fb }
  case distributor of
   porous:
    zo := 0;
   perforated:
    zo := dholes * 5.2 * pow( rhog(Tinf(t),p)*dholes/(rhop*dp), 0.3)
          * ( 1.3*pow( sqr(uo(t))/(g*dholes), 0.2) - 1 );
  end;

 fb := 16.4*pow((z-zo)*100,-0.6)     { Agarwal's expression }

end;
```

```
function h(Tb,time:real):real;
{ returns the heat transfer coefficient between the (body or coating) and
the
  bed at t=time when the (body or coating) temperature seen by the bed is
Tb }
const
  { coefficients found by regression of experimental data }
  k1 =  6.34306430318085E+0002;
  k2 =  1.86977290834096E+0001;
  k3 = -3.32317739489358E+0002;
  k4 =  1.41282637943212E+0001;
  k5 =  1.24393959417218E-0003;
  k6 =  1.02103525074608E-0003;
var
  Tinftime,Tf,ux:real;
begin
  if h_is_const = yes then
    h := hconst
  else     { use own experimental measurements }
    { this was determined with dp=589-701um, pbed=patm and is
probably valid
      for Tbed=350-600degC & uo=0.25-0.65ms^-1 at Tbed,patm }
    begin
      Tinftime := Tinf(time);
      Tf := (Tinftime + Tb)/2;
      ux := uo(time)-umf(Tinftime,p);
      if ux <= 0 then
        error('in H: bed not fluidized');
      h := k1*(1-gexp(-k2*ux))*(1+k5*Tf) + k3*(1-gexp(-
k4*ux))*(1+k6*Tf)
    end
end;


  { no initialisation needed for unit }
end.
```

CESOLVE

```
unit cesolve;

{ this unit contains routines for calculating the average erosion rate,
  implementing the coating-erosion model and guiding its solution }

{$N+}     { use extension of standard Pascal floating point types }

interface

uses
  vardefns;

{ functions and procedures }

  procedure solve;


implementation

{ comment out the $DEFINE directive if a step by step commentary on
the
  solution is NOT wanted }

(* {$DEFINE VERBOSE} *)

uses
  crt,extras,propcond,recipes,graph,grapher;

const
  { types for BCrc }
  convection = 0;
  coating = 1;

  { rcnew zero function values at rcnew=rcold (must be positive) }
  non_zero = 1;

  { for extrapolation method of solving equations - sub = sequence of
factors
    for increasing the number of time steps }
  subNtmax = 10;
  sub:array[1..subNtmax] of byte = (1,2,3,4,6,8,12,16,24,32);

  nextrmax = 201;     { save at most nextrmax points of a simulation run
}

  previous = 0;       { used to indicate previous estimate by extrapolation
}

  basefreq = 2;       { number of base steps per second - extrapolation
method }

type
  extr1array = array[0..subNtmax] of real;
  extr2array = array[0..subNtmax,1..nvar] of real;

var
  ri,ro,r,T_fsCC,Tnew_fsCC : realarraynvar;

theta2,Dbend2,z1,z2,I3,KI1,KI2,t_fRx,mbcpb,hAb,Z_fsNC,X_fsNC,Tb
new_fsNC,

rb2,rb3,deltime_fsNC,Tb_fsNC,Tinfav_fsNC,chi_fsNC,h_fsNC,kAb,rh
ocp2k,
  rhocp,time_fsCC,deltime_fsCC,h_fsCC,Tinfav_fsCC : real;
  BCrc : byte;
  rcnewextr,subinv : extr1array;
  Tnewextr : extr2array;
  Lequiv : real;

procedure setuplinearcvs(rc:real);
{ locate control volume boundaries (ri[i] & ro[i]) linearly along the r-
axis
  from rb to rc }
var
  i:byte;
begin
  { NB: cv 1 never changes size, so don't reset it }
  for i := 2 to N-1 do
    ri[i] := (i-2)/(N-2)*(rc-rb)+rb;
  ri[N] := rc;
  for i := 2 to N-1 do
    ro[i] := ri[i+1];
  ro[N] := rc
end;

procedure setupr;
{ locate nodal positions (r[i]) according to Patankar's Practice B - one at
  the centre of each control volume and one on both boundaries }
var
  i:word;
begin
  { NB: node 1 never changes position, so don't reset it }
  for i := 2 to N-1 do
    r[i] := (ri[i]+ro[i])/2;
  r[N] := ri[N]      { also = ro[N] }
end;
```

```
function fangle(theta:real):real;
{ returns the ratio of the erosion rate for a tube inclined at an angle of
  theta (radians) to the horizontal to the rate for a horizontal tube under
  the same conditions and in the same position using data from Nieh et
al.
  (1991) }
begin
  fangle := 1 - 0.3544*theta
end;

{$F+}
function fR1(theta:real):real;
{ returns a value proportional to the local erosion rate of a tube inclined
  at angle theta to the horizontal - used along the bend of the U-tube
heater }
var
  z,ub,fb:real;
begin
  z := z1 - Dbend2*cos(theta);
  getbubprops(z,t_fRx,ub,fb);
  fR1 := fb*pow(ub,2.1)*fangle(theta)
end;

function fR2(z:real):real;
{ returns a value proportional to the local erosion rate of a vertical tube
  at height z - used along the straight section of the U-tube heater }
var
  ub,fb:real;
begin
  getbubprops(z,t_fRx,ub,fb);
  fR2 := fb*pow(ub,2.1)
end;
{$F-}

function Rerosion(time:real):real;
{ calculate the average erosion rate (m/s) at time t }
var
  I1,I2:real;
begin

  if Rerosion_is_const = yes then

    Rerosion := Rerosionconst

  else

  { calculate surface-area-weighted-average erosion rate for the U-tube
    heater based on local erosion rates estimated from the works of Zhu et
    al. (1991) and Nieh et al. (1991). }

    begin

      t_fRx := time;      { to allow fR1 and fR2 access to the time }

      case Rerosioncalc of
        fast:     { quick integration - accurate to 1% }
          begin
            qtrap(fR1,0,theta2,I1);
            qtrap(fR2,z1,z2,I2)
          end;
        slow:     { slower integration - accurate to 0.0001% }
          begin
            qromb(fR1,0,theta2,I1);
            qromb(fR2,z1,z2,I2)
          end;
      end;

      Rerosion := KI1*I1 + KI2*I2

    end

end;

procedure setupk(var T,r,ro,ki,ko:realarraynvar);
{ set up thermal conductivities, ki[i] and ko[i], used by nodal equations
  NB: bypass usual function k(T) for thermal conductivity when it is
constant
      to gain a little extra speed }
var
  i:byte;
  kcalc:realarraynvar;
begin

  if k_is_const = yes then       { ie. k is temperature independent }
    for i := 1 to N do
      begin
        ki[i] := kconst;
        ko[i] := kconst
      end
  else
    begin      { use Patankar's radial averaging for kii and koi }
      for i := 1 to N do
        kcalc[i] := k(T[i]);
      ko[1] := kcalc[2];
      for i := 2 to N-1 do
        begin
          ki[i] := ko[i-1];
          ko[i] := ln(r[i]/r[i+1]) / ( ln(ro[i]/r[i+1])/kcalc[i+1] +
                                       ln(r[i]/ro[i])/kcalc[i] )
        end;
      ki[N] := kcalc[N-1]
    end

end;

procedure solve_BODY_CONV(var
Tb,time,deltime,Tbnew,rcnew:real; var ok:boolean);
{ advance solution by deltime for the case of rc=rb and convection only
}
const
  Tbtol = 0.001;
var
  X,Y,tav,tend,Qbextav,Tinfav,chi,Tbnewlast,Xnew:real;
begin
  {$ifdef VERBOSE}
    writeln('SOLVING BODY_CONVECTION');
  {$endif}

  { calculate the new body temperature }

  if all_are_const = yes then
    begin
      X := mbcpb/deltime;
      Y := hAb;
      Tbnew := ( Qbextconst + Y*Tinfconst + X*Tb ) / (X+Y)
    end
  else
    begin
      tav := time + deltime/2;
      tend := time + deltime;
      Qbextav := Qbext(tav);
      Tinfav := Tinf(tav);
      chi := mb/deltime;
      X := chi*cpb(Tb);
      Tbnew := Tb;      { to start off iterative calcs }
      repeat
        Tbnewlast := Tbnew;
```

```
    Xnew := chi*cpb(Tbnew);
    Y := h(Tbnew,tend)*Ab;
    Tbnew := ( Qbextav + Y*Tinfav + X*Tb ) / (Xnew+Y)
   until abs(Tbnew-Tbnewlast) <= Tbtol
  end;

 { return the new radius of the coating layer, rcnew=rc=rb (ie. same as
old
   = radius of the body) }

 rcnew := rb;

 { no need to remesh, since there is no coating layer }

 ok := Tbnew <= Tm

end;

{$F+}
function fsNCconst(rcnew:real):real;
{ function returns zero when correct value of rcnew is given as argument
 - used by SOLVE_NEW_COAT when properties are constant }
var
 Y,Tbnew,b,a,rcnew2,rcnew3,Ecoat,Econv,Econd:real;
begin

 if rcnew=rb then
  fsNCconst := non_zero
 else
  begin
   Y := kAb/(rcnew-rb);
   Tbnew := ( Z_fsNC + Y*Tm ) / (X_fsNC+Y);
   Tbnew_fsNC := Tbnew;

   b := (Tm-Tbnew)/(rcnew-rb);     { temp. gradient at end of time step
}
   a := Tbnew - Tinfconst - b*rb;
   rcnew2 := sqr(rcnew);
   rcnew3 := rcnew2*rcnew;
   Ecoat := rhocp*( a/2*(rcnew2-rb2) + b/3*(rcnew3-rb3) );
   Econv := hconst*rcnew*(Tm-Tinfconst)*deltime_fsNC;
   Econd := -kconst*rb*b*deltime_fsNC;

   fsNCconst := Econd - Econv - Ecoat
  end
```

```
end;

function fsNCvar(rcnew:real):real;
{ function returns zero when correct value of rcnew is given as argument
 - used by SOLVE_NEW_COAT when properties are variable }
const
 Tbtol = 0.001;
var

Tbnewlast,Tav,Xnew,Y,Tbnew,b,a,rcnew2,rcnew3,Ecoat,Econv,Econd:
real;
begin

 if rcnew=rb then
  fsNCvar := non_zero
 else
  begin
   Tbnew := Tb_fsNC;     { to start off iterative calcs }
   repeat
    Tbnewlast := Tbnew;
    Tav := (Tbnew + Tm)/2;
    Xnew := chi_fsNC*cpb(Tbnew);
    Y := k(Tav)*Ab/(rcnew-rb);
    Tbnew := ( Z_fsNC + Y*Tm ) / (Xnew+Y)
   until abs(Tbnew-Tbnewlast) <= Tbtol;
   Tbnew_fsNC := Tbnew;

   b := (Tm-Tbnew)/(rcnew-rb);     { temp. gradient at end of time step
}
   a := Tbnew - Tinfav_fsNC - b*rb;
   rcnew2 := sqr(rcnew);
   rcnew3 := rcnew2*rcnew;
   Tav := (Tbnew + Tm)/2;
   Ecoat := rho*cp(Tav)*( a/2*(rcnew2-rb2) + b/3*(rcnew3-rb3) );
   Econv := h_fsNC*rcnew*(Tm-Tinfav_fsNC)*deltime_fsNC;
   Econd := -k(Tav)*rb*b*deltime_fsNC;

   fsNCvar := Econd - Econv - Ecoat
  end

end;
{$F-}

procedure solve_NEW_COAT(Tb,time,deltime:real;
                 var Tnew:realarraynvar; var rcnew:real);
{ advance solution by deltime for the case of rc=rb at the start but with
 new coating forming in this step }
const
 rctol = 1e-13;
var
 rclow,rchigh,timeav,Tbnew,dTdr:real;
 i:byte;
begin
 {$ifdef VERBOSE}
  writeln(' ---> SOLVING NEW_COATING');
 {$endif}

 rclow := rb+1e-14;
 rchigh := rb*1.05;

 { calculate the new body temperature, the temperature profile and the
  radius of the coating layer }

 if all_are_const = yes then
  begin
   X_fsNC := mbcpb/deltime;
   Z_fsNC := Qbextconst + X_fsNC*Tb;
   deltime_fsNC := deltime;
   rcnew := zbrent(fsNCconst,rclow,rchigh,rctol,rb)
  end
 else
  begin
   Tb_fsNC := Tb;
   timeav := time + deltime/2;
   Tinfav_fsNC := Tinf(timeav);
   chi_fsNC := mb/deltime;
   Z_fsNC := Qbext(timeav) + chi_fsNC*cpb(Tb)*Tb_fsNC;
   h_fsNC := h(Tm,time+deltime);
   deltime_fsNC := deltime;
   rcnew := zbrent(fsNCvar,rclow,rchigh,rctol,rb)
  end;

 Tbnew := Tbnew_fsNC;     { recover Tbnew from global variable }

 { now, mesh up the coating layer - ie. assign Tnew[i], r[i], ri[i] & ro[i]
}
 setuplinearcvs(rcnew);
 setupr;
 dTdr := (Tm-Tbnew)/(rcnew-rb);

 Tnew[1] := Tbnew;
 for i := 2 to N-1 do
```

```
  Tnew[i] := Tbnew + dTdr*(r[i]-rb);
 Tnew[N] := Tm
end;

procedure remesh(rc,time,deltime:real; var TBR:realarraynvar;
rcBR:real;
                          var TAR:realarraynvar; rcAR:real);
{ this procedure adjusts the position of the control volumes, the nodes
and
 interpolates the nodal temperatures when the coating layer changes size
 from rc (at beginning of time step) to rcBR (after coating but before
 erosion) to rcAR (the value after erosion). The "enthalpy integral"
method
 mentioned in Sparrow et al. (1977) is used for the temperature
 interpolation. }
label
 NEXTi,calcTARi;
const
 TARitol = 0.001;
var
 riBR,roBR,rBR,Hspec:realarraynvar;     { BR = before remeshing }
 dTdr,Hsum,Tav,cpTav,bb,aa,rc2,rc3,roi2,roi3,TARilast:real;
 i,j:byte;
begin

 { calculate Hspec[j] which is proportional to the specific enthalpy of
  the material in the cv around node j before remeshing }

 for j := 1 to N do
  Hspec[j] := cp(TBR[j])*TBR[j];

 copyarray(ri,riBR,N);
 copyarray(ro,roBR,N);
 copyarray(r,rBR,N);

 setuplinearcvs(rcAR);
 setupr;
 { NB: now r[i], ri[i] & ro[i] refer to the values after remeshing (AR) }

 { temperature at object surface is unchanged }
 TAR[1] := TBR[1];

 if rcAR > rc then
  { these calculations are needed only if some new coating remains after
   erosion }
  begin
   { temperature gradient in the newly-formed coating region }
   dTdr := (Tm-TBR[N])/(rcBR-rc);

   { other quantities needed for Ecoat-type calculation }
   Tav := (TBR[N] + Tm)/2;
   cpTav := cp(Tav);
   bb := dTdr;

   { NB: aa different from before since Hspec is based on T, not T-Tm
}
   aa := TBR[N] - bb*rc;
   rc2 := sqr(rc);
   rc3 := rc2*rc
  end;

 { NB: i = new cv's = AR
     j = old cv's = BR }

 { interpolate temperatures for internal nodes by enthalpy integral
method
   NB: there is some unnecessary looping here, but it is clearer than the
   slightly faster version }

 { step through new internal cv's i }
 for i := 2 to N-1 do
  begin

   if ri[i] >= rc then
    { new cv i lies entirely in newly-formed coating region }
    TAR[i] := TBR[N] + dTdr*(r[i]-rc)
   else
    { must now step through all the old cv's j }
    begin

     { but first, check new coating region }
     if (ri[i]<rc) and (ro[i]>rc) then
      { PART of new cv i lies in newly-formed coating region
       - so, calculate its contribution now }
      begin
       { this is very similar to calculation of Ecoat elsewhere }
       roi2 := sqr(ro[i]);
       roi3 := roi2*ro[i];
       Hsum := cpTav*( aa*(roi2-rc2) + 2*bb/3*(roi3-rc3) )
      end
     else
      { none of i lies in new coating region - so, zero contribution }
      Hsum := 0;

     { ok, now step through the new cv's j adding up contributions }
     for j := 2 to N-1 do
      if (ri[i]>=riBR[j]) and (ro[i]<=roBR[j]) then
       { new cv i lies completely in old cv j }
       begin
        TAR[i] := TBR[j];
        goto NEXTi     { don't need any more calcs for this i }
       end
      else if (ri[i]>=riBR[j]) and (ri[i]<=roBR[j])
            and (ro[i]>=roBR[j]) then
       { old cv j overlaps inner part of new cv i }
       Hsum := Hsum + Hspec[j]*(sqr(roBR[j])-sqr(ri[i]))
      else if (ri[i]<=riBR[j]) and (ro[i]>=roBR[j]) then
       { old cv j lies entirely in new cv i }
       Hsum := Hsum + Hspec[j]*(sqr(roBR[j])-sqr(riBR[j]))
      else if (riBR[j]>=ri[i]) and (riBR[j]<=ro[i])
            and (roBR[j]>=ro[i]) then
       { old cv j overlaps outer part of new cv i }
       begin
        Hsum := Hsum + Hspec[j]*(sqr(ro[i])-sqr(riBR[j]));
        goto calcTARi     { since this must be last j in i }
       end;

     calcTARi:
      { now calculate TAR[i] }
      if cp_is_const = yes then
       TAR[i] := Hsum / ( cpconst*(sqr(ro[i]) - sqr(ri[i])) )
      else
       begin
        TAR[i] := TBR[j];     { to start off iterative calcs }
        repeat
         TARilast := TAR[i];
         TAR[i] := Hsum / ( cp(TAR[i])*(sqr(ro[i]) - sqr(ri[i])) )
        until abs(TAR[i]-TARilast) <= TARitol
       end
    end;

   NEXTi:
  end;

 { calculate material temperature on coating-bed boundary (node N)
depending
   on the amount of erosion that has taken place }
```

```
  if rcAR >= rc then

   { for erosion which only removes part of the newly-formed layer, use
     linear T-r profile in new coating region }
   TAR[N] := TBR[N] + dTdr*(rcAR-rc)

  else

   { for more erosion than above, use old linear T-r profile in interior of
     coating evaluated at the new boundary position }
   begin
     j := 2;
     while rBR[j] < rcAR do
       inc(j);
     dTdr := (TBR[j]-TBR[j-1])/(rBR[j]-rBR[j-1]);
     TAR[N] := TBR[j-1] + dTdr*(rcAR-rBR[j-1])
   end

end;

procedure solve_ERODE(var TBE:realarraynvar;
rcBE,rc,time,deltime:real;
                var TAE:realarraynvar; var rcAE:real);
{ this procedure should be called after the coating problem has been
solved
  for the time step. it performs both EROSION CALCULATIONS and
ADJUSTS THE
  NODAL POSITIONS & TEMPERATURES. rc is the radius before
coating, TBE[i] and
  rcBE are the values after coating but before erosion and TAE[i] and
rcAE are
  the values after erosion }
var
  Rerosionav,dTdr:real;
  i:byte;
begin

  Rerosionav := Rerosion(time + deltime/2);

  if (Rerosionav=0) and ( (rcBE=rc) or (rc=rb) ) then

    { this traps two cases:
      a) new coating formation with no erosion
      b) convection only with a coating layer present but without erosion
     this is the easiest solution - before ERODE = after ERODE
       NB: we must still remesh the case of continued coating with no
erosion
       since the new coating formed in the time step has not yet been
       incorporated into the nodal scheme }
     begin
       copyarray(TBE,TAE,N);
       rcAE := rcBE
     end

   else

     { EITHER: erosion does occur OR (coating continues without erosion
- here
       just need to remesh to include the new bit of coating) }
     begin

       { calculate new radius }
       rcAE := rcBE - Rerosionav * deltime;

       if rcAE <= rb then
         { so much erosion that all the coating is lost => rcAE=rb,
TbAE=TbBE
           (ie. TAE[1]=TBE[1] & ignore TAE[i] for i>1 }
         begin
           rcAE := rb
         end
       else
         begin

           { check if this is erosion of coating that has just formed }
           if rc = rb then
             { another easy solution - temp profile must be linear }
             begin
               setuplinearcvs(rcAE);
               setupr;
               dTdr := (TBE[N]-TBE[1])/(rcBE-rb);      { slope }
               TAE[1] := TBE[1];
               for i := 2 to N do
                 TAE[i] := TBE[1] + dTdr*(r[i]-rb)
             end
           else
             { can't avoid it - the hard solution }
             remesh(rc,time,deltime,TBE,rcBE,TAE,rcAE)

         end
     end
end;

procedure calccoeffs(var T:realarraynvar; time,deltime:real;
                var Tnew:realarraynvar; rcnew:real;
                var a,b,c,d:realarraynvar);
{ evaluates coefficients of nodal temperatures for use in solving the
  discretisation eqns which form a tridiagonal matrix:
        a[i]*T[i-1] + b[i]*T[i] + c[i]*T[i+1] = d[i]
  with a[1],c[N] undefined. This procedure works for both the cases of
  coating and of convection only on the outer boundary }
var
  X,Xnew,Y,Z,chi,chichi,timeav:real;
  ki,ko:realarraynvar;
  i:byte;
begin
  if all_are_const = yes then
    begin

      { coefficients for first node }
      X := mbcpb/deltime;
      Y := kAb/(r[2]-r[1]);
      b[1] := X + Y;
      c[1] := -Y;
      d[1] := Qbextconst + X*T[1];

      { coefficients for nodes 2 to (N-1) }
      chi := rhocp2k/deltime;
      for i := 2 to N-1 do
        begin
          X := chi*( sqr(ro[i]) - sqr(ri[i]) );
          Y := ro[i]/(r[i+1]-r[i]);
          Z := ri[i]/(r[i]-r[i-1]);
          a[i] := -Z;
          b[i] := X + Y + Z;
          c[i] := -Y;
          d[i] := X*T[i]
        end;

      { coefficients for node N }
      if BCrc = convection then
        begin
          X := kconst / ( hconst * (r[N]-r[N-1]) );
          a[N] := -X;
          b[N] := X + 1;
          d[N] := Tinfconst
```

```
    end
  else     { BCrc = coating }
    begin
      a[N] := r[N] - rcnew;
      b[N] := rcnew - r[N-1];
      d[N] := (r[N]-r[N-1])*Tm
    end

 end
else     { coefficients are time- or temperature- dependent }
 begin

  { coefficients for first node }
  chi := mb/deltime;
  X := chi*cpb(T[1]);
  Xnew := chi*cpb(Tnew[1]);
  Y := k(Tnew[2])*Ab/(r[2]-r[1]);
  timeav := time + deltime/2;
  b[1] := Xnew + Y;
  c[1] := -Y;
  d[1] := Qbext(timeav) + X*T[1];

  { coefficients for nodes 2 to (N-1) }
  chichi := rho/(2*deltime);
  setupk(Tnew,r,ro,ki,ko);
  for i := 2 to N-1 do
   begin
     chi := chichi*( sqr(ro[i]) - sqr(ri[i]) );
     X := chi*cp(T[i]);
     Xnew := chi*cp(Tnew[i]);
     Y := ko[i]*ro[i]/(r[i+1]-r[i]);
     Z := ki[i]*ri[i]/(r[i]-r[i-1]);
     a[i] := -Z;
     b[i] := Xnew + Y + Z;
     c[i] := -Y;
     d[i] := X*T[i]
   end;

  { coefficients for node N }
  if BCrc = convection then
   begin
     X := k(Tnew[N-1]) / ( h(Tnew[N],time+deltime) * (r[N]-r[N-1])
);
     a[N] := -X;
     b[N] := X + 1;
     d[N] := Tinf(timeav)
    end
  else     { BCrc = coating }
   begin
     X := k(Tnew[N-1]) * (rcnew-r[N]);
     Y := k((Tnew[N]+Tm)/2) * (r[N]-r[N-1]);
     a[N] := -X;
     b[N] := X + Y;
     d[N] := Y*Tm
    end

 end
end;

procedure calcerrors(var Tnew,Tnewlast,a,b,c,d:realarraynvar;
                     var residmax:real; residtol:real;
                     var Terrmax:real; Terrtol:real; var ok:boolean);
{ used to check for the convergence of iterative calculations when a
  coating layer is present.
  Requires on entry values for residmax & Terrmax, the errors from the
  previous iteration. On exit these values are updated.
  If the maximum relative errors in temperature and the residuals
between
  the previous and current iterations agree to the required tolerance or,
are
  unlikely to be further reduced, ok is set to true }
const
  eps = 1e-6;     { a small number - deals with round-off error }
var
  i,residpos,Terrpos:byte;
  residold,Terrold,fresid,fTerr:real;
  resid,Terr:extended;
begin
  residold := residmax;
  residmax := 0;
  residpos := 0;

  for i := 1 to N do
    begin
      if i = 1 then
        resid := abs(b[i]*Tnew[i] + c[i]*Tnew[i+1] - d[i])
      else if i = N then
        resid := abs(a[i]*Tnew[i-1] + b[i]*Tnew[i] - d[i])
      else     { nodes 2 to N-1 }
        resid := abs( a[i]*Tnew[i-1] + b[i]*Tnew[i] + c[i]*Tnew[i+1]
                  - d[i] );
    if resid > residmax then
      begin
        residmax := resid;
        residpos := i
      end
  end;

  fresid := abs((residmax-residold)/residold);     { fractional error }

  Terrold := Terrmax;
  Terrmax := 0;
  Terrpos := 0;

  for i := 1 to N do
   begin
     Terr := abs(Tnewlast[i]-Tnew[i]);
     if Terr > Terrmax then
       begin
         Terrmax := Terr;
         Terrpos := i
       end
   end;

  fTerr := abs((Terrmax-Terrold)/Terrold);     { fractional error }

  if ( (fresid <= residtol) or (residmax <= eps) ) and
     ( (fTerr  <= Terrtol ) or (Terrmax  <= eps) ) then
    ok := true
  else
    ok := false

end;

procedure solve_COAT_CONV(var T:realarraynvar;
rc,time,deltime:real;
                  var Tnew:realarraynvar; var rcnew:real; var ok:boolean);
{ advance solution by deltime for the case of rc>rb and convection only
}
const
  residtol = 0.05;
  Terrtol = 0.0001;
var
  residmax,Terrmax,rcnew_int,Rerosionav,rcmin:real;
  a,b,c,d,Tnewlast,Tnew_int:realarraynvar;
  done:boolean;
  i :integer;
```

```
begin
 {$ifdef VERBOSE}
  writeln('SOLVING COATING_WITH_CONVECTION');
 {$endif}

 BCrc := convection;

 { calculate the new body temperature, new temperature profile and new
  radius of the coating layer IGNORING THE EFFECT OF
EROSION (the variables
  involved are suffixed with _int (intermediate values) ) }

 rcnew_int := rc;

 if all_are_const = yes then
  begin
   { NB: here an initial guess for Tnew is not needed and rcnew=rc }
   calccoeffs(T,time,deltime,Tnew_int,rcnew_int,a,b,c,d);
   tridag(a,b,c,d,Tnew_int,N)
  end
 else
  begin
   copyarray(T,Tnew_int,N);     { to start off iterative calcs }
   { initialise errors with large values }
   residmax := 100;
   Terrmax := 100;
   repeat
    copyarray(Tnew_int,Tnewlast,N);
    { NB: here Tnew is needed for iterative calcs but rcnew is not }
    calccoeffs(T,time,deltime,Tnew_int,rcnew_int,a,b,c,d);
    tridag(a,b,c,d,Tnew_int,N);

calcerrors(Tnew,Tnewlast,a,b,c,d,residmax,residtol,Terrmax,Terrtol,don
e)
   until done
  end;

 { test to see if convection only actually would take place, or if coating
  takes place aswell. If coating also occurs, then exit the procedure here
}

 if Tnew_int[N] > Tm then     { coating also takes place }
  { do no more calculations here - solve COAT_COAT for this time
step }
  ok := false
 else     { ok, convection only }
  begin

   ok := true;

   { erode the coating and remesh as necessary }

   Rerosionav := Rerosion(time + deltime/2);

   if Rerosionav=0 then     { no erosion }
    begin
     copyarray(Tnew_int,Tnew,N);
     rcnew := rcnew_int
     { no need to remesh, as nodal positions haven't changed }
    end
   else     { there is some erosion }
    begin

     { calculate new radius based on erosion rate }
     rcnew := rcnew_int - Rerosionav * deltime;

     { calculate minimum allowable radius based on surface
temperature
       restriction - cannot erode beyond Tm }
     i := N;
     repeat
      dec(i)
     until ((Tnew_int[i]>Tm) or (i=1));
     if Tnew_int[i] > Tm then
      rcmin := r[i] + (r[i+1]-r[i])*(Tm-Tnew_int[i])/(Tnew_int[i+1]-
Tnew_int[i])
     else
      rcmin := rb;
     if rcnew < rcmin then
      rcnew := rcmin;

     if rcnew <= rb then
      { so much erosion that all the coating is lost }
      begin
       Tnew[1] := Tnew_int[1];
       rcnew := rb;
       { no need to remesh, as no coating layer is present }
      end
     else
      { some coating is left, so remesh it }
      remesh(rc,time,deltime,Tnew_int,rcnew_int,Tnew,rcnew)
    end
  end

end;

{$F+}
function fsCCconst(rcnew:real):real;
{ function returns zero when correct value of rcnew is given as argument
 - used by SOLVE_COAT_COAT when properties are constant }
var
 bb,aa,rcnew2,rcnew3,rN2,rN3,Ecoat,Econv,Econd:real;
 a,b,c,d,Tnew:realarraynvar;
begin

 if rcnew=r[N] then
  fsCCconst := non_zero
 else
  begin
   calccoeffs(T_fsCC,time_fsCC,deltime_fsCC,Tnew,rcnew,a,b,c,d);
   tridag(a,b,c,d,Tnew,N);

   copyarray(Tnew,Tnew_fsCC,N);

   bb := (Tm-Tnew[N])/(rcnew-r[N]);     { temp. gradient at end of
time step }
   aa := Tnew[N] - Tinfconst - bb*r[N];
   rcnew2 := sqr(rcnew);
   rcnew3 := rcnew2*rcnew;
   rN2 := sqr(r[N]);
   rN3 := rN2*r[N];
   Ecoat := rhocp*( aa/2*(rcnew2-rN2) + bb/3*(rcnew3-rN3) );
   Econv := hconst*rcnew*(Tm-Tinfconst)*deltime_fsCC;
   Econd := -kconst*r[N]*bb*deltime_fsCC;

   fsCCconst := Econd - Econv - Ecoat
  end

end;

function fsCCvar(rcnew:real):real;
{ function returns zero when correct value of rcnew is given as argument
 - used by SOLVE_COAT_COAT when properties are variable }
const
 residtol = 0.05;
 Terrtol = 0.0001;
var
 residmax,Terrmax:real;
```

```
  ok:boolean;
  a,b,c,d,Tnew,Tnewlast:realarraynvar;
  Tav,bb,aa,rcnew2,rcnew3,rN2,rN3,Ecoat,Econv,Econd:real;
begin

  if rcnew=r[N] then
    fsCCvar := non_zero
  else
    begin
      copyarray(T_fsCC,Tnew,N);      { to start off iterative calcs }
      { initialise errors with large values }
      residmax := 100;
      Terrmax := 100;
      repeat
        copyarray(Tnew,Tnewlast,N);
        { NB: here Tnew is needed for iterative calcs but rcnew is not }
        calccoeffs(T_fsCC,time_fsCC,deltime_fsCC,Tnew,rcnew,a,b,c,d);
        tridag(a,b,c,d,Tnew,N);

calcerrors(Tnew,Tnewlast,a,b,c,d,residmax,residtol,Terrmax,Terrtol,ok)
      until ok;

      copyarray(Tnew,Tnew_fsCC,N);

      Tav := (Tnew[N] + Tm)/2;
      bb := (Tm-Tnew[N])/(rcnew-r[N]);      { temp. gradient at end of
time step }
      aa := Tnew[N] - Tinfav_fsCC - bb*r[N];
      rcnew2 := sqr(rcnew);
      rcnew3 := rcnew2*rcnew;
      rN2 := sqr(r[N]);
      rN3 := rN2*r[N];
      Ecoat := rho*cp(Tav)*( aa/2*(rcnew2-rN2) + bb/3*(rcnew3-rN3) );
      Econv := h_fsCC*rcnew*(Tm-Tinfav_fsCC)*deltime_fsCC;
      Econd := -k(Tav)*r[N]*bb*deltime_fsCC;

      fsCCvar := Econd - Econv - Ecoat
    end

end;
{$F-}

procedure solve_COAT_COAT(var T:realarraynvar;
rc,time,deltime:real;
                var Tnew:realarraynvar; var rcnew:real);
{ advance solution by deltime for the case of rc>rb and coating
occurring }
const
  rctol = 1e-13;
var
  rclow,rchigh:real;
  Tnew_int:realarraynvar;
begin
  {$ifdef VERBOSE}
    writeln(' ---> SOLVING COATING_WITH_COATING');
  {$endif}

  BCrc := coating;

  rclow := rc+1e-14;
  rchigh := rc*1.05;

  copyarray(T,T_fsCC,N);
  deltime_fsCC := deltime;

  { calculate the new body temperature, new temperature profile and new
    radius of the coating layer }

  if all_are_const = yes then
    { NB: time_fsCC does not need to be defined for the constant case }
    rcnew := zbrent(fsCCconst,rclow,rchigh,rctol,rc)
  else
    begin
      time_fsCC := time;
      Tinfav_fsCC := Tinf(time+deltime/2);
      h_fsCC := h(Tm,time+deltime);
      rcnew := zbrent(fsCCvar,rclow,rchigh,rctol,rc)
    end;

  if rcnew <= rc then
    writeln('rc= ',rc,'f(rc)= ',fsCCconst(rc));
  { recover Tnew_int[i] from global variable }
  copyarray(Tnew_fsCC,Tnew_int,N);

  { remesh the coated layer }

  remesh(rc,time,deltime,Tnew_int,rcnew,Tnew,rcnew)

end;

procedure solve_deltime(var T:realarraynvar; rc,time,deltime:real;
                var Tnew:realarraynvar; var rcnew:real);
{ advance solution by deltime without checking on the adequacy of the
size
  of the time step, but properly accounting for time- and temperature-
  variable properties }
var
  ok:boolean;
begin

  if rc = rb then      { no coating is present at the start of this step }
    begin

      { assume no coating occurs, only convection from body }
      solve_BODY_CONV(T[1],time,deltime,Tnew[1],rcnew,ok);

      if not(ok) then      { coating does occur }
        { solve for the new coating formed }
        solve_NEW_COAT(T[1],time,deltime,Tnew,rcnew);

    end
  else      { a coating layer is present at the start of this step }
    begin

      { assume no new coating forms, only convection }
      solve_COAT_CONV(T,rc,time,deltime,Tnew,rcnew,ok);

      if not(ok) then      { new coating does form }
        { solve with coating }
        solve_COAT_COAT(T,rc,time,deltime,Tnew,rcnew);

    end
end;

procedure initialise;
{ initialise some derived variables, flags etc. }
var
  j:byte;
begin

  { calculate a few derived quantities }
  Abeddivnh := pi/4*sqr(Dbed)/nholes;
  Ab := pi*Dtube*( 2*Ltube-Dbend-Dtube+0.5*pi*Dbend );
  rb := Dtube/2;

  { calculate equivalent length = length of cylinder having same volume
as
```

```
  U-tube heater }
 Lequiv := 2*Ltube - Dtube + (pi/2-1)*Dbend;

 if Rerosion_is_const = no then     { calculate a few things here }
   begin                            { to save time later on }
     theta2 := pi/2;
     Dbend2 := Dbend/2;
     z1 := ztube + Dtube/2 + Dbend2;
     z2 := ztube + Ltube;
     I3 := Ltube - Dtube/2 + Dbend2*(theta2 - 1);
     KI1 := Dbend2 * C_Zhu*rhop*pow(dp,1.2)*(1.04-psi) / I3;
     KI2 := C_Zhu*rhop*pow(dp,1.2)*(1.04-psi) * fangle(theta2) / I3
   end;

 { number of nodes in coating (2 on boundaries and (N-2) in interior) }
 { NB: must be <= (nvar+1) defined in the VARDEFNS unit }
 N := 22;

 { set first node and cv positions here since they never change }
 ri[1] := rb;
 ro[1] := rb;
 r[1] := rb;

 rb2 := sqr(rb);
 rb3 := rb2*rb;

 { NB: the program runs in two "modes" - one in which all the physical
   and thermal properties are constant and another in which at least one
of
   these may vary. The all-constant mode may run considerably faster (at
   least twice) than the variable mode (which allows more realistic
problems
   to be investigated) }

 if (Qbext_is_const=yes) and (Tinf_is_const=yes) and
(cpb_is_const=yes) and
    (k_is_const=yes) and (cp_is_const=yes) and (h_is_const=yes) and
    (Rerosion_is_const=yes) then
     all_are_const := yes
 else
     all_are_const := no;

 if all_are_const = yes then
   { calculate a few things here to save time later }
   begin
     { for SOLVE_BODY_CONV }
     mbcpb := mb*cpbconst; { also for calccoeffs }
     hAb := hconst*Ab;
     { for calccoeffs }
     kAb := kconst*Ab;   { also for SOLVE_NEW_COAT }
     rhocp2k := rho*cpconst/(2*kconst);
     { for fsNCconst & fsCCconst }
     rhocp := rho*cpconst
   end;

 { initialise flags for solution storage }
 gotGT1 := false;
 gotGT2 := false;

 { initialise reciprocal of number of substeps array }
 if Ntsteps_is_const = no then
   for j := 1 to subNtmax do
     subinv[j] := 1/sub[j];

end;

procedure displaypc(i,n:longint);
{ display % of problem completed }
var
 nn:longint;
begin
 memw[$B800:(152+2*(i mod 4))] := i+$100;
 if n < 100 then
   nn := 1
 else
   nn := n div 100;
 if (i mod nn) = 0 then
   write('Completed: ',i/n*100:0:0,'%   ',#13)
end;

procedure Gsave1st;
{ store initial conditions for later graphing }
begin
 nGpts := 1;
 Gtime[1] := 0;
 Grc[1] := rb;
 if all_are_const = yes then  { not good way }
   GTb[1] := Tbinit
 else
   GTb[1] := Tb_expt[1];
 GTrc[1] := GTb[1]
end;

procedure Gsavepoint(i,nn:longint; time,deltime,rcold,rcnew:real;
                     var Tnew:realarraynvar);
{ stores a data point if necessary for later graphing }
const
 eps = 1e-12;     { a small number }
var
 mass:real;
begin

 if ( ((ngraph-1)>=nn) or
     (abs(i/(nn-1)-(nGpts+1)/(ngraph-1))<=abs((i+1)/(nn-1)-
(nGpts+1)/(ngraph-1))) or
     (i=(nn-1))
   ) and (nGpts<ngraph)
  then
  begin
    inc(nGpts);

    Gtime[nGpts] := time+deltime;
    Grc[nGpts] := rcnew;
    GTb[nGpts] := Tnew[1];
    if rcnew > rb then
      GTrc[nGpts] := Tnew[N]
    else
      GTrc[nGpts] := GTb[nGpts]
  end;

 if (abs(rcnew-rb)>eps) and (rcold=rb) then
   { catch the first formation of coating }
   begin
     Gcopyarray(Tnew,GT1,N);
     Gcopyarray(r,Gr1,N);
     Gtime1 := time+deltime;
     gotGT1 := true
   end;

 if (abs(rcnew-rb)>eps) and (i=(nn-1)) then
   { catch the last step }
   begin
     Gcopyarray(Tnew,GT2,N);
     Gcopyarray(r,Gr2,N);
     Gtime2 := time+deltime;
     gotGT2 := true
   end;
end;
```

```
procedure displaystep(time,deltime,rcnew:real; var
Tnew:realarraynvar);
{ displays the results of the current time step }
var
  A:real;
  j:byte;
begin
  writeln('time: ',time+deltime:0:6);
  if rcnew=rb then
    begin
      A := Tinfconst + Qbextconst/(hconst*Ab);
      A := A + (Tbinit-A)
                *exp(-hconst*Ab*time/(mb*cpbconst));
      write('Tbnew = ',Tnew[1]:10:4,'   Tbnon-sintering = ',A:10:4);
      writeln(' difference = ',Tnew[1]-A :10:4);
    end
  else
    for j := 1 to N div 2 do      { only works properly for even N }
      writeln(j:3,' ',Tnew[j]:10:4,'     ',j+N div 2:3,' ',Tnew[j+N div
2]:10:4);
  writeln('rc =  ',rcnew:0:8);
  waitkey
end;

procedure regress(var x,y:extr1array; n:byte; var a,b:real);
{ performs linear regression on x[i],y[i] data and so calculates a & b:
  y = a + bx is the line of best fit }
var
  i:byte;
  sumx,sumy,sumx2,sumxy:real;
begin
  sumx := 0;
  sumy := 0;
  sumx2 := 0;
  sumxy := 0;
  for i := 1 to N do
    begin
      sumx := sumx + x[i];
      sumy := sumy + y[i];
      sumx2 := sumx2 + sqr(x[i]);
      sumxy := sumxy + x[i]*y[i]
    end;
  b := ( n*sumxy - sumx*sumy ) / ( n*sumx2 - sqr(sumx) );
  a := sumy/n - b*sumx/n
end;
```

```
procedure extrapolate_profile(startNt,subNt:byte; var
Tnew:realarraynvar;
                              rcnew:real);
{ called by EXTRAPOLATE to find the temperature profile in the
coating when
  the body temperature and coating radius have been successfully
extrapolated
  NB: it is assumed that Tnew[1] = Tbnew has already been set - this
  procedure only sets Tnew[i], i=2..N }
var
  i,j:byte;
  b:real;
  subinvdat,dat:extr1array;
begin

  if startNt<>subNt then
    { more than one data point available for each position - regress them }
    for i := 2 to N do
      begin
        for j := 1 to (subNt-startNt+1) do
          begin
            subinvdat[j] := subinv[startNt-1+j];
            dat[j] :=  Tnewextr[startNt-1+j,i]
          end;
        regress(subinvdat,dat,subNt-startNt+1,Tnew[i],b)
      end
  else
    { only one data point available for each position - just use it }
    for i := 2 to N do
      Tnew[i] := Tnewextr[subNt,i];

  { must also remmesh control volume and reset nodal temperatures }
  setuplinearcvs(rcnew);
  setupr

end;

procedure extrapolate(subNt:byte; var Tnew:realarraynvar; var
rcnew:real;
                      var soln_ok:boolean);
{ called by SOLVE when using the extrapolation method - extrapolates
the
  subrun solutions contained in the global arrays RCNEWEXTR and
TNEWEXTR.
  subNt is the number of the latest subrun. If the extrapolation is
successful,
  soln_ok is set to true and Tnew & rcnew contain the extrapolated
solutions
  on exit. Successful extrapolation is based on Tb & rc, not on the
complete
  temperature profile }
const
  rctol = 1e-9;
  Tbtol = 1e-3;
var
  subinvdat,rcdat,Tbdat:extr1array;
  rcest,Tbest,b1,b2:real;
  j,startNt:byte;
begin

  { choose starting number of substep, startNt, for the extrapolation }
  if (rcnewextr[subNt]>rb) and (rcnewextr[1]=rb) then
    { some inconsistency with presence or absence of the coating -
      restrict the range of substeps used }
    begin
      startNt := 2;
      while rcnewextr[startNt]=rb do
        inc(startNt)
    end
  else
    { no inconsistency - use all available information }
    startNt := 1;

  { now, do the regression ---> extrapolation }
  if startNt<>subNt then
    { more than one data point available - regress them }
    begin
      for j := 1 to (subNt-startNt+1) do
        { step through different numbers of substeps }
        begin
          subinvdat[j] := subinv[startNt-1+j];
          rcdat[j] :=  rcnewextr[startNt-1+j];
          Tbdat[j] :=  Tnewextr[startNt-1+j,1];
        end;
      regress(subinvdat,rcdat,subNt-startNt+1,rcest,b1);
      regress(subinvdat,Tbdat,subNt-startNt+1,Tbest,b2)
    end
  else
    { only one data point available - just use it }
    begin
```

```
    rcest := rcnewextr[subNt];
    Tbest := Tnewextr[subNt,1];
    b1 := 0;
    b2 := 0
   end;

  if subNt = 3 then
   { first call to this procedure - just store the extrapolated result }
   begin
    soln_ok := false;
    rcnewextr[previous] := rcest;
    Tnewextr[previous,1] := Tbest
   end
  else
   { second or later call to this procedure - compare previous
extrapolations
     with the present one }
   begin

    if (abs(rcest-rcnewextr[previous]) <= rctol) and
      (abs(Tbest-Tnewextr[previous,1]) <= Tbtol) then
     soln_ok := true
    else
     soln_ok := false;

    if soln_ok or (not(soln_ok) and (subNt=subNtmax)) then
     { here, the solution is ok or we have run out of substeps and it is
       not ok. Either way, we must return an answer in Tnew and rcnew
}
     begin
      { must be careful, extrapolation may give illegal rcnew }
      if rcest > rb then
       rcnew := rcest
      else
       rcnew := rb:
      { accept Tbest, despite adequacy or otherwise of rcest }
      Tnew[1] := Tbest;
      if rcnew > rb then
       extrapolate_profile(startNt,subNt,Tnew,rcnew);
     end
    else
     { the current extrapolation failed, but we can try again, so save the
       current extrapolations for comparison with next attempt }
     begin
      rcnewextr[previous] := rcest;
      Tnewextr[previous,1] := Tbest
     end

   end;

end;

procedure solve;
{ integrates the coating-erosion model from t=0 to t=t_end }
label
 FINISHED_STEP_I;
var
 i:longint;
 j,s,k:byte;
 deltime,time,rcold,rcnew,rcoldstore:real;
 Told,Tnew,Toldstore:realarraynvar;
 soln_ok:boolean;
begin

 clrscr;
 writeln(title);
 writeln;
 writeln('Ruminating...');

 initialise;

 { set initial conditions }
 if all_are_const = yes then  { not good way }
  Told[1] := Tbinit
 else
  Told[1] := Tb_expt[1];

 Told[1] := Tbinit;
 Tb_expt[1] := Tbinit;

 for i := 2 to N do
  Told[i] := 0;
 rcold := rb;

 Tbinit := Told[1];
 Gsave1st;

 if Ntsteps_is_const = yes then

  { just step through the solution without checking on adequacy using
    Ntsteps time steps }
  begin

  deltime := 1/Ntsteps*t_end;

  writeln('Solution method: Fixed time step');
  writeln('Number of steps: ',Ntsteps);
  writeln('Time step:       ',deltime:0:5,' s');

  for i := 0 to (Ntsteps-1) do
   { ok, now step through the solution }
   begin
    time := i/Ntsteps * t_end;
    solve_deltime(Told,rcold,time,deltime,Tnew,rcnew);

    displaypc(i,Ntsteps);
    Gsavepoint(i,Ntsteps,time,deltime,rcold,rcnew,Tnew);
    {$ifdef VERBOSE }
     displaystep(time,deltime,rcnew,Tnew);
    {$endif}

    rcold := rcnew;
    copyarray(Tnew,Told,N)
   end

 end

else

 { use extrapolation methods to achieve a more accurate solution }
 begin

  { set basic number of steps - basefreq steps per second }
  Ntsteps := trunc(basefreq*t_end);

  deltime := 1/Ntsteps*t_end;

  writeln('Solution method:     Extrapolation to zero step size');
  writeln('Base number of steps: ',Ntsteps);
  writeln('Base time step:       ',deltime:0:5,' s');

  for i := 0 to (Ntsteps-1) do
   { step through the base steps }
   begin

    { store the conditions at the beginning of this base time step }
    rcoldstore := rcold;
    copyarray(Told,Toldstore,N);
```

```
for j := 1 to subNtmax do
 { step through the subruns (runs with differing numbers of
  substeps) for this base step }
 begin

  { (re)set initial conditions }
  rcold := rcoldstore;
  copyarray(Toldstore,Told,N);
  setuplinearcvs(rcold);
  setupr;

  deltime := 1/(Ntsteps*sub[j]) * t_end;

  for s := 0 to (sub[j]-1) do
   { step through the substeps for this subrun }
   begin
    time := (i + s/sub[j])/Ntsteps * t_end;

    solve_deltime(Told,rcold,time,deltime,Tnew,rcnew);

    {$ifdef VERBOSE}
     displaystep(time,deltime,rcnew,Tnew);
    {$endif}

    rcold := rcnew;
    copyarray(Tnew,Told,N)
   end;

  { save results for subrun j for later extrapolation }
  rcnewextr[j] := rcnew;
  for k := 1 to N do
   Tnewextr[j,k] := Tnew[k];

  if j >= 3 then
   begin
    extrapolate(j,Tnew,rcnew,soln_ok);
    if soln_ok then
     goto FINISHED_STEP_I
   end

 end;

FINISHED_STEP_I:

 time := i/Ntsteps*t_end;
      deltime := 1/Ntsteps*t_end;
      rcold := rcoldstore;
      Gsavepoint(i,Ntsteps,time,deltime,rcold,rcnew,Tnew);

      displaypc(i,Ntsteps-1);

      rcold := rcnew;
      copyarray(Tnew,Told,N);

    end

  end


end;


 { no initialisation needed for unit }
end.
```

Appendix F:

MEASURES USED FOR DATA COMPARISON

To compare experimental data with a model or a descriptive equation, objective measures of the agreement between them are needed. In this thesis, such data include: the minimum fluidization velocity (Section 3.5.2), the heat transfer coefficient (Section 3.5.3), and the sintering temperature (Section 5.4.4).

If $x_{expt\,i}$ is one of N experimental data points (i = 1,2,...,N) and $x_{pred\,i}$ is the corresponding predicted value, then the following measures may be defined:

Sum of the Square Error, SSE:

$$SSE = \sum_{i=1}^{N}\left[(x_{expt\,i} - x_{pred\,i})^2\right] \tag{F.1}$$

Root Mean Square (RMS) Error:

$$\text{RMS Error} = \sqrt{\frac{SSE}{N}} \tag{F.2}$$

Mean Percentage Error:

$$\text{Mean Percentage Error} = \frac{1}{N}\sum_{i=1}^{N}\left[\left|\frac{x_{expt\,i} - x_{pred\,i}}{x_{expt\,i}}\right|\right] \text{x } 100\% \tag{F.3}$$

Appendix G:

EXPERIMENTAL DATA AND MODEL COMPARISONS

Table G.1 summarises the conditions for each coating-erosion experiment and the mass of coating that was present at the end of the run. Included also are the sintering temperatures that were determined by parameter estimation as described in Section 5.4. Figure G.1 is a key to the general categories, A - E, of deposition patterns.

In Figures G.2 - G.38 the experimental and predicted temperature histories of the immersed body are plotted together for comparison. The instantaneous experimental conditions and some other information are provided in Tables G.2 - G.38.

Table G.1: Summary of the experimental conditions covered in the coating-erosion study, details of the coating present at the end of the experiment, and the corresponding sintering temperatures as determined by data fitting.

Expt. No.	t_{end} (s)	$Q_{b\ ext}$ [1] (W)	u_o [1] (ms^{-1}) [2]	T_∞ [1] (°C)	Mass of Coating (g)	Spatial Distribn. [3]	T_s (°C)
1	660	510	0.261	537	0.3883	B	701.4
2	205	507	0.257	527	0.1807	B	694.8
3	680	508	0.261	539	0.6944	B	700.8
4	900	512	0.272	529	0.5775	B	685.0
5	120	725	0.278	538	1.1161	B	724.0
6	140	630	0.262	546	1.4862	B+E	724.9
7	400	634	0.301	554	0.4610	B	715.1
8	245	640	0.279	547	0.9030	B	717.7
9	900	514	0.266	486	0.0078	A	660.3
10	900	509	0.268	500	0.4111	B	665.9
11	900	514	0.289	569	1.1287	B	708.7
12	960	631	0.571	591	0.1261	A	750.6
13	1230	633	0.513	587	0.1186	A	752.4
14	1280	632	0.449	588	0.1101	A	750.5
15	1530	634	0.391	583	0.1040	A	748.4
16	800	726	0.500	566	0.0973	A	749.3
17	680	724	0.380	564	0.0906	A	742.7
18	610	728	0.344	560	0.2467	C	740.8
19	360	725	0.313	550	0.7122	C	729.9
20	120	735	0.265	525	2.6955	C+D	720.8
21	1740	435	0.274	554	0.7877	C	689.8
22	1600	508	0.283	573	3.0614	C	718.0
23	500	676	0.318	558	0.8828	C	725.2
24	320	678	0.311	541	0.4848	C	712.7
25	330	507	0.260	532	1.4299	B	692.1
26	915	659	0.316	557	0.7964	B	728.1
27	560	756	0.339	546	0.3952	B	735.6
28	120	640	0.263	518	3.6571	C+D	689.1
29	350	551	0.270	539	2.6284	C+D	696.5
30	1200	552	0.277	554	2.0545	C	716.5
31	1080	616	0.321	568	0.9901	B	730.1
32	1410	451	0.319	566	0.0399	A	691.2
33	665	627	0.296	540	0.4237	B	711.5
34	680	512	0.265	551	1.0749	B	707.0
35	200	516	0.259	536	3.6990	C+D	687.8
36	1220	506	0.265	551	0.9789	B	707.4
37	440	512	0.271	571	2.7078	B+E	709.5

Notes:

1. Average values over the experiment.
2. Units are ms^{-1} at T_∞,p.
3. Spatial distribution of the coating on the heater; see Figure G.1.

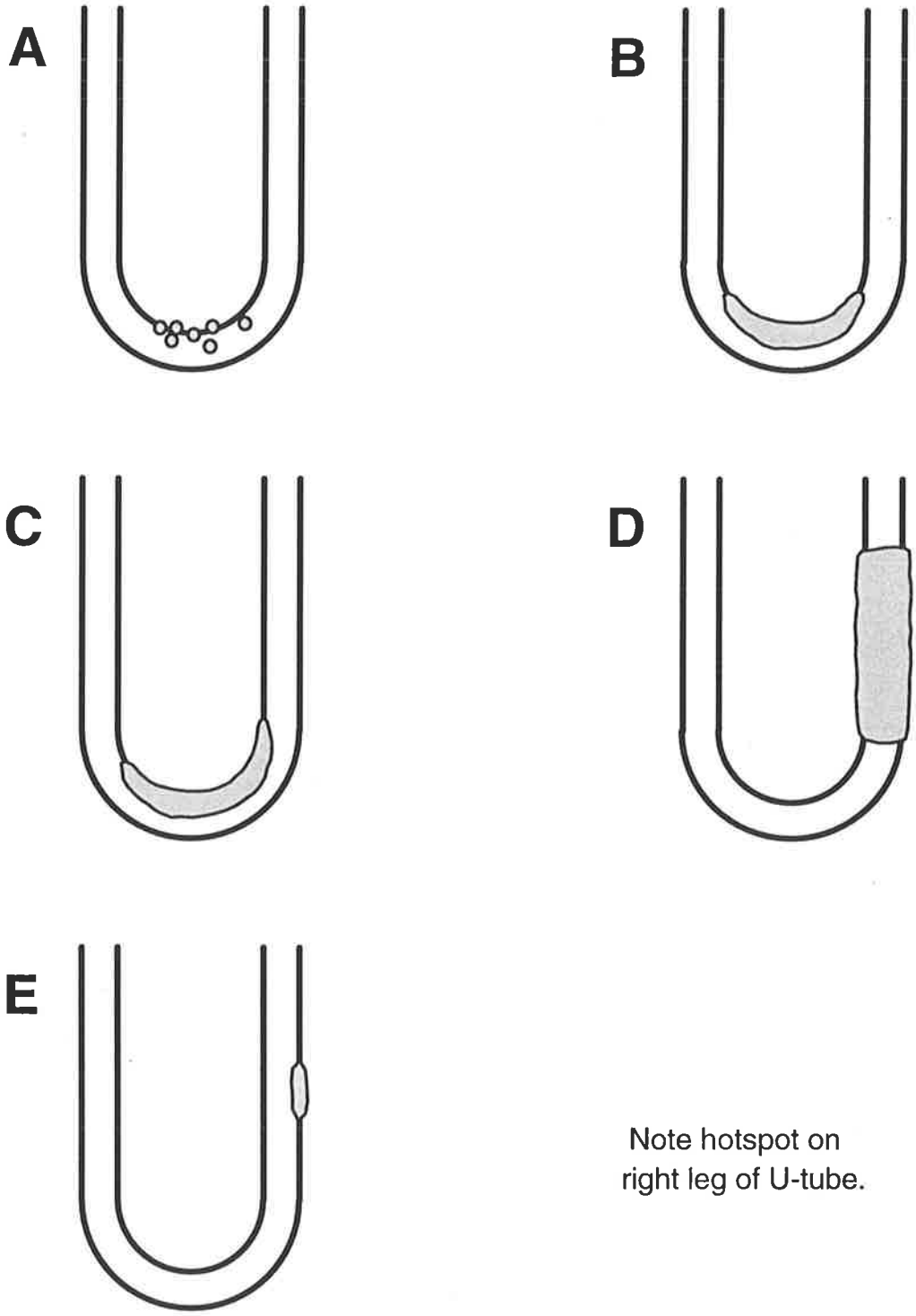

Figure G.1: General categories of deposit shape and position.

Experiment 1:

Table G.2: Data from experiment 1.

t (s)	$Q_{b\,ext}$ (W)	u_o (ms^{-1})	T_∞ (°C)	T_b (°C)
0	0	0.255	520	519
30	510	0.256	520	584
60	510	0.257	522	638
120	510	0.258	526	670
180	508	0.259	531	678
240	510	0.260	533	684
300	510	0.261	537	688
390	513	0.262	540	693
480	510	0.263	545	699
570	510	0.264	548	701
645	510	0.265	551	701
660	510	0.265	552	701
Average:	**510**	**0.261**	**537**	-
Coating Mass:	**0.3883 g**	**Spatial Distribution:**		**B**
Sintering Temperature:		**701.4 °C**		

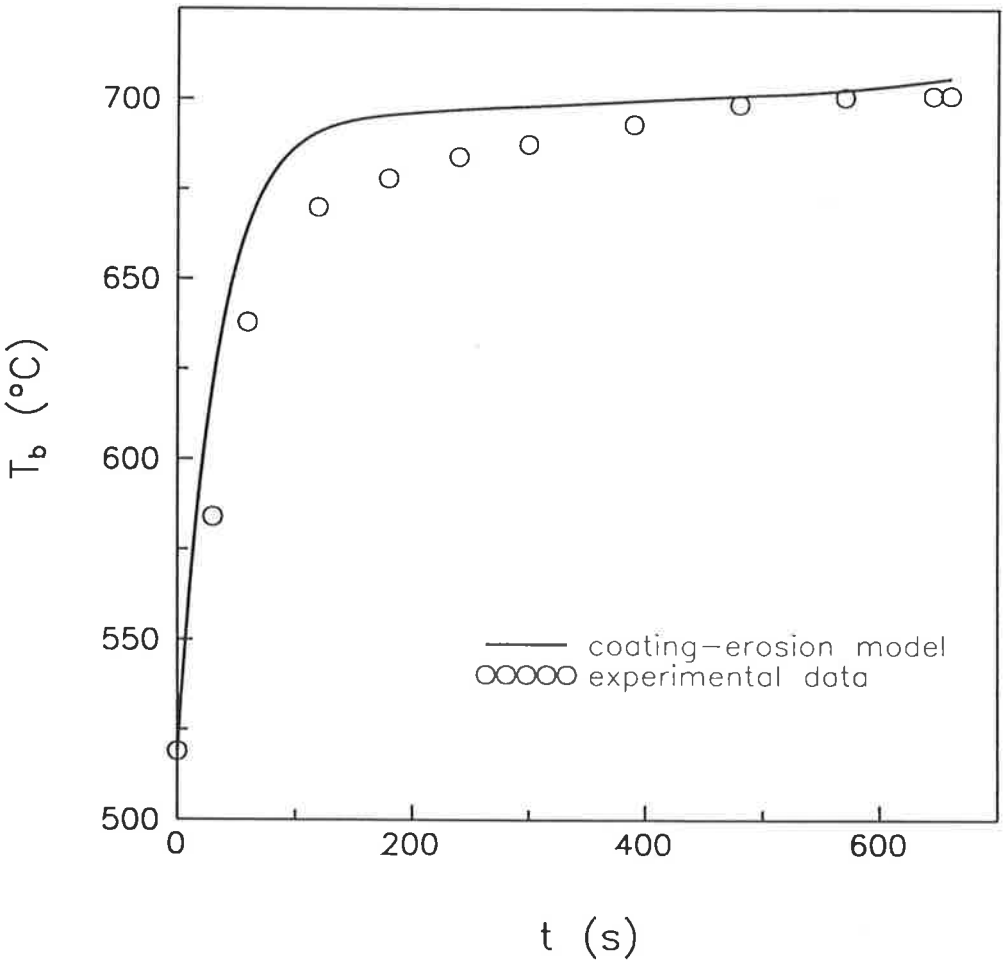

Figure G.2: Comparison of temperature histories of the body for experiment 1.

Experiment 2:

Table G.3: Data from experiment 2.

t (s)	$Q_{b\,ext}$ (W)	u_o (ms^{-1})	T_∞ (°C)	T_b (°C)
0	0	0.255	519	521
30	510	0.255	521	583
50	510	0.256	522	626
60	510	0.256	523	638
100	510	0.257	527	664
140	505	0.258	530	676
190	499	0.259	534	680
205	497	0.260	535	681
Average:	**507**	**0.257**	**527**	-
Coating Mass:	**0.1807 g**	**Spatial Distribution:**		**B**
Sintering Temperature:		**694.8 °C**		

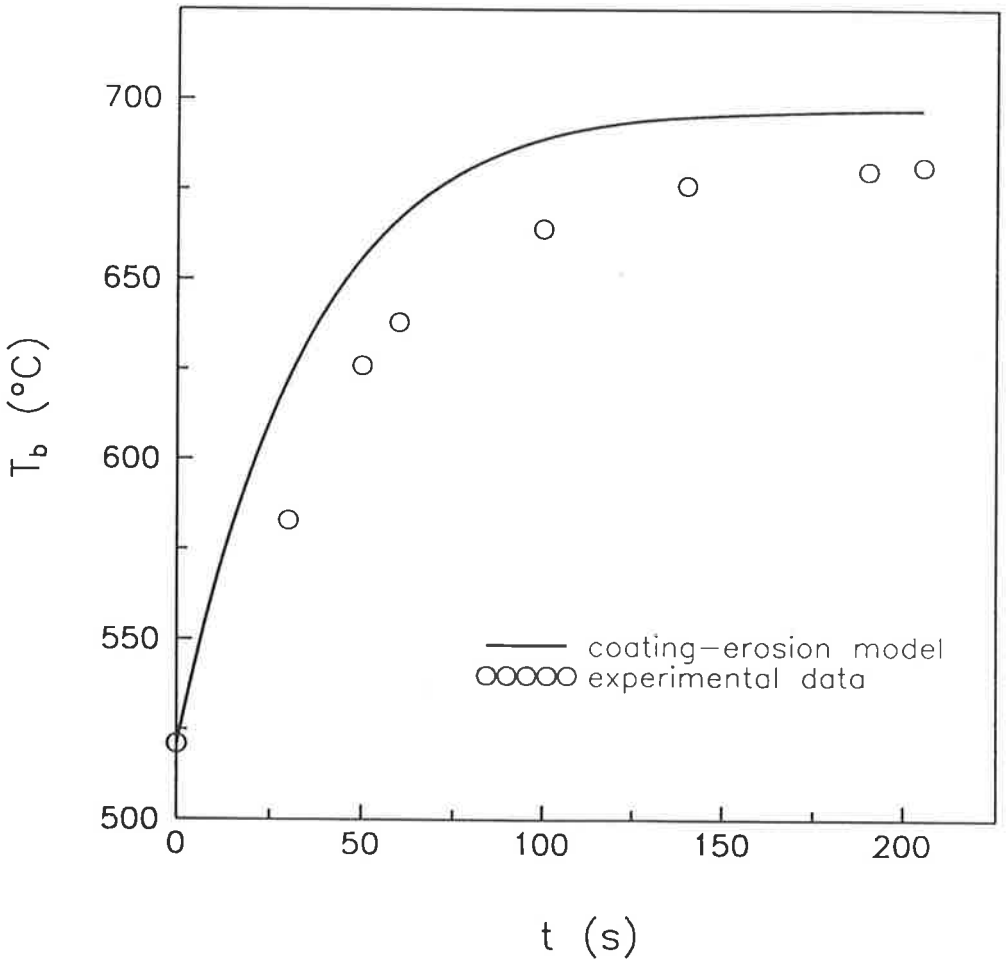

Figure G.3: Comparison of temperature histories of the body for experiment 2.

Experiment 3:

Table G.4: Data from experiment 3.

t (s)	$Q_{b\,ext}$ (W)	u_o (ms^{-1})	T_∞ (°C)	T_b (°C)
0	0	0.254	518	520
30	508	0.255	520	581
60	508	0.255	522	633
120	508	0.258	528	668
180	508	0.258	530	677
240	505	0.260	535	681
300	510	0.261	537	687
360	508	0.262	542	692
450	508	0.263	544	696
540	510	0.264	547	700
600	510	0.266	551	702
665	510	0.267	555	703
680	510	0.267	556	703
Average:	**508**	**0.261**	**539**	-
Coating Mass:	**0.6944 g**	**Spatial Distribution:**		**B**
Sintering Temperature:		**700.8 °C**		

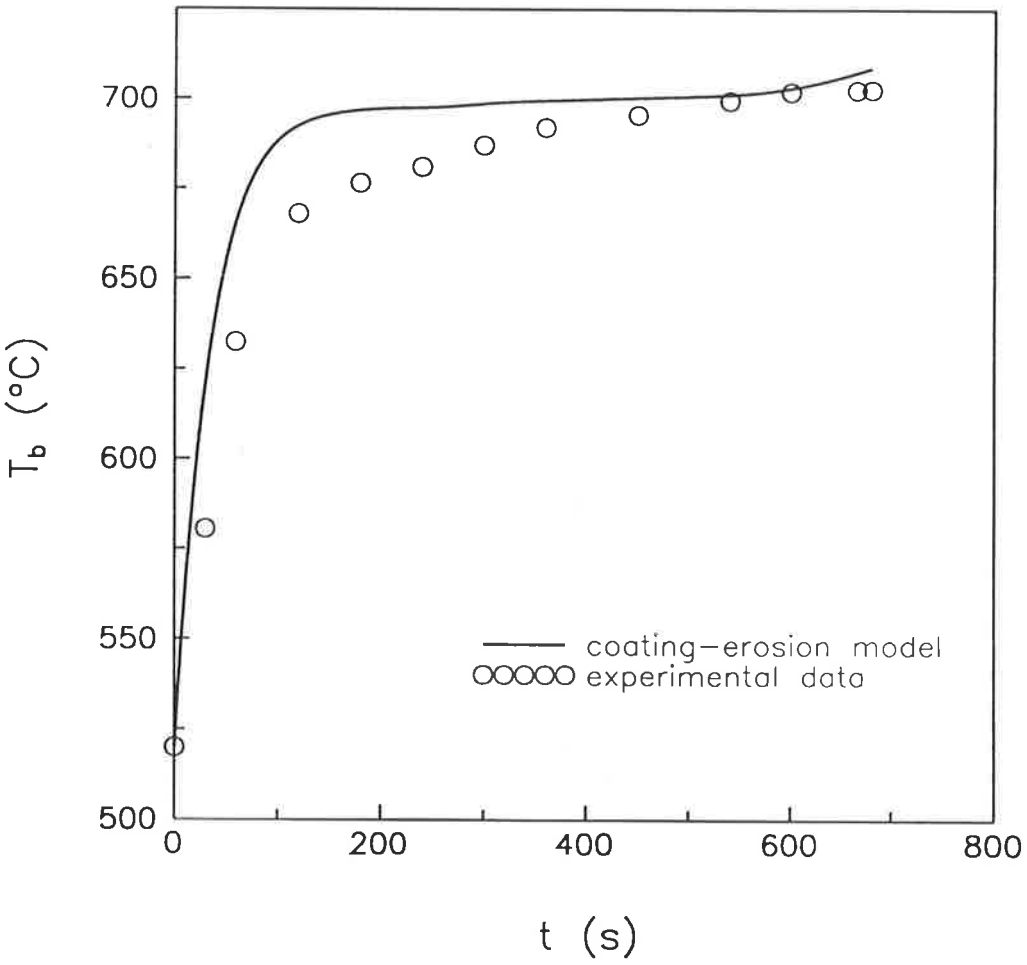

Figure G.4: Comparison of temperature histories of the body for experiment 3.

Experiment 4:

Table G.5: Data from experiment 4.

t (s)	$Q_{b\,ext}$ (W)	u_o (ms^{-1})	T_∞ (°C)	T_b (°C)
0	0	0.265	502	504
30	513	0.265	504	566
45	513	0.265	504	602
60	513	0.265	505	627
120	515	0.267	511	660
180	510	0.269	517	668
240	515	0.270	522	675
330	515	0.271	525	680
420	515	0.272	530	686
510	513	0.274	534	687
600	510	0.274	538	692
690	508	0.276	542	696
780	508	0.276	544	697
880	508	0.276	547	700
900	508	0.277	547	700
Average:	**512**	**0.272**	**529**	-
Coating Mass:	**0.5775 g**	**Spatial Distribution:**		**B**
Sintering Temperature:		**685.0 °C**		

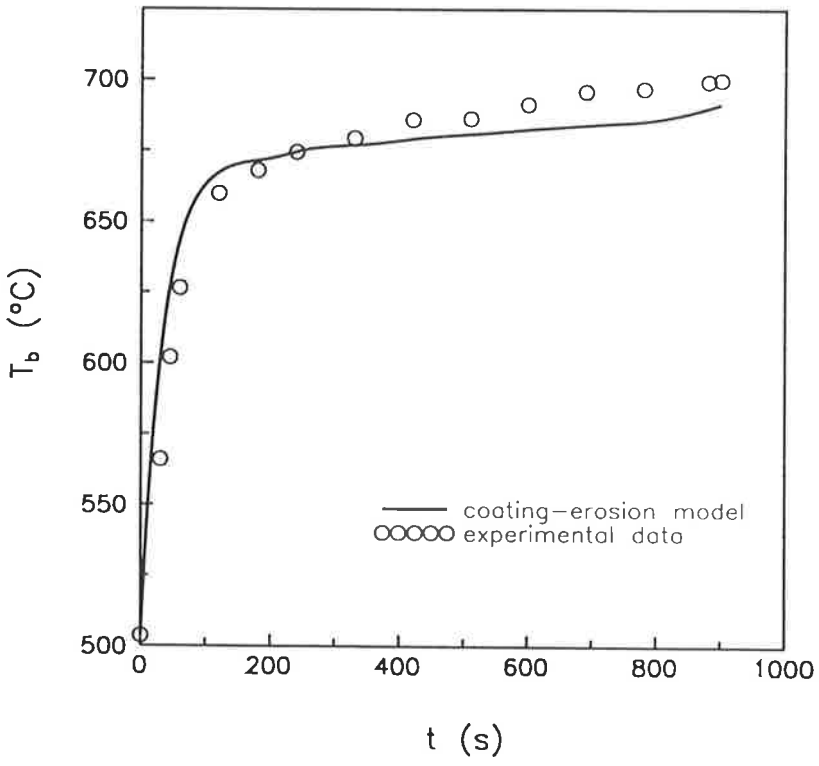

Figure G.5: Comparison of temperature histories of the body for experiment 4.

Experiment 5:

Table G.6: Data from experiment 5.

t (s)	$Q_{b\,ext}$ (W)	u_o (ms^{-1})	T_∞ (°C)	T_b (°C)
0	0	0.276	532	535
30	725	0.277	535	611
60	725	0.278	538	688
110	725	0.280	543	729
120	725	0.280	544	737
Average:	**725**	**0.278**	**538**	-
Coating Mass:	**1.1161 g**	**Spatial Distribution:**		**B**
Sintering Temperature:		**724.0 °C**		

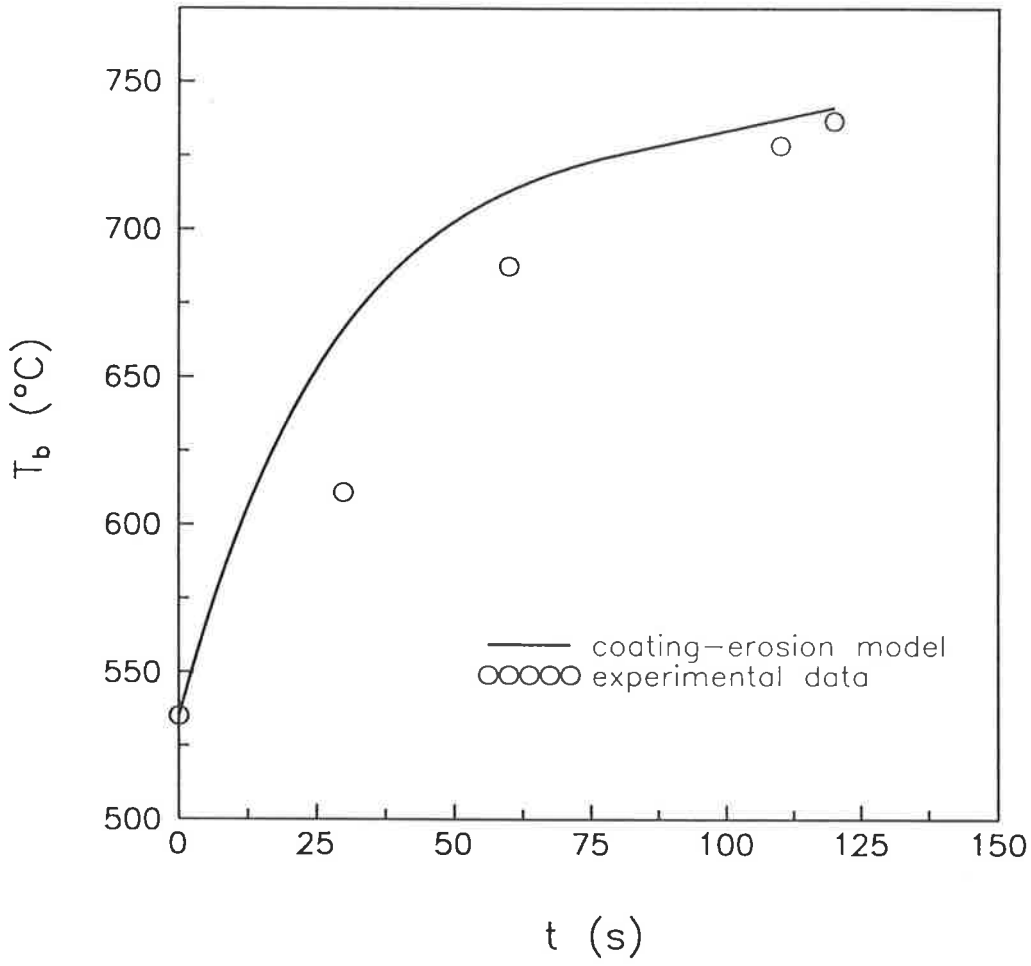

Figure G.6: Comparison of temperature histories of the body for experiment 5.

Experiment 6:

Table G.7: Data from experiment 6.

t (s)	$Q_{b\,ext}$ (W)	u_o (ms^{-1})	T_∞ (°C)	T_b (°C)
0	0	0.260	540	542
30	630	0.261	542	612
60	630	0.262	545	679
120	630	0.263	550	727
140	630	0.264	552	743
Average:	**630**	**0.262**	**546**	-
Coating Mass:	**1.4862 g**	**Spatial Distribution:**		**B+E**
Sintering Temperature:		**724.9 °C**		

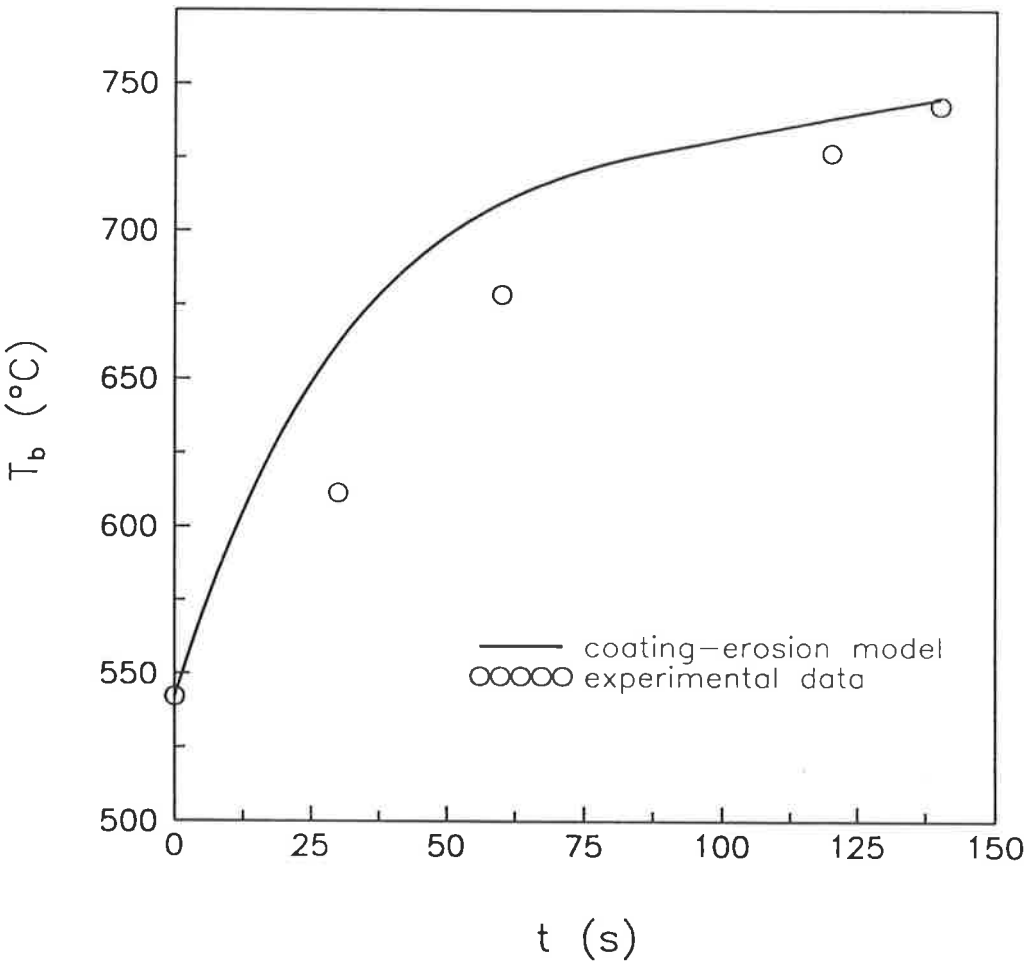

Figure G.7: Comparison of temperature histories of the body for experiment 6.

Experiment 7:

Table G.8: Data from experiment 7.

t (s)	$Q_{b\,ext}$ (W)	u_o (ms^{-1})	T_∞ (°C)	T_b (°C)
0	0	0.294	536	540
30	638	0.296	539	610
60	638	0.297	542	673
120	638	0.299	549	704
180	635	0.300	553	715
240	630	0.302	559	721
330	633	0.304	564	728
380	634	0.305	566	731
400	634	0.305	568	732
Average:	**634**	**0.301**	**554**	-
Coating Mass:	**0.4610 g**	**Spatial Distribution:**		**B**
Sintering Temperature:		**715.1 °C**		

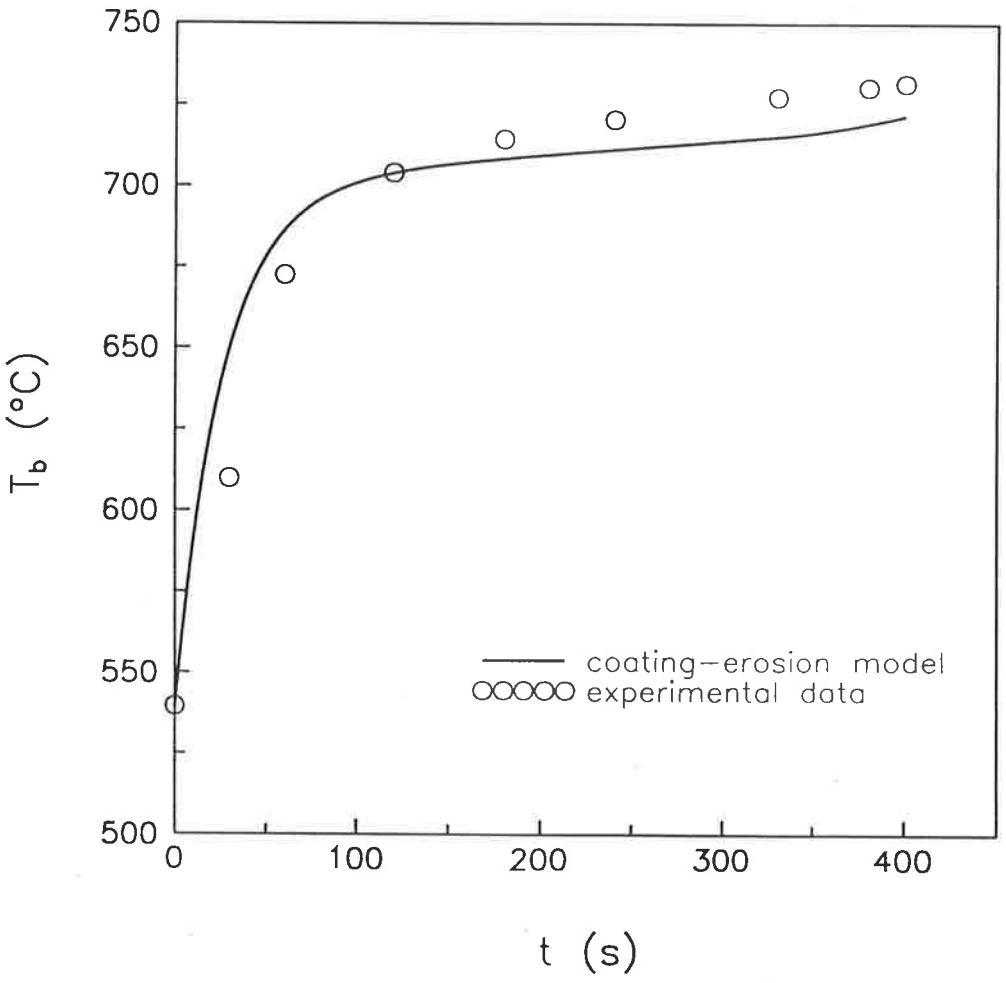

Figure G.8: Comparison of temperature histories of the body for experiment 7.

Experiment 8:

Table G.9: Data from experiment 8.

t (s)	$Q_{b\,ext}$ (W)	u_o (ms^{-1})	T_∞ (°C)	T_b (°C)
0	0	0.276	536	538
30	640	0.277	539	611
60	640	0.278	541	674
120	640	0.280	548	711
180	640	0.281	552	724
230	640	0.282	555	730
245	640	0.282	555	732
Average:	**640**	**0.279**	**547**	-
Coating Mass:	**0.9030 g**	**Spatial Distribution:**		**B**
Sintering Temperature:	**717.7 °C**			

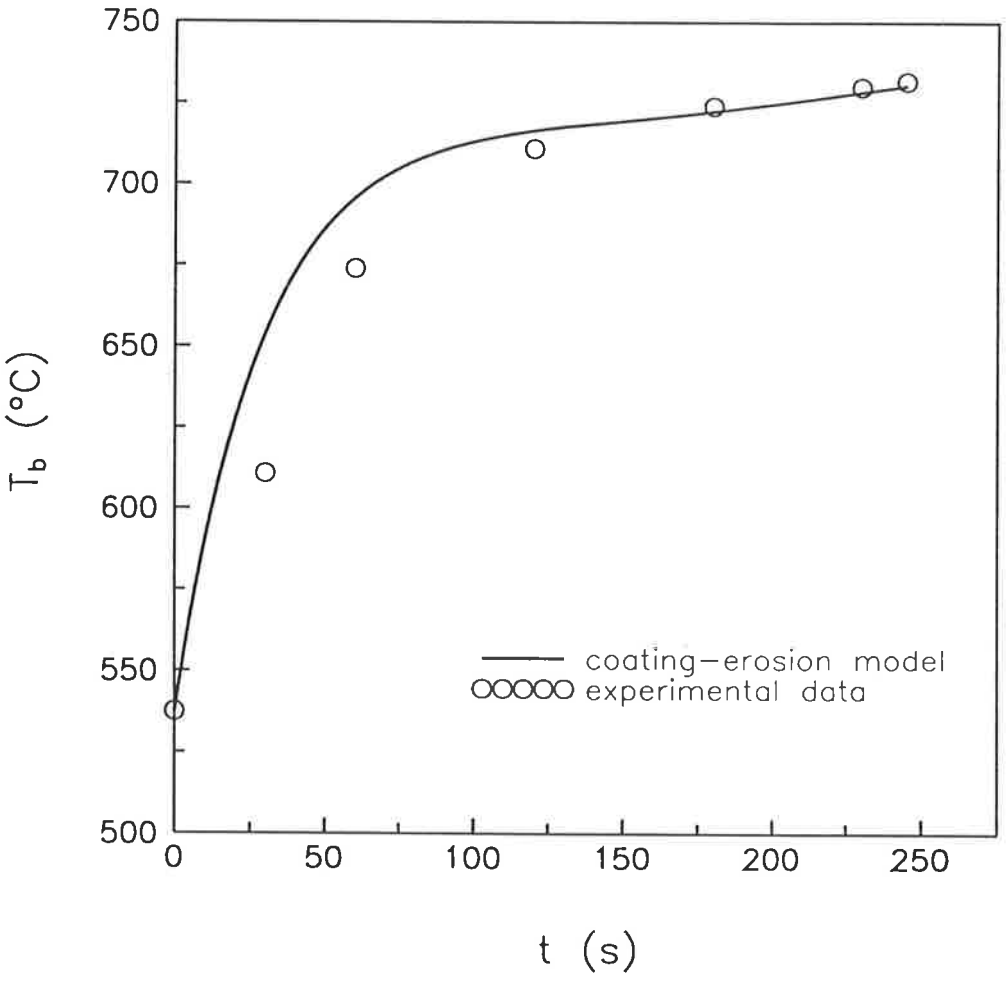

Figure G.9: Comparison of temperature histories of the body for experiment 8.

Experiment 9:

Table G.10: Data from experiment 9.

t (s)	$Q_{b\,ext}$ (W)	u_o (ms^{-1})	T_∞ (°C)	T_b (°C)
0	0	0.255	455	456
30	518	0.257	459	516
60	518	0.258	463	592
120	518	0.260	467	641
180	513	0.262	473	650
240	515	0.263	478	656
300	510	0.264	480	652
360	510	0.265	483	655
420	510	0.266	487	653
480	510	0.267	488	655
540	510	0.267	489	657
600	508	0.269	493	658
660	520	0.270	498	659
720	520	0.270	498	662
780	520	0.272	501	667
840	515	0.272	504	668
900	510	0.273	506	670
Average:	**514**	**0.266**	**486**	-
Coating Mass:	**0.0078 g**	**Spatial Distribution:**		**A**
Sintering Temperature:		**660.3 °C**		

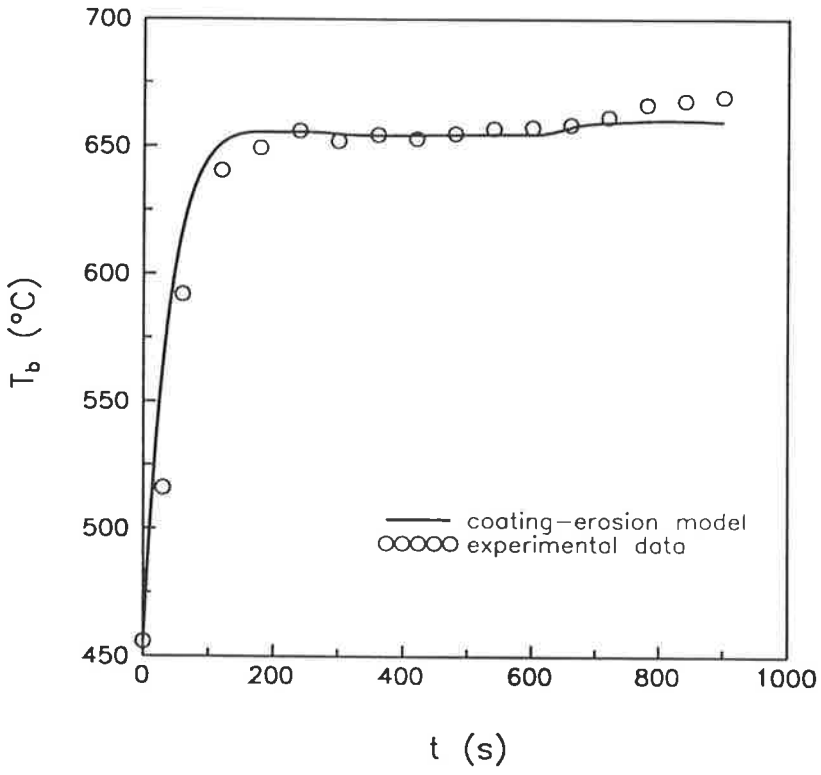

Figure G.10: Comparison of temperature histories of the body for experiment 9.

Experiment 10:

Table G.11: Data from experiment 10.

t (s)	$Q_{b\,ext}$ (W)	u_o (ms^{-1})	T_∞ (°C)	T_b (°C)
0	0	0.260	472	474
30	510	0.260	475	537
60	510	0.261	477	605
120	510	0.263	482	651
180	508	0.265	488	659
240	510	0.266	491	663
300	508	0.266	494	664
360	508	0.268	498	665
420	510	0.268	498	666
480	505	0.269	501	669
540	510	0.269	503	668
600	510	0.271	509	672
660	510	0.272	511	676
720	510	0.272	513	675
780	508	0.273	517	678
840	508	0.273	518	680
900	508	0.274	519	683
Average:	**509**	**0.268**	**500**	-
Coating Mass:	**0.4111 g**	**Spatial Distribution:**		**B**
Sintering Temperature:	**665.9 °C**			

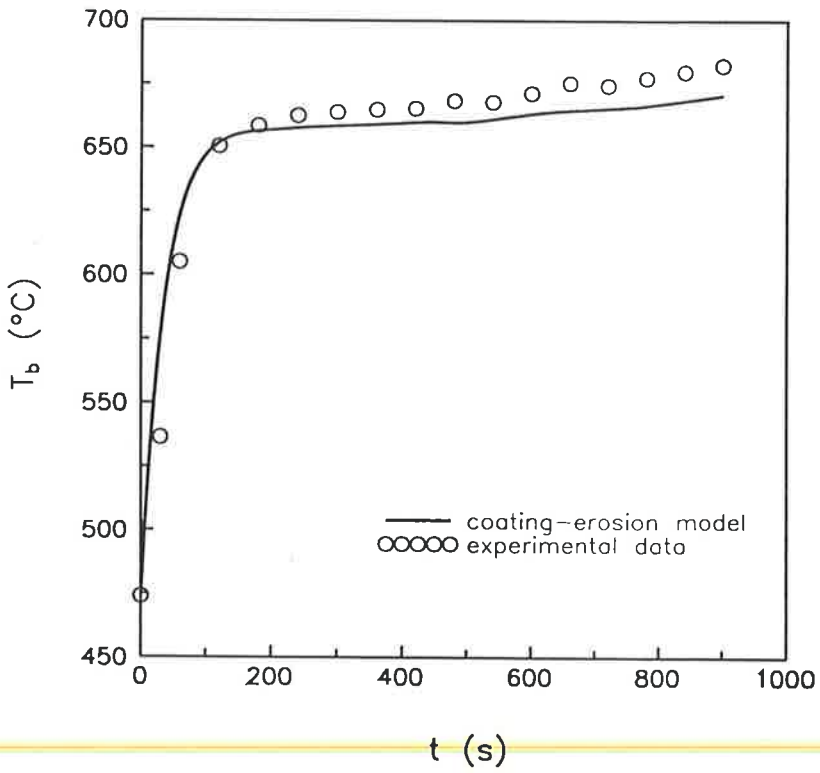

Figure G.11: Comparison of temperature histories of the body for experiment 10.

Experiment 11:

Table G.12: Data from experiment 11.

t (s)	$Q_{b\,ext}$ (W)	u_o (ms^{-1})	T_∞ (°C)	T_b (°C)
0	0	0.280	545	546
30	523	0.281	546	607
60	523	0.282	548	660
120	520	0.283	553	691
180	520	0.285	557	697
240	520	0.286	560	705
300	513	0.287	564	708
360	515	0.288	566	710
420	513	0.289	569	712
480	510	0.290	572	714
540	510	0.291	576	718
600	508	0.292	578	721
660	508	0.292	579	722
720	510	0.293	581	726
780	513	0.294	584	725
840	515	0.294	586	727
900	518	0.295	588	729
Average:	**514**	**0.289**	**569**	-
Coating Mass:	**1.1287 g**	**Spatial Distribution:**		**B**
Sintering Temperature:		**708.7 °C**		

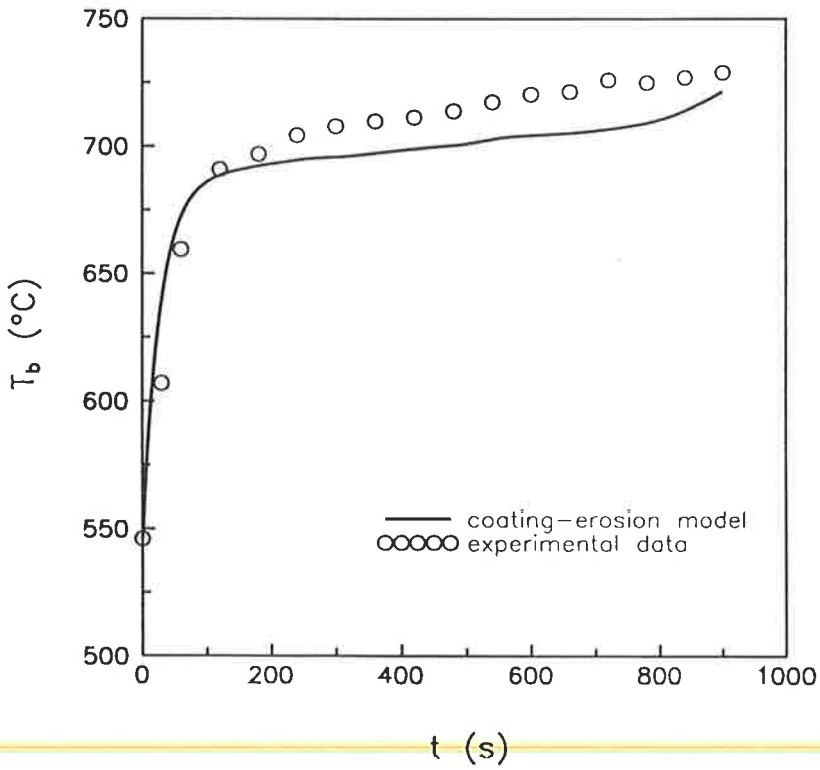

Figure G.12: Comparison of temperature histories of the body for experiment 11.

Experiment 12:

Table G.13: Data from experiment 12.

t (s)	$Q_{b\,ext}$ (W)	u_o (ms^{-1})	T_∞ (°C)	T_b (°C)
0	0	0.547	554	553
30	638	0.548	557	612
60	638	0.550	560	668
120	635	0.555	568	693
180	630	0.559	573	701
300	633	0.565	582	708
430	630	0.571	591	717
540	630	0.576	597	724
660	630	0.579	604	730
840	630	0.585	612	739
950	630	0.588	617	745
960	630	0.588	618	746
Average:	**631**	**0.571**	**591**	-
Coating Mass:	**0.1261 g**	**Spatial Distribution:**		**A**
Sintering Temperature:		**750.6 °C**		

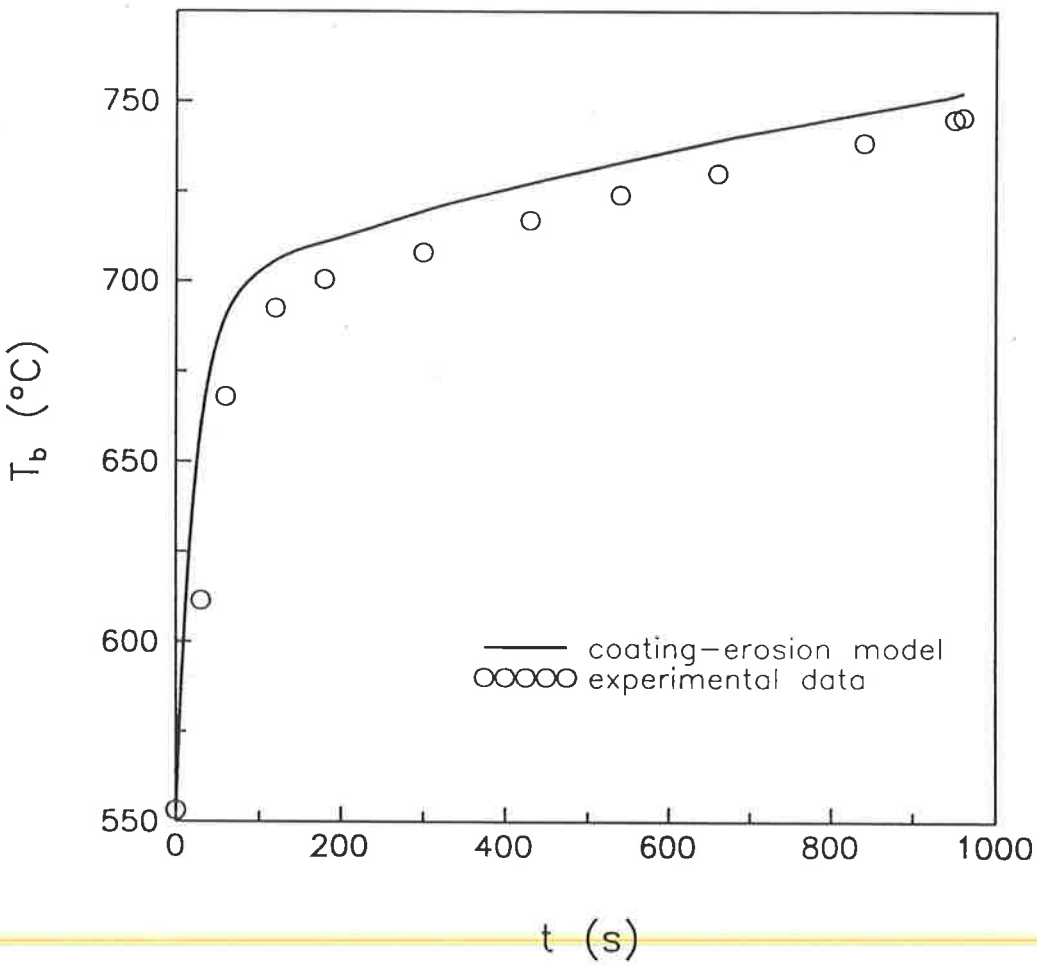

Figure G.13: Comparison of temperature histories of the body for experiment 12.

Experiment 13:

Table G.14: Data from experiment 13.

t (s)	$Q_{b\,ext}$ (W)	u_o (ms^{-1})	T_∞ (°C)	T_b (°C)
0	0	0.484	538	538
30	638	0.486	541	589
60	638	0.488	544	649
120	635	0.493	552	679
180	635	0.497	560	687
240	635	0.500	565	691
300	633	0.504	570	697
430	628	0.508	578	704
540	635	0.513	586	711
720	635	0.519	597	722
900	630	0.524	606	730
1110	633	0.529	614	738
1200	634	0.531	618	742
1230	634	0.532	619	744
Average:	**633**	**0.513**	**587**	-
Coating Mass:	**0.1186 g**	**Spatial Distribution:**		**A**
Sintering Temperature:		**752.4 °C**		

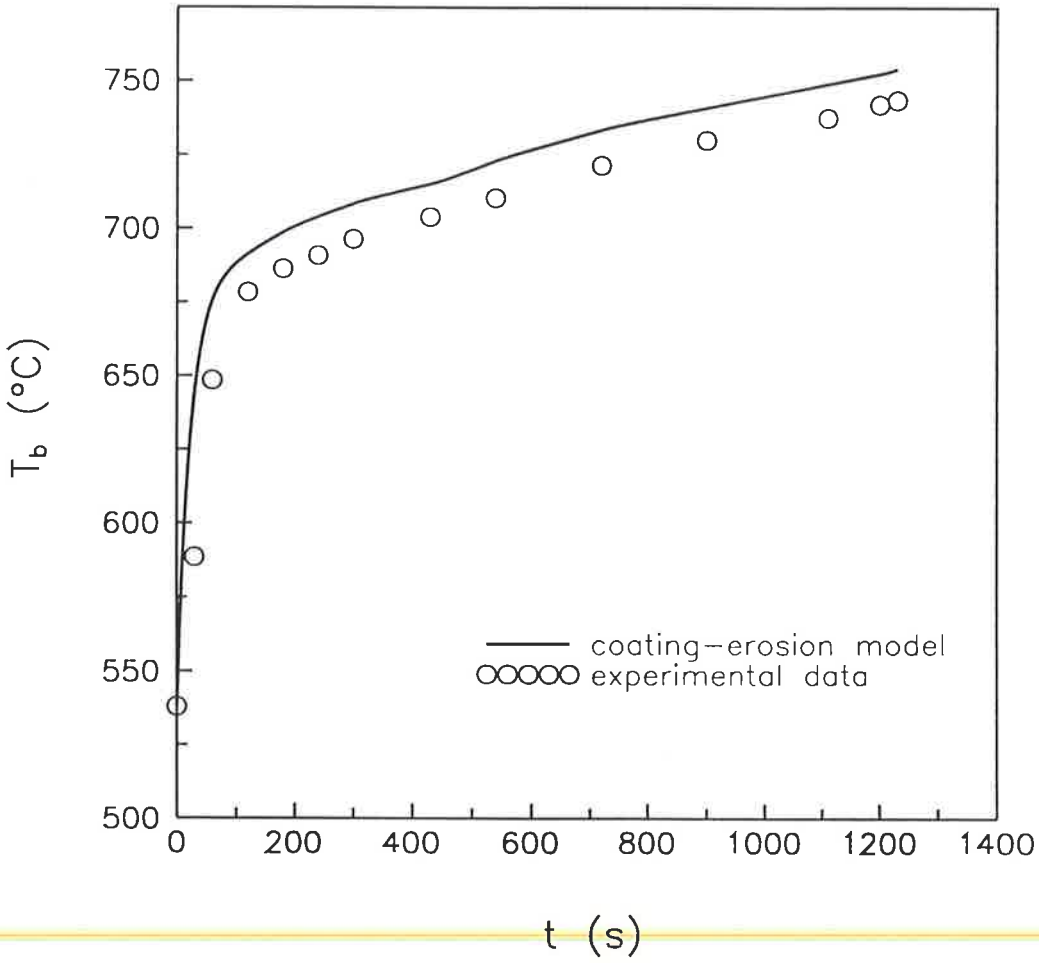

Figure G.14: Comparison of temperature histories of the body for experiment 13.

Experiment 14:

Table G.15: Data from experiment 14.

t (s)	$Q_{b\,ext}$ (W)	u_o (ms^{-1})	T_∞ (°C)	T_b (°C)
0	0	0.425	542	541
30	638	0.426	545	601
60	635	0.428	548	654
120	635	0.433	556	683
180	633	0.436	561	689
250	630	0.439	567	695
300	630	0.440	571	700
360	630	0.442	575	703
480	633	0.446	582	710
660	635	0.451	592	717
840	633	0.456	601	726
1035	630	0.459	608	732
1200	630	0.462	615	738
1280	630	0.464	618	741
Average:	**632**	**0.449**	**588**	-
Coating Mass:	**0.1101 g**	**Spatial Distribution:**		**A**
Sintering Temperature:		**750.5 °C**		

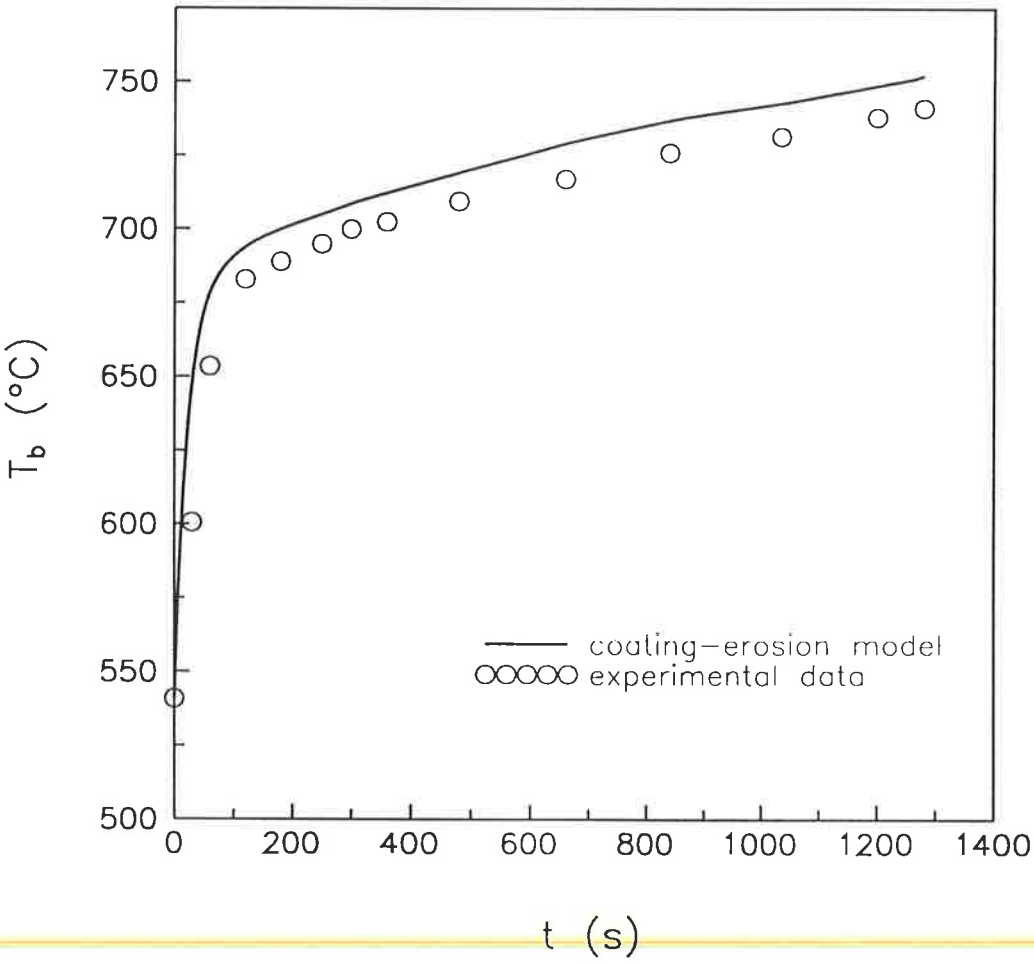

Figure G.15: Comparison of temperature histories of the body for experiment 14.

Experiment 15:

Table G.16: Data from experiment 15.

t (s)	$Q_{b\,ext}$ (W)	u_0 (ms^{-1})	T_∞ (°C)	T_b (°C)
0	0	0.367	531	531
30	635	0.369	535	592
60	635	0.370	538	649
120	638	0.374	546	677
180	638	0.376	552	686
240	635	0.377	555	690
330	635	0.381	564	695
480	630	0.386	573	705
730	633	0.391	585	713
960	633	0.397	596	723
1210	638	0.402	604	732
1380	638	0.403	609	735
1500	638	0.404	613	740
1530	638	0.405	614	741
Average:	**634**	**0.391**	**583**	-
Coating Mass:	**0.1040 g**	**Spatial Distribution:**		**A**
Sintering Temperature:		**748.4 °C**		

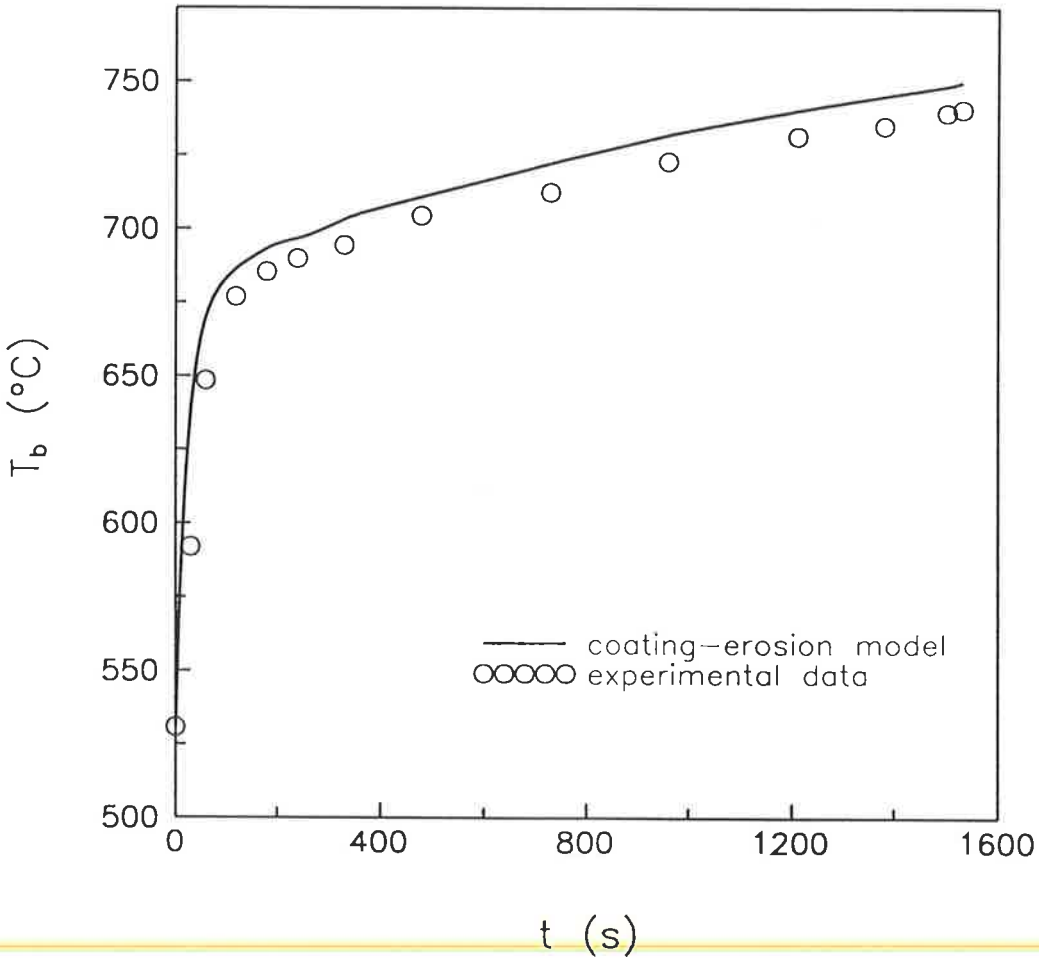

Figure G.16: Comparison of temperature histories of the body for experiment 15.

Experiment 16:

Table G.17: Data from experiment 16.

t (s)	$Q_{b\,ext}$ (W)	u_o (ms^{-1})	T_∞ (°C)	T_b (°C)
0	0	0.476	525	525
30	725	0.478	529	599
60	725	0.479	532	659
120	725	0.484	541	690
180	728	0.489	548	698
240	728	0.493	556	707
300	728	0.496	561	714
360	725	0.500	567	718
420	725	0.503	571	721
480	725	0.505	575	725
540	728	0.508	579	727
605	728	0.509	583	733
720	725	0.514	590	740
780	725	0.516	594	742
800	725	0.517	595	743
Average:	**726**	**0.500**	**566**	**-**
Coating Mass:	**0.0973 g**	**Spatial Distribution:**		**A**
Sintering Temperature:		**749.3 °C**		

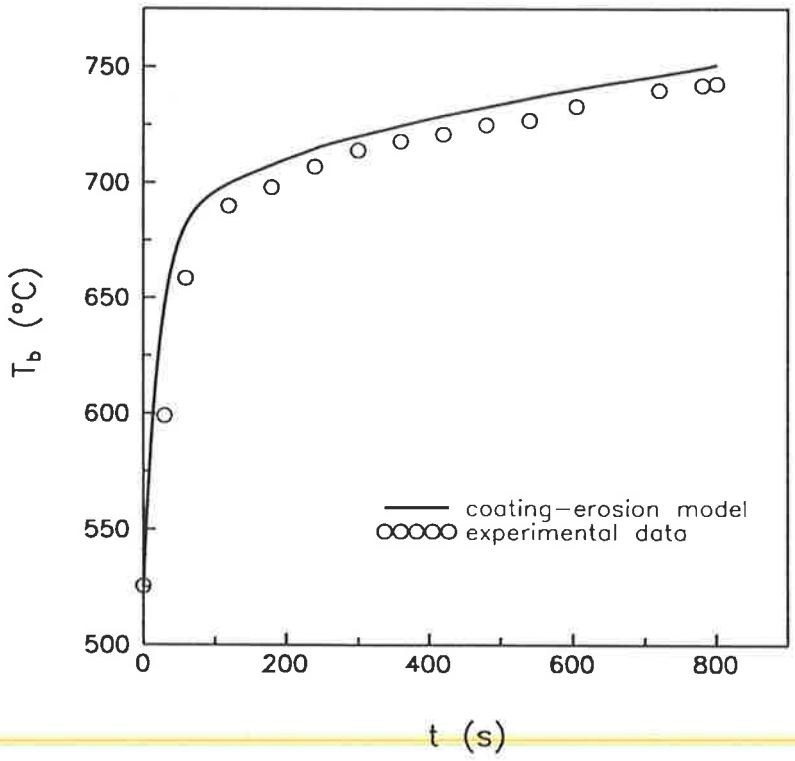

Figure G.17: Comparison of temperature histories of the body for experiment 16.

Experiment 17:

Table G.18: Data from experiment 17.

t (s)	$Q_{b\,ext}$ (W)	u_o (ms^{-1})	T_∞ (°C)	T_b (°C)
0	0	0.364	528	529
30	728	0.366	532	608
60	728	0.367	536	667
120	728	0.372	545	701
180	720	0.375	553	708
240	725	0.378	559	714
300	725	0.379	564	719
360	725	0.380	565	724
420	725	0.384	573	727
480	720	0.386	577	733
540	723	0.388	582	735
600	725	0.389	584	738
660	725	0.390	587	740
680	725	0.390	587	741
Average:	**724**	**0.380**	**564**	-
Coating Mass:	**0.0906 g**	**Spatial Distribution:**		**A**
Sintering Temperature:		**742.7 °C**		

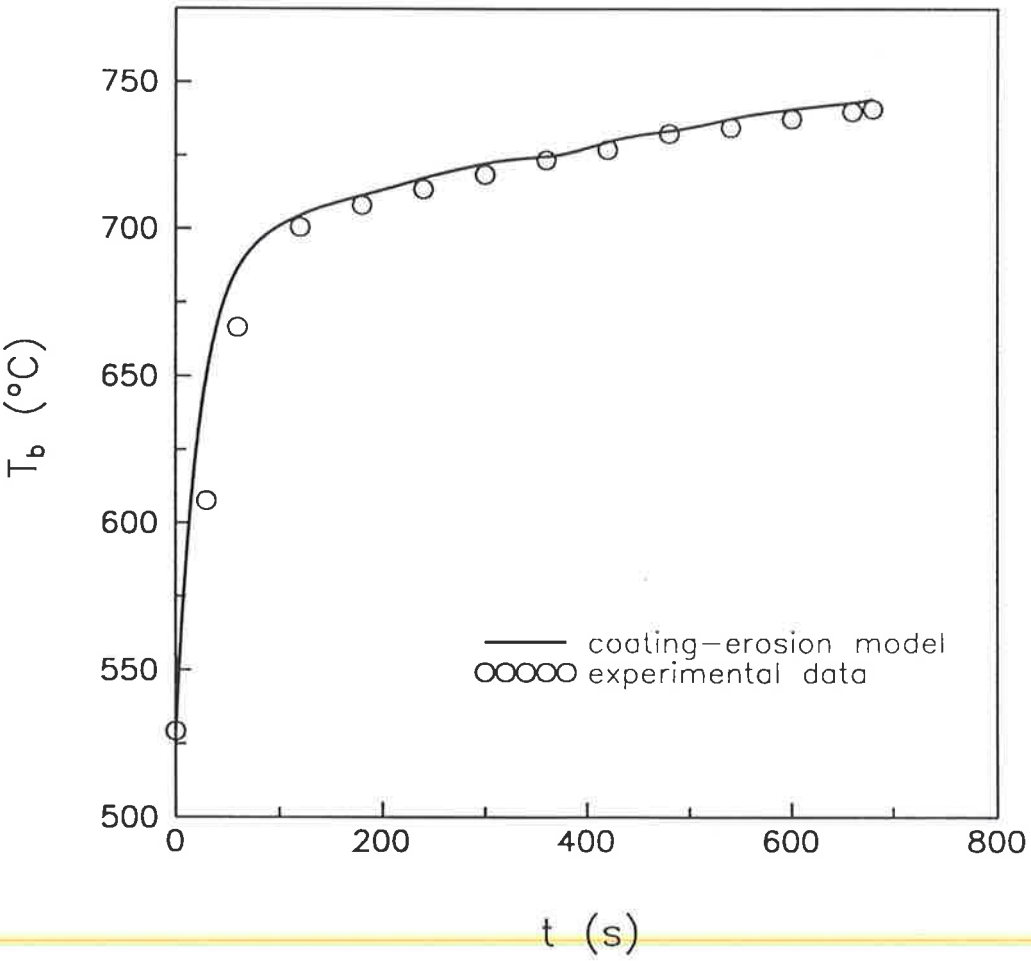

Figure G.18: Comparison of temperature histories of the body for experiment 17.

Experiment 18:

Table G.19: Data from experiment 18.

t (s)	$Q_{b\,ext}$ (W)	u_o (ms^{-1})	T_∞ (°C)	T_b (°C)
0	0	0.330	525	526
30	728	0.332	528	605
60	728	0.333	532	667
120	728	0.337	543	703
180	725	0.340	549	711
240	728	0.343	556	717
300	730	0.345	562	722
360	728	0.348	569	729
420	730	0.349	572	733
480	728	0.350	576	735
540	728	0.352	580	738
590	728	0.353	583	742
610	728	0.354	584	744
Average:	**728**	**0.344**	**560**	**-**
Coating Mass:	**0.2467 g**	**Spatial Distribution:**		**C**
Sintering Temperature:		**740.8 °C**		

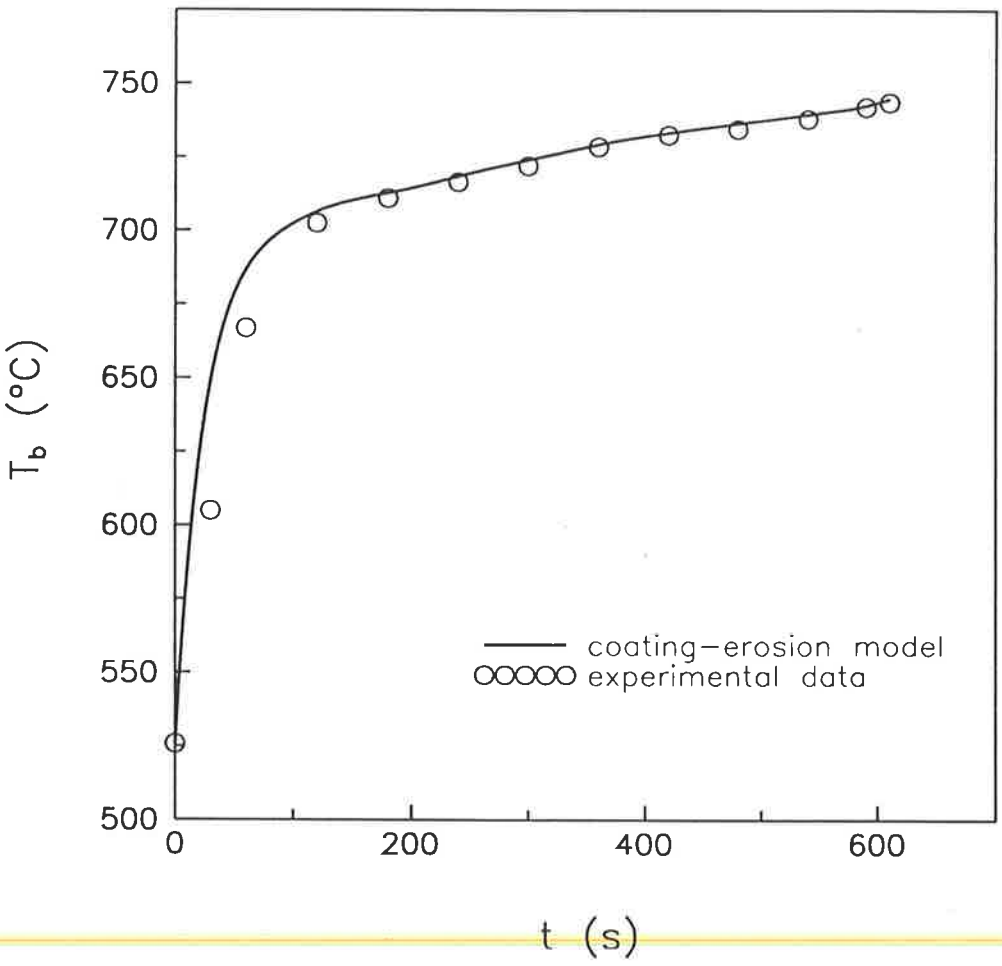

Figure G.19: Comparison of temperature histories of the body for experiment 18.

Experiment 19:

Table G.20: Data from experiment 19.

t (s)	$Q_{b\,ext}$ (W)	u_o (ms^{-1})	T_∞ (°C)	T_b (°C)
0	0	0.303	526	528
30	725	0.305	531	609
60	725	0.307	535	679
120	728	0.310	544	716
180	725	0.313	552	725
240	725	0.316	559	731
300	725	0.318	564	740
345	725	0.320	569	740
360	725	0.320	570	740
Average:	**725**	**0.313**	**550**	-
Coating Mass:	**0.7122 g**	**Spatial Distribution:**		**C**
Sintering Temperature:		**729.9 °C**		

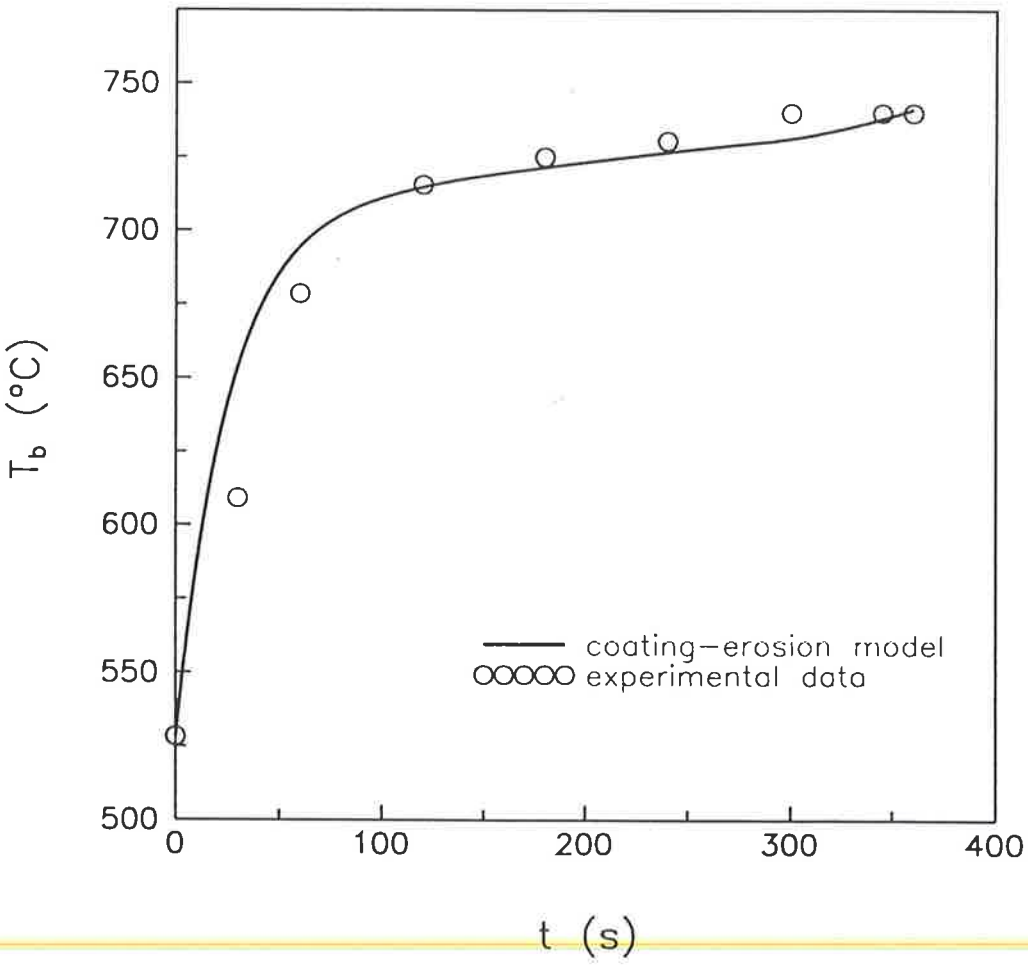

Figure G.20: Comparison of temperature histories of the body for experiment 19.

Experiment 20:

Table G.21: Data from experiment 20.

t (s)	$Q_{b\,ext}$ (W)	u_o (ms^{-1})	T_∞ (°C)	T_b (°C)
0	0	0.262	514	521
30	735	0.263	519	607
60	735	0.265	525	683
120	735	0.269	536	740
Average:	**735**	**0.265**	**525**	-
Coating Mass:	**2.6955 g**	**Spatial Distribution:**		**C+D**
Sintering Temperature:	**720.8 °C**			

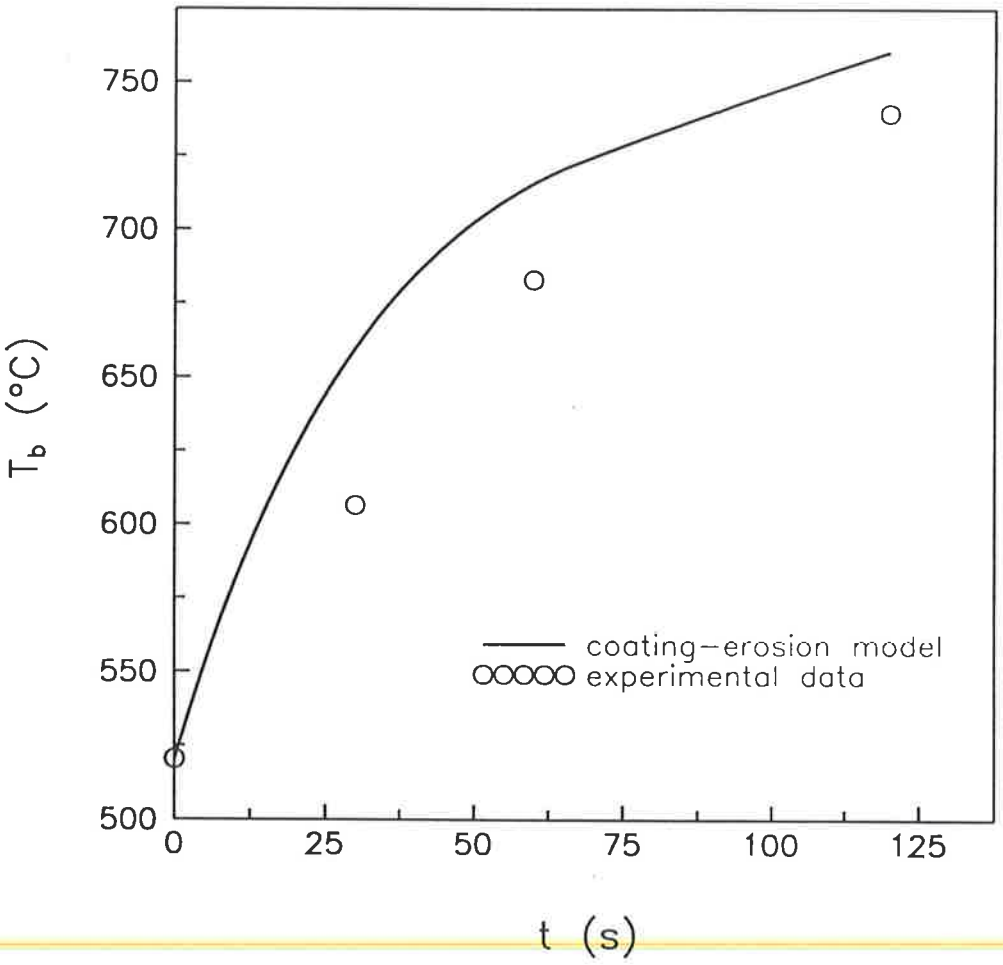

Figure G.21: Comparison of temperature histories of the body for experiment 20.

Experiment 21:

Table G.22: Data from experiment 21.

t (s)	$Q_{b\,ext}$ (W)	u_0 (ms^{-1})	T_∞ (°C)	T_b (°C)
0	0	0.258	505	510
30	445	0.258	507	567
60	445	0.259	509	623
100	448	0.260	513	653
150	445	0.263	521	671
200	445	0.264	525	677
240	445	0.265	528	674
300	435	0.267	535	672
370	435	0.268	537	677
425	430	0.270	542	679
520	433	0.271	546	680
660	435	0.273	553	684
730	435	0.273	554	683
840	433	0.274	558	685
960	435	0.275	561	686
1120	435	0.277	564	691
1450	430	0.281	575	691
1570	435	0.282	577	694
1680	435	0.282	578	694
1740	435	0.282	579	694
Average:	**435**	**0.274**	**554**	-
Coating Mass:	**0.7877 g**	**Spatial Distribution:**		**C**
Sintering Temperature:		**689.8 °C**		

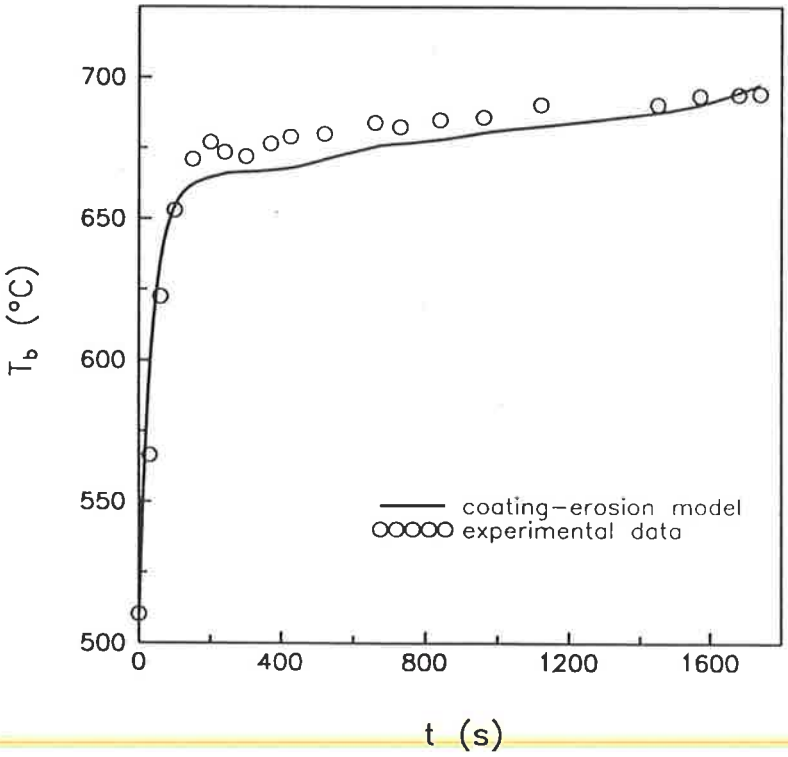

Figure G.22: Comparison of temperature histories of the body for experiment 21.

Experiment 22:

Table G.23: Data from experiment 22.

t (s)	$Q_{b\,ext}$ (W)	u_o (ms^{-1})	T_∞ (°C)	T_b (°C)
0	0	0.269	532	538
30	505	0.270	535	595
60	505	0.271	538	645
120	505	0.272	541	677
180	503	0.274	545	684
240	503	0.275	548	689
300	500	0.276	551	692
390	503	0.278	557	698
480	500	0.279	561	701
580	503	0.281	567	707
660	500	0.282	571	706
780	503	0.284	575	713
900	515	0.286	581	716
1035	515	0.287	585	722
1140	518	0.289	590	725
1260	513	0.289	592	731
1380	513	0.290	594	735
1500	515	0.291	598	734
1580	515	0.292	601	738
1600	515	0.293	602	738
Average:	**508**	**0.283**	**573**	-
Coating Mass:	**3.0614 g**	**Spatial Distribution:**		**C**
Sintering Temperature:		**718.0 °C**		

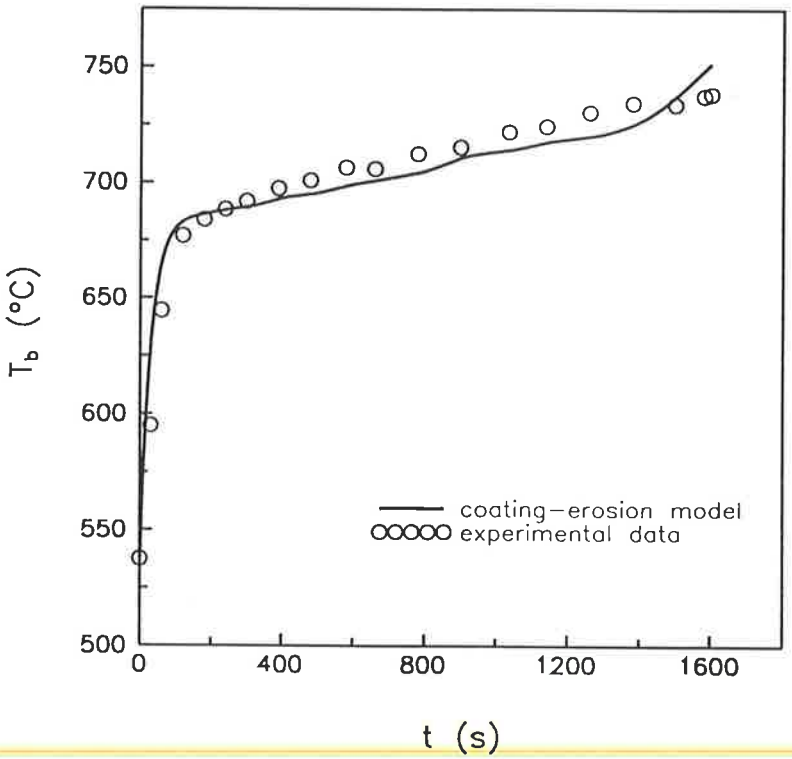

Figure G.23: Comparison of temperature histories of the body for experiment 22.

Experiment 23:

Table G.24: Data from experiment 23.

t (s)	$Q_{b\,ext}$ (W)	u_o (ms^{-1})	T_∞ (°C)	T_b (°C)
0	0	0.307	531	533
30	680	0.308	534	605
60	680	0.309	537	667
120	678	0.313	546	701
170	678	0.315	551	710
230	678	0.318	559	717
300	673	0.321	566	722
360	675	0.322	569	727
420	673	0.325	573	728
485	673	0.326	578	734
500	673	0.327	579	735
Average:	**676**	**0.318**	**558**	-
Coating Mass:	**0.8828 g**	**Spatial Distribution:**		**C**
Sintering Temperature:		**725.2 °C**		

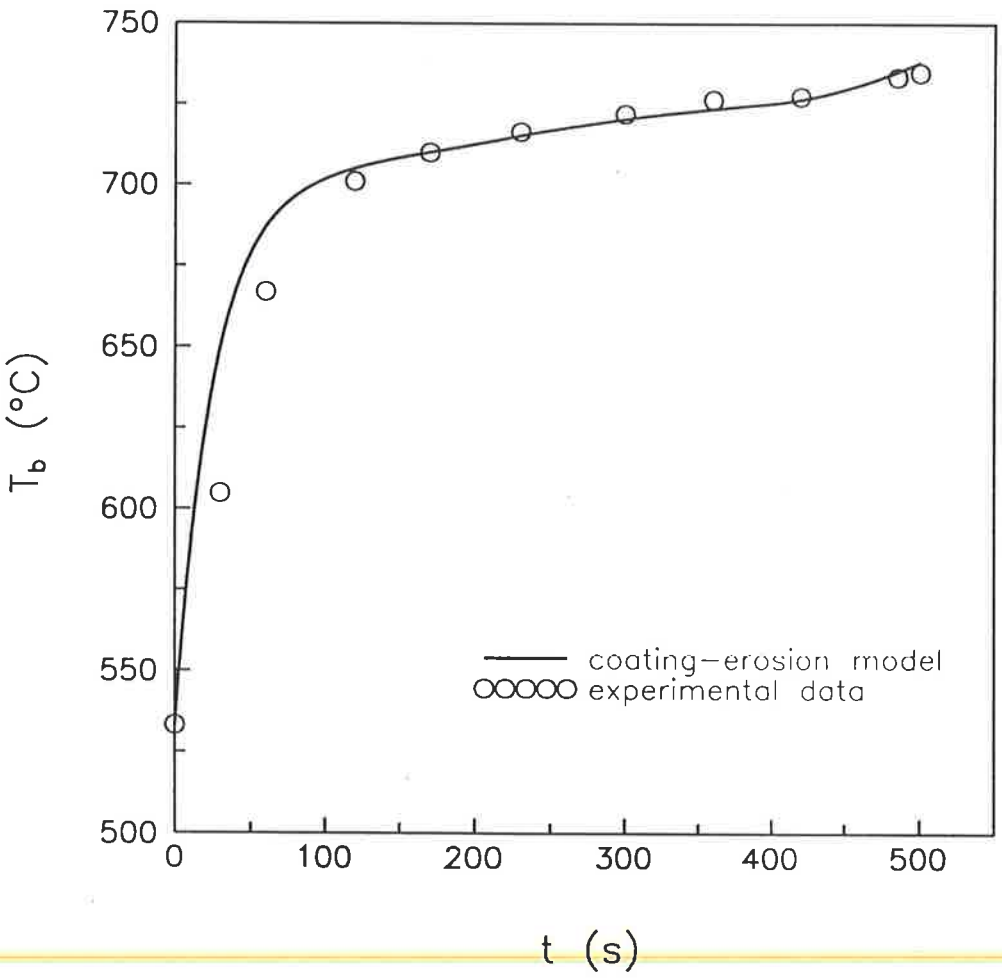

Figure G.24: Comparison of temperature histories of the body for experiment 23.

Experiment 24:

Table G.25: Data from experiment 24.

t (s)	$Q_{b\,ext}$ (W)	u_o (ms^{-1})	T_∞ (°C)	T_b (°C)
0	0	0.302	519	523
60	678	0.305	527	652
120	678	0.309	537	689
180	678	0.312	544	698
240	678	0.315	551	707
300	678	0.317	558	710
320	678	0.318	561	711
Average:	**678**	**0.311**	**541**	-
Coating Mass:	**0.4848 g**	**Spatial Distribution:**		**C**
Sintering Temperature:		**712.7 °C**		

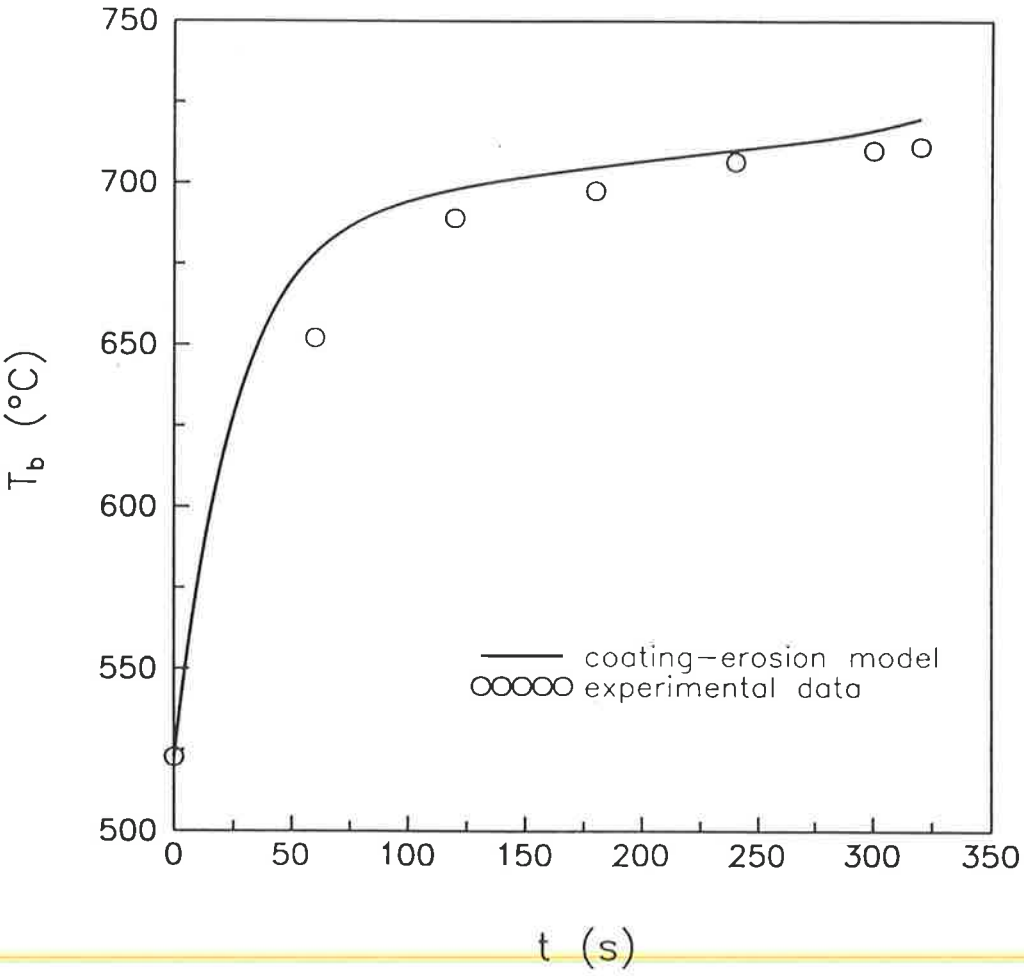

Figure G.25: Comparison of temperature histories of the body for experiment 24.

Experiment 25:

Table G.26: Data from experiment 25.

t (s)	$Q_{b\,ext}$ (W)	u_o (ms^{-1})	T_∞ (°C)	T_b (°C)
0	0	0.256	518	516
30	510	0.256	521	588
60	510	0.257	524	651
120	510	0.260	531	690
180	508	0.260	533	700
250	505	0.262	537	703
315	503	0.263	541	707
330	502	0.263	542	707
Average:	**507**	**0.260**	**532**	-
Coating Mass:	**1.4299 g**	**Spatial Distribution:**		**B**
Sintering Temperature:		**692.1 °C**		

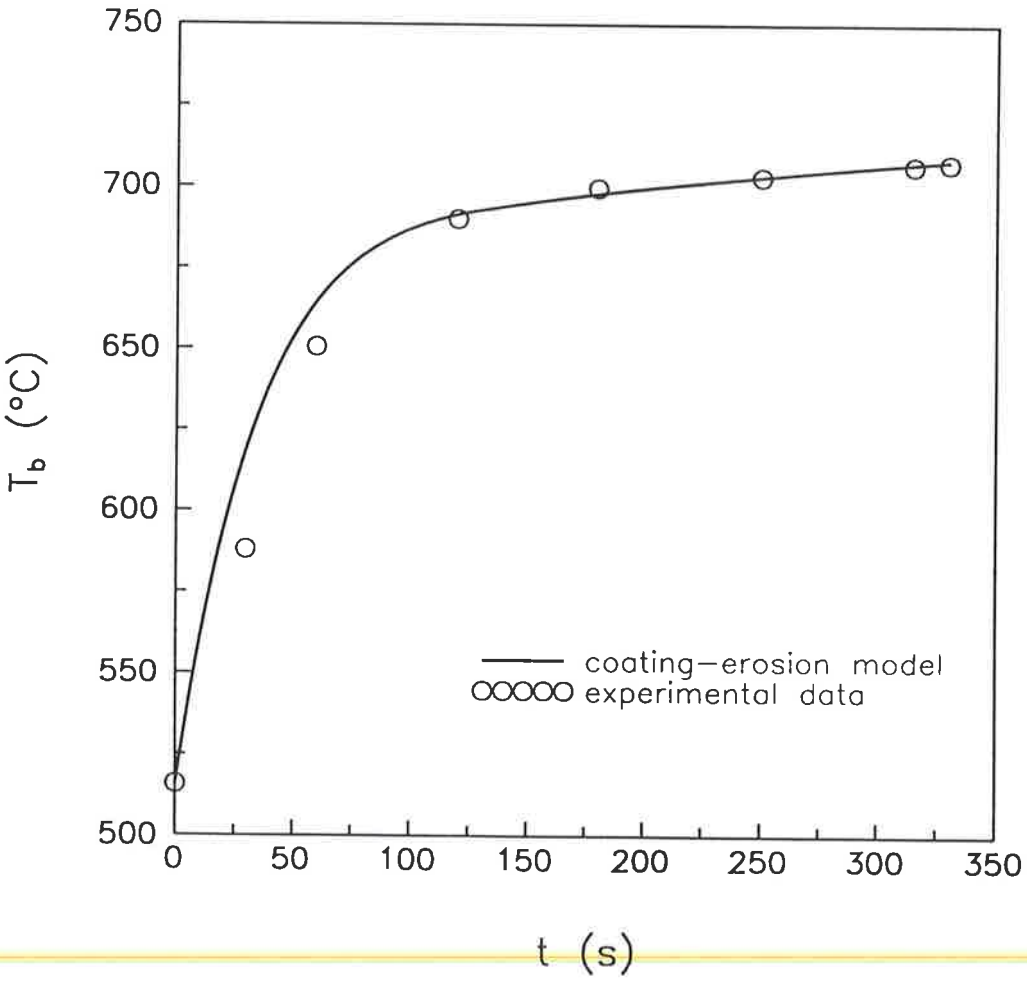

Figure G.26: Comparison of temperature histories of the body for experiment 25.

Experiment 26:

Table G.27: Data from experiment 26.

t (s)	$Q_{b\,ext}$ (W)	u_o (ms^{-1})	T_∞ (°C)	T_b (°C)
0	0	0.300	519	521
30	655	0.301	519	590
60	655	0.302	523	652
140	655	0.306	533	692
190	658	0.309	540	700
250	655	0.311	546	703
360	658	0.316	555	714
480	660	0.319	563	720
600	660	0.320	570	727
750	663	0.324	576	734
840	663	0.325	580	738
900	663	0.326	582	740
915	663	0.326	583	740
Average:	**659**	**0.316**	**557**	-
Coating Mass:	**0.7964 g**	**Spatial Distribution:**		**B**
Sintering Temperature:		**728.1 °C**		

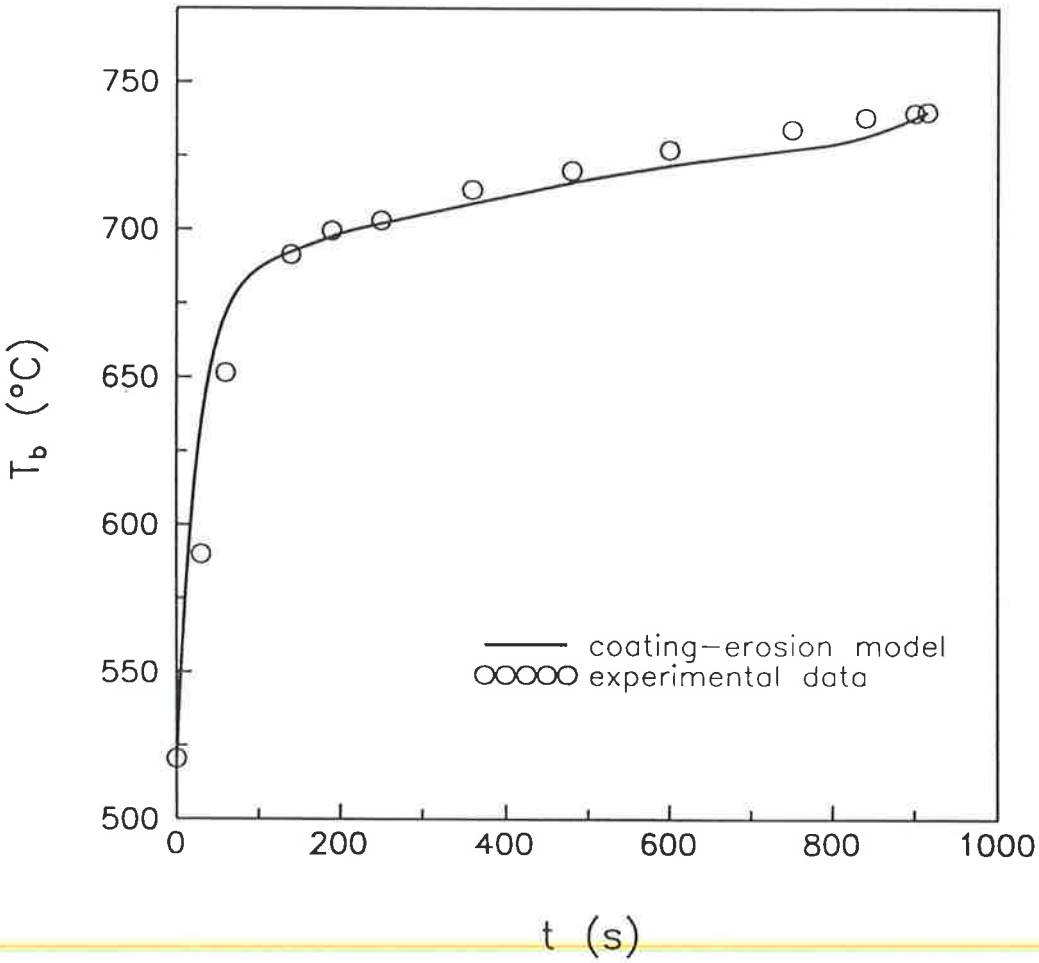

Figure G.27: Comparison of temperature histories of the body for experiment 26.

Experiment 27:

Table G.28: Data from experiment 27.

t (s)	$Q_{b\,ext}$ (W)	u_o (ms^{-1})	T_∞ (°C)	T_b (°C)
0	0	0.325	512	513
30	755	0.326	516	591
60	755	0.328	519	665
120	755	0.331	528	702
180	755	0.335	538	713
240	758	0.339	545	719
300	755	0.341	552	726
360	755	0.343	556	729
420	758	0.346	563	733
480	758	0.347	567	737
540	758	0.348	571	742
560	758	0.349	572	744
Average:	**756**	**0.339**	**546**	-
Coating Mass:	**0.3952 g**	**Spatial Distribution:**		**B**
Sintering Temperature:		**735.6 °C**		

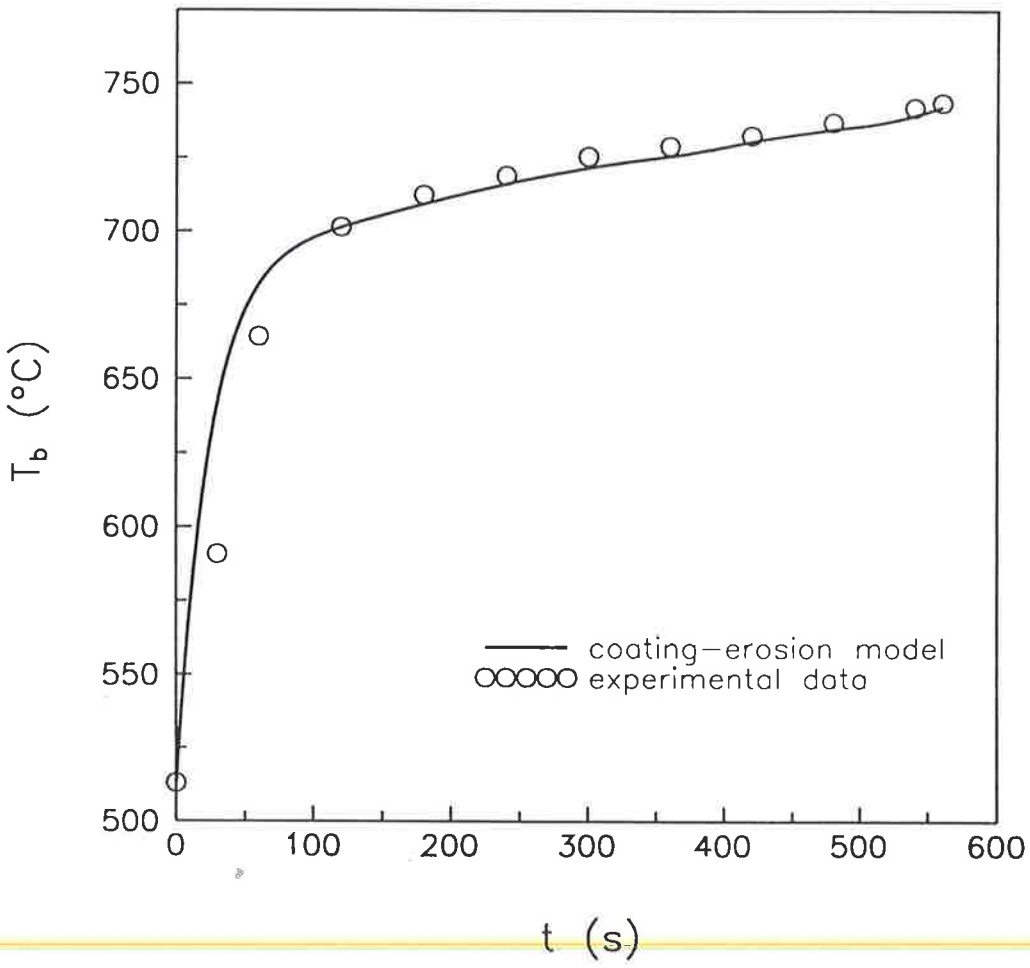

Figure G.28: Comparison of temperature histories of the body for experiment 27.

Experiment 28:

Table G.29: Data from experiment 28.

t (s)	$Q_{b\,ext}$ (W)	u_o (ms^{-1})	T_∞ (°C)	T_b (°C)
0	0	0.260	508	514
30	640	0.262	513	595
60	640	0.264	518	672
110	640	0.266	527	730
120	640	0.267	529	741
Average:	**640**	**0.263**	**518**	-
Coating Mass:	**3.6571 g**	**Spatial Distribution:**		**C+D**
Sintering Temperature:		**689.1 °C**		

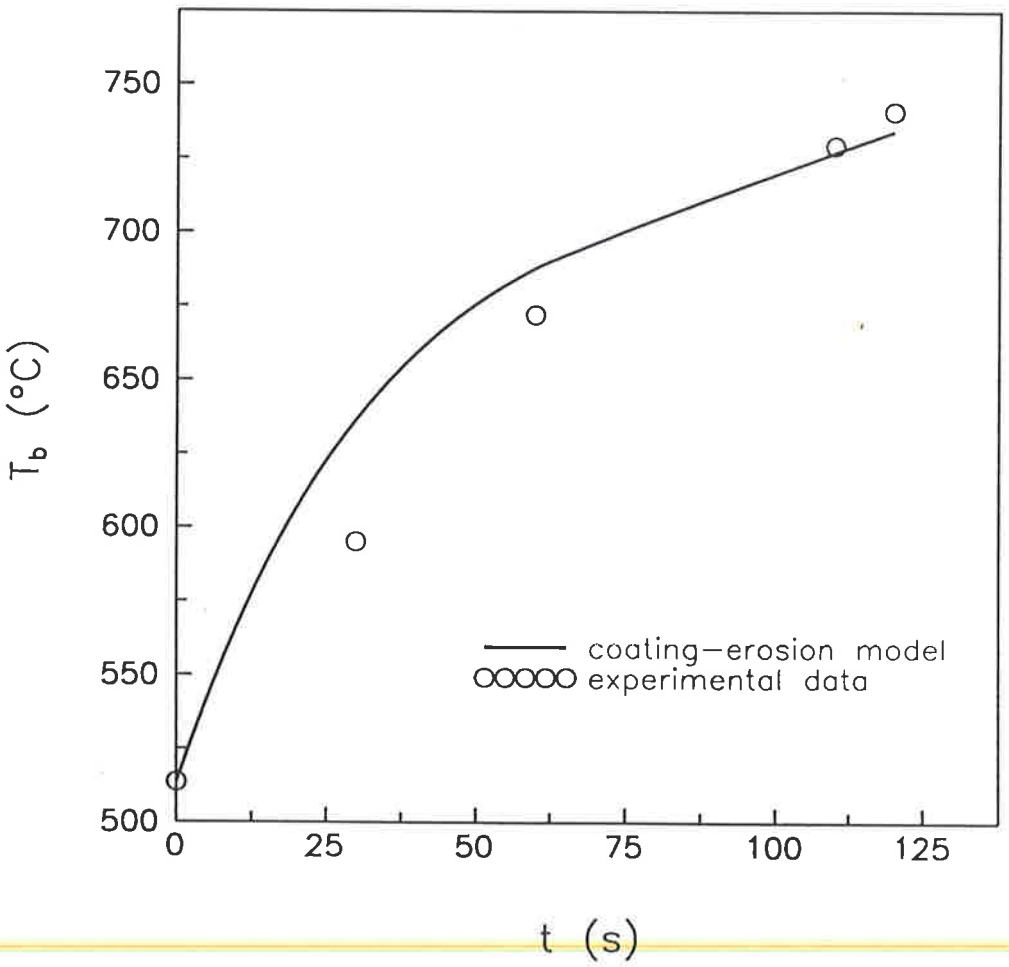

Figure G.29: Comparison of temperature histories of the body for experiment 28.

Experiment 29:

Table G.30: Data from experiment 29.

t (s)	$Q_{b\,ext}$ (W)	u_o (ms^{-1})	T_∞ (°C)	T_b (°C)
0	0	0.262	518	524
30	555	0.263	521	591
60	555	0.265	525	651
100	558	0.267	530	688
140	553	0.269	537	702
180	553	0.270	539	706
230	553	0.272	545	713
270	545	0.274	551	720
320	545	0.277	557	720
340	545	0.278	560	721
350	545	0.278	562	722
Average:	**551**	**0.270**	**539**	-
Coating Mass:	**2.6284 g**	**Spatial Distribution:**		**C+D**
Sintering Temperature:		**696.5 °C**		

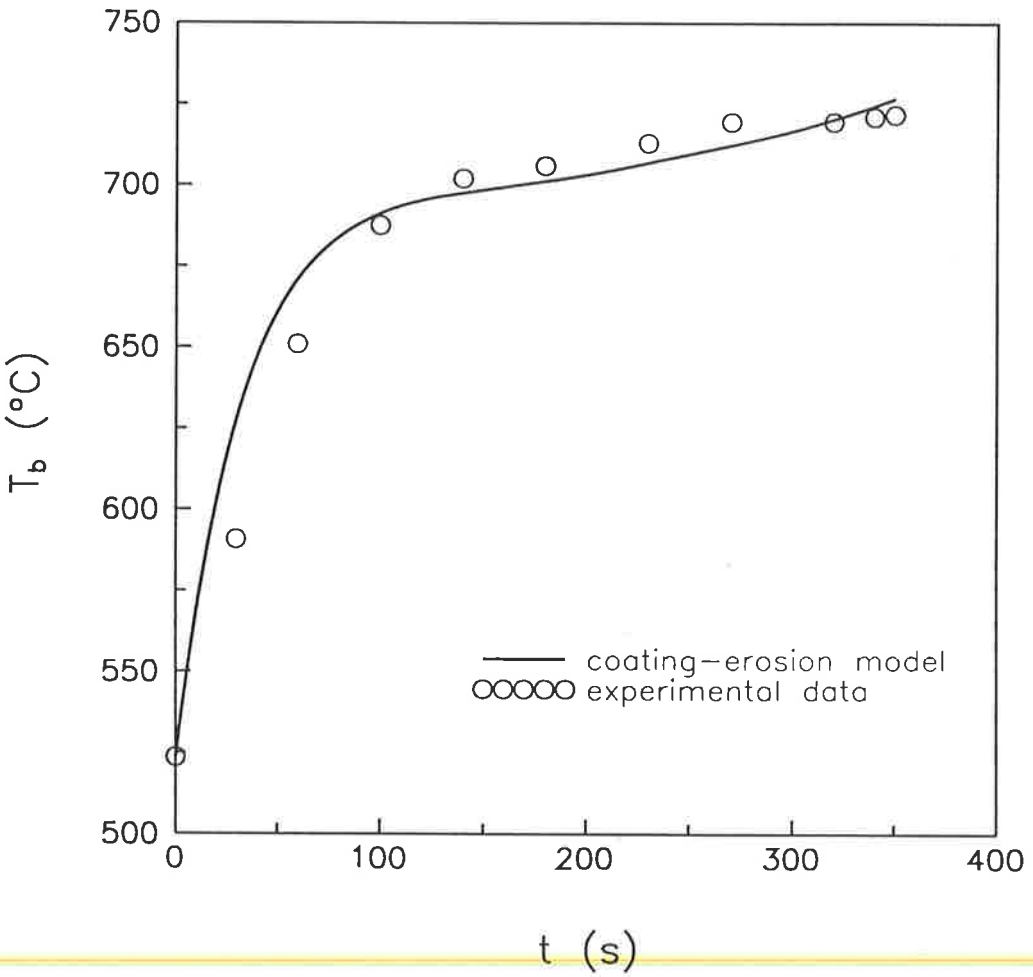

Figure G.30: Comparison of temperature histories of the body for experiment 29.

Experiment 30:

Table G.31: Data from experiment 30.

t (s)	$Q_{b\,ext}$ (W)	u_o (ms^{-1})	T_∞ (°C)	T_b (°C)
0	0	0.263	510	513
30	550	0.264	514	582
60	550	0.265	518	633
120	550	0.268	526	672
180	550	0.269	527	683
240	550	0.272	536	690
300	550	0.272	537	694
360	550	0.273	541	696
420	550	0.274	544	700
510	550	0.276	550	707
600	550	0.278	556	709
720	550	0.280	563	712
840	553	0.282	570	720
960	555	0.284	577	724
1080	555	0.285	580	727
1180	555	0.286	582	734
1200	555	0.286	583	735
Average:	**552**	**0.277**	**554**	-
Coating Mass:	**2.0545 g**	**Spatial Distribution:**		**C**
Sintering Temperature:		**716.5 °C**		

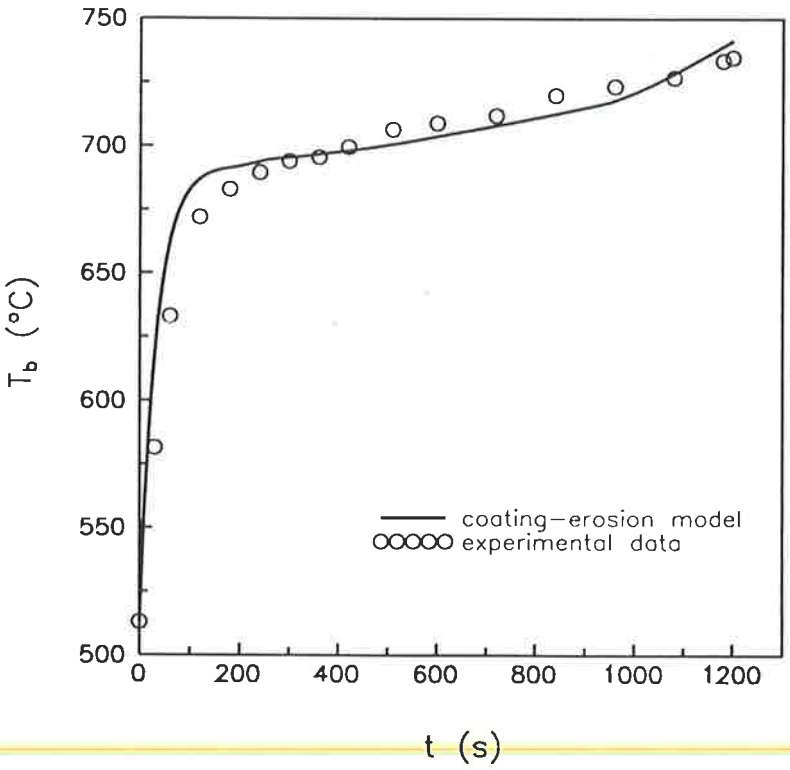

Figure G.31: Comparison of temperature histories of the body for experiment 30.

Experiment 31:

Table G.32: Data from experiment 31.

t (s)	$Q_{b\,ext}$ (W)	u_o (ms^{-1})	T_∞ (°C)	T_b (°C)
0	0	0.305	523	527
30	615	0.306	526	591
60	615	0.307	528	649
120	613	0.310	537	682
180	610	0.312	544	694
240	615	0.315	551	698
300	618	0.317	557	704
360	618	0.318	560	708
420	623	0.320	565	711
480	620	0.322	569	715
580	613	0.324	575	720
660	615	0.325	578	723
750	618	0.327	584	727
840	618	0.328	588	731
930	615	0.330	591	734
1020	615	0.331	596	737
1070	615	0.332	598	740
1080	615	0.333	599	740
Average:	**616**	**0.321**	**568**	-
Coating Mass:	**0.9901 g**	**Spatial Distribution:**		**B**
Sintering Temperature:		**730.1 °C**		

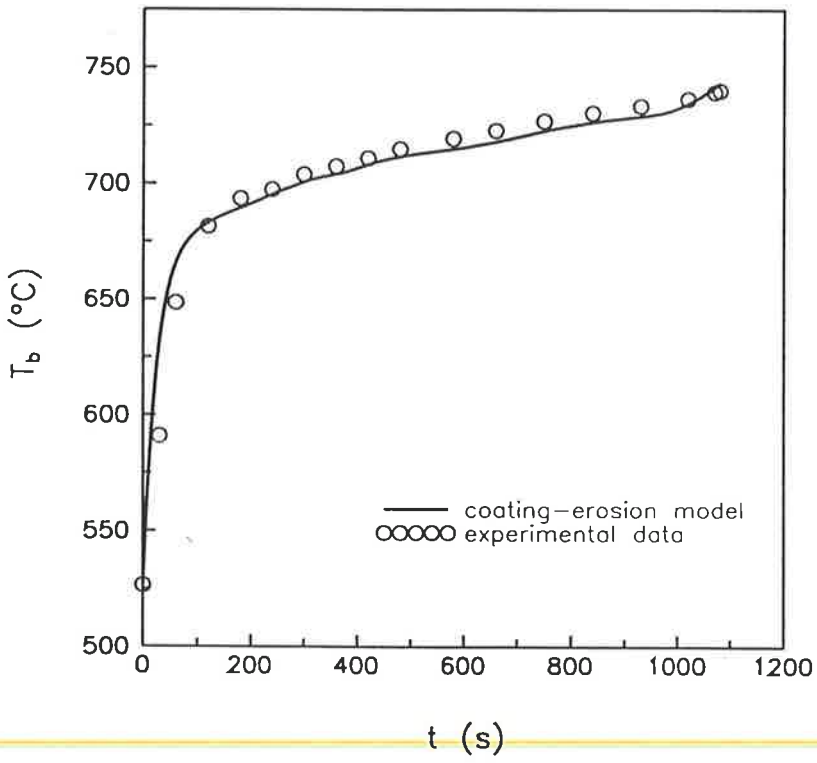

Figure G.32: Comparison of temperature histories of the body for experiment 31.

Experiment 32:

Table G.33: Data from experiment 32.

t (s)	$Q_{b\,ext}$ (W)	u_o (ms^{-1})	T_∞ (°C)	T_b (°C)
0	0	0.305	528	531
30	455	0.306	530	582
60	455	0.307	533	621
120	453	0.309	539	644
180	450	0.311	545	653
240	453	0.312	548	656
300	450	0.314	552	659
390	450	0.315	556	660
480	453	0.318	561	665
570	453	0.319	564	669
660	453	0.320	567	672
750	453	0.321	570	675
840	450	0.322	573	676
960	450	0.324	578	679
1080	450	0.325	581	682
1200	450	0.326	584	685
1320	450	0.327	587	687
1390	450	0.328	588	688
1410	450	0.328	589	688
Average:	**451**	**0.319**	**566**	-
Coating Mass:	**0.0399 g**	**Spatial Distribution:**		**A**
Sintering Temperature:		**691.2 °C**		

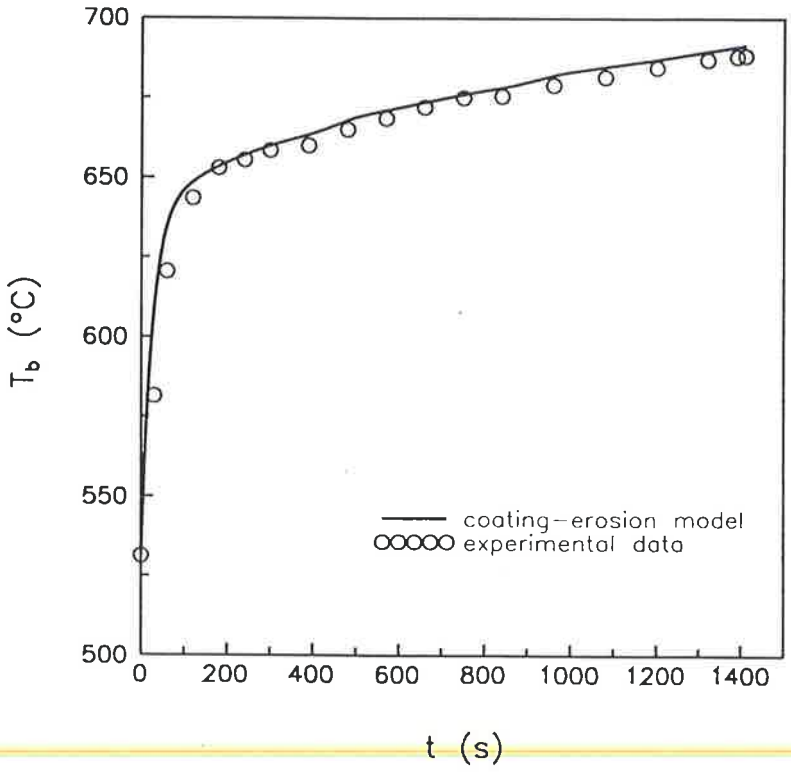

Figure G.33: Comparison of temperature histories of the body for experiment 32.

Experiment 33:

Table G.34: Data from experiment 33.

t (s)	$Q_{b\,ext}$ (W)	u_o (ms^{-1})	T_∞ (°C)	T_b (°C)
0	0	0.284	508	510
40	628	0.286	512	615
60	628	0.287	514	647
120	628	0.289	521	688
185	625	0.292	528	696
240	628	0.294	535	701
310	625	0.295	539	708
390	628	0.298	546	712
480	628	0.301	553	717
570	628	0.303	559	721
650	628	0.305	564	725
665	628	0.305	565	726
Average:	**627**	**0.296**	**540**	-
Coating Mass:	**0.4237 g**	**Spatial Distribution:**		**B**
Sintering Temperature:		**711.5 °C**		

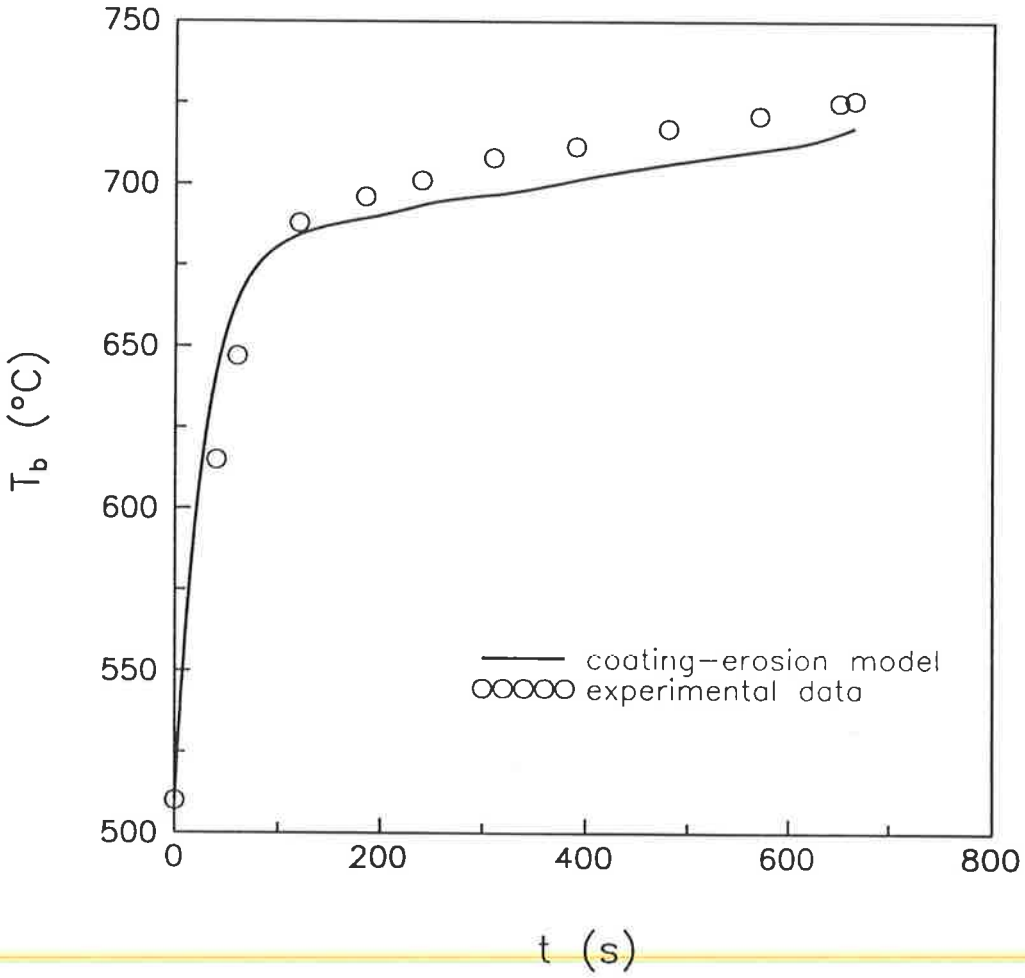

Figure G.34: Comparison of temperature histories of the body for experiment 33.

Experiment 34:

Table G.35: Data from experiment 34.

t (s)	$Q_{b\,ext}$ (W)	u_o (ms^{-1})	T_∞ (°C)	T_b (°C)
0	0	0.258	530	533
30	515	0.259	532	594
60	515	0.260	535	647
140	510	0.262	542	687
210	513	0.263	546	694
270	513	0.264	550	702
340	510	0.265	552	705
420	510	0.266	555	711
510	513	0.267	559	711
600	515	0.269	563	714
665	515	0.270	566	714
680	515	0.270	567	714
Average:	**512**	**0.265**	**551**	-
Coating Mass:	**1.0749 g**	**Spatial Distribution:**		**B**
Sintering Temperature:		**707.0 °C**		

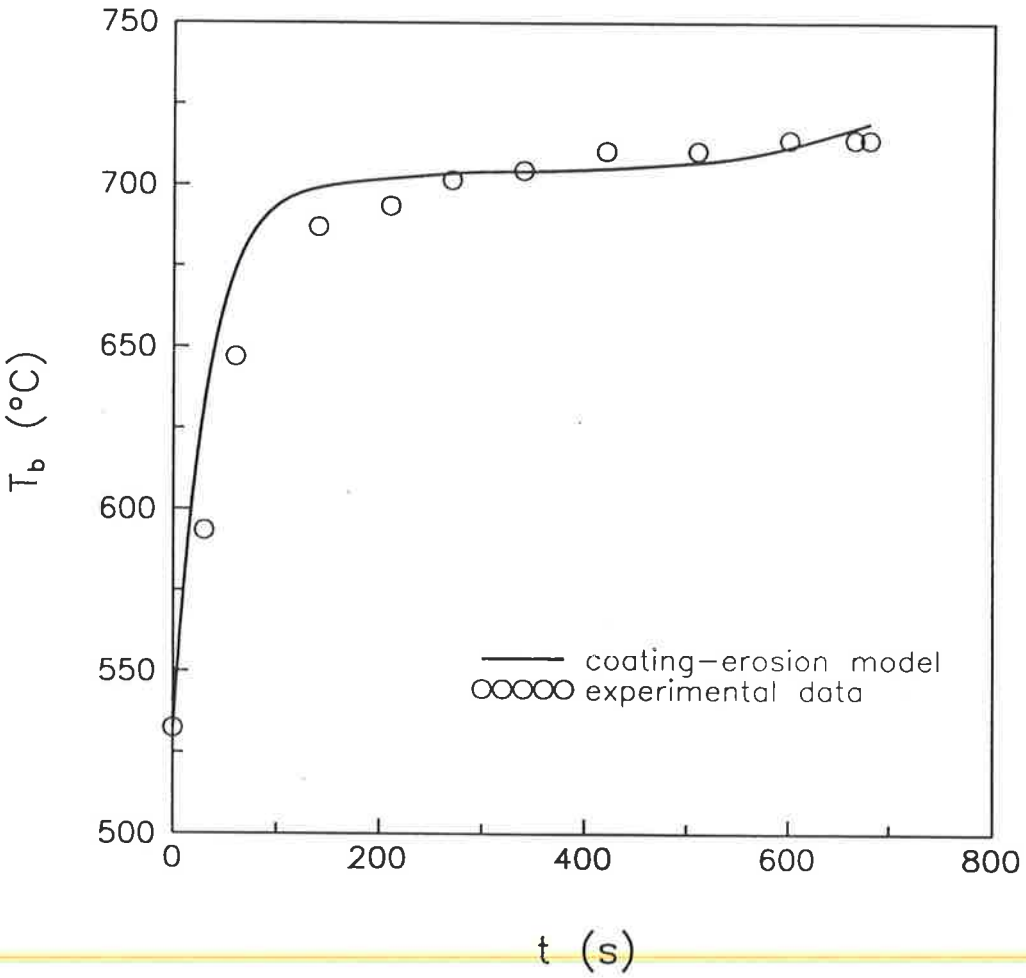

Figure G.35: Comparison of temperature histories of the body for experiment 34.

Experiment 35:

Table G.36: Data from experiment 35.

t (s)	$Q_{b\,ext}$ (W)	u_o (ms^{-1})	T_∞ (°C)	T_b (°C)
0	0	0.257	530	537
30	515	0.258	532	593
60	515	0.259	535	641
120	518	0.259	537	678
180	518	0.260	539	702
200	518	0.260	539	710
Average:	**516**	**0.259**	**536**	-
Coating Mass:	**3.6990 g**	**Spatial Distribution:**		**C+D**
Sintering Temperature:		**687.8 °C**		

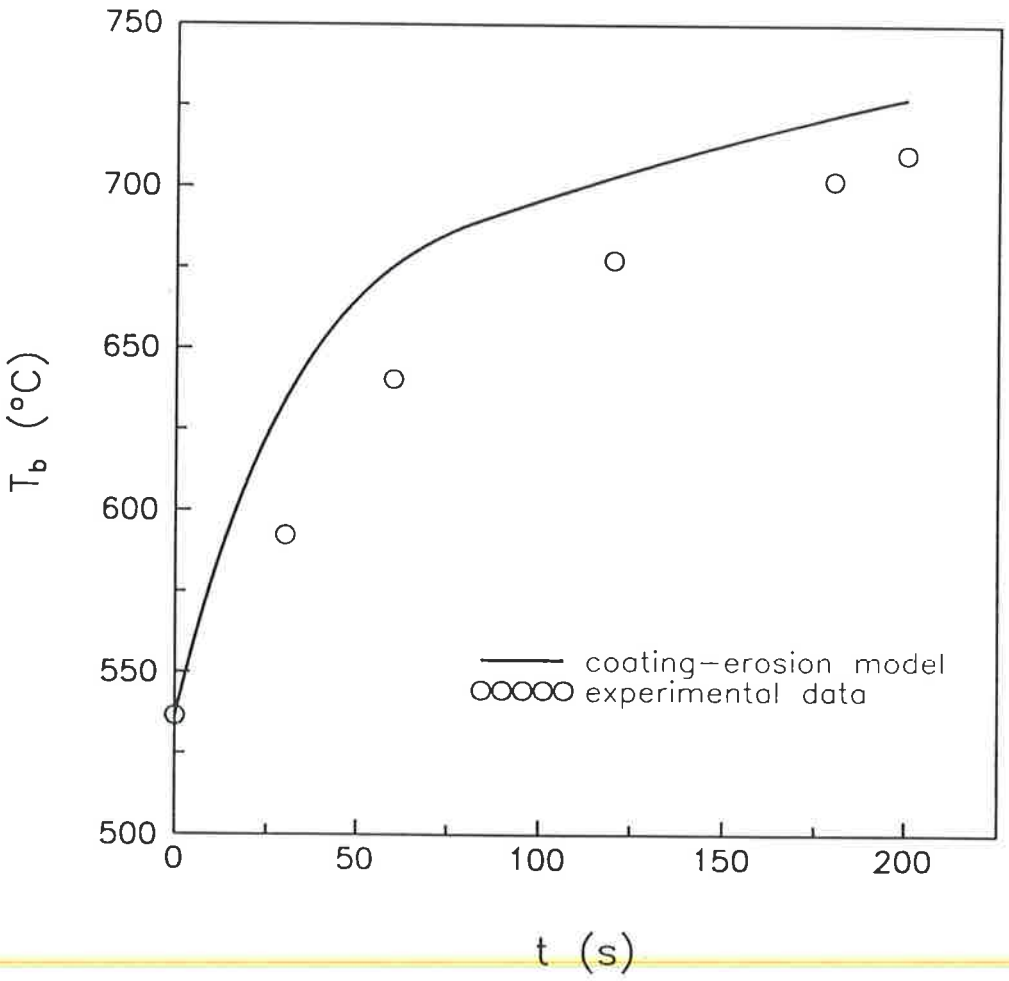

Figure G.36: Comparison of temperature histories of the body for experiment 35.

Experiment 36:

Table G.37: Data from experiment 36.

t (s)	$Q_{b\,ext}$ (W)	u_o (ms^{-1})	T_∞ (°C)	T_b (°C)
0	0	0.254	517	518
30	510	0.255	520	584
60	510	0.256	522	636
120	508	0.258	530	671
180	508	0.259	534	682
245	508	0.260	535	688
300	508	0.261	539	691
390	510	0.262	543	696
450	505	0.263	545	698
540	505	0.264	550	701
630	505	0.266	553	705
720	505	0.267	556	706
810	508	0.268	559	710
900	505	0.269	563	712
990	508	0.270	566	716
1080	500	0.271	570	714
1150	500	0.272	571	716
1200	500	0.272	572	719
1220	500	0.272	573	720
Average:	**506**	**0.265**	**551**	-
Coating Mass:	**0.9789 g**	**Spatial Distribution:**		**B**
Sintering Temperature:		**707.4 °C**		

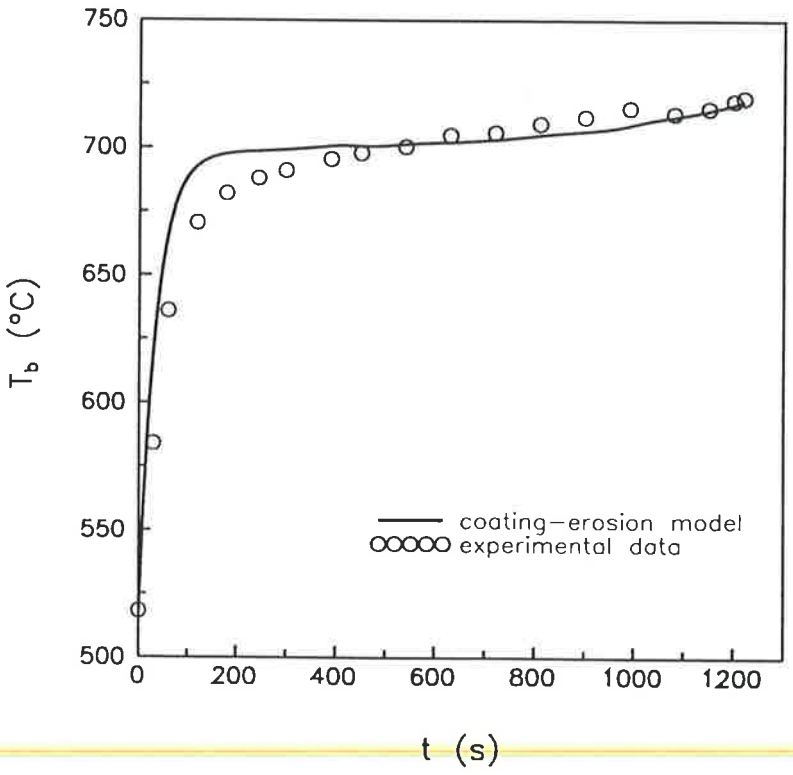

Figure G.37: Comparison of temperature histories of the body for experiment 36.

Experiment 37:

Table G.38: Data from experiment 37.

t (s)	$Q_{b\,ext}$ (W)	u_o (ms^{-1})	T_∞ (°C)	T_b (°C)
0	0	0.269	562	563
30	515	0.269	562	620
60	515	0.269	563	673
120	503	0.270	566	706
180	513	0.271	570	717
240	513	0.272	573	722
300	513	0.272	575	724
360	513	0.272	576	727
420	513	0.273	576	731
440	513	0.273	577	732
Average:	**512**	**0.271**	**571**	-
Coating Mass:	**2.7078 g**	**Spatial Distribution:**		**B+E**
Sintering Temperature:		**709.5 °C**		

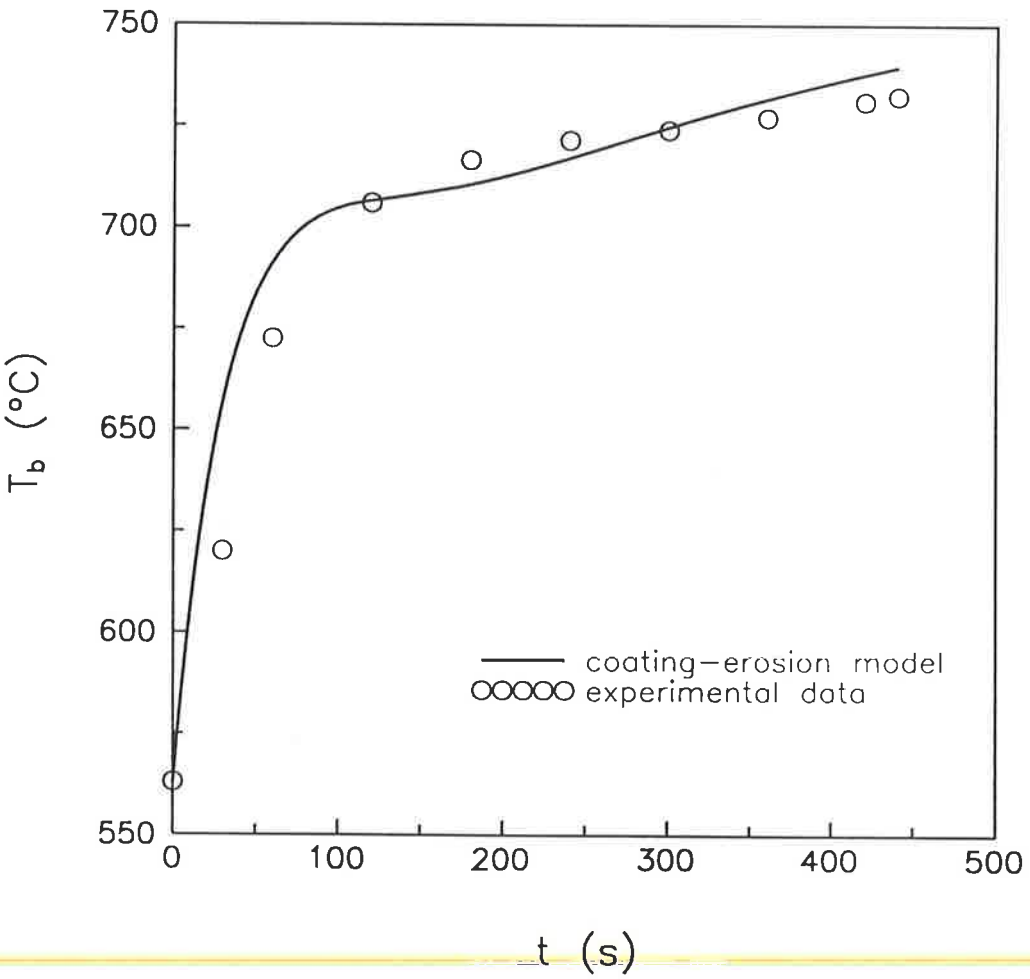

Figure G.38: Comparison of temperature histories of the body for experiment 37.

Appendix H:

VARIABLE-POROSITY COATING

It is well recognised that high temperature sintering is a time- and temperature-dependent process. As the temperature is increased, and as time passes, the voidage of a particle assemblage will decrease through sintering at elevated temperatures. The driving force for sintering is the reduction of the surface area. In the present case, if it were possible to follow the history of an individual particle once it had stuck to the coating layer, it is reasonable to expect that the voidage in its immediate neighbourhood decrease as the experiment progressed. Thus, particles near the heater should have a lower local porosity than those that are close to the surface, since they have been there a longer time. Further, in Chapter 4, the presence of a temperature profile in the coating layer was predicted - the temperature in the layer should decrease with increasing distance from the heater. This situation is complicated by the high local porosity of a packed bed next to a flat surface (Dullien, 1979, p137). Hence, there are good reasons why we should expect a time-dependent porosity profile in the coating layer. The voidage should be low close to (but not at) the heater surface and high at the coating-bed interface; at a given location, the voidage should decrease with time. Section 5.4.3 relates some initial observations on the internal structure of the coating layer. For the present, it is sufficient to say that the porosity of the coating was variable, but that its variation has not been quantified.

A principal assumption of the coating erosion model is that the density of the coating is constant (Section 4.2), which, in effect, means that ε does not change. Further, to

simplify the comparison of the theory and the experiments it was decided to use the same coating voidage for all of the experiments. However, exactly which voidage value to use is a difficult choice. Certainly, from inspection of the coating fragments, ε is seen to lie in the range 0 (non-porous solid) to 0.42 (randomly packed bed of uniform spheres). The voidage used in the theory is an "effective voidage" - some average over the duration of the experiment and over the thickness of the coating. Tentatively, the coating porosity was taken as the arithmetic mean of the upper and lower limits mentioned above, that is, $\varepsilon = 0.21$.

If the assumption of constant density were not made, the model, equations (4.8) to (4.17), would be more complex. For example the mass balance, equation (4.16a) would need to be rewritten as:

$$\frac{d}{dt}\left(\int_{r_b}^{r_c(t)} \rho\left(\varepsilon(T|_r, \tau)\right).2\pi r L \, dr \right) = \left(\mathcal{R}_c - \mathcal{R}_e\right).\rho\left(\varepsilon(T_i, \tau)\right).2\pi r_c(t) L \qquad \text{(H.1)}$$

which includes the "constitutive equations":

$\rho = \rho(\varepsilon)$, which is merely equation (5.4);

$\varepsilon = \varepsilon(T, \tau)$; (H.2)

$\tau = \tau(r, t)$; (H.3)

where τ is the age of the coating at radius, r, and time, t.

Sintering Theory

Equation (H.2) is based on a model of sintering. There are a number of mechanisms by which sintering may occur (Kuczynski, 1972; German, 1984): surface diffusion, evaporation-condensation (both classified as surface transport mechanisms); lattice diffusion, grain boundary diffusion, plastic flow and viscous flow (which are bulk transport processes). For a given material, several mechanisms may be active at the

same time, and their relative contributions can change with temperature. Over a wide range of temperatures, the sintering of ordinary soda glass takes place predominantly by Newtonian viscous flow (Weyl and Marboe, 1964; Kuczynski, 1972). Frenkel (Kuczynski, 1972) analysed this situation theoretically and found that the diameter, x, of the bond neck between two spheres of diameter, d_p, varies as:

$$\left(\frac{x}{d_p}\right)^2 = \frac{3\gamma t}{\mu d_p} \qquad \text{(H.4)}$$

at the start of the sintering process, where γ is the surface tension, μ is the viscosity and t is time. Note that equation (H.4) indicates that the sintering rate is affected by temperature since the viscosity of glass is usually correlated as:

$$\mu = A e^{\left(\frac{B}{T-C}\right)} \qquad \text{(H.5)}$$

where A, B, and C depend on the composition of the glass; and γ is almost independent of temperature (de Jong, 1989). An alternative derivation by Rumpf et al. (1978) yields a constant of 3.2 instead of 3 in equation (H.4). Klose and Lent (1985) present an analysis that may apply beyond the initial stage of sintering as it exhibits the correct limit of $x \rightarrow d_p$ as $t \rightarrow \infty$, unlike equation (H.4). Expressions analogous to equation (H.4) for other sintering mechanisms have been summarised by Kuczynski (1972).

The bond neck diameter is related to the linear fractional shrinkage of the particles, $(\Delta L/L_o)$, by:

$$\frac{\Delta L}{L_o} \approx \frac{1}{4}\left(\frac{x}{d_p}\right)^2 \qquad \text{(H.6)}$$

Finally, the relationship between the interparticle shrinkage and the porosity of a random assembly of particles is:

$$\varepsilon = 1 - \frac{1-\varepsilon_o}{(1-\Delta L / L_o)^3} \qquad \text{(H.7)}$$

where ε_o is the initial porosity. Equation (H.7) strictly applies when no new bond necks form and no particle rearrangement occurs as sintering progresses. Although some rearrangement and extra bond creation does take place (Exner and Petzow, 1975; Jagota et al., 1990), leading to "somewhat anomalous" overall sintering rates, equation (H.7) will be retained here for simplicity. Exner and Petzow (1975) demonstrated that the extent to which these two processes take place depends on the composition of the surrounding gas. For example, new particle bonds form in a planar arrangement of glass beads about five times more often in wet air as in dry air. They tentatively attributed this and similar results to the modification of the viscosity of a thin surface layer of the glass by certain gases (such as water vapour and oxygen). The application of an external force can significantly increase the rate of sintering. Rumpf et al. (1978) have analysed this case to obtain an additional term in equation (H.4), and also allowed for plastic deformation of the particles in the contact zone. Two types of external force may act on the coating layer in the present experimental system. The first is a small hydrostatic force due to the depth of immersion of the object in the fluidized bed. Secondly, there are strong impulse forces caused by the impact of wake particles from bubbles colliding with the object (Livshits et al., 1978; Nguyen and Grace, 1978; Hosny and Grace, 1984; Levy et al., 1992).

Equations (H.4), (H.6) and (H.7) apply only to the initial stage of sintering, generally recognised as $x/d_p < 0.3$, in which small bond necks form where particles touch. The driving force for this process is the need to eliminate the high curvature gradients in the

particle contact zones. The pore space of the particle assembly is completely connected and is very uneven.

As the sintering process continues, the pores remain fully interconnected, but become smoother as the particles loose their individuality. Various models for the intermediate stage of sintering have been developed from more appropriate geometrical descriptions of the particle assemblage. For example, Scherer (1977) viewed the particle structure as a regular cubic array of intersecting solid cylinders of uniform diameter. Kuczynski (1975), by contrast, focussed on the pore space, which he described as a continuous cylindrical void of varying diameter meandering through a block of solid material.

The final stage of sintering is entered when the pore space becomes discontinuous, breaking up into a collection of isolated spherical voids. Analyses of the final stage have been presented by Mackenzie and Shuttleworth (1949) and Kuczynski (1975). Table H.1 is a summary of the main characteristics of the three broad stages of sintering.

Discussions of the above and of other sintering studies (including those dealing with non-spherical particles, a wide distribution of pore sizes, different mechanisms and other materials) may be found in: Coble and Burke (1963), Kingery (1965), Kuczynski (1972), Exner and Petzow (1980), German (1984), and Rabinovich (1985). Recent experimental and theoretical studies (Rahaman et al., 1987; Ducamp and Raj, 1989; Jagota et al., 1990) into the sintering of glass spheres have pointed out the advantages and deficiencies of earlier approaches. German (1984) concluded that "*although the status of sintering theory is incomplete, there are several recognised principles worthy of notice.*" It is thought that equations (H.4), (H.6) and (H.7) will provide an adequate initial description of how the porosity of the coating will vary with time and temperature, as required by equation (H.2).

Table H.1: Summary of the general characteristics of the sintering of a particle assembly (Kuczynski, 1972; German, 1984).

	Initial Stage	Intermediate Stage	Final Stage
Stage limit	$x/d_p < 0.3$	$x/d_p > 0.3$ up to $\varepsilon > 0.08$	$\varepsilon < 0.08$
Speed of densification	fast	slow	very slow
Nature of pore structure	continuous, uneven	continuous, smooth	isolated spherical voids
Geometrical observations	formation and growth of bond necks	neck growth continues, pores smoothen and contract	shrinkage of isolated pores
Comments		stage which most influences the final compact properties	gas trapped in pores can substantially limit the densification rate

Note:

1 Stage boundaries are not exact. For example, pore closure begins at about $\varepsilon = 0.2$.

The Age Function

The other constitutive relation required by equation (H.1) is the "age function", $\tau(r,t)$. The age of the coating at position r at time t is simply:

$$\tau(r,t) = t - t_o(r,t) \qquad \text{(H.8)}$$

where $t_o(r,t)$ is the time of formation of the coating element which is at $\{r,t\}$. A mass balance may be used to track the position of the element at $\{r,t\}$ backwards through time to find when it was formed, that is at $\{r_c(\, t_o(r,t)\,),\, t_o(r,t)\}$:

$$\int_{r_b}^{r_c(t_o(r,t))} \rho\left(T|_{r',t_o(r,t)}, \tau(r', t_o(r,t))\right) 2\pi r' L \, dr' = \int_{r_b}^{r} \rho\left(T|_{r',t}, \tau(r', t)\right) 2\pi r' L \, dr' \tag{H.9}$$

Clearly, equation (H.9) is very strongly implicit in τ. An analytical solution is not possible since $r_c(t)$ and $T(r,t)$ are not known analytically themselves. Direct numerical solution of equation (H.9) is likely to need significant computer time. However, calculation of τ fits naturally into the numerical scheme outlined in Section 4.3.2. When the positions of the control volumes and the nodal temperatures are adjusted after each time step, the average age of the coating in each control volume can be similarly updated. The new porosity can be calculated by equations (H.4) - (H.7). If the new porosity differs too much from its assumed value, then iteration is required for that time step.

It has been demonstrated how the coating-erosion model may be modified to allow a coating layer of variable porosity. Future research may lie in verifying the approach presented above, possibly including careful microscopic examination of the coating (see Section 5.4.3 for a possible technique).